HYDROTHERMAL PREPARATION OF NANOFIBERS FROM THAI ILMENITE MINERAL FOR PHOTO ELECTRODE OF DYE-SENSITIZED SOLAR CELL

ATHAPON SIMPRADITPAN

A THESIS SUBMITTED IN PARTIAL FULFILLMENT
OF THE REQUIREMENT FOR THE DEGREE OF
DOCTOR OF PHILOSOPHY IN NANOSCIENCE AND NANOTECHNOLOGY
COLLEGE OF NANOTECHNOLOGY
KING MONGKUT'S INSTITUTE OF TECHNOLOGY LADKRABANG
2015
KMITL-2015-NT-D-001-003

HYDROTHERMAL PREPARATION OF NANOFIBERS FROM THAI ILMENITE MINERAL FOR PHOTO ELECTRODE OF DYE-SENSITIZED SOLAR CELL

ATHAPON SIMPRADITPAN

A THESIS SUBMITTED IN PARTIAL FULFILLMENT
OF THE REQUIREMENT FOR THE DEGREE OF
DOCTOR OF PHILOSOPHY IN NANOSCIENCE AND NANOTECHNOLOGY
COLLEGE OF NANOTECHNOLOGY
KING MONGKUT'S INSTITUTE OF TECHNOLOGY LADKRABANG
2015

KMITL-2015-NT-D-001-003

หัวข้อวิทยานิพนธ์	การเตรียมเส้นใยนาโนด้วยวิธีการไฮโดรเทอร์มอลจากแร่อิลเมไนท์ของไทยเพื่อเป็นขั้วไฟฟ้าของเซลล์พลังงานแสงอาทิตย์ชนิดสีย้อมไวแสง
นักศึกษา	นายอรรถพล สิมประดิษฐ์พันธุ์
รหัสประจำตัว	54670101
ปริญญา	ปรัชญาดุษฎีบัณฑิต
สาขาวิชา	นาโนวิทยาและนาโนเทคโนโลยี
พ.ศ.	2558
อาจารย์ที่ปรึกษาวิทยานิพนธ์	รศ.ดร.วิษณุ เพชรภา
อาจารย์ที่ปรึกษาวิทยานิพนธ์ร่วม	ผศ.ดร.สรพงษ์ ภวสุปรีย์

บทคัดย่อ

งานวิจัยนี้ได้เตรียมเส้นใยนาโนจากแร่อิลเมไนท์ราคาถูกของไทยด้วยกระบวนการไฮโดรเทอร์มอลที่ไม่ซับซ้อนยุ่งยาก โดยใช้ชุดถังปฏิกรณ์ที่ผลิตเองในประเทศ ตัวอย่างที่ได้นำมาทำการวิเคราะห์และทดสอบสมบัติต่างๆ ดังนี้ โครงสร้างผลึกทำการวิเคราะห์ด้วยเทคนิคการเลี้ยวเบนลำรังสีเอกซ์ องค์ประกอบของธาตุทำการวิเคราะห์ด้วยเทคนิคเอกซเรย์ฟลูออเรสเซนต์และสเปกโตรสโคปีของอนุภาคอิเล็กตรอนที่ถูกปลดปล่อยด้วยรังสีเอกซ์ โครงสร้างทางจุลภาคทำการวิเคราะห์ด้วยกล้องจุลทรรศน์อิเล็กตรอนแบบส่องกราดและกล้องจุลทรรศน์อิเล็กตรอนแบบส่องผ่าน พื้นที่ผิวจำเพาะทำการวิเคราะห์ด้วยเทคนิค Brunauer–Emmett–Teller และสมบัติการดูดกลืนทางแสงทำการวิเคราะห์ด้วยเทคนิคยูวี-วิซิเบิล สเปกโตรสโกปี จากการทดลองพบว่าโครงสร้างผลึกของตัวอย่างที่สังเคราะห์ได้ที่อุณหภูมิต่างๆ มีผลึกเป็นแบบไฮโดรเจนไททาเนต ($H_2Ti_xO_{2x+1}$) อย่างไรก็ตามตัวอย่างที่สังเคราะห์ได้ที่อุณหภูมิ 100 °C เป็นเวลา 24 และ 48 ชั่วโมง และ 110 °C เป็นเวลา 24 ชั่วโมง มีโครงสร้างผลึกแบบรูไทล์ซึ่งเป็นโครงสร้างผลึกของแร่อิลเมไนท์ที่ใช้เป็นสารตั้งต้นปะปนอยู่ และพบว่าตัวอย่างที่สังเคราะห์ได้ที่อุณหภูมิ 100 °C เป็นเวลา 24 และ 48 ชั่วโมง และ 110 °C เป็นเวลา 24 ชั่วโมง มีลักษณะรูปร่างรวมตัวกันเป็นกลุ่มก้อนและมีลักษณะคล้ายกับท่อนาโนบางส่วน ขณะที่ตัวอย่างที่สังเคราะห์ได้ที่อุณหภูมิ 100 °C เป็นเวลา 72 ชั่วโมง 110 °C เป็นเวลา 48 และ 72 ชั่วโมง 120-130 °C เป็นเวลา 24, 48 และ 72 ชั่วโมง มีลักษณะรูปร่างเป็นเส้นใยนาโน นอกจากนี้พบว่า ค่าพื้นที่ผิวจำเพาะของตัวอย่างที่สังเคราะห์ได้มีแนวโน้มเพิ่มขึ้นเมื่ออุณหภูมิในการสังเคราะห์เพิ่มขึ้น ตัวอย่างที่เตรียมได้มีค่าการดูดกลืนแสงในช่วงความยาวคลื่น 300-500 nm และมีแนวโน้มเพิ่มขึ้นเมื่ออุณหภูมิในการสังเคราะห์เพิ่มขึ้น เส้นใยนาโนที่ผ่านการให้ความร้อนโดยการเผาที่อุณหภูมิ 300-400 °C มีโครงสร้างผลึกแบบ TiO_2 (B) ขณะที่

เส้นใยนาโนที่ผ่านการให้ความร้อนโดยการเผาที่อุณหภูมิ 500 °C มีโครงสร้างผลึกแบบ TiO_2 (B) และอนาเทสปะปนกัน นอกจากนี้เส้นใยนาโนที่ผ่านการให้ความร้อนโดยการเผาที่อุณหภูมิ 600-1,000 °C มีโครงสร้างผลึกแบบอนาเทส รูไทล์ และ Fe_2O_3 ปะปนกัน โดยเส้นใยนาโนเกิดการเปลี่ยนแปลงไปเป็นแท่งนาโนและอนุภาคนาโนที่อุณหภูมิในการเผาประมาณ 800-1,000 °C พื้นที่ผิวจำเพาะและค่าการดูดกลืนแสงมีแนวโน้มลดลงเมื่ออุณหภูมิในการให้ความร้อนโดยการเผาเพิ่มขึ้น

การนำไปประยุกต์ใช้งานด้านเซลล์พลังงานแสงอาทิตย์ชนิดสีย้อมไวแสงพบว่า เซลล์พลังงานแสงอาทิตย์ชนิดสีย้อมไวแสงที่เตรียมได้จากอนุภาคนาโนไททาเนียมไดออกไซด์เชิงพาณิชย์ผสมกับเส้นใยนาโนที่ผ่านการให้ความร้อนโดยการเผาที่อุณหภูมิ 800 °C เป็นเวลา 2 ชั่วโมง ที่ปริมาณร้อยละ 5 โดยน้ำหนัก มีค่าประสิทธิภาพสูงที่สุดที่ร้อยละ 3.90 ดังนั้นเส้นใยนาโนที่สังเคราะห์ได้สามารถนำไปประยุกต์ใช้งานเป็นขั้วไฟฟ้าในเซลล์แสงอาทิตย์ชนิดสีย้อมไวแสง

คำสำคัญ : ไททาเนียมไดออกไซด์, แร่อิลเมไนท์, ไฮโดรเทอร์มอล, เส้นใยนาโน, เซลล์พลังงานแสงอาทิตย์ชนิดสีย้อมไวแสง

Thesis Title	Hydrothermal Preparation OF Nanofibers from Thai Ilmenite Mineral for Photoelectrode of Dye-Sensitized Solar Cell
Student	Mr. Athapon Simpraditpan
Student ID	54670101
Degree	Doctor of Philosophy
Program	Nanoscience and Nanotechnology
Year	2015
Thesis Advisor	Assoc. Prof. Dr. Wisanu Pecharapa
Thesis Co-Advisor	Asst. Prof. Dr. Sorapong Pavasupree

ABSTRACT

This research focuses on the preparation of nanofibers from low-cost Thai ilmenite mineral via simple hydrothermal method with a Teflon-lined stainless steel autoclave. The prepared samples were characterized and tested by various methods. The crystalline structure was investigated by X-ray diffraction (XRD). The chemical composition was examined by X-ray fluorescence (XRF) and X-ray photoelectron spectroscopy (XPS). The morphology was characterized by scanning electron microscopy (SEM) and transmission electron microscopy (TEM). The specific surface area was measured by the Brunauer-Emmett-Teller analysis (BET). Optical absorption properties were tested by UV-Vis spectroscopy. The crystalline structures of all the as-synthesized nanofibers demonstrated a layered hydrogen titanate $H_2Ti_xO_{2x+1}$ structure. However, the prepared samples synthesized under hydrothermal temperature at 100 °C for 24 and 48 h and 110 °C for 24 h were consisted of rutile phase of the starting ilmenite mineral. The as-synthesized samples synthesized at 100 °C for 24 and 48 h and 110 °C for 24 h exhibited cluster-like morphology with some structure of nanotubes, while the as-synthesized samples synthesized at 100 °C for 72 h,110 °C for 48 and 72 h, 120-130 °C for 24, 48 and 72 h showed the some fiber-like morphology. Furthermore, the BET specific surface area of the as-synthesized sample tended to increase with increasing hydrothermal temperature.

The absorption spectra of the as-synthesized nanofibers exhibit a significant enhancement in the wavelength region of 300-500 nm and absorbance spectra tend to increase with increasing hydrothermal temperature. Furthermore, the as-synthesized nanofibers calcined at 300-400 °C showed TiO_2 (B) whereas the nanofibers calcined at 500 °C revealed a mixture of two phases of TiO_2 (B) and anatase. The nanofibers calcined at high temperature of 600-1,000 °C showed a mixture of tri-crystalline of anatase, rutile, and Fe_2O_3. The transformation of nanofiber structure to nanorod and submicron nanoparticle structure was occurred at 800-1,000 °C. The BET specific surface area and absorbance spectra of the calcined sample tends to decrease with increasing calcination temperature.

For dye-sensitized solar cell (DSSC) application, DSSC fabricated from 5 wt.% nanofibers calcined at 800 °C for 2 h mixed with P25 showed the highest η approximately 3.90%. Therefore, the prepared nanofibers could be potentially utilized as working electrode in dye-sensitized solar cell (DSSC).

Keywords : Titanium dioxide, Ilmenite mineral, Hydrothermal, Nanofibers, Dye-sensitized solar cell

ACKNOWLEDGEMENT

I would like to express my sincere thanks to my thesis advisor, Assoc. Prof. Dr. Wisanu Pecharapa and Asst. Prof. Dr. Sorapong Pavasupree for their valuable help and constant encouragement throughout the course of this research. I am most grateful for their teaching and advice, not only the research methodologies but also many other methodologies in life. I would not have achieved this far and this thesis would not have been completed without all the support that I have always received from them.

I am grateful for the Dr. Wirat Jarernboon and others person for suggestions of dye-sensitized solar cell. I would like to thank College of Nanotechnology, King Mongkut's Institute of Technology Ladkrabang (KMITL) for give us the educational and research opportunities.

In addition, this work has been supported by the National Nanotechnology Center (NANOTEC), NSTDA, Ministry of Science and Technology, Thailand and through the NANOTEC program of the Centers of Excellence Network, Energy Policy and Planning Office (EPPO), Ministry of Energy, Thailand, Sakorn Minerals Co., Ltd., Thailand and the Nanotechnology for Textile and Polymer Research Group (NanoTeP) of the Faculty of Engineering, Rajamangala University of Technology Thanyaburi (RMUTT), Thailand for thesis scholarship.

Finally, I most gratefully acknowledge my parents and my friends for all their support throughout the period of this research.

CONTENTS

Page

CONTENTS (CONT.)

CONTENTS (CONT.)

LIST OF TABLES

Table **Page**

LIST OF FIGURES

LIST OF FIGURES (CONT.)

Figure **Page**

LIST OF FIGURES (CONT.)

LIST OF FIGURES (CONT.)

Figure **Page**

LIST OF FIGURES (CONT.)

CHAPTER 1

INTRODUCTION

1.1 Motivation

Titanium oxide TiO_2 is one of the most attractive metal oxides for a multipurpose range of potential and novel applications, including humidity sensors, optoelectronic devices, lithium ion batteries, hydrogen storage, dye sensitized solar cell (DSSC), water treatment materials, catalysts, and gas sensors [1-3]. Especially, photocatalytic and energy application of TiO_2 for environmental protection were investigated from many researchers.

One-dimensional (1D) TiO_2 nanostructures including nanowires, nanorods, nanowhiskers, nanotubes and nanofibers have been intensively studied and researched due to their exceptional properties including chemical stability, biocompatibility, high photocatalytic reactivity and cost-effectiveness [4-7]. 1D-TiO_2 nanomaterials have been intensively investigated for their applications in photovoltaic device, photocatalysis, catalytic support and gas sensing [8-9]. There are many methods for synthesizing low-dimensional TiO_2-related nanomaterials, such as electrospinning, hydrogen treatment, anodic porous alumina templating, carbon nanotube inner templating, supramolecular assembly templating, anodic oxidation of a titanium sheet and hydrothermal method [10-11]. Among these methods, the hydrothermal method for the synthesis of TiO_2 nanotubes, firstly proposed by Kasuga et al. [12-13], has been widely exploited for low-dimensional nanostructures [14-15]. In contrast to other techniques, the hydrothermal method offers an inexpensive and environmentally friendly route, the ability to prepare a wide range of low-dimensional TiO_2 nanostructures, such as nanoparticles, nanowires, nanofibers and nanoribbons, and capability to control chemical, homogeneity, purity and phase composition under moderate conditions [16-18].

Due to the reduction of energy source in the earth, such as fossil fuel and natural gas. Many researchers have focused the new and different sources of energy, including wind-power, hydro-power, nuclear-power, geothermal energy, biomass, biofuel and solar energy [19-20]. Among them, solar energy is free, renewable and clean. Moreover, solar energy does not cause pollution and can be used in inaccessible areas where it is too difficult to extend the electricity power grid [21]. A solar cell is a device that directly converts the light energy into electrical energy through the process of photovoltaic [22]. Previously, silicon (Si) has been used as a commercial photovoltaic solar cell material to prepare the Si solar cell devices. The required production process for this type of solar cell is complicated and rather expensive. Furthermore, it is inflexible and must be fixed in a stable frame and protected against any aggressive [23]. As a consequence, an alternative approach for solar cell is to develop new materials and assembling methods for cheap solar cells. As one of the third-generation solar cells, dye-sensitized solar cell (DSSC) proposed by O'Regan and Grätzel has attracted substantial interest since 1991 [24]. DSSCs have received great attention as an alternative to silicon-based solar cells due to their cost-effective fabrication and relatively high performance conversion efficiency. Lightweight and flexible DSSC is convenient for transportation and can be used in complex environments. Most of the previous studies on the photoanodes of DSSC were based on TiO_2 for improving the performance of the DSSCs [25].

In this work, the direct synthesis of nanofibers from an ilmenite mineral is firstly reported. The nanofibers were prepared by the simple hydrothermal method using a low-cost ilmenite mineral as the starting material. Characterization of the prepared nanofibers is also reported. The photovoltaic properties of the DSSCs based on prepared nanofibers were investigated.

1.2 Objective

1.2.1 To study theories and principles of hydrothermal method for nanostructured materials synthesis.

1.2.2 To study the possibility of titanate nanofibers preparation by hydrothermal method from low-cost Thai ilmenite mineral.

1.2.3 To study the effect of hydrothermal process parameters and heat treatment on properties of nanofibers.

1.2.4 To study chemical properties, structural properties, morphology and optical properties of prepared materials.

1.2.5 To study the functionality of the prepared nanofibers fabricated in dye sensitized solar cell application.

1.3 Scope of Study

1.3.1 Review theories and principles of hydrothermal method for nanostructured materials synthesis.

1.3.2 Synthesize nanofibers by simple hydrothermal method under various conditions with a Teflon-lined stainless steel autoclave unit using low-cost Thai ilmenite mineral as starting materials.

1.3.3 Characterize the chemical properties, structural properties, morphology and optical properties of prepared materials.

1.3.4 Utilize the prepared nanofibers as a working electrode for dye sensitized solar cell.

1.4 Expected Results

1.4.1 Nanofibers can be synthesized by simple hydrothermal method using low-cost Thai ilmenite mineral as starting materials.

1.4.2 Properties and their applications of prepared nanofibers will be acknowledged.

1.4.3 The definition and noteworthy properties of nanofibers, hydrothermal and dye-sensitized solar cell will be clearly understood.

1.4.4 The enhancement of efficiency in the DSSC applications with prepared nanofibers will be demonstrated.

CHAPTER 2

THEORETICAL BACKGROUNDS

2.1 Titanium Dioxide

2.1.1 History of Titanium Dioxide [26]

Titanium was discovered by William Gregor in 1791 [26]. This happened of novice material was initialed by the studying mineralogy of Gregor, which led him to discover a sample of a black sandy substance in his neighborhood, and named it menachanite. Four years later in 1795, Martin H. Klaproth, found a new chemical element in this mineral, called it Titanium. This discovery was humongous monsters that ruled the world in Greek mythology. This pure element of titanium was not able to use immediately, however, it is the first step for synthesis titanium dioxide (TiO_2) in the future [26].

2.1.2 Structural and Properties of Titanium Dioxide [27-29]

Titanium dioxide (TiO_2) is a naturally occurring oxide of the element titanium. It is known as titanium (IV) oxide or titania. TiO_2 appears fine white powder with chemical formula TiO_2 are shown in Figure 2.1. The main source of TiO_2 is ilmenite, leucoxene and rutile mineral. The structure of TiO_2 was appeared three phases: anatase, brookite and rutile [27] as shown in Figure 2.2. The crystalline structures of anatase and rutile phase are tetragonal while brookite phase is orthorhombic structure. A rutile unit cell contains six atoms, with lattice constants of a_0 = 4.593 Å and c_0 = 2.958 Å. An anatase unit cell contains twelve atoms per unit cell with lattice parameters a_0 = 3.785 Å and c_0 = 9.511 Å. Last phase, brookite unit cell parameters are a_0 = 5.4558 Å and c_0 = 5.1429 Å with eight atom per unit cell [28]. Each structure exhibits different physical properties, which lead to their different applications. Due to the larger band gap of anatase of 3.2 eV, compared with 3.0 eV for rutile, the photocatalytic performance of anatase structure is higher than rutile phase. This is attributed to a larger band gap reduced electron-hole recombination, parameters that contribute to improved performance. However, some investigations demonstrated that rutile TiO_2 nanostructured had better photocatalytic efficiency of some organic pollutants and heavy transition metal ions than nanostructured of anatase TiO_2 [29]. This result attributed to rutile has a smaller band gap of 3.0 eV with excite at long wavelengths that extend into the visible light region at 410 nm.

The phase transformation of TiO_2 is occurred with changing treatment temperature. In general, the titanate structure of the as-synthesized is transformed into anatase phase with increasing temperature to 500-600 °C while rutile phase was appeared in very high temperature about 600-1,000 °C [27].

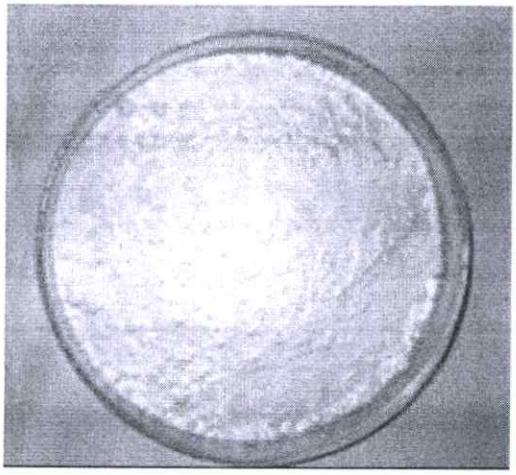

Figure 2.1 TiO_2 powder.

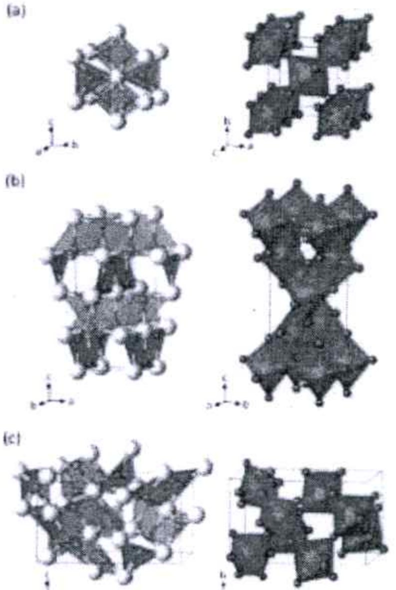

Figure 2.2 Crystalline structure of TiO_2; (a) anatase; (b) rutile and (c) brookite phase [30].

Table 2.1 Physical properties of TiO_2 [31].

Physical properties of TiO_2	
Molecular weight	79.87 g/mol
Density	4.23 g/cm^3
Melting point	1870 °C
Boiling point	2972 °C
Porosity	0%
Dielectric constant (1MHz)	85
Thermal conductivity (25°C)	11.7 WmK^{-1}
Electrical resistivity (25°C)	10^{12} ohm.cm
Electrical resistivity (700°C)	2.5×10^4 ohm.cm
Young's modulus	230 GPa

The physical properties of TiO_2 are shown in Table 2.1. The band gap energy of TiO_2 is 3.2 eV, include strong ultraviolet absorptivity, non-toxicity, long-term photostability, chemical stability, biocompatibility, high photoreactivity and cost-effectiveness. Due to these extraordinary properties, TiO_2 is utilized in several applications for photocatalyst materials, electronic and energy-related devices, such as photocatalyst for organic pollutants degradation, self-cleaning ceramics and glass, antiseptic and antibacterial compositions, water-splitting catalysts for hydrogen generation, humidity sensor, optoelectronic device, lithium ion battery, hydrogen storage and dye-sensitized solar cells (DSSCs) [27]. The conventional processes for production of pigment grade TiO_2 and titanium metal are schematically presented in Figure 2.3. The sulphate process and the chloride process to manufacture titanium pigment differ in their chemistry and raw material requirements. The chloride process has rule to the pigment industry because of their advantages over the sulphate process such as cost-effective and waste management. However, the sulphate process may use low-grade titanium as raw material, while the chloride process needs a high grade of rutile [32]. Therefore, many different process to prepare TiO_2 nanomaterials, i.e., sol–gel, micelle and inverse micelle, solvothermal, chemical vapor deposition, electro-deposition, hydrothermal and so on [33-35].

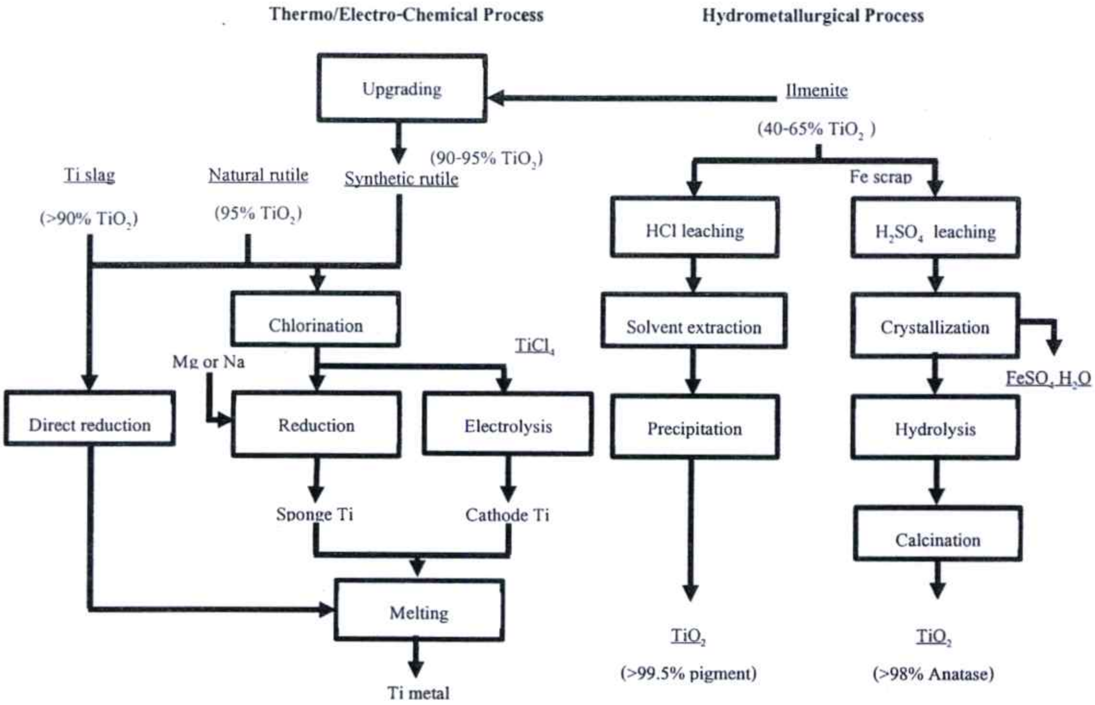

Figure 2.3 Schematic of processes for the production of Ti metal and pigment TiO_2 [32].

2.2 Ilmenite Mineral

2.2.1 History of Ilmenite Mineral [36-37]

Ilmenite is discovered at Ilmen Lake in the Ilmen Mountains, Miask in the southern portion of the Ural Mountains of Russia. Ilmenite form in igneous rocks derived from the upper mantle. It found at the depths of 400 km with high pressures of 12–13 GPa. Ilmenite forms as a primary mineral in mafic igneous rocks and is concentrated into layers by a process called "magmatic segregation". Ilmenite is a component of a magma, which the heavier crystals of ilmenite fall to the bottom of the magma chamber and collect in layers. It is these layers that constitute a rich ore body for titanium miners. Ilmenite also occurs in pegmatites and some metamorphic rocks as well as in the sedimentary rocks that are formed from the weathering and erosion of them [36–37].

2.2.2 Structural and Properties of Ilmenite Mineral

Ilmenite is an interesting naturally mineral because it is one of the major sources of TiO_2 which is often produced by sulfate and chloride processes. Ilmenite is present in tron-black or steel-gray as show in Figure 2.4. The crystalline structure of ilmenite is $FeTiO_3$ with compose

50% of TiO_2 as show in Figure 2.5. The ilmenite crystal structure is an ordered derivative of the corundum structure; in corundum all cations are identical but in ilmenite Fe^{2+} and Ti^{4+} ions occupy alternating layers perpendicular to the trigonal c axis. The ilmenite crystal structure is configured of FeO_6 and TiO_6 octahedra.

Ilmenite is a metallic to submetallic mineral is use to megnet application due to weakly magnetic properties. It is often associated with magnetite and therefore ilmenite is a minor ore of iron as the magnetite and ilmenite are processed for their iron contents. The magnetic properties and of ilmenite are of specific importance in commercial extraction via magnetic separation [36–37]. Table 2.2 presented the physical properties of ilmenite mineral.

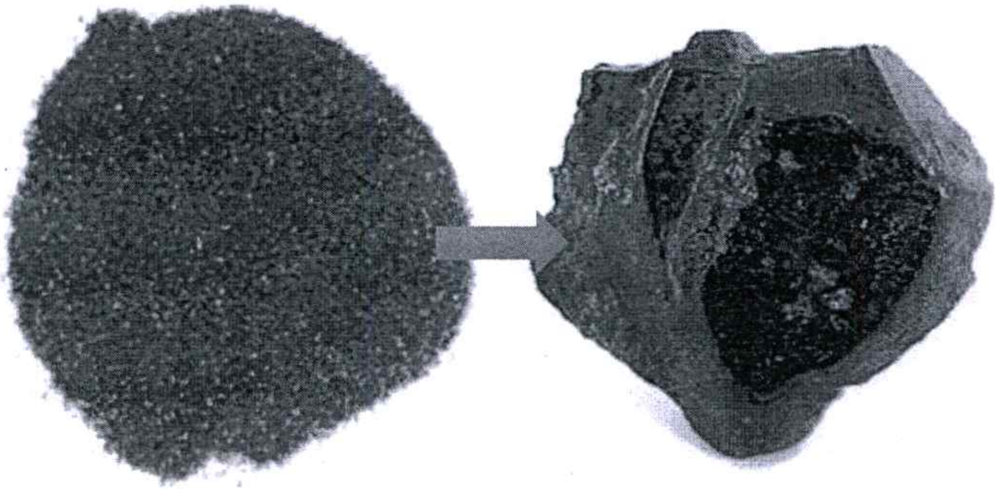

Figure 2.4 Ilmenite mineral [36].

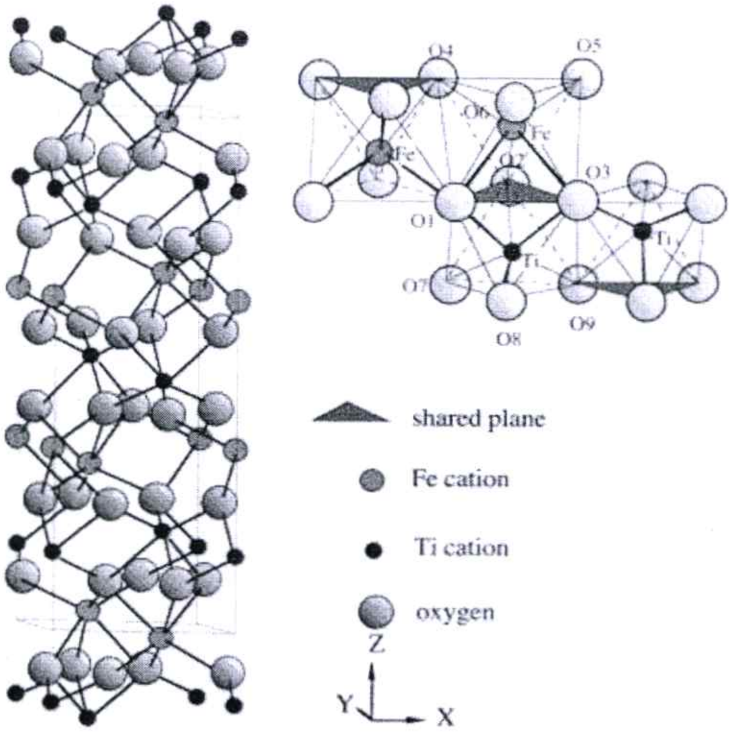

Fig 2.5 Structure of $FeTiO_3$ and configuration of FeO_6 and TiO_6 octahedra [38].

Table 2.2 Physical properties of ilmenite mineral [36].

Physical properties of ilmenite mineral	
Luster	Metallic, Sub-Metallic
Diaphaneity (Transparency)	Opaque
Colour	Iron black or black
Streak	Black to reddish brown
Hardness (Mohs)	5 - 6
Hardness (Vickers)	VHN_{100}=566 - 698 kg/mm^2
Tenacity	Brittle
Fracture	Conchoidal, Sub-Conchoidal
Density (measured)	4.68 - 4.76 g/cm^3
Density (calculated)	4.789 g/cm^3

2.3 Hydrothermal Technology [39-40]

2.3.1 History of Hydrothermal Technology

Hydrothermal processing is described to any chemical reaction of heterogeneous of substance in the aqueous solvents under high pressure and temperature conditions. Hydrothermal process use to dissolve and recrystallize materials that insoluble under natural conditions. The British geologist, Sir Roderick Murchison (1792-1871) was first described to hydrothermal, it is the phenomenon of water at higher pressure and temperature, leading to the formation of various rocks and minerals in the earth's crust. In general, the largest single crystal formed in nature and some single crystals created by man in experimental. These occurring two are important of the beginning of hydrothermal. Furthermore, in the original Greek meaning of the words 'hydros' meaning water and 'thermos' meaning heat. Thus, the meaning of hydrothermal is relate to the reaction of water under high temperature and pressure. Recently, Byrappa and Yoshimura define hydrothermal as any heterogeneous chemical reaction in the presence of a solvent (whether aqueous or non-aqueous) above the room temperature and at pressure greater than 1 atm in a closed system [39].

Among various technologies for preparation of advanced materials, the hydrothermal technique occupies several advantages over conventional technologies because this processes covers the preparation of fine to ultra fine crystals, bulk single crystals, hydrothermal transformation, hydrothermal sintering, hydrothermal decomposition, hydrothermal stabilization of structures, hydrothermal dehydration, hydrothermal extraction, hydrothermal treatment, hydrothermal phase equilibria, hydrothermal electrochemical reactions, hydrothermal recycling, hydrothermal microwave supported reactions, hydrothermal mechanochemical, hydrothermal sonochemical, hydrothermal electrochemical processes, hydrothermal fabrication, hot pressing, hydrothermal metal reduction, hydrothermal leaching, hydrothermal corrosion, and so on. Thus it is clear that the hydrothermal processing of advanced materials is a highly interdisciplinary subject and the technique is popularly used by physicists, chemists, ceramists, hydrometallurgists, materials scientists, engineers, biologists, geologists, technologists, and so on [39-40].

2.3.2 Hydrothermal Technology for Nanomaterials

The hydrothermal processing of nanomaterials can be described to process of super-heated aqueous solution. for preparation of sub-micron to nanoparticles. Nanostructured materials exhibit unique and interesting properties including, improvement of physical, chemical, electrical and mechanical properties[41]. Moreover, for processing nanomaterials, the hydrothermal technique offers special advantages because of the highly controlled diffusivity in a strong solvent media in a closed system, high purity, controlled stoichiometry, high quality, narrow particle size distribution, controlled morphology, uniformity, less defects, dense particles, high crystallinity, excellent reproducibility, controlled microstructure, simple equipment, higher dispersion, higher rates of reaction, lower temperature operations in the presence of the solvent, lower energy consumption, fast reaction times, lowest residence time, avoidance of pollution and so on [39-40]. Figure 2.6 and Figure 2.7 shows pressure temperature map of materials processing techniques and different size of materials prepared by hydrothermal and conventional techniques, respectively.

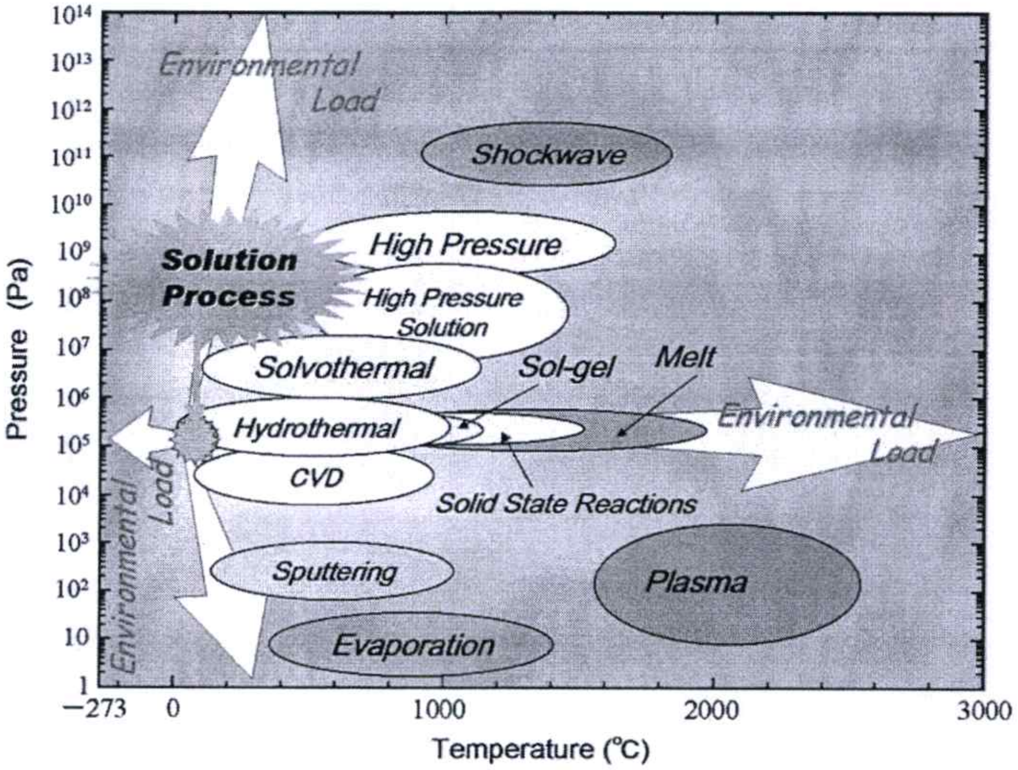

Figure 2.6 Pressure temperature map of materials processing techniques [40].

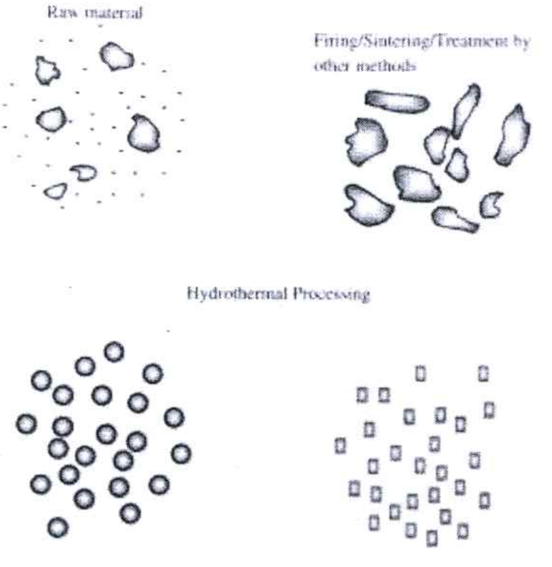

Figure 2.7 Different size of materials prepared by hydrothermal and conventional techniques [40].

The hydrothermal technology for synthesize nanomaterials was originated in 1845 when Schafthaul synthesized fine powders of sub-microscopic to quartz nanoparticles using a papin's digester containing freshly precipitated silicic acid [42]. This first report carried out to the synthesis of nanomaterials which interest and importance for materials education and materials industry on current time. Recent research shows the synthesis of nanomaterials by hydrothermal technique such as Zhu et al. have reported the synthesis of silver dendrite nanostructures using anisotropic nickel nanotubes [43] via mild hydrothermal reactions. The nickel nanotubes acted as a reducing agent. Xie et al. and Liu et al. have reported the hydrothermal synthesis of cobalt nanorods and nanobelts with and without surfactants. Niu et al. have prepared NiCu alloy nanocrystallites at low temperatures under hydrothermal conditions [44]. Jiao et al. have reported the hydrothermal preparation of ZrO_2 nanocrystallites using organic additives [45]. Sorescu et al. have synthesized nanocrystalline rhombohedral In_2O_3 under hydrothermal conditions at about 200 °C in 4 h [46]. This In_2O_3 has a corundum structure and is a high pressure phase crystallizing with a rhombohedral structure. The hydrothermally treated product was post-annealed at 500 °C. Several workers have prepared the a-Fe_2O_3 (hematite) phase as nanoparticles under hydrothermal conditions (using both aqueous and non-aqueous solvents) with or without surfactants [47-49]. Interestingly, TiO_2-derived nanotubes obtained via hydrothermal method was first synthesized by Kasuga et al. in 1998-99. This nanotubes had diameter and length about 8 nm and 100 nm, respectively. It is enchanting microstructure and promising photoelectrochemical applications [12, 50]. Figure 2.8 shows the nanostructured materials including, nanotubes, nanosheets, nanofibers and nanowires synthesized via hydrothermal method. The definition of these materials can be attributed to (1):Nanosheets is a two-dimensional nanostructure with thickness in a scale ranging from 1 to 100 nm, (2): Nanotube is a hollow cylindrical or toroidal tube measuring nanometers in diameter, (3): Nanofibers are defined as fibers with diameters less than 100 nanometers. Nanofibers are nanomaterials that have a large length-diameter ratio, (4): Nanowires is a nanostructured materials with the diameter constrained to tens of nanometers or less and an unconstrained length with aspect ratio greater than 1,000 . Nanowires also show other peculiar electrical properties due to their size.

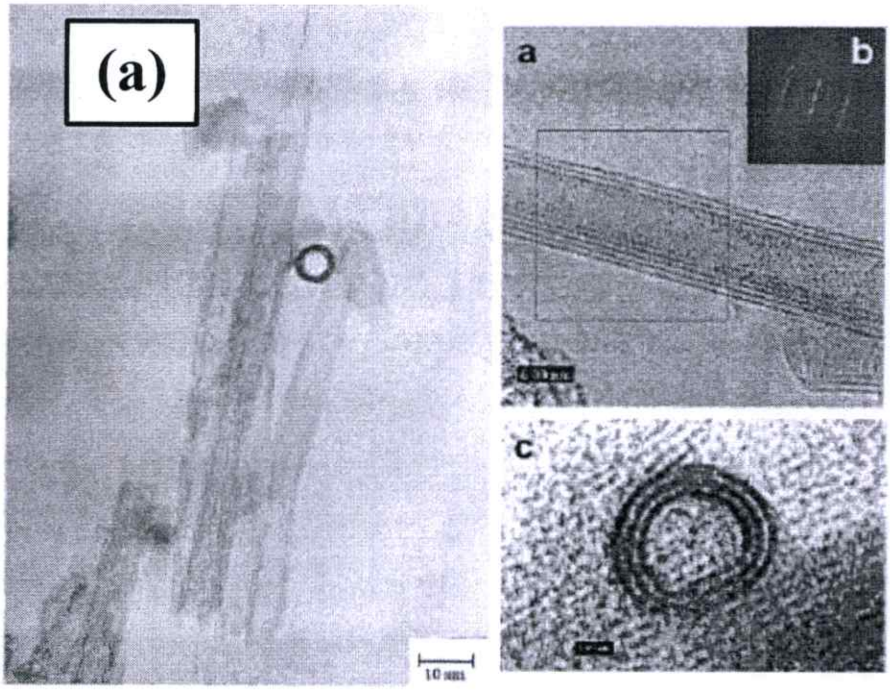

Figure 2.8 The nanostructured materials synthesized via hydrothermal method; (a) nanotubes, (b) nanosheets, (c) nanofibers and (d) nanowires [12, 17 51-52].

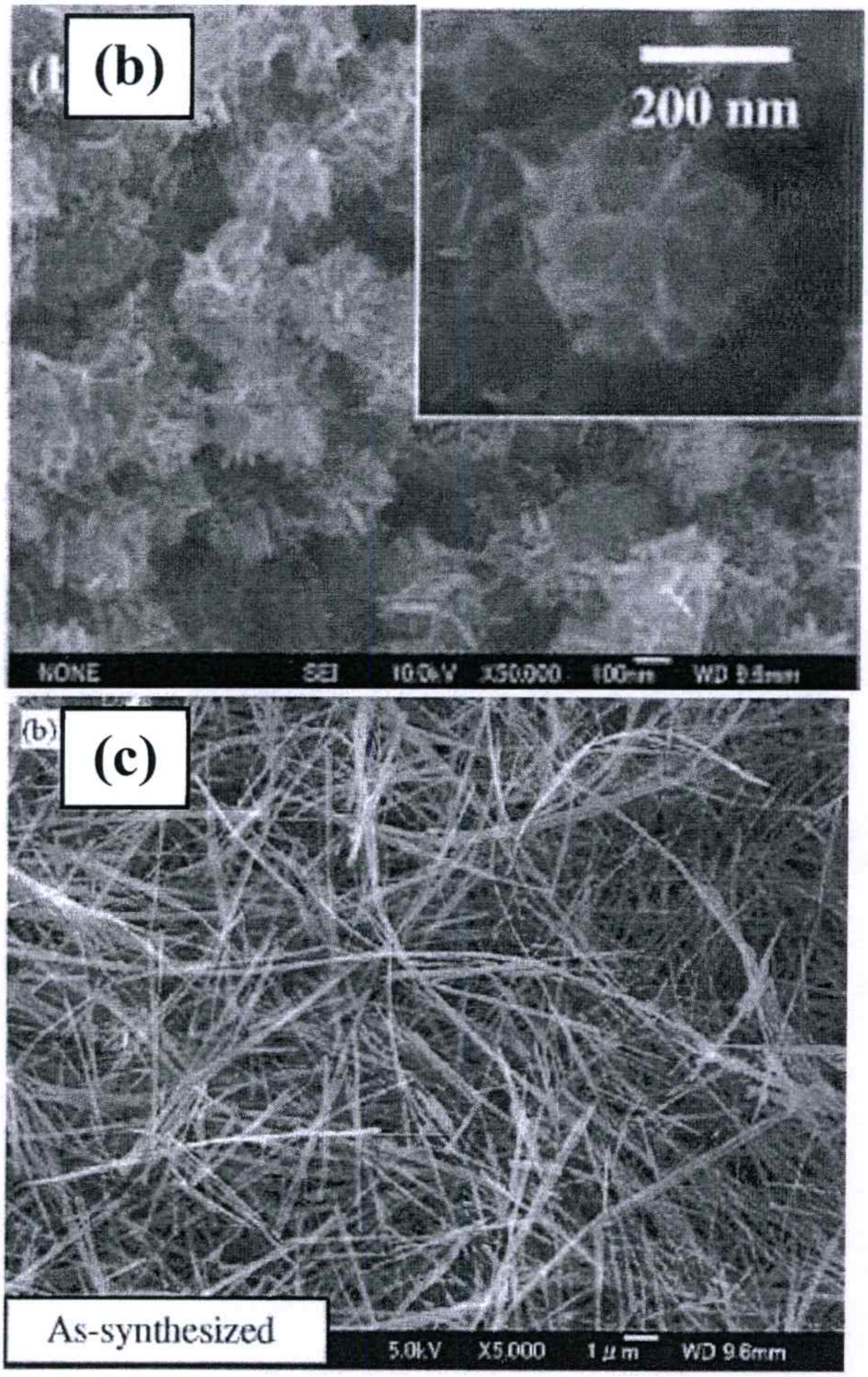

Figure 2.8 (cont.) The nanostructured materials synthesized via hydrothermal method; (a) nanotubes , (b) nanosheets, (c) nanofibers and (d) nanowires [12, 17, 51-52].

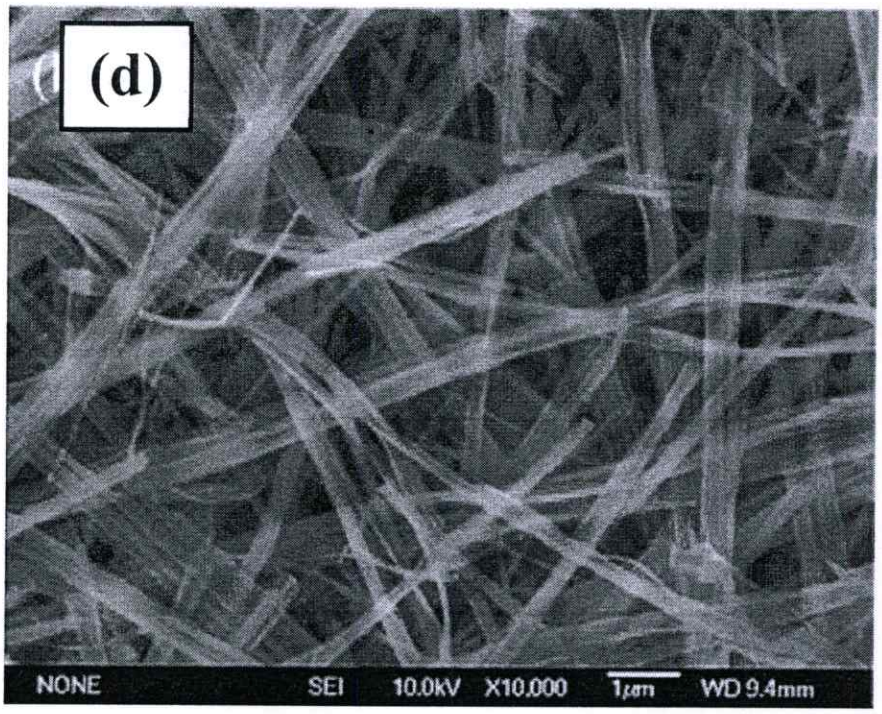

Figure 2.8 (cont.) The nanostructured materials synthesized via hydrothermal method; (a) nanotubes , (b) nanosheets, (c) nanofibers and (d) nanowires [12, 17, 51-52].

2.3.3 Factor in Hydrothermal Processing of Nanomaterials

2.3.3.1 Effect of the Starting Materials

The hydrothermal synthesis of nanomaterials such as nanotubes, nanowires, nanofibers, nanosheets and nanoparticles and so on can be prepared from different starting materials such as rutile or anatase TiO_2, commercial grade TiO_2 nanoparticles (Degussa P25), titanium butoxide, Tetra-n-butyl titanate and ilmenite, rutile and leucoxene mineral [53-66]. S. Pavasupree et al. [54-55] and Jitputti et al. [56] using titanium (IV) butoxide as the starting materials to synthesize TiO_2 nanoparticles by hydrothermal method. S. Pavasupree et al. [52, 57] synthesized titanate nanofibers by hydrothermal method using natural rutile sand as the starting materials. Yu et al. and R. Yoshida et al. [58-59] using TiO_2 powder as the starting materials to synthesize TiO_2-derived nanotubes by hydrothermal treatment. D. Aphairaj et al. [60-61] synthesized nanotubes using natural leucoxene mineral as the starting materials by the hydrothermal method. Jitputti et al. [51] using titanium tetraisopropoxide as the starting materials to prepare flower-like titanate superstructure by simple hydrothermal process. Jitputti et al. [52],

K. Pal et al. [62] Yoshida et al. [63], K Asagoe et al. [64] and Suzuki et al. [65] using TiO_2 powder as the starting materials to produce TiO_2 nanowires through the one step hydrothermal process Interestingly, Lidija and his worker [66] reported the effect of size of rutile mineral using as the starting material on the morphology of nanomaterials by hydrothermal process. The diameter were influenced the morphology of prepared samples. When diameter of rutile mineral is 10-200 μm, the nanofibers were obtained while reducing diameter of ruitile mineral to 0.28 μm, the nanotubes were achieved.

2.3.3.2 Effect of Hydrothermal Temperature

The hydrothermal temperature is one of the factors influencing structural and morphological of titania nanomaterials [67]. Many researchers have synthesized nanomaterials by hydrothermal process at various temperature. In general, titanate nanosheets could be formed at temperatures lower than 100 °C . Sreekantan and Lai found that the delaminating step of spherical-shape precursors led to the formation of nanosheets at 90 °C. On the other hand, reported that the delaminating step occurred in the presence of sodium ions at an initial temperature of 70 °C, this phenomenon led to the formation of two-dimensional nanosheets. For temperatures lower than 100 °C, almost all researchers concluded that nanotubes did not form, but leading to the formation of nanosheets. In contrast, increasing hydrothermal temperature from 100 to 150 °C, titanate nanosheets grew and curled up to form nanotubes, nanofibers, nanowires and nanorods [68-69]. Yoshida et al. synthesized $TiO_2(B)$ nanowires and TiO_2 anatase nanowires by the hydrothermal processing in 10M NaOH aq. at 150 °C [63]. Yuan and Su [70] stated that the yield of nanotubes up to 80-90% increased with the hydrothermal temperature raising to 100-150 °C. Seo et al. found that the amount and length of titania nanotubes increase with the hydrothermal temperature of 100-200 °C. Tsai and Teng reported that the high surface area titania nanotubes was found at temperature of 130 °C [71]. Ma et al. [72] found that the combination of a hydrothermal temperature 130-150 °C of 24-72 h obtained purity of titanate nanotubes. Hydrothermal temperature played an important role in promoting the nucleation and crystal growth of the titanate nanotubes. The degree of crystallinity in the final product increased with raising the hydrothermal temperature. The optimum operating temperatures between 125 and 150 °C produced high yield of titanate nanotubes. The formation of nanotubes began to decrease at temperatures higher than 180 °C with the formation of nanorods [73]. However, Lee et al. [74] observed that the nanorod formation phenomenon occurred even at 160 °C, a temperature lower than that reported by Lan et al. With the hydrothermal temperature increasing to 160 °C, the pore volume and specific surface area of the titanate nanotubes were reduced due to (a) the limitation of the interlayer spaces; and (b) sodium ions is replaced by protons after washing process with acid and deionized water. Lee et al. [75] investigated the nanorods formation mechnism at a temperature of 170 °C. They found interlayer transformation of titanate nanotubes to be changed at 170 °C. The interlayer spaces started to decrease influenced to the pore volume and surface area of the sample became smaller when the temperature was higher than 170 °C.

2.3.3.3 Effect of Hydrothermal Time

The hydrothermal time is another important factor that affects the structure and morphological of titania nanomaterials, as well as the temperature. E. Horvath et al. [76] reported the production of nanotubes increased with raising the hydrothermal time treatment. Thorne et al. [77] found that the production of nanotubes increased from 0 to 80% when the duration of hydrothermal treatment increased from 2 to 72 h at 150 °C.

2.3.4 Instrumentation in Hydrothermal Processing

Hydrothermal process involved preparation of materials in corrosive aqueous solution under high temperature and pressure. Therefore, an autoclave can be used at extreme condition. This preparation must perform by endurable apparatus and safety place of experimental. Thus, an ideal hydrothermal autoclave should have the following characteristics [39-40]:

i. Inertness to acids, bases and oxidizing agents.

ii. Ease of assembly and disassembly.

iii. Sufficient length to obtain a desired temperature gradient.

iv. Leak-proof with unlimited capabilities to the required temperature and pressure range.

v. Can be used at high pressure and temperature experiments for long periods with no damage.

2.4 Dye sensitized Solar Cell (DSSC)

Dye sensitized solar cells (DSSCs) are high potential device of thin-film photovoltaic cell or semiconductor photovoltaic that currently attracting extensive and intense academic and industrial interest because of their ability to directly convert solar radiation into electric current. DSSCs have attracted worldwide attention in the past twenty years due to their comparative advantage taking into account both energy conversion efficiency and low fabrication cost compared with silicon-based solar cells. Moreover, DSSCs have many advantages such as, environmentally friendly photovoltaics, transparency and flexible device.

DSSC is categorized into photoelectrochemical type because of redox electrolyte mechanism in its cell. In general, DSSC consist of a mesoporous anode formed by film of metal oxide that serves as the electron acceptor and a transport layer coated with a thin layer of sensitizer-dye molecules for light absorption and electron injection into the TiO_2 conduction band. DSSC has been used as Building Integrated Photovoltaics (BIPV) such as flat roof, skylight. The conversion efficiency varies between 6-10 % depending on the module size and the technology is currently on the pilot plant scale [78-79].

2.4.1 History of Dye sensitized Solar Cell

The history of dye sensitized solar cells (DSSC) started in 1972 with a chlorophyll sensitized zinc oxide (ZnO) electrode. For the first time, photons were converted into an electric current by charge injection of excited dye molecules into a wide band gap semiconductor. In this year, a lot of fundamental research was prepared on ZnO-single crystals. These devices showed lower efficiency due to a monolayer of dye molecules on a flat surface can only absorb up to 1% of the incident light [80]. Therefore, nanoporous TiO_2 electrodes was interested in next time because of its a roughness factor of ca. 1,000 . In 1991, B. Oregan and M. Grätzel were the first pioneer to fabricate dye-sensitized nanocrystalline solar cells, the energy conversion efficiency was reached to 7.1% with incident photon to electrical current conversion efficiency (IPCE) was approximately 80% [24, 81]. This device has some advantages, including low-cost and simplicity to operating. This photovoltaic device is consisted of working electrode, dye-sensitizer, redox mediator and counter electrode, called as dye-sensitized solar cell (DSSC). This simple structure and low-cost technology have further stimulated great research interest to improve the efficiency of dye-sensitized solar cells which has attained ca.10% [78].

2.4.2 Structure and Material in Dye sensitized Solar Cell

The schematic structure of DSSC is shown in Figure 2.9. DSSC is composed of three main parts; counter electrode, working electrode and electrolyte. The DSSC component and functionalities of each part are described in this section.

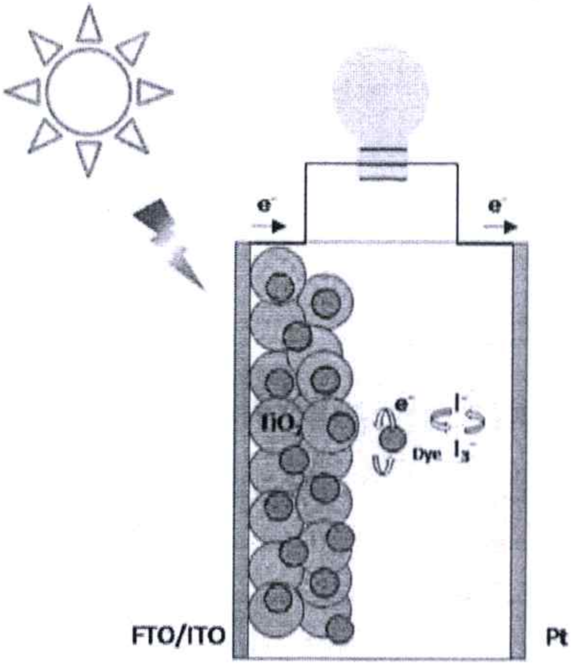

Figure 2.9 The schematic structure of DSSC.

2.4.2.1 Counter Electrode

The counter electrode serves to transfer electrons from the external circuit to electrolyte solution. The counter electrode must have the following properties, good electrical conductivity, high porosity for increases the reaction surface area and must be a good catalytic. The material is used as the counter electrode is metal, platinum (Pt), but due to the expensive platinum metals may use other materials instead of carbon powders, carbon nanotubes or conducting polymer such as PEDOT or polypyrrole as the counter electrode.

2.4.2.2 Working Electrode

1) Transparent Conducting Oxide-Coated Glass Substrate

Transparent conducting oxide-coated glass is typically used as the substrate for metal oxide photoelectrode. Transparent conducting oxide-coated glass has low sheet resistance and high transparency in visible light, their properties maybe promoted performance of DSSC. Due to its high resistance in air of Indium-tin oxide (ITO), fluorine-doped tin oxide (FTO) is chosen to use as the transparent conducting glass substrate in DSSC electrode owing to low sheet resistance, good conductivity and more stable at high temperature.

2) Oxide Semiconductor Layer

Metal oxide is the renowned materials for semiconductor layer in DSSC because of their exceptional stability against photo-corrosion on optical excitation in the band gap [82]. The well-known oxide included ZnO, CdSe, CdS, WO_3, Fe_2O_3, SnO_2, Nb_2O_5, Ta_2O_5 and TiO_2. For high DSSC performance, TiO_2 is preferred as the photoelectrode material due to good chemical stability in solution, high porosity, nontoxic and cost-effectiveness. The interesting properties of nanostructured TiO_2 electrodes such as nanotubes, nanofibers and nanosheets have been studied for the development of DSSC efficiency due to their unique properties supported to high dye adsorption, increased porous structure, improved electron harvesting and convenient charge transfer, resulting to the increase of DSSC performance.

3) Dye Sensitizer

Dye molecules of proper molecular structure are used to sensitized metal oxide surface of working electrode are function of light absorption and electron generation in the device by inject excited electron into metal oxide. Good properties of dye sensitizer are long-term chemical stability, high absorption in visible light and non-toxic. Ru complex photosensitizers was developed by Gräzel's group, one legendary example is the cis-Di(thiocyanato)bis(2,2'-bipyridyl)-4,4'-dicarboxylate) ruthenium(II), coded as N3 or N-719 dye it has been an outstanding solar light absorber and charge-transfer sensitizer. The red dye or N3 dye is capable of absorbing photons of wavelength ranging from 400 nm to 900 nm (see Figure 16) because of metal to ligand charge transfer transition [83]. Dye sensitizer extracted from natural such as shiso leaf pigments, Black rice, Fruit of calafate, Rosella and Natural anthocyanins have been investigated for DSSC because of reducing environment pollutions and low-cost production comparing to Ru complex dye. Therefore the natural dye is also one of dye sensitizer for the improvement in DSSC technology opportunities [82].

2.4.2.3 Redox Electrolyte

In the DSSCs, iodine (I^-) and triiodide (I_3^-) usually used as an electrolyte. It is locate between the working electrode and the counter electrode. This electrolyte can regenerate the oxidized dye molecules and hence completing the electric circuit by mediating electrons between the working electrode and counter electrode. Generally, NaI, LiI and R4NI (tetraalkylammonium iodide) are the recognized mixture of iodide typically used as electrolyte. Due to ion conductivity in the electrolyte is effect to cell performance. Thus, solvent with lower viscosity is highly optional to use electrolyte. Furthermore, counter cations of iodides such as Na$^+$, Li$^+$, and R4N$^+$ may be affect the cell performance mainly due to their adsorption on working electrode or ion conductivity. It has been found that addition of *tert*-butylpyridine to the redoxing electrolyte improves cell performance. The ideal characteristics of the redox electrolyte in DSSC device have been described by Wolfbauer et al. (2001) as follows [84];

I. Redox potential thermodynamically (energetically) favorable with respect to the redox potential of the dye to maximize cell voltage;

II. High solubility to the solvent to ensure high concentration of charge carriers in the electrolyte;

III. High diffusion coefficients in the used solvent to enable efficient mass transport;

IV. Absence of significant spectral characteristics in the visible region to prevent absorption of incident light in the electrolyte;

V. High stability of both the reduced and oxidized forms of the couple to enable long operating life;

VI. Highly reversible couple to facilitate fast electron transfer kinetics;

VII. Chemically inert toward all other components in the DSSC.

2.4.3 Operating Principle of Dye sensitized Solar Cell

DSSC is typically composed of three parts, including dyed-metal oxide layer used as working electrode, redox electrolyte and counter electrode. The mechanism of DSSC is generally similar to the mechanism of the excited chlorophyll by sunlight in plant photosynthesis. The mechanism of the dye-sensitized solar cell is illustrated in Figure 2.10, showing schematically the relative energy levels of a working DSSC. The sunlight with photon is absorbed by the dye molecule adsorbed on the layer of metal oxide and an electron from a molecular ground state S_0 is excited to a higher lying excited state S^* (1). The exited electron is injected to the conduction band of the metal oxide layer departed from the dye molecule and the dye molecule ground state is oxidized to an oxidized state S^+ (2). The injected electron transport through the metal oxide structure to the transparent conducting glass substrate (working-electrode) and finally through an external load to the counter-electrode (3). At the counter-electrode, the redox reaction was occurred, triiodide (I_3^-) in the electrolyte transformed to iodine ($3I^-$) by the electron from working-electrode (4). The oxidized dye molecule was reduced by the iodine in the electrolyte (5). The voltage generated under illumination relates to the difference between the Fermi level of the electron in the solid and the redox potential of the electrolyte. Overall, the device generates electric power from light without suffering any permanent chemical transformation [85]. This mechanism is summarized in equation 2.1-2.4.

1. The incident photon is absorbed by dye molecule adsorbed on the TiO_2 layer.

2. The dye molecule is excited from the ground state (S_0) to the excited state (S^*). The excited electrons are injected into the conduction band of the TiO_2 electrode, while the dye molecule is oxidized to an oxidized state (S^+).

$$S + h\nu \longrightarrow S^* \qquad (2.1)$$

$$S^* \longrightarrow S^+ + e^- \ (TiO_2) \qquad (2.2)$$

3. The injected electrons in the conduction band of TiO_2 are transported to TiO_2 nanoparticles followed to the transparent conducting glass substrate. These electrons finally transport to the counter electrode through the circuit.

4. The oxidized dye molecule (S^+) accepts electrons from the I^- ion redox mediator. It is reduced by this electron to the ground state (S), and the I^- is oxidized to the oxidized state, I_3^-.

$$S^+ + e^- \longrightarrow S \qquad (2.3)$$

5. The oxidized redox mediator, I_3^-, diffuses toward the counter electrode and then it is reduced to I^- ions.

$$I_3^- + 2\,e^- \longrightarrow 3\,I^- \qquad (2.4)$$

The efficiency of a DSSC is depends on four energy levels of the component: the excited state (approximately LUMO) and the ground state (HOMO) of the dye-sensitizer, the Fermi level of the TiO_2 electrode and the redox potential of the mediator (I^-/I_3^-) in the electrolyte.

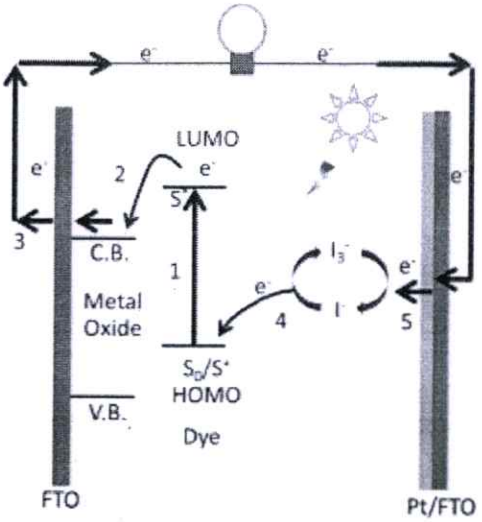

Figure 2.10 Principle of operation of the dye-sensitized solar cell.

2.5 Characterization

2.5.1 X-ray Diffraction Spectroscopy (XRD)

X-ray Diffraction is a non-destructive technique use to analyze the detailed information about the internal lattice of crystalline substances, including bond-lengths, bond-angles, details of site-ordering and unit cell dimensions. These techniques are based on observing the scattered intensity of an X-ray beam hitting a sample as a function of incident and scattered angle, polarization, and wavelength or energy [89-90].

X-ray diffraction spectroscopy consist of three parts, an X-ray tube, a sample holder, and an X-ray detector. X-rays are generated in a cathode ray tube by heating a filament to produce electrons, accelerating the electrons toward a target by applying a voltage, and impact of the electrons with the target material. When electrons have sufficient energy to dislodge inner shell electrons of the target material, characteristic X-ray spectra are produced. These spectra consist of several components, the most common being K_α and K_β. K_α consists, in part, of K_{α_1} and K_{α_2}. K_{α_1} has a slightly shorter wavelength and twice the intensity as K_{α_2}. The specific wavelengths are characteristic of the target material. Filtering, by foils or crystal monochro-meters, is required to produce monochromatic X-rays needed for diffraction. $K_{\alpha_1}$and K_{α_2} are sufficiently close in wavelength such that a weighted average of the two is used. Molybdenum is the most common target material for single-crystal diffraction, with MoK_α radiation = 0.7107Å. These X-rays are collimated and directed onto the sample. When the geometry of the incident X-rays impinging the sample satisfies the Bragg Equation (equation 2.12), constructive interference occurs. A detector records and processes this X-ray signal and converts the signal to a count rate which is then output to a device such as a printer or computer monitor. Figure 2.11 shows principle of X-ray diffraction in material.

$$n\lambda = 2d \sin\theta \tag{2.12}$$

where n is an integer,

λ is the wavelength of incident wave,

d is the spacing between the planes in the atomic lattice and

θ is the angle between the incident ray and the scattering planes.

This law relates the wavelength of electromagnetic radiation to the diffraction angle and the lattice spacing in a crystalline sample. These diffracted X-rays are then detected, processed and counted. By changing the geometry of the incident rays, the orientation of the centered crystal and the detector, all possible diffraction directions of the lattice should be attained.

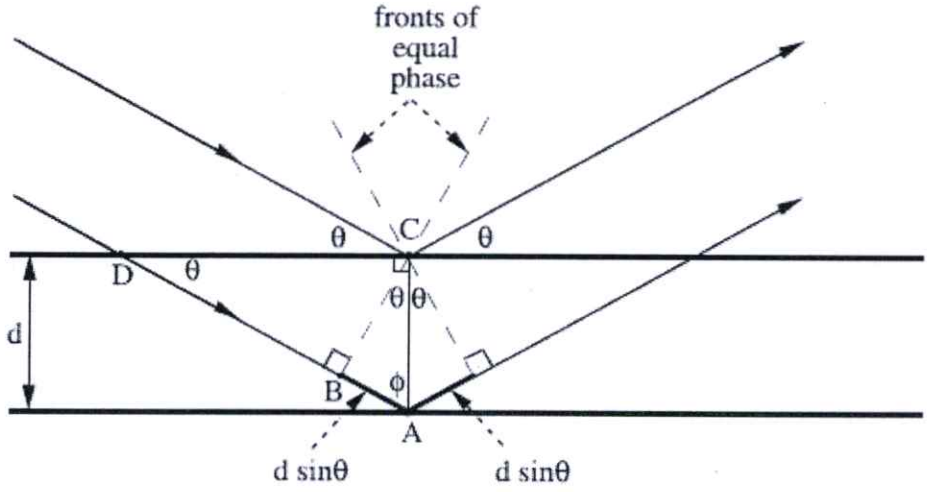

Figure 2.11 Diffraction of X-ray in material [90].

The crystalline size of the solid material can be calculated from XRD peak in a diffraction pattern from Scherrer's equation as follows [90];

$$\tau = \frac{K\lambda}{\beta\cos\theta} \tag{2.13}$$

where τ is crystallite size,

κ is constant dependent on crystallite shape (0.9),

λ is X-ray wavelength (1.5405 Å),

β is full width at half maximum (FWHM) and,

θ is the angle of diffraction.

2.5.2 X-ray Fluorescence Spectroscopy (XRF)

X-ray fluorescence spectrometry (XRF) is non-destructive technique used for an elemental analysis of rocks, minerals, sediments and fluids. This technique have been used extensively in science and industry. The advantage of this technique including simplicity, low cost, and the stability. The principle of XRF involve to the behavior of atoms when they interact with X-ray radiation. In this process, a sample is illuminated by an intense X-ray beam, the incident X-ray beam is typically produced from a Rh target, although W, Mo, Cr and others can also be used, depending on the application. In this step, some of the energy is scattered, but some is also absorbed within the sample in a manner that depends on its chemistry, resulting to excitation of atom. The excited sample in turn emits X-rays along a spectrum of wavelengths characteristic of the types of atoms present in the sample. The atoms in the sample absorb X-ray energy by ionizing, ejecting electrons from the lower (usually K and L) energy levels. The ejected electrons are replaced by electrons from an outer, higher energy orbital. This energy is released due to the decreased binding energy of the inner electron orbital compared with an outer one. This energy release is in the form of emission of characteristic X-rays indicating the type of atom present. If a sample has many elements present, as is typical for most minerals and rocks, the use of a Wavelength Dispersive Spectrometer much like that in an EPMA allows the separation of a complex emitted X-ray spectrum into characteristic wavelengths for each element present. Various types of detectors (gas flow proportional and scintillation) are used to measure the intensity of the emitted beam. The flow counter is commonly utilized for measuring long wavelength (>0.15 nm) X-rays that are typical of K spectra from elements lighter than Zn. The scintillation detector is commonly used to analyze shorter wavelengths in the X-ray spectrum (K spectra of element from Nb to I; L spectra of Th and U). X-rays of intermediate wavelength (K spectra produced from Zn to Zr and L spectra from Ba and the rare earth elements) are generally measured by using both detectors in tandem. The intensity of the energy measured by these detectors is proportional to the abundance of the element in the sample. The exact value of this proportionality for each element is derived by comparison to mineral or rock standards whose composition is known from prior analyses by other techniques [91]. A diagram of the components of a XRF spectrometry is shown in Figure 2.12, and Figure 2.13 shows the generation of X-ray fluorescence radiation.

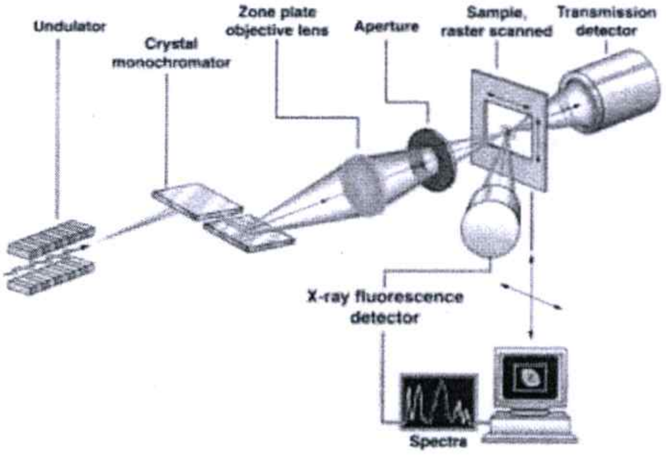

Figure 2.12 Basic components of X-Ray fluorescence spectrometry [92].

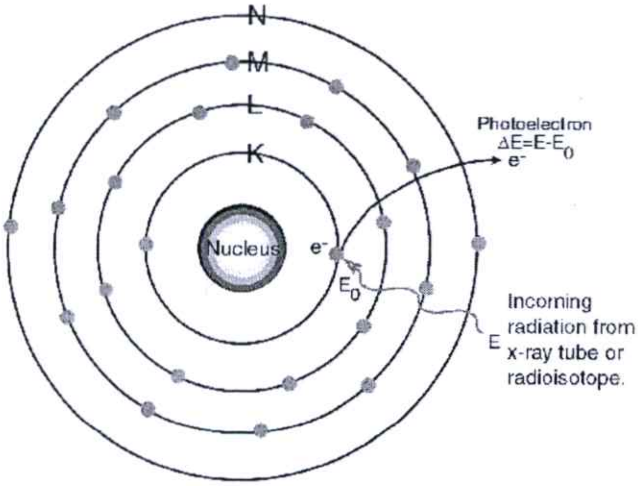

Figure 2.13 The generation of X-ray fluorescence radiation [93].

2.5.3 X-ray Photoelectron Spectroscopy (XPS)

X-ray Photoelectron Spectroscopy (XPS) is quantitative spectroscopic technique and nondestructive analysis which develop in the mid-1960's by Kai Siegbahn and his research group at the University of and Uppsala, Sweden. This technique is used to analyze elemental composition, empirical formula, chemical state and electronic state within surface of material by the photoelectric effect. The sample is irradiated with mono-energetic x-rays causing photoelectrons to be emitted from the sample surface that escape from depths greater than 10 nm. An electron energy analyzer determines the binding energy of the photoelectrons. From the binding energy and intensity of a photoelectron peak, the elemental identity, chemical state, and quantity of an element are determined. This technique is used to analyze surface information of several materials including: metal, semiconductors, polymers, elements, glasses, ceramics, paints, papers, woods, teeth, bones, medical implants, bio-materials, viscous oils and so on [94-95]. A diagram of a typical XPS instrument is illustrated in Figure 2.14.

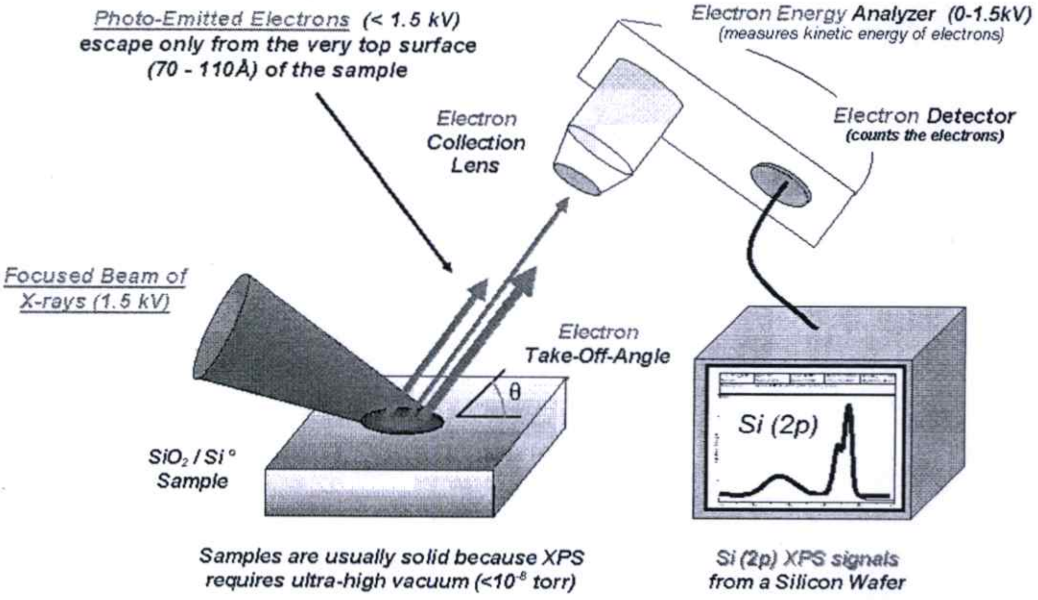

Figure 2.14 Basic components of XPS system [96].

Photoelectron spectroscopy is based upon photoelectric effect given by the Einstein relation;

$$E = h\nu \tag{2.14}$$

where h is Planck's constant (6.62x10-34 J·s)

ν is frequency of the radiation (Hz).

In XPS, the photon is absorbed by an atom in a molecule or solid, leading to ionization and the emission of a core (inner shell) electron. First, the energy of an incident photon ($h\nu$) is transferred to a bound electron. If the energy is greater than the binding energy of the electron and overcomes the work function (ϕ) of the solid, the photoelectron will occur followed as Figure 2.15 and equation 2.15 [97];

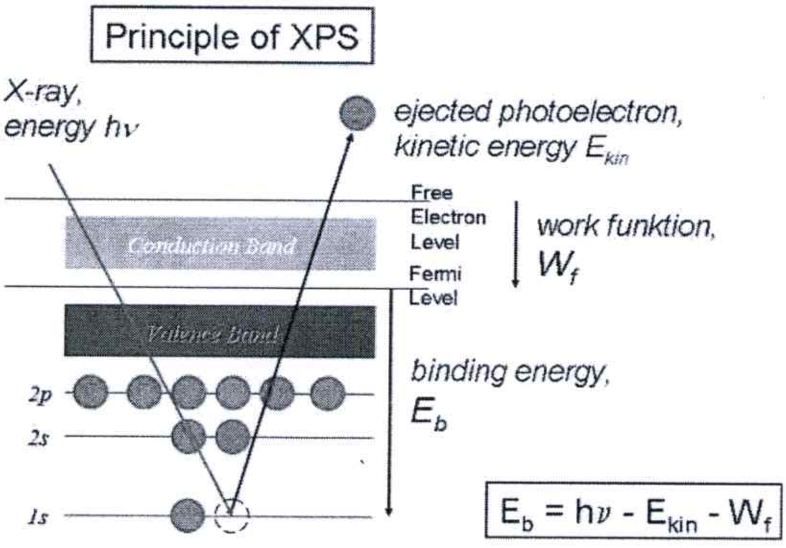

Figure 2.15 Schematic representation of the photoemission [98].

$$A + h\nu \longrightarrow A^* + e^- + \phi \tag{2.15}$$

Due to the emission of the electron, the inner shell of the atom (A) is ionized. The energy conservation requires as shown in equation 2.16;

$$E(A) + h\nu = E(A^*) + E(e^-) + \phi \tag{2.16}$$

Since the electron's energy is presented as kinetic energy (KE). Equation 2.16 can be rearranged to give the following expression (equation 2.17) for the KE of the photoelectron;

$$KE = h\nu - [E(A^*) - E(A)] - \phi \tag{2.17}$$

The final term in brackets, representing the difference in energy between the ionized and neutral atoms, is generally called the binding energy (BE) of the electron leads to the following commonly quoted equation 2.18;

$$KE = h\nu - BE - \phi \tag{2.18}$$

2.5.4 Scanning Electron Microscopy (SEM)

The scanning electron microscope (SEM) is an instrument that produces a largely magnified image by using electrons instead of light to form an image. SEM is scientific instrument used to analyze the microstructure of materials. SEM uses a focused beam of high-energy electrons to generate a variety of signals at the surface of the sample. The various signals that originate from interactions between electron and sample reveal information, including outside morphology, chemical composition, and crystalline structure and orientation of materials making up the sample. In most applications, data are collected over a selected area of the surface of the sample, and 2-dimensional image is generated that displays spatial variations in these properties. The magnification of SEM techniques can be able to magnified ranging from 20 to approximately 30,000 magnified with spatial resolution of 50 to 100 nm. The SEM is also capable of performing analyses of selected point locations on the sample to determine chemical compositions using Energy Dispersive X-Ray Spectrometer (EDS) mode [99-101].

The SEM generates a beam of incident electrons in an electron column above the sample chamber by an electron gun. The electrons are produced by a thermal emission source, such as a heated tungsten filament, or by a field emission cathode. The energy of the incident electrons ranges of 100 eV to 30 keV depending on the evaluation objectives. The electrons are focused into a small beam by electromagnetic lenses in the SEM column. Scanning coils near the end of the column direct and position the focused beam onto the sample surface. The electron beam is scanned in a raster pattern over the surface for imaging. The beam can also be focused at a single point or scanned along a line for x-ray analysis. The beam can be focused to a final probe diameter as small as about 10 Å. To create an SEM image, the incident electron beam is scanned in a raster pattern across the sample's surface. The emitted electrons are detected for each position in the scanned area by an electron detector. The intensity of the emitted electron signal is displayed as brightness on a cathode ray tube (CRT). By synchronizing the CRT scan to that of the scan of the incident electron beam, the CRT display represents the morphology of the sample surface area scanned by the beam. Magnification of the CRT image is the ratio of the image display size to the sample area scanned by the electron beam. Figure 2.16 shows the schematic of the operation of SEM.

The variety of signals are produced by primary electrons-sample interactions including secondary electrons (SE), backscattered electrons (BSE), diffracted backscattered electrons (EBSD), photons (characteristic X-rays), visible light (cathodoluminescence; CL), and heat as shown in Figure 2.17. The incident electrons cause electrons to be emitted from the sample due to elastic and inelastic scattering within the sample's surface and near-surface material. High-energy electrons that are ejected by an elastic collision of an incident electron, typically with a sample atom's nucleus, are referred to as backscattered electrons. The energy of backscattered electrons will be comparable to that of the incident electrons. Emitted lower-energy electrons resulting from inelastic scattering are called secondary electrons. Secondary electrons can be formed by collisions with the nucleus where substantial energy loss occurs or by the ejection of loosely bound electrons from the sample atoms. The energy of secondary electrons is typically 50 eV or less [99-101].

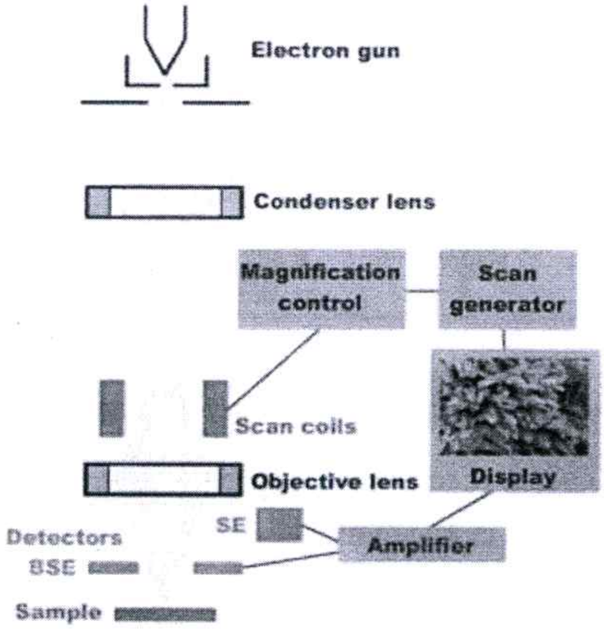

Figure 2.16 SEM instrument and schematic of the operation [102].

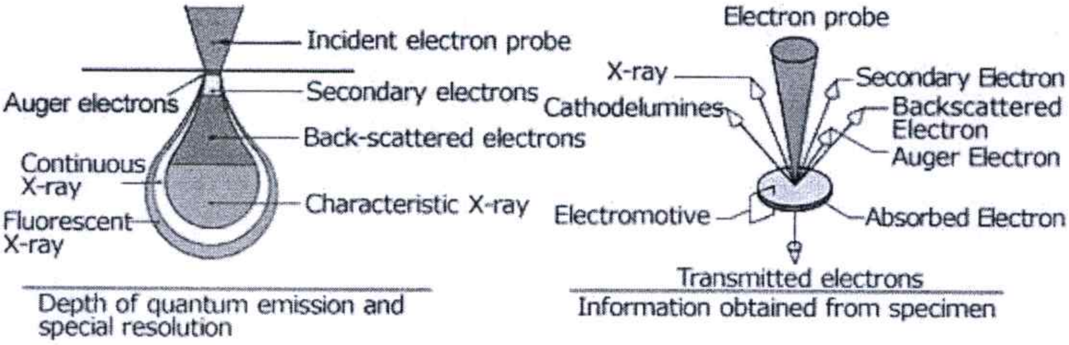

Figure 2.17 Interaction of the electron beam and sample in SEM [103].

2.5.5 Transmission Electron Microscopy (TEM)

The transmission electron microscope (TEM) operates on the same basic principles as the light microscope but uses electrons instead of light similar to SEM, and their much lower wavelength makes it possible to get a resolution a thousand times better than with a light microscope.

The principle of TEM attributed to a beam of electrons is transmitted through an ultra-thin specimen, interacting with the specimen as it passes through. An image is formed from the interaction of the electrons transmitted through the specimen; the image is magnified and focused onto an imaging device, such as a fluorescent screen, on a layer of photographic film, or to be detected by a sensor such as a charge-coupled device (CCD) camera. TEM technique is extensively used to analyze in a range of scientific fields, in both physical and biological sciences, including cancer research, virology, materials science as well as pollution, nanotechnology, and semiconductor research. The components and operation of TEM are illustrated in Figure 2.18.

At smaller magnifications TEM image contrast is due to absorption of electrons in the material, due to the thickness and composition of the material. At higher magnifications complex wave interactions modulate the intensity of the image, requiring expert analysis of observed images. Alternate modes of use allow for the TEM to observe modulations in chemical identity, crystal orientation, electronic structure and sample induced electron phase shift as well as the regular absorption based imaging [104-105].

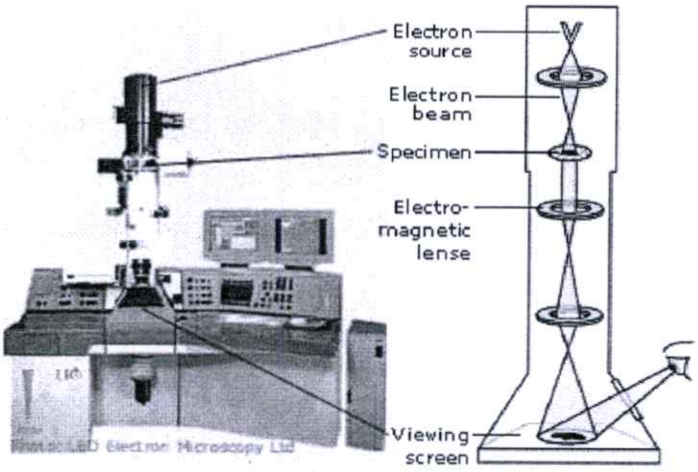

Figure 2.18 TEM instrument and schematic of the operation [106].

2.5.6 The Brunauer-Emmett-Teller Analysis (BET)

The Brunauer-Emmett-Teller (BET) analysis was developed by Stephen Brunauer, Paul Emmett and Edward Teller in 1938. BET analysis provides precise specific surface area evaluation of materials by physical adsorption of a nitrogen gas on the surface of the solid and by calculating the amount of adsorbate gas corresponding to a monomolecular layer on the surface. The amount of gas adsorbed can be measured by a volumetric or continuous flow procedure. The technique encompasses external area and pore area evaluations to determine the total specific surface area in m^2/g yielding important information in studying the effects of surface porosity and particle size in many applications. BJH analysis can also be employed to determine pore area and specific pore volume using adsorption and desorption techniques. This technique characterizes pore size distribution independent of external area due to particle size of the sample. Specific surface area determinations measuring the external surface area and open pores of macroporous and mesoporous materials, along with pore volume and area distributions that characterize porosity below the effective range of mercury intrusion porosimetry are techniques that can be especially useful for studies of artificial bone materials, catalysts, particle and gas filtration, fuel cell technology, absorbents, sintering studies, zeolites and reactivity studies of materials among a variety of other applications [107-108]. Figure 2.19 shows the schematic of the BET instrument.

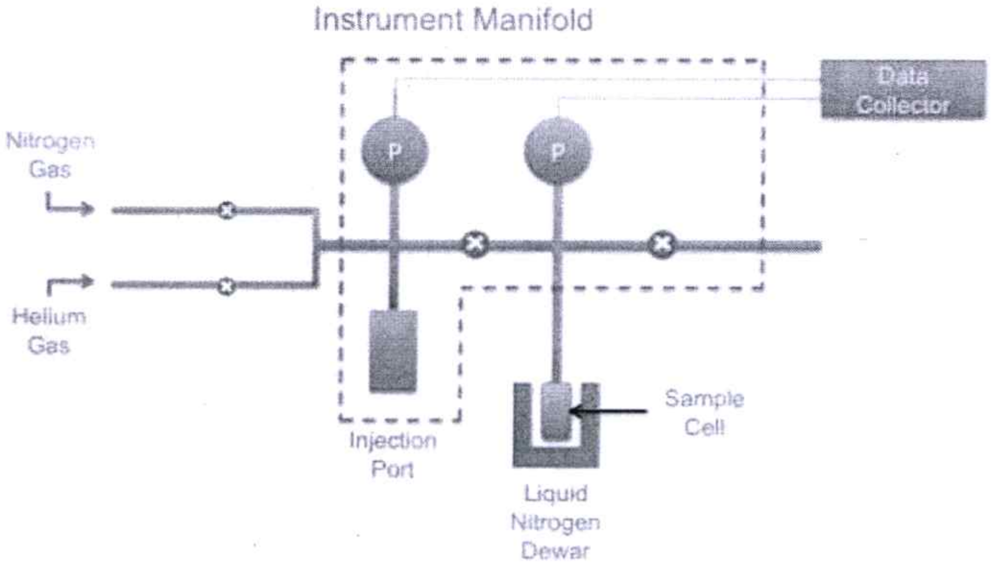

Figure 2.19 Schematic of the BET instrument [109].

2.5.7 UV-Vis Spectroscopy

UV/Vis spectrophotometer is an instrument used for measuring light intensity in ultraviolet (UV) region falls in the range between 190-380 nm and the visible region fall between 380-750 nm that passes through or absorbs by sample. This technique can be used in specifying the type and the quantity of the substance that is present in the sample. The most of substance are organic compounds, complex compounds and inorganic compounds that can absorb light in this region. In UV/Vis spectrophotometer mechanism, a beam of light from UV and visible light source is separated into its component wavelengths by a prism or diffraction grating. Each monochromatic beam in turn is split into two equal intensity beams by a half-mirrored device. One beam, the sample beam, passes through a small transparent container (cuvette) containing a solution of the compound being studied in a transparent solvent. The other beam, the reference, passes through an identical cuvette containing only the solvent. The intensities of these light beams are measured and compared by electronic detectors. The intensity of the reference beam, which should have suffered little or no light absorption, is defined as I0. The intensity of the sample beam is defined as I. Over a short period of time, the spectrometer automatically scans all the component wavelengths in the manner described [110-111]. Figure 2.20 shows diagram of the components of a typical spectrometer

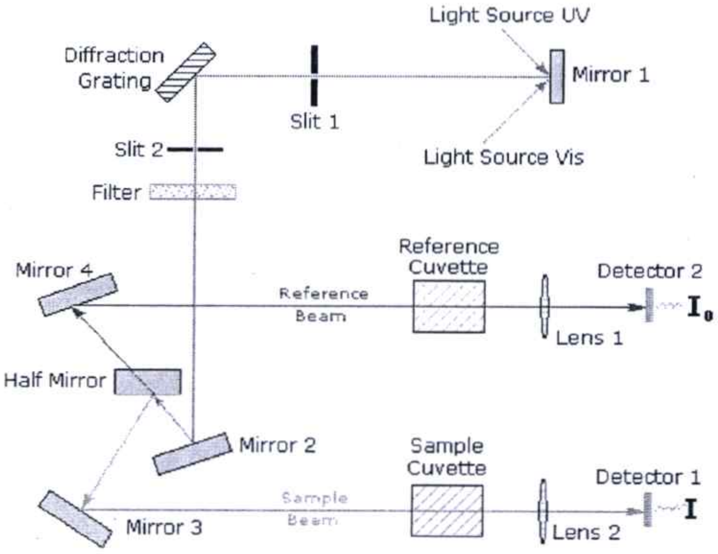

Figure 2.20 Basic components of UV-Vis spectrometer [111].

Ultraviolet and visible radiation interacts with matter which causes electronic transitions (promotion of electrons from the ground state to a high energy state). The following electronic transitions are possible:

p - p* (pi to pi* transition)

n - p* (n to pi star transition)

s - s* (sigma to sigma star transition)

n - s* (n to sigma star transition)

The sigma to sigma* transition requires an absorption of a photon with a wavelength which does not fall in the UV-vis region. Thus, only pi to pi* and n to pi* transitions occur in the UV-vis region are observed [112]. Figure 2.21 shown electronic transitions diagram.

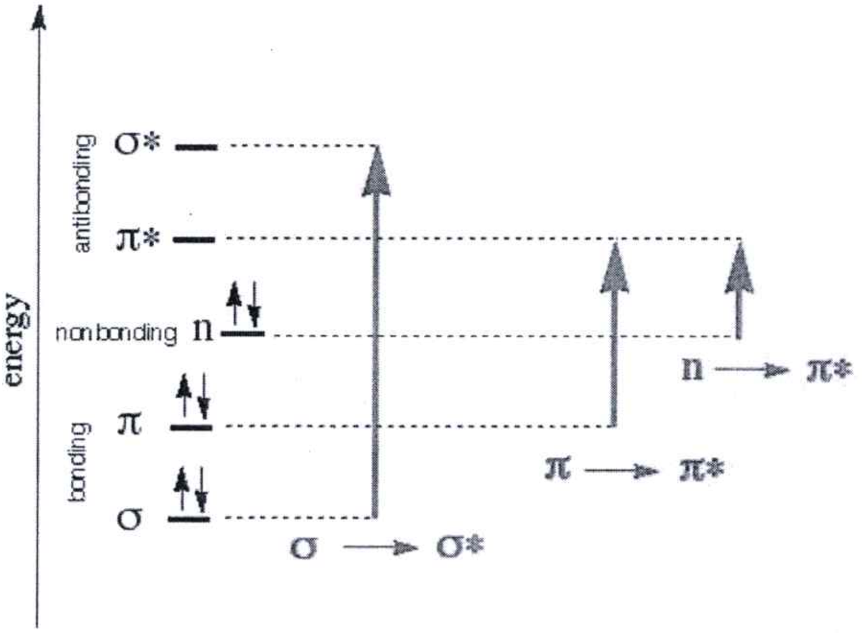

Figure 2.21 Electronic transitions diagram [112].

2.6 Literature Review

Pavasupree et al. [17] TiO_2 synthesized nanofibers from natural leucoxene mineral via a hydrothermal process. The diameter of prepared nanofibers was about 12-58 nm in width and about 3-22 mu m in length. The specific surface area of the synthesized nanofibers approximately 55 m^2/g.

H. Yu et al. [59] prepared titanate nanoribbons by hydrothermal method in 10M NaOH solution at 200 °C for 48 h using rutile-type TiO_2 powders as the starting materials. Then, the prepared titanate nanoribbons were hydrothermally post-treated at 150 °C for 12-36 h. After hydrothermally post treatment, the titanate transform to anatase phase with Na^+ ions in the titanate nanoribbons was removed. The prepared titanate nanoribbons maintained the nanoribbon structured. Furthermore, the specific surface area and the pore volume were increase compared the starting materials.

D. Aphairaj et al. [61] synthesized titanate nanotubes by hydrothermal method at 105 °C for 24 h using natural leucoxene mineral as the starting material. The crystalline structure of the starting natural leucoxene mineral consists of the mixed rutile and anatase phase whereas the prepared sample appeared the hydrogen titanate ($H_2Ti_3O_7$). The prepared nanotubes showed internal diameter of 4-6 nm, external diameter of 8-10 nm, and the length of 0.2-1 μm.

Jitputti et al. [53] prepared TiO_2 nanowires via the hydrothermal process in 10 M NaOH at 150 °C for 72 h followed by calcination at 300-1,000 °C for 2 h. The as-synthesized demonstrated titanate structure, and the prepared sample show maintaining 1D morphology at 300-400 °C and further transformed into anatase structure at 500-800 °C and rod-shaped rutile structure was occurred at 900-1,000 °C. TiO_2 NWs treated at 500 °C exhibited higher photocatalytic H_2 evolution than that of starting TiO_2 powder (Degussa P-25).

Yoshida et al. [63] synthesized TiO_2(B) nanowires and TiO_2 anatase nanowires by the hydrothermal processing in 10M NaOH aq. at 150 °C. After that, the as-synthesized was calcined at 300-800 °C. The crystalline structure of the as-synthesized samples were converted into TiO_2(B) and anatase phase with maintaining 1-D morphology at 300-500 °C and 600-800 °C, respectively. At 900 °C, they transformed into rod-shaped rutile grains.

Muneer M. Ba-Abbad et al. [113] synthesized titanium dioxide nanoparticles by sol-gel technique using the titanium tetra-isopropoxide as starting material. After heat treatment at temperatures over 500 °C, the anatase to rutile ratio was decreased. The results of photodegradation after 90 min irradiation time at pH of 6, the efficiency of 99, 98 and 92 % was obtained for 50 mg/l of chlorophenols namely, 2-chlorophenol (2-CP), 2, 4-dichlorophenol (2,4-DCP) and 2, 4,6-trichlorophenol (2,4,6T-CP), receptively.

R. Yoshida et al. [58] synthesized TiO_2-derived nanotubes by hydrothermal treatment in NaOH (aq.) under the hydrothermal treatment at 120 °C, the nanotubes grew longer until 12 h, and became almost constant length for more than 12 h. After calcination above 350 °C, partially titanate nanotubes transformed to of anatase structure. At higher heat-treatment temperatures, the crystalline structure changed from anatase into rutile phase, and the nanotubes converted into $Na_2Ti_6O_{13}$ nanorods.

S. Pavasupree et al. [57] synthesized titanate nanofibers by hydrothermal method at 150 °C for 72 h using natural rutile sand as the starting materials. The as-synthesized sample showed the diameters of 20-50nm and the lengths of 10-100 mm with titanate layer. After calcination at 40 °C and 70 °C , the prepared samples almost appeared TiO_2(B) phase and anatase phase, respectively with maintained nanofiber morphology. At higher temperature than 900 °C, the morphology of prepared samples change into rutile-type TiO_2 rod-like structure.

J. Jitputti et al. [56] prepared nanocrystalline mesoporous TiO_2 via hydrothermal treatment. The nanocrystalline mesoporous TiO_2 calcined at 400-600 °C showed better photocatalytic H_2 production than that of commercial TiO_2 (Ishihara ST-01), especially the nanocrystalline mesoporous TiO_2 calcined at 550 °C for 1 h showed optimum rate for H_2 production (1.41 mmol/m^2).

J. Jitputti et al. [62] successfully prepared flower-like titanate superstructure by simple hydrothermal process without any surfactant or template. flower-like titanate had diameter of about 250-450 nm and BET surface area (SBET) of 350.7 m^2/g. After heat treatment at 500 °C, the titanate nanosheets were converted into anatase TiO_2 with moderate deformation of their structures. The as-prepared flower-like titanate heat treated at 500 °C showed high photocatalytic activity for H_2 evolution from water splitting reaction than that of commercial TiO_2 anatase powder (ST-01).

S. Pavasupree et al. [114] prepared nanosheet TiO_2 with mesoporous structure were by hydrothermal method at 130 °C for 12 h. The crystalline structure exhibited anatase TiO_2 with width approximately 50-100 nm and several nanometers in thickness. The average pore diameter of the as-synthesized nanosheet TiO_2 was about 3-4 nm. The as-synthesized nanosheet TiO_2 had the specific surface area and pore volume about 642 m^2/g and 0.774 cm^3/g, respectively. The nanosheet structure was changed into nanorods/nanoparticles composite with anatase TiO_2 structure after heat treatment at 300–500 °C. Increasing temperature to 600-700 °C, the nanosheet showed almost nanoparticles with a mixture of anatase and rutile TiO_2 structure.

M. Nag et al. [115] synthesized of rutile titania with different morphologies via hydrothermal method at low temperatures (40-150 °C) without any additives and their application as efficient photocatalyst for environmental remediation. The prepared sample shows the optical band-gap in the range of 2.8-3.1 eV with specific surface area between 70 and 140 m^2/g depending on the synthesis conditions. The best performance of photodegra-dation of the pollutant azo-dye, methyl orange in presence and absence of oxygen was obtained when using nanocrystalline rutile titania synthesized at 40 °C for 16 h as catalyst.

D. Aphairaj et al. [60] synthesized anatase TiO_2 nanotubes using natural leucoxene mineral as the starting materials by the hydrothermal method at 105 °C of 24 h. The crystalline structure of the assynthesized samples revealed titanate phase. After calcined at 400 °C, the as-synthesized samples showed anatase TiO_2 with inner and outer diameters of about 6 nm and 16 nm, respectively, and lengths in the range of 20-100 nm. The BET surface area of the anatase TiO_2 nanotubes approximately 82.98 m^2/g. The photocatalytic activity of the anatase TiO_2 nanotubes exhibited higher than that of commercial anatase TiO_2 nanoparti-cles (JRC-01).

Suzuki et al. [65] prepared nanowire-structured TiO_2 by a hydrothermal method followed by calcination in air at 300 °C for 4 h. The sample was composed of fine nanowires and relatively large particles. The 5-10 % nanowire /nanoparticle composite electrode showed higher DSC performance than the fully nanowire-structured TiO_2.

K Asagoe et al. [64] prepared TiO_2 anatase nanowires by a hydrothermal process. The diameter and length of nanowires ranges from 10-70 nm and several μm, respectively. The crystalline structure of as-synthesized nanowires consisted of hydrogen titanate phase. In this work, electrode of DSSC based on TiO_2 nanoparticle/TiO_2 nanowire composite were fabricat-ed. The TiO_2 nanoparticle/TiO_2 nanowire composite cells showed DSSC efficiency about 6.53%, which higher than ordinary nanoparticle cells (5.59%) and fully nanowire cells (2.42%).

S. Ngamsinlapasathian et al. [116] synthesized one-dimensional nanotube structure by surfactant-assisted templating mechanism using tetraisopropyl orthotitanate (TIPT) modified with acethylacetone (ACA)/laurylamine hydrochloride (LAHC). In this work, DSSC efficiency of the electrode using nanotube +2% P25 nanoparticles showed higher short-circuit photocurrent density and solar energy conversion efficiency than that of P25 nanoparticles electrode.

S. Pavasupree et al. [54] synthesized nanorods/nanoparticles TiO_2 with mesoporous structure by hydrothermal method at 150 °C for 20 h. The diameter and the lengths of nanorods were about 10-20 nm and 100-200 nm, respectively while the nanoparticles had diameter about 5-10 nm. The nanorods/nanoparticles TiO_2 had the specific surface area and pore volume about 203 m^2/g and 0.655 cm^3/g, respectively. The photocatalytic activity (I_3^- concentration) of nanorods/nanoparticles TiO_2 with mesoporous structure was higher than the nanorods TiO_2, nanofibers TiO_2, mesoporous TiO_2, and commercial TiO_2 (ST-01, P-25, JRC-01, and JRC-03). The nanorods/nanoparticles TiO_2 with mesoporous structure exhibited solar energy conversion efficiency about 7.12% while the DSSC efficiency using P25 was 5.82%.

S. Ngamsinlapasathian et al. [118] prepared nanocrystalline mesoporous titania via surfactant-assisted templating technique using tetraisopropyl orthotitanate modified with acethylacetone and laurylamine hydrochloride as template. This material was applied for the electrode of compared to P25 electrode. The DSSC efficiency of mesoporous titania +5% P25 sintered at 450 °C for 1 h was higher than that of the cell sintered at other temperature and the cell based on P25.

S. Pavasupree et al. [55] synthesized mesoporous anatase TiO_2 nanopowder by hydrothermal treatment at 130 °C for 12 h. The specific BET surface area and average pore diameter about 193 m^2/g and 3-4 nm, respectively. The photocatalytic activity of mesoporous anatase TiO_2 nanopowders showed higher than the nanorods TiO_2, nanofibers TiO_2 mesoporous TiO_2, and commercial TiO_2 nanoparticles (P25, JRC-01, and JRC-03). In DSSC application, the cell based on mesoporous anatase TiO_2 as working electrode showed efficiency about 6.30%, while DSSC efficiency of the cell using P-25 as working electrode was about 5.82%.

J. Jiu et al. [118] synthesized single-crystalline anatase TiO_2 nanorods by a surfactant-assisted hydrothermal method. TiO_2 nanorods had pure highly crystalline anatase phase. The prepared sample had the lengths and diameter approximately 100-300 nm and diameters of 20-30 nm, respectively. An efficiency of DSSC based on single-crystalline anatase TiO_2 nanorods as working electrode reached to 7.29%.

K. Fan et al. [119] synthesized anatase TiO_2 fusiform nanorods by a two step hydrothermal method. The diameters and lengths of prepared sample were about 20-80 nm and 200-400 nm, respectively. This paper shows efficiency of DSSC based on 10 wt% TiO_2 nanorods/P25 composite as working electrode achieve to 4.68%, with a 66.5% improvement compared to the bare P25-based solar cell. This should be attributed to the express way for charge transport of nanorods, resulting to reduce electron and hole recombination, and enhanced light scattering of the nanorods to increase light harvesting efficiency of DSSC.

A.E. Shalan et al. [120] synthesized titania nanorods and nanoparticles by low temperature hydrothermal process. The crystallite size and the relative crystallinity of the anatase phase were increased with increasing the heat treatment temperature. The diameter of the titania nanorods was 6.7 nm with 22 nm in length while nanoparticles was 13 nm in diameter.

Efficiency of DSSC fabricated with oriented TiO_2 nanorods showed solar energy conversion efficiency of 7.2% which higher than that of DSSC based on mesoporous TiO_2 nanoparticles due to their high surface area, hierarchically mesoporous structures, low charge recombine-tion and fast electron-transfer rate. In addition, increasing calcination temperature of the prepared nanoparticles, the efficiency of the assembly solar cells was decreased to 1.7% due to the agglomeration of the particles and difficulty of electron movement.

J.S. Im et al. [121] investigated the efficiency of DSSC based on the bi-semiconductors of TiO_2 and Fe_2O_3 as a photoelectrode, and the effect of size of the semiconductors on DSSC efficiency was studied. A high DSSC efficiency (5.451%) was obtained from DSSC based on reduced size bi-semiconductors of TiO_2 and Fe_2O_3 due to the effects of electron trapping and electron charge transfer improvement at the semiconductor/dye/electrolyte interface of the Fe_2O_3 co-semiconductor and the size reduction. This unique effect was beneficial to prohibit the recombination of electrons in the CB of TiO_2 with those in the dye or the electrolyte.

L. Francis et al. [122] prepared TiO_2 nanofibers with rutile structure by electrospinning method using a polymeric sol containing a titanium precursor and poly(vinylpyrrolidone) as the starting materials. The continuous fibers with grain size of 15-20 nm were transformed into nanorods by mechanical grinding. In this work, the nanofibers and rutile nanorods were used as the working electrode of DSSC. The short circuit current density and efficiency of DSSC fabricated from rutile nanorods as a working electrode are about 12 mA/cm^2 and 4.5%, respectively. They were higher than that of DSSC fabricated from the rutile nanofibers. These results described to the nanorods structure are much shorter and hence can have much lower resistance that in turn can cause higher currents.

From literature review, nanotubes and nanofibers can be prepared at various temperatures and times depend on the starting materials. Therefore, in this research is focused to effect of hydrothermal time and temperature in order to examine the optimal condition for preparation of nanofibers. The effect of calcination temperature on morphology and crystalline structure of prepared nanofibers were investigated. Furthermore, DSSCs performance based on prepared nanofibers were measured.

CHAPTER 3

EXPERIMENTS

The synthesis TiO_2 nanofibers by hydrothermal method are described in this chapter. The utilizations of prepared nanofibers for photoelectrode of DSSC are also explained.

3.1 Materials and Equipments

3.1.1 Materials, Equipments for TiO_2 Nanofibers Synthesis

Materials

1) Ilmenite mineral
2) Sodium hydroxide (NaOH)
3) Hydrochloric acid (HCl, 37%)
4) Distillated water

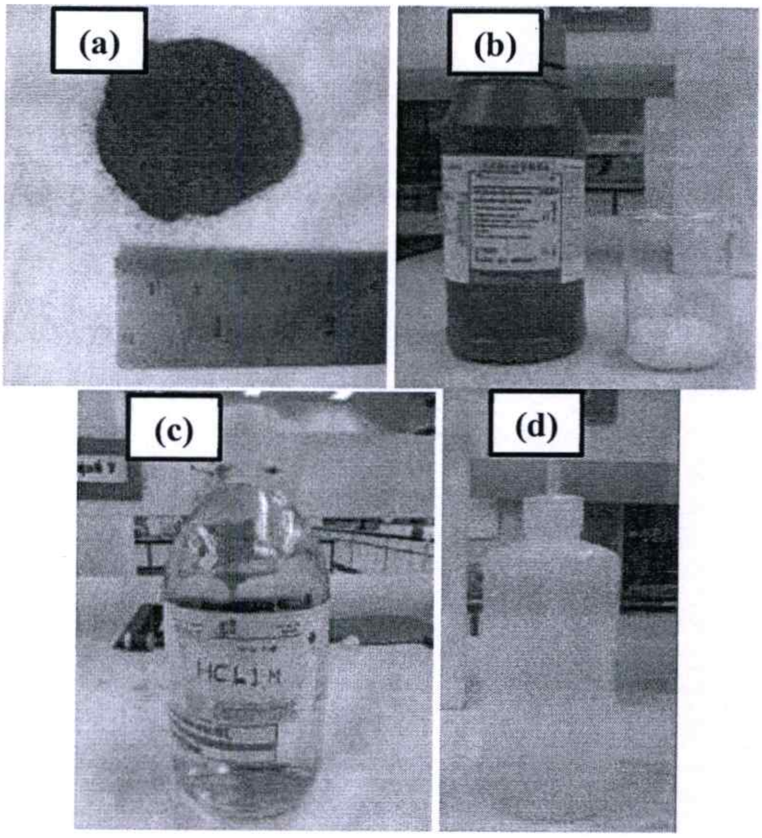

Figure 3.1 Materials for TiO_2 nanofibers synthesis (a) ilmenite mineral, (b) sodium hydroxide, (c) hydrochloric acid and (d) distillated water.

Equipments

1) a Thai made Teflon-lined stainless steel autoclave (Figure 3.2 and 3.3)

2) Vacuum dryer (Figure 3.4)

3) Hot air oven (Figure 3.5)

4) Digital weighting apparatus (Figure 3.6)

5) Hot plate stirrer, model: HTS-1003 (Figure 3.7)

6) Furnace (Figure 3.8)

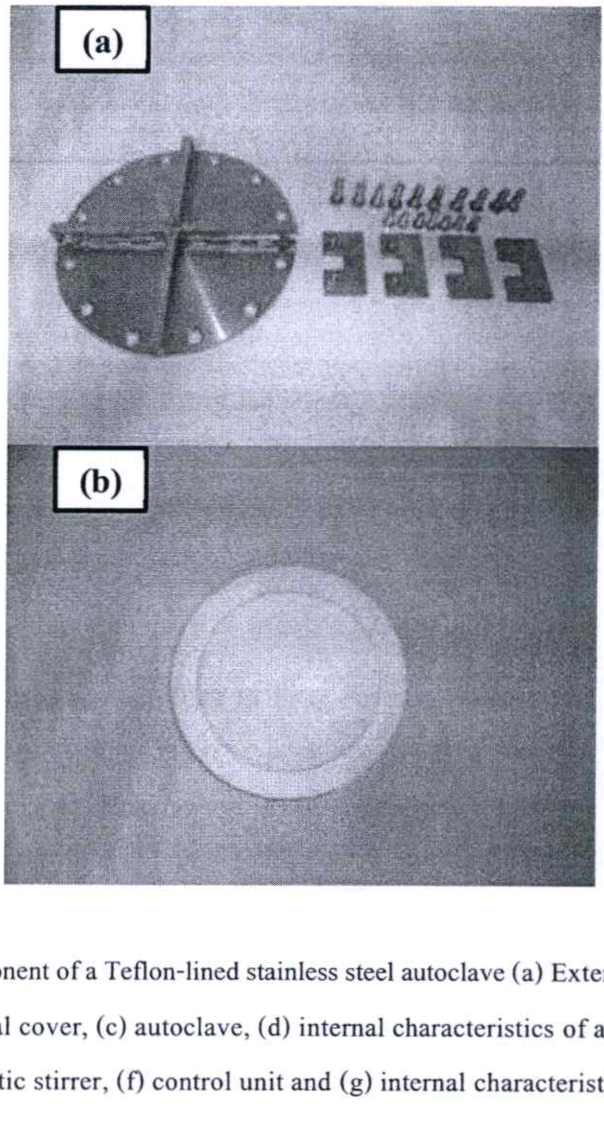

Figure 3.2 Component of a Teflon-lined stainless steel autoclave (a) External cover (b) Internal cover, (c) autoclave, (d) internal characteristics of autoclave, (e) magnetic stirrer, (f) control unit and (g) internal characteristics of control unit.

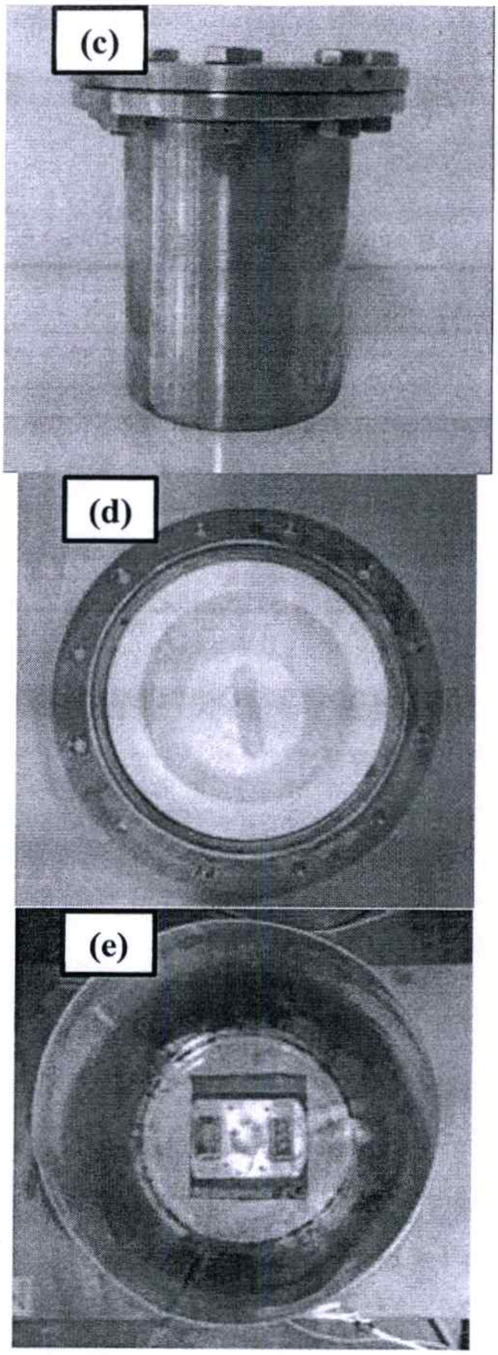

Figure 3.2 (Cont.) Component of a Teflon-lined stainless steel autoclave (a) external cover (b) internal cover, (c) autoclave, (d) internal characteristics of autoclave, (e) magnetic stirrer, (f) control unit and (g) internal characteristics of control unit.

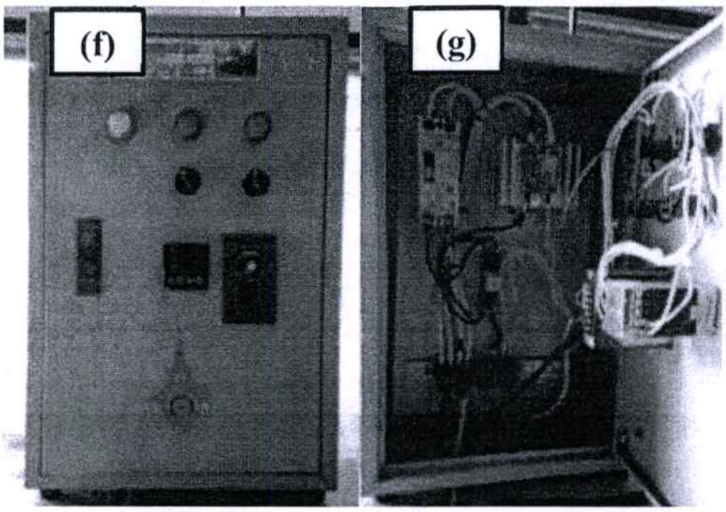

Figure 3.2 (Cont.) Component of a Teflon-lined stainless steel autoclave (a) external cover (b) internal cover, (c) autoclave, (d) internal characteristics of autoclave, (e) magnetic stirrer, (f) control unit and (g) internal characteristics of control unit.

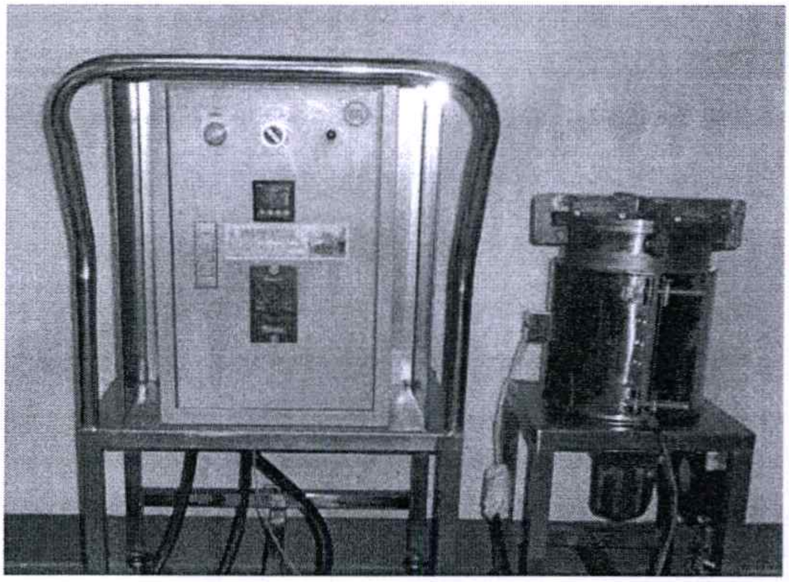

Figure 3.3 a Thai made Teflon-lined stainless steel autoclave and control unit.

Figure 3.4 Vacuum filler.

Figure 3.5 Hot air oven.

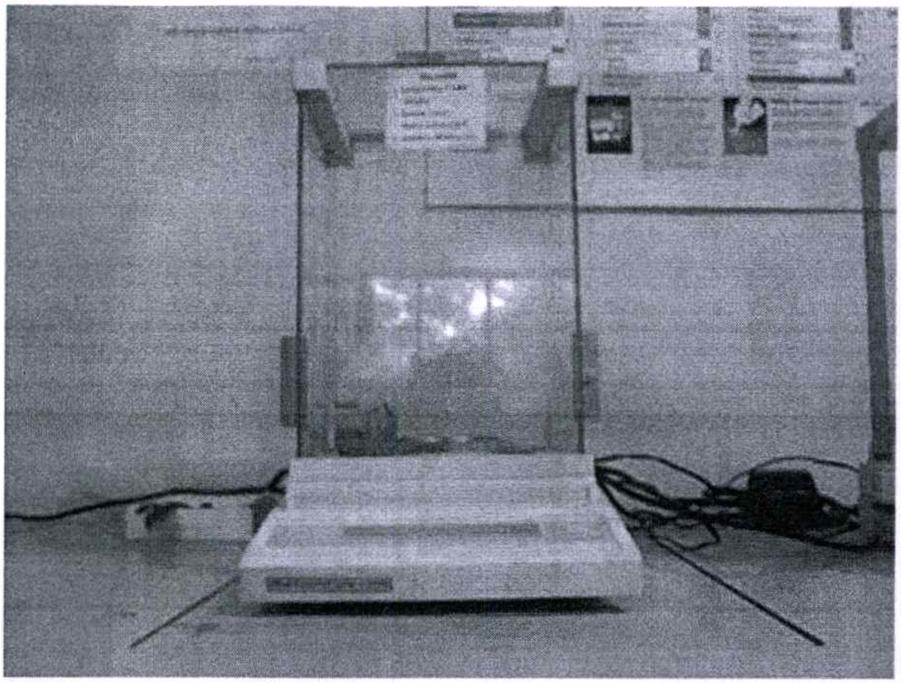

Figure 3.6 Digital weighting apparatus.

Figure 3.7 Hot plate stirrer.

Figure 3.8 Furnace.

3.1.2 Materials and Equipments of Dye sensitized Solar Cell

1) As-synthesized nanofibers

2) Commercial grade nanoparticles (Degussa, P25)

3) Deionized water (DI)

4) Nitric acid

5) Ethyl cellulose

6) Terpineol

7) Ethanol

8) Fluorine-doped tin oxide substrate

9) N719 dye solution [cis-bis(isothiocyanato)bis(2,2′-bipyridyl-4,4′-dicarboxylato)-ruthenium (II)bis-tetrabutylammonium]

10) Iodine (I_2)

11) Litium iodine (LiI)

12) Acrylonitrile

13) PV Cell Test simulator, model 16S-300-005-V4.0

3.2 Experimental

3.2.1 Synthesis of TiO_2 Nanofibers

3.2.1.1 Preparation of Titanate Nanofibers

In this research, titanate nanofibers were synthesized by simple hydrothermal method using a natural ilmenite mineral (Sakorn Minerals Co., Ltd., Thailand) as the starting material. The detail of preparation of titanate nanofibers was attributed in this part, and the experimental procedure of this research is schematically shown in Figure 3.9 and 3.10.

Step 1: 5 g of the black granules of ilmenite mineral (used without purification) were placed in a Teflon-lined stainless steel autoclave, followed by adding 200 mL of 10 M NaOH (aq.).

Step 2: The mixture of the starting material was heated at different temperatures i.e., 100, 110 and 120 °C for 72 h and stirred by magnetic bar. The effect of hydrothermal temperature on the structure of titanate nanofibers was investigated. Referring to recent review, the non-tubular needle-shape fibers were synthesized by hydrothermal method with NaOH concentration of 5-15 M at the temperature range of 100-160 °C [17].

Step 3: After the heat treatment via hydrothermal method, the autoclave was allowed to cool to room temperature by natural condition.

Step 4: After cooling process, the resulting product was washed several times with an HCl (aq.) solution and distilled water.

Step 5: In the last step, the precipitate was dried with hot air oven, and the titanate powder was obtained.

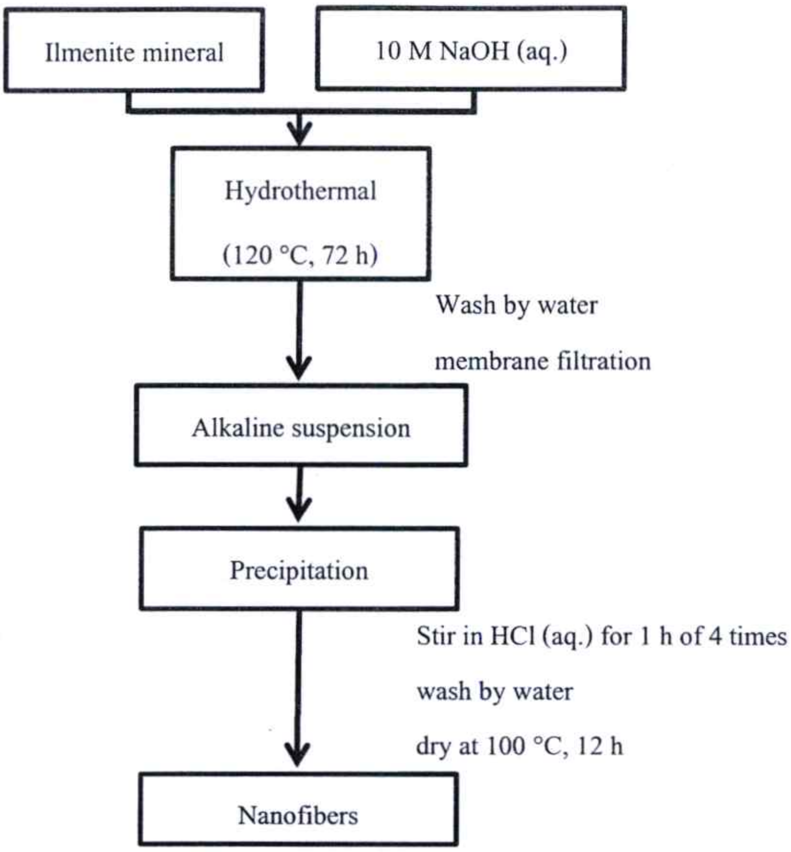

Figure 3.9 The experimental procedure of synthesis of titanate nanofibers.

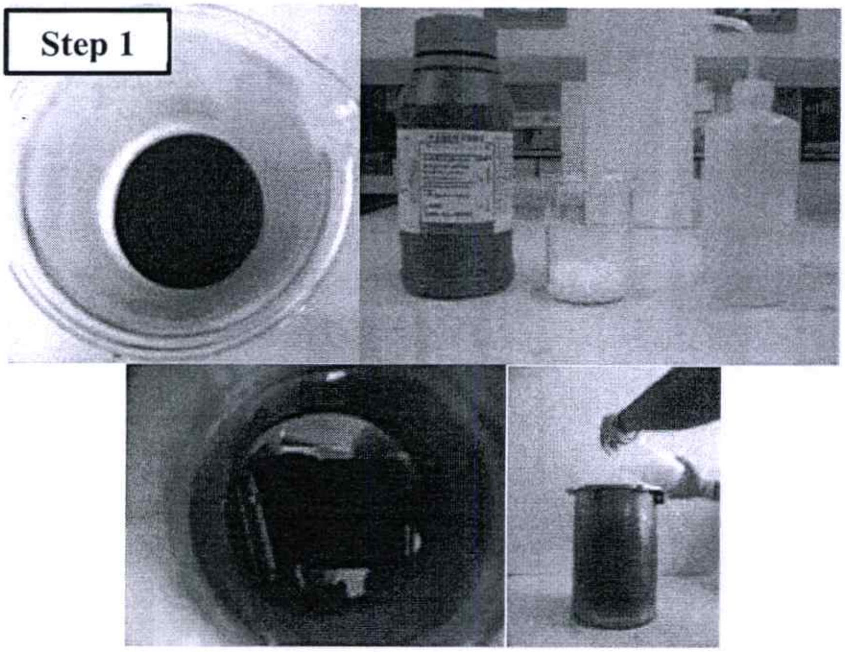

Figure 3.10 The experimental procedure of synthesis of titanate nanofibers.

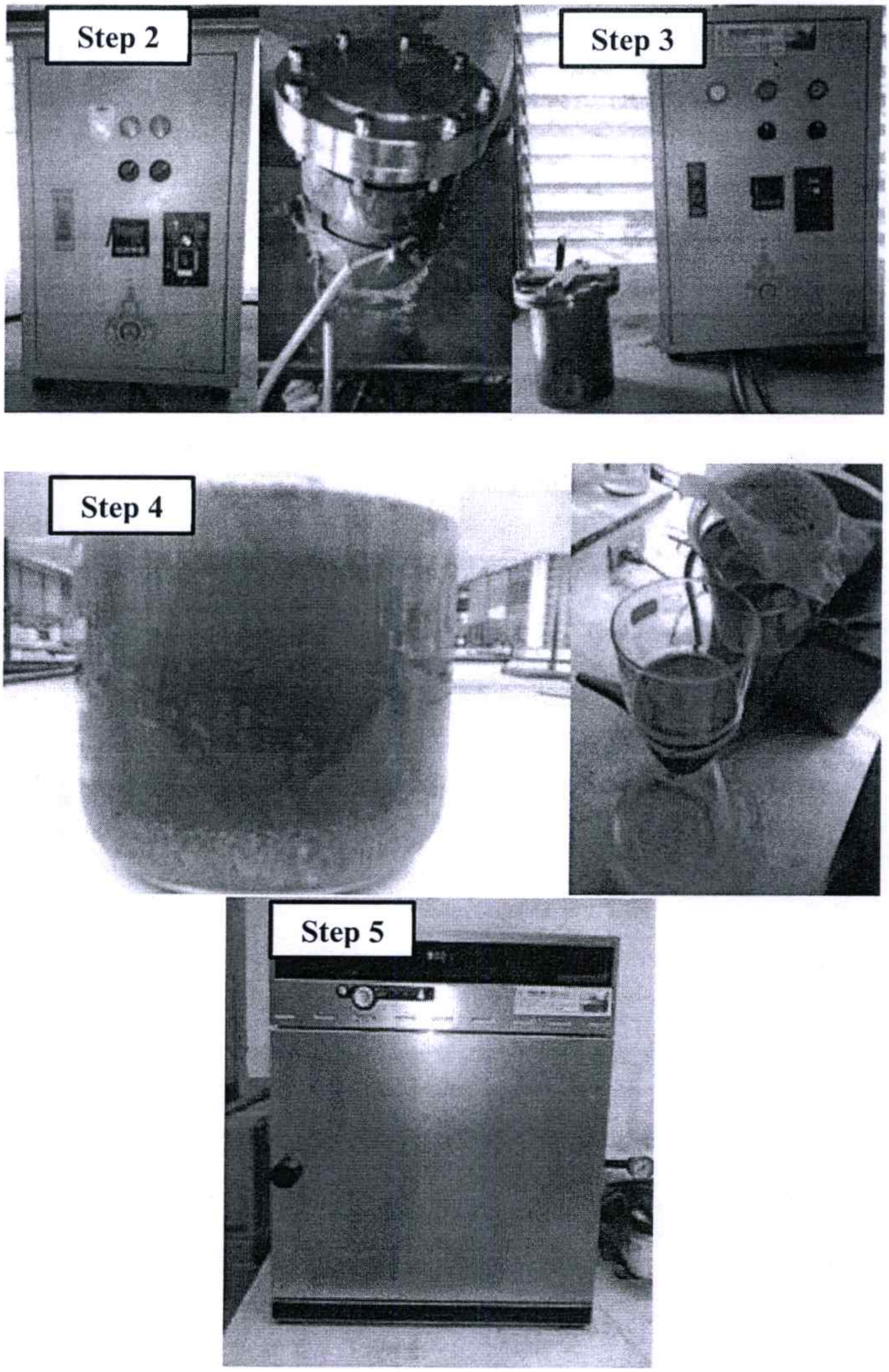

Figure 3.10 (cont.) The experimental procedure of synthesis of titanate nanofibers.

3.2.1.2 Post-Heat Treatment of TiO_2-Related Nanofibers

Titanate nanofibers, obtained by the above-mentioned method, were heated in an air atmosphere at 300–1,000 °C for 2 h. Crucibles containing as-synthesized nanofibers were put into a furnace of 300–1,000 °C. After 2 h heat-treatment, they were cooled down to the room temperature by natural condition.

3.2.2 Fabrication of DSSC based on TiO_2-Related Nanofibers-Nanocomposite as Working Electrode

3.2.2.1 Fabrication of DSSC with Titanate Nanofibers/Commercial Grade TiO_2 Nanoparticles (TNF/P25) Working Electrode

1) Five pastes containing mixed TiO_2 nanoparticles (Degussa P-25) and titanate nanofibers (TNF/P25) were prepared with nanofibers concentration of 0, 5, 10, 15 and 100 wt%. The each sample was labeled as NF0, NF5, NF10, NF15 and NF100, respectively. 6 g of each nanocomposite was blended with 1 ml nitric acid and 1 ml deionized water as dispersive materials. After that the mixture was ground in a white mortar for 5 min.

2) The 25 ml absolute ethanol was added into each of mixture solution, followed by grinding for 5 min. Then, the mixed solution was transferred into a beaker which containing 100 ml absolute ethanol.

3) The mixed solution was stirred with magnetic stirrer for 5 min, followed by sonication with ultrasonic for 5 min.

4) 20 ml terpineol binder and ethyl cellulose were added into the mixture solution. After that the mixed solution was stirred with magnetic stirrer for 5 min. The mixed solution was homogenized using homogenizer at 7000 rpm for 30 min.

5) The mixed solution was evaporated by hot plate and stirred at 100 °C to obtain a viscous paste of nanocomposite.

6) Titanate nanofibers/commercial grade TiO_2 nanoparticles paste was deposited on F-doped SnO_2-coated glass (FTO glass) by doctor blade technique. These working electrodes film were dried at 150 °C for 1 h in ambient condition, followed by annealing at 500 °C for 60 min to eliminate the impurities then cooled down to room temperature.

7) Dye sensitization was performed by immersing a TiO_2 film in concentration 3×10^{-4} mol of dye solution (N719, Solaronix SA, Switzerland) at room temperature for at least 24 h in a sealed beaker and dark condition. The sensitization was completed after the colors at the top and

the bottom were the same. The sensitized films were washed once in absolute ethanol solution, and then dried in hot air condition. Finally, titanate nanofibers/commercial grade TiO_2 nanoparticles working electrodes in each condition were obtained.

8) DSSC was assembled in a typical sandwich-type cell by placing a platinum-coated conducting glass on the dye-sensitized electrode separated by surlyn film to prevent short circuit of the device. They were clipped to immobilize by binder clip. The structure of DSSC is shown in Figure 3.11.

9) Liquid electrolyte consisting of 0.1 M I2, 0.5 M LiI, and 0.5 M 0.2 M *t*-butyl pyridine dispersed in 3 ml acetonitrile was injected into the electrodes. Finally, the photovoltaic properties of the prepared samples were immediately investigated by a solar simulator under AM1.5G condition.

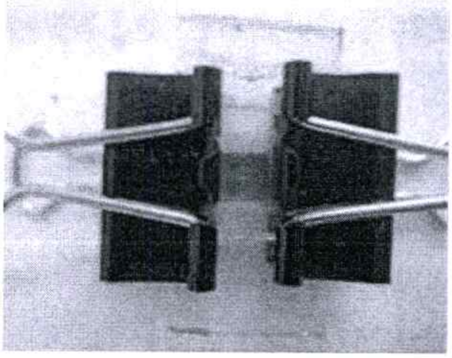

Figure 3.11 The DSSC device fabricated from TNF/P25.

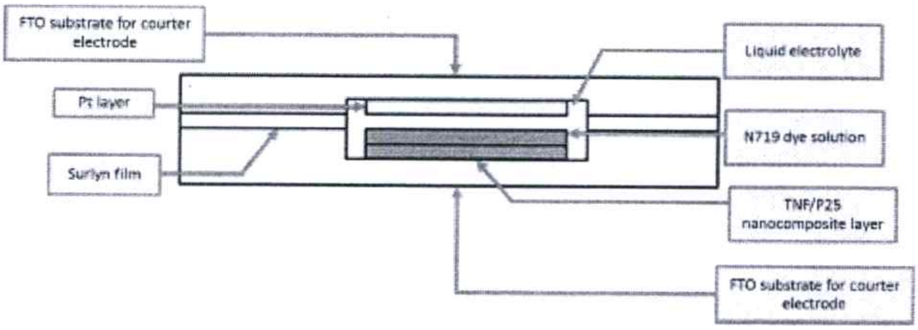

Figure 3.12 The structure of DSSC with TNF/P25 working electrode.

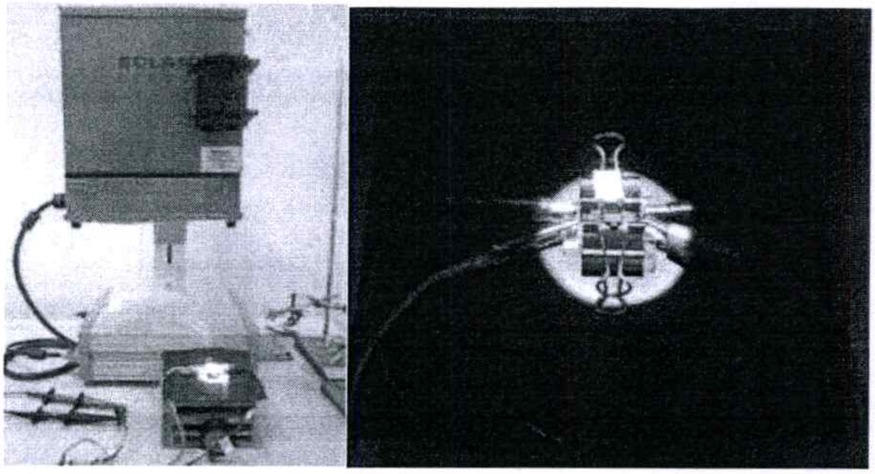

Figure 3.13 The DSSC devices were investigated by a solar simulator under AM1.5G condition.

3.3 Characterization

3.3.1 X-ray Diffraction Spectroscopy

The phase and crystallinity of the samples were characterized by X-ray diffraction (XRD, X'Pert PRO MPD model pw 3040/60, PANalytical) with Cu $K\alpha$ (λ= 0.154 nm) irradiation at a scan rate of 0.02° 2θ s^{-1} and a 2θ range of 10-90° (Figure 3.12).

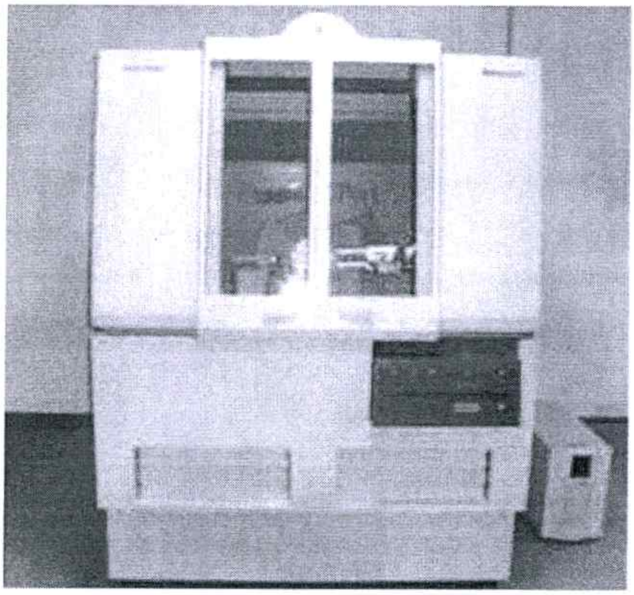

Figure 3.14 X-ray diffraction (XRD, X'Pert PRO MPD model pw 3040/60, PANalytical)

3.3.2 X-ray Fluorescent Spectrometry

The chemical compositions of ilmenite mineral and prepared samples were investigated by X-ray fluorescent spectrometry (XRF, Philips, PW-2404, 4 kW) (Figure 3.13).

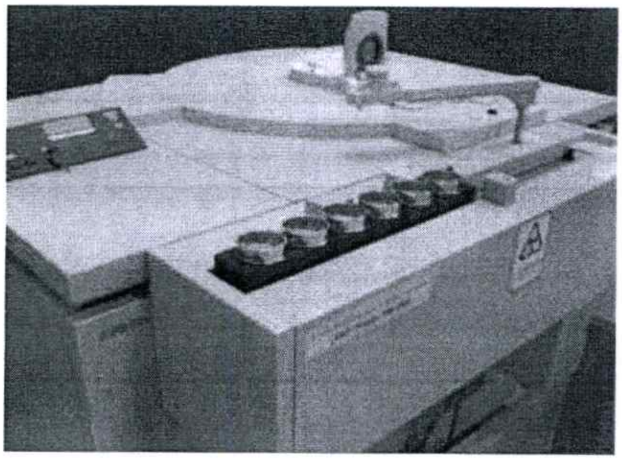

Figure 3.15 X-ray fluorescent spectrometry (XRF, Philips, PW-2404, 4 kW) [123].

3.3.3 X-ray Photoelectron Spectroscopy

The composition on material surface and oxidation state of atom were investigated by X-ray Photoelectron Spectroscopy (Kratos Analytical AXIS Ultra DLD) (Figure 3.14).

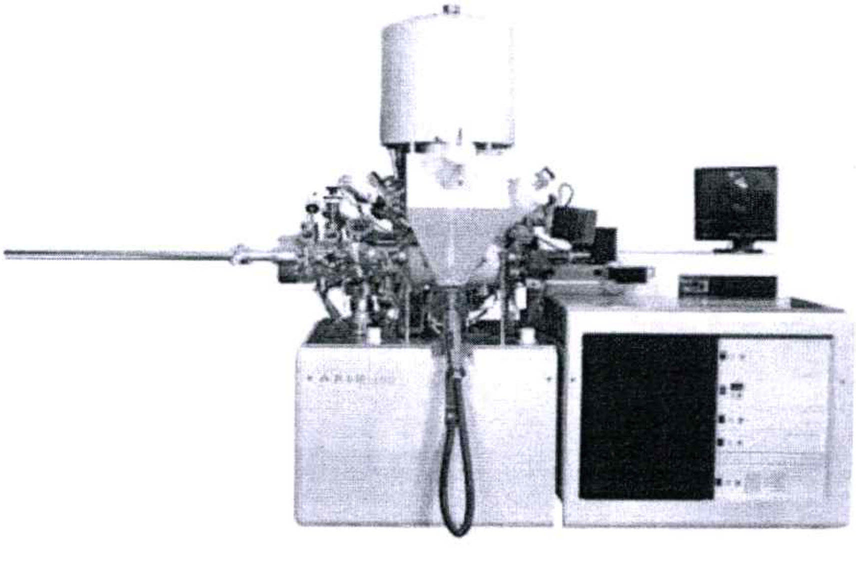

Figure 3.16 X-ray Photoelectron Spectroscopy (Kratos Analytical AXIS Ultra DLD) [124].

3.3.4 Scanning Electron Microscope

The microstructure of ilmenite mineral, as-synthesized product and working electrode of TiO_2 nanocomposite was analyzed by scanning electron microscopy (SEM, JEM-6510, JEOL), with accelerating voltages of 5-20 kV. Sample surface was coated by platinum particle for enhancing conductivity. The distribution of the sizes of the nanofiber diameters was analyzed by SEM (Figure 3.15).

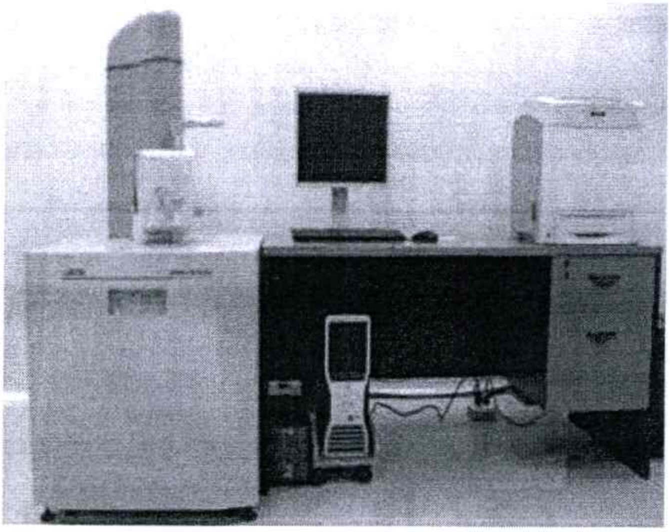

Figure 3.17 Scanning electron microscope (JEM-6510, JEOL).

3.3.5 Transmission Electron Microscope

The structural properties of ilmenite mineral, as-synthesized product were monitored by transmission electron microscope (TEM, JEOL JEM-2010 Electron Microscope). The structure of nanofibers was confirmed by TEM analysis (Figure 3.16).

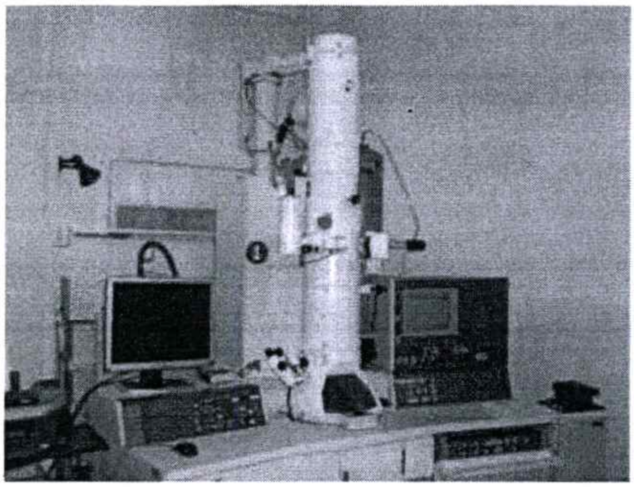

Figure 3.18 Transmission electron microscope (JEOL JEM-2010 Electron Microscope).

3.3.6 Brunauer-Emmett-Teller Analysis

Nitrogen adsorption measurements (Quantachrome Instruments, Autosorb-1) were used to determine the Brunauer-Emmett-Teller (BET) specific surface area (Figure 3.17).

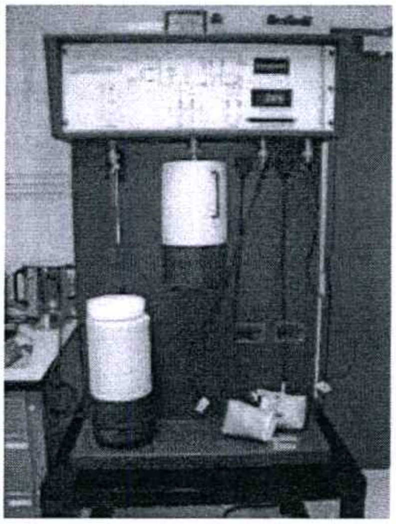

Figure 3.19 Brunauer-Emmett-Teller (BET) specific surface area analysis.

3.3.7 Ultraviolet–Visible Spectroscopy

The optical properties of the as-synthesized nanofibers were investigated of optical properties by UV light absorption using UV-Vis spectroscopy PG Instruments, T90 (Figure 3.18) compared with commercial grade TiO_2 nanoparticles (ST-01). Dye degradation by prepared nanofibers was proved by this technique.

Figure 3.20 UV-Vis spectroscopy PG Instruments, T90.

CHAPTER 4

RESULTS AND DISCUSSION

4.1 The Structure and Morphology of TiO_2-Derived Nanofibers

4.1.1 The Effect of Hydrothermal Condition on Properties of As-Synthesized Nanofibers

The characteristic of the starting ilmenite mineral and the as-synthesized sample are shown in Figure 4.1 (a-b). The starting ilmenite mineral was black-colored. After the reaction in the hydrothermal process, the as-synthesized sample synthesized under all conditions was brown-colored. This phenomenon indicated that a large portion of Fe impurities could be removed by the NaOH (aq.) hydrothermal treatment and neutralization/washing processes [16].

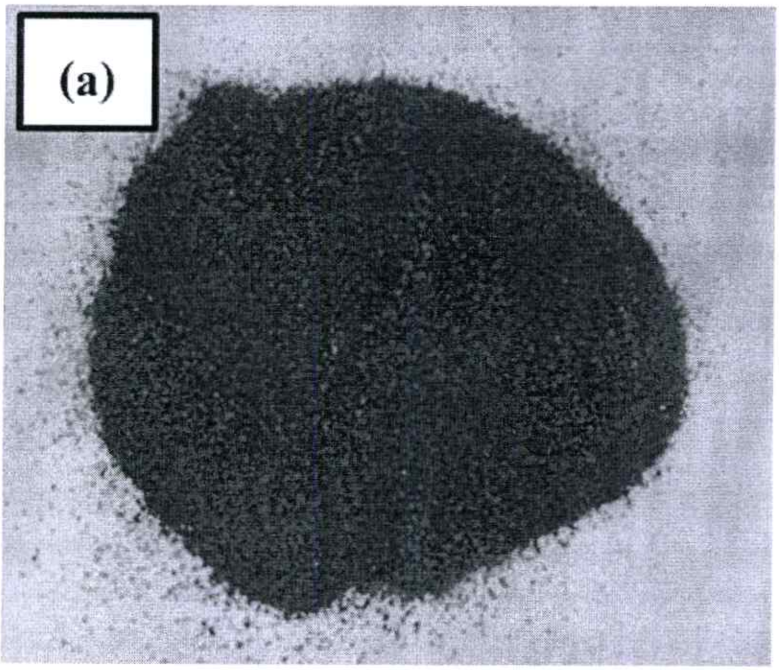

Figure 4.1 Powders of (a) the starting ilmenite mineral and (b) the as-synthesized sample.

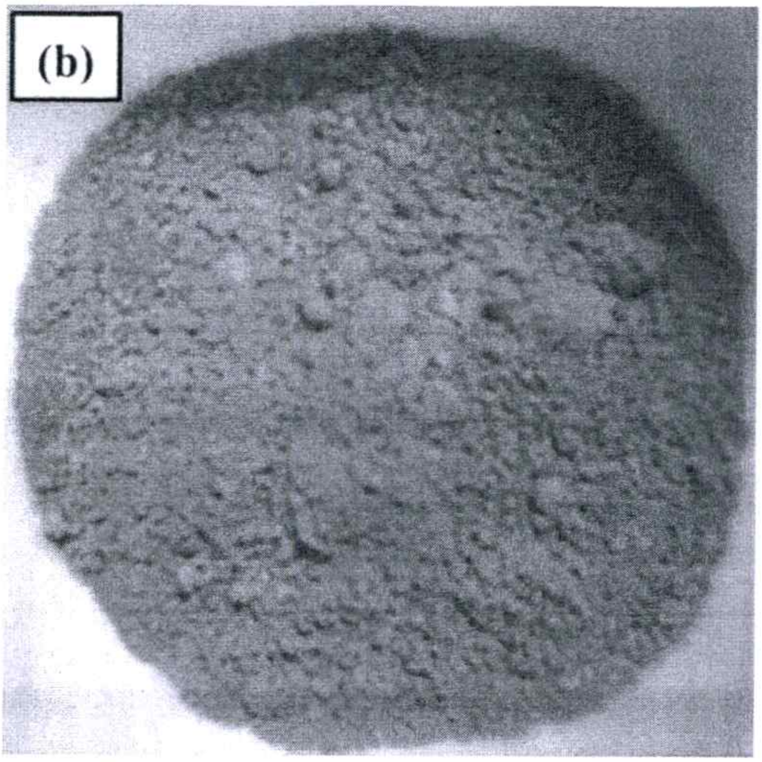

Figure 4.1 (Cont.) Powders of (a) the starting ilmenite mineral and (b) the as-synthesized sample.

Figure 4.2 and 4.5 show the XRD patterns of the prepared samples synthesized under hydrothermal temperature at 100 and 110 °C for various hydrothermal time such as 24, 48 and 72 h. The XRD pattern of the as-synthesized nanofibers prepared under six conditions revealed the hydrogen titanate $H_2Ti_xO_{2x+1}$, e.g., trititanate ($H_2Ti_3O_7$) [17, 52]. The XRD patterns of samples synthesized under hydrothermal temperature at 100 °C for 24, 48 h and 110 °C for 24 h are similar. However, by increasing the reaction time from 24 to 48 h for the samples synthesized under hydrothermal temperature at 100 °C, the diffraction peaks are well defined. The prepared samples synthesized under hydrothermal temperature at 100 °C for 24 and 48 h and 110 °C for 24 h consisting rutile phase located at 2θ values of 27.38°. The result indicating the starting ilmenite mineral existed in the prepared samples. This data attributed to at these temperature the starting ilmenite mineral was not completely dissolved, and only some starting ilmenite mineral transform to nanostructured in hydrothermal process. The rutile peaks of the starting ilmenite mineral trended to decrease and do not appear with increasing hydrothermal time. The characteristic peak at around $2\theta \sim 10°$ indicates that the nanotubes are composed of a layered titanate [17]. From XRD patterns of these samples are shown in Figure 4.2 and 4.5. As can be seen, the diffraction peak at $2\theta \sim 10^{\circ}$ related to the interlayer spacing is narrowed and shifted to higher angles with increasing the time and temperature. This interlayer spacing decrease can be associated with the release of structural water, taking place at high temperatures [58]. This phenomenon indicating the transformation of tube to a cylindrical wire, nanorod or nanofiber structure [125]. In this work, the transformation of TiO_2 crystal structures containing in ilmenite mineral to titanate phase can be described to some Ti–O–Ti bonds break into the layered titanates Ti–O–Na and Ti–OH during treatment of TiO_2 by NaOH. The Na^+ ions of some Ti–O–Na were displaced by H^+ ions to form Ti–OH bonds in the washing process [126-127]. In order to produce TiO_2 nanotubes/nanofibers with different crystallographic phases such as anatase, rutile and brookite, thermal dehydration reactions in air are carried out at high temperatures.

Figure 4.3 shows the SEM image of the starting ilmenite mineral. The starting ilmenite mineral is in granule form of 150-200 μm in diameter. Figure 4.4 (a-c) and 4.6 (a-c) show the SEM images of the as-synthesized sample synthesized under hydrothermal temperature at 100 and 110 °C for various hydrothermal time such as 24, 48 and 72 h. After hydrothermal treatment at different times, the as-synthesized sample synthesized under hydrothermal temperature at 100 °C for 24 and 48 h and 110 °C for 24 h showed the major structure of cluster-like morphology with some structure of tube-like morphology, while the as-synthesized sample synthesized under hydrothermal temperature at 100 °C for 72 h and 110 °C for 48 and 72 h showed the some fiber-like morphology. Most of nanofibers had a shorter shape with uneven surface. In general, hydrothermal treatment at a slightly higher temperature (120-150 °C or higher) or in stronger alkali solution (conc. NaOH(aq.)or KOH(aq.)) results in the formation of solid nanowires (or even long nanofibers) rather than scrolled nanotubes, because the normal unidirectional crystal growth becomes preferential at these conditions. The crystal growth of the 1-D nanostructure can be explained by following mechanism. The natural ilmenite granules were coarse so that they slowly dissolved into NaOH solution, which suppressed the nucleation and assisted preferential crystal growth along with the 0 1 0 direction of trititanate [16].

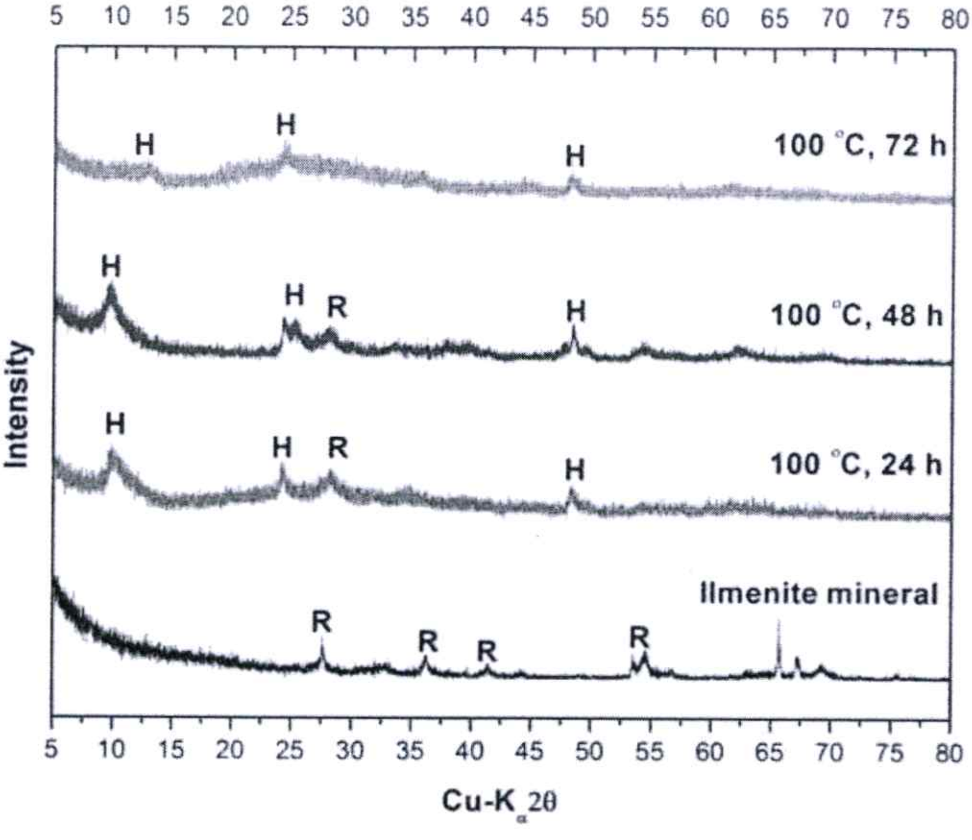

Figure 4.2 XRD patterns of the starting ilmenite mineral and the as-synthesized sample prepared by hydrothermal method at 100 °C for 24, 48 and 72 h, H = hydrogen titanate and R = rutile TiO_2.

Figure 4.3 SEM image of the starting ilmenite mineral.

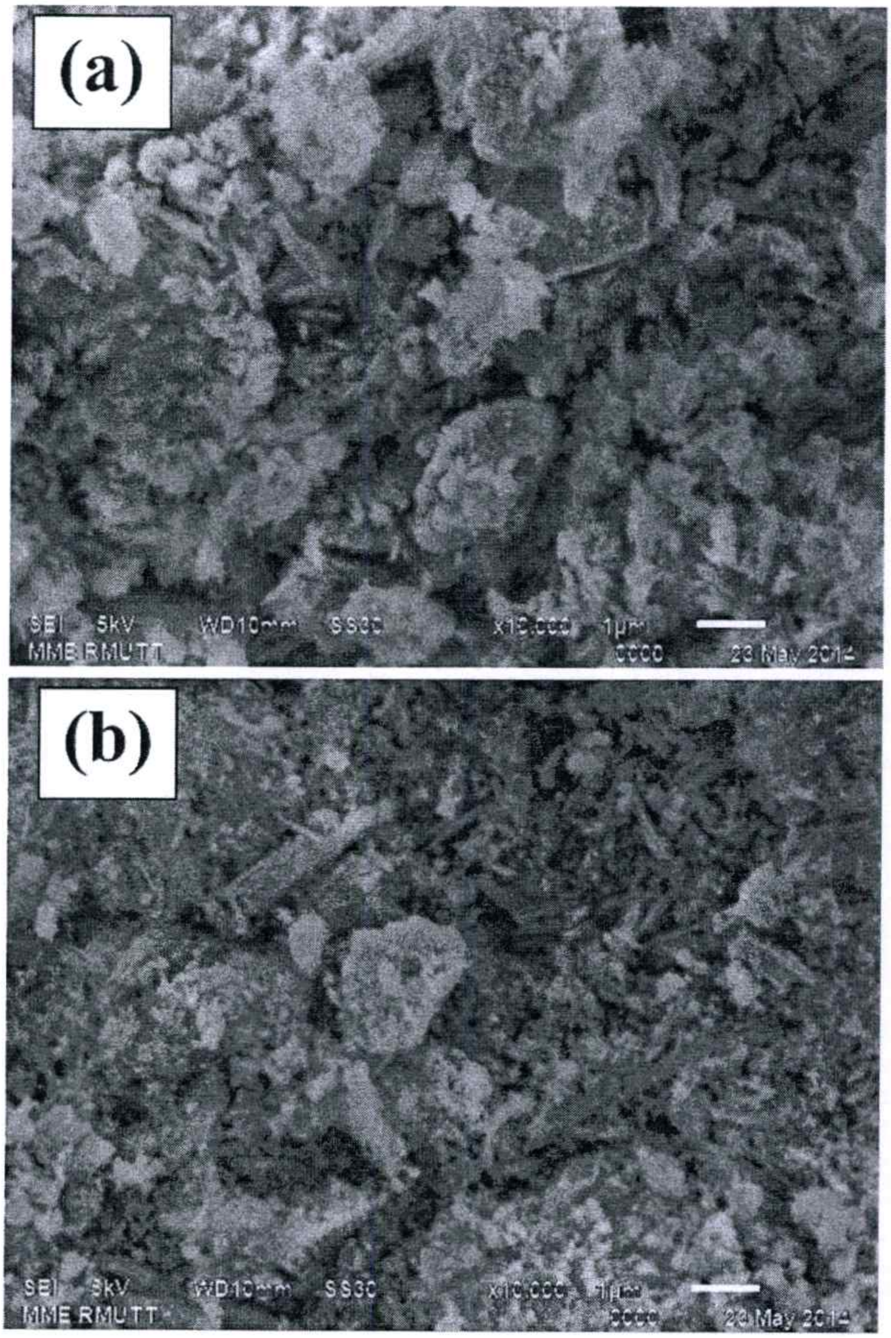

Figure 4.4 SEM images of the as-synthesized sample prepared by hydrothermal method at 100 °C for (a) 24, (b) 48 and (c) 72 h.

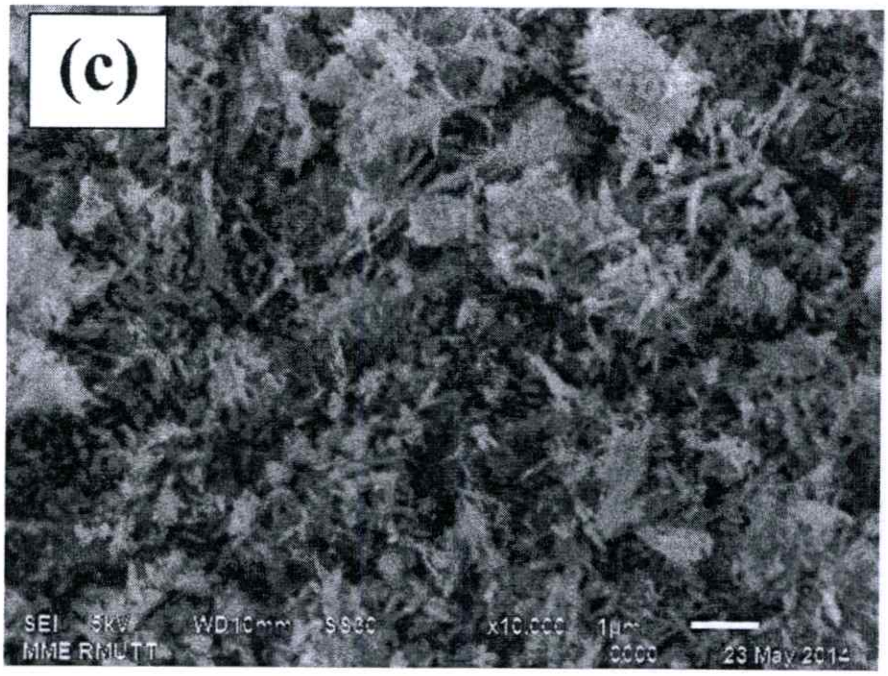

Figure 4.4 (cont.) SEM images of the as-synthesized sample prepared by hydrothermal method at 100 °C for (a) 24, (b) 48 and (c) 72 h.

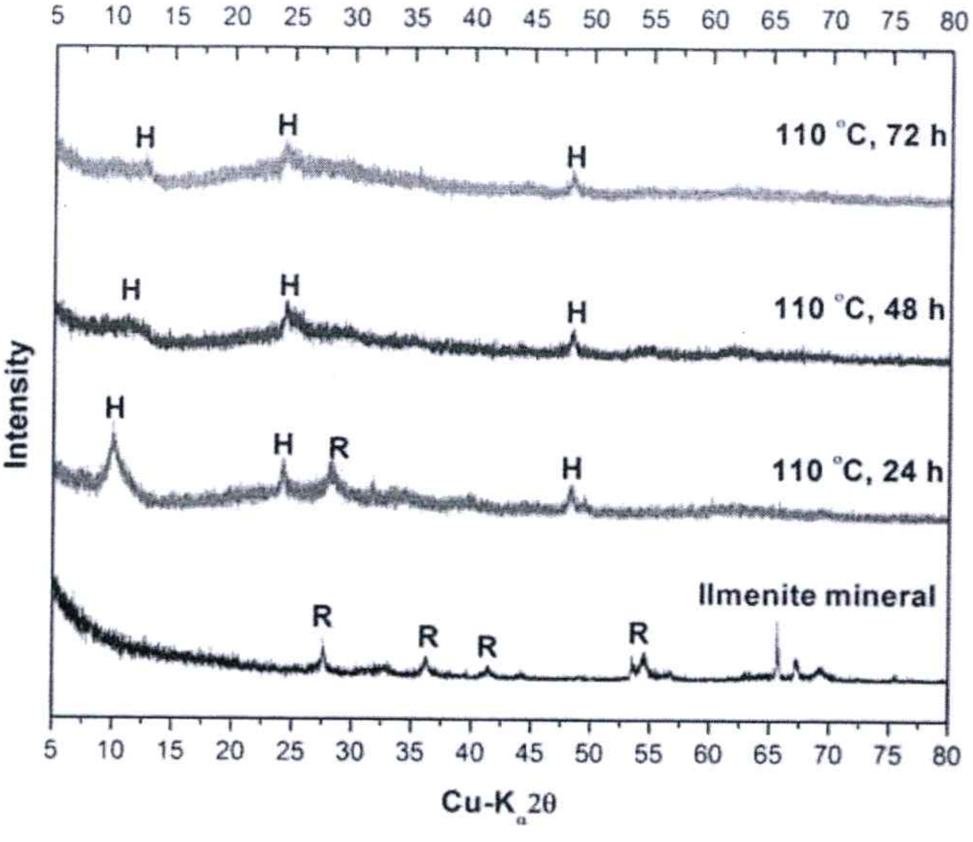

Figure 4.5 XRD patterns of the starting ilmenite mineral and the as-synthesized sample prepared by hydrothermal method at 110 °C for 24, 48 and 72 h, H = hydrogen titanate and R = rutile TiO_2.

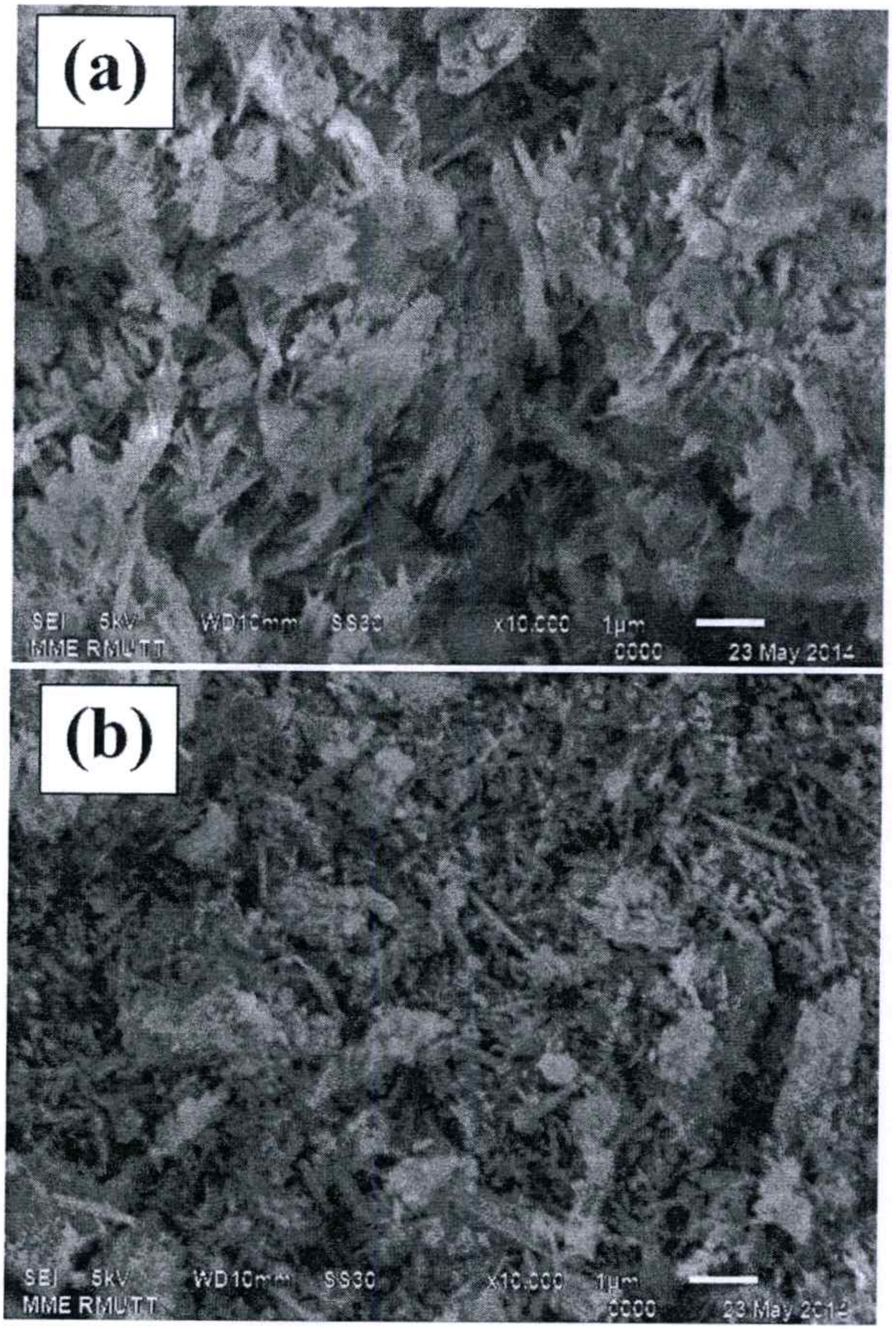

Figure 4.6 SEM images of the as-synthesized sample prepared by hydrothermal method 110 °C for (a) 24, (b) 48 and (c) 72 h.

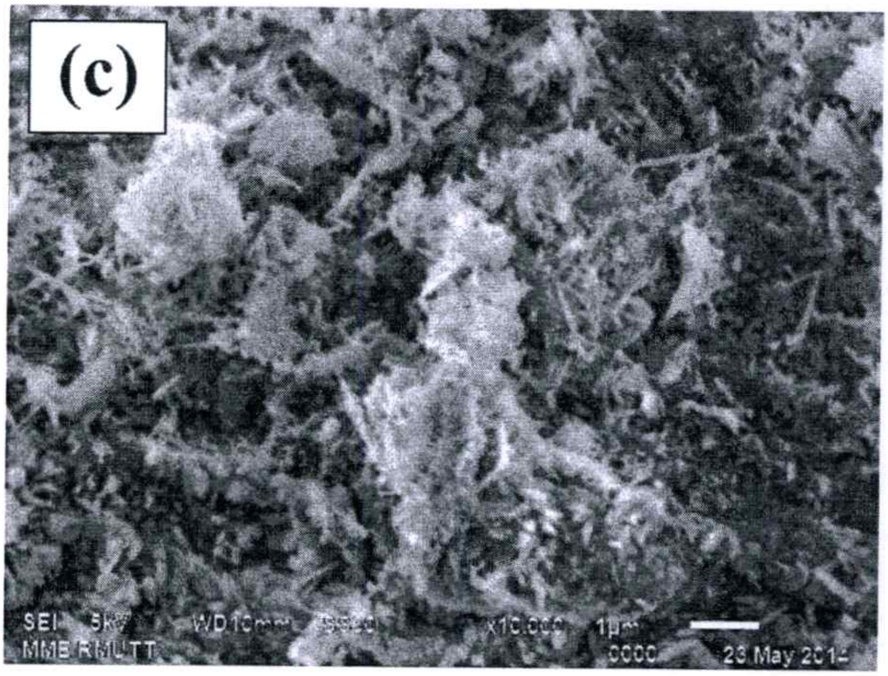

Figure 4.6 (cont.) SEM images of the as-synthesized sample prepared by hydrothermal method 110 °C for (a) 24, (b) 48 and (c) 72 h.

Figure 4.7 (a and b) shows the TEM images of the as-synthesized sample synthesized under hydrothermal temperature at 100 and 110 °C for 24 h. From TEM images, the as-synthesized sample synthesized under hydrothermal temperature at 100 and 110 °C for 24 h similar to cluster and nanotube morphology.

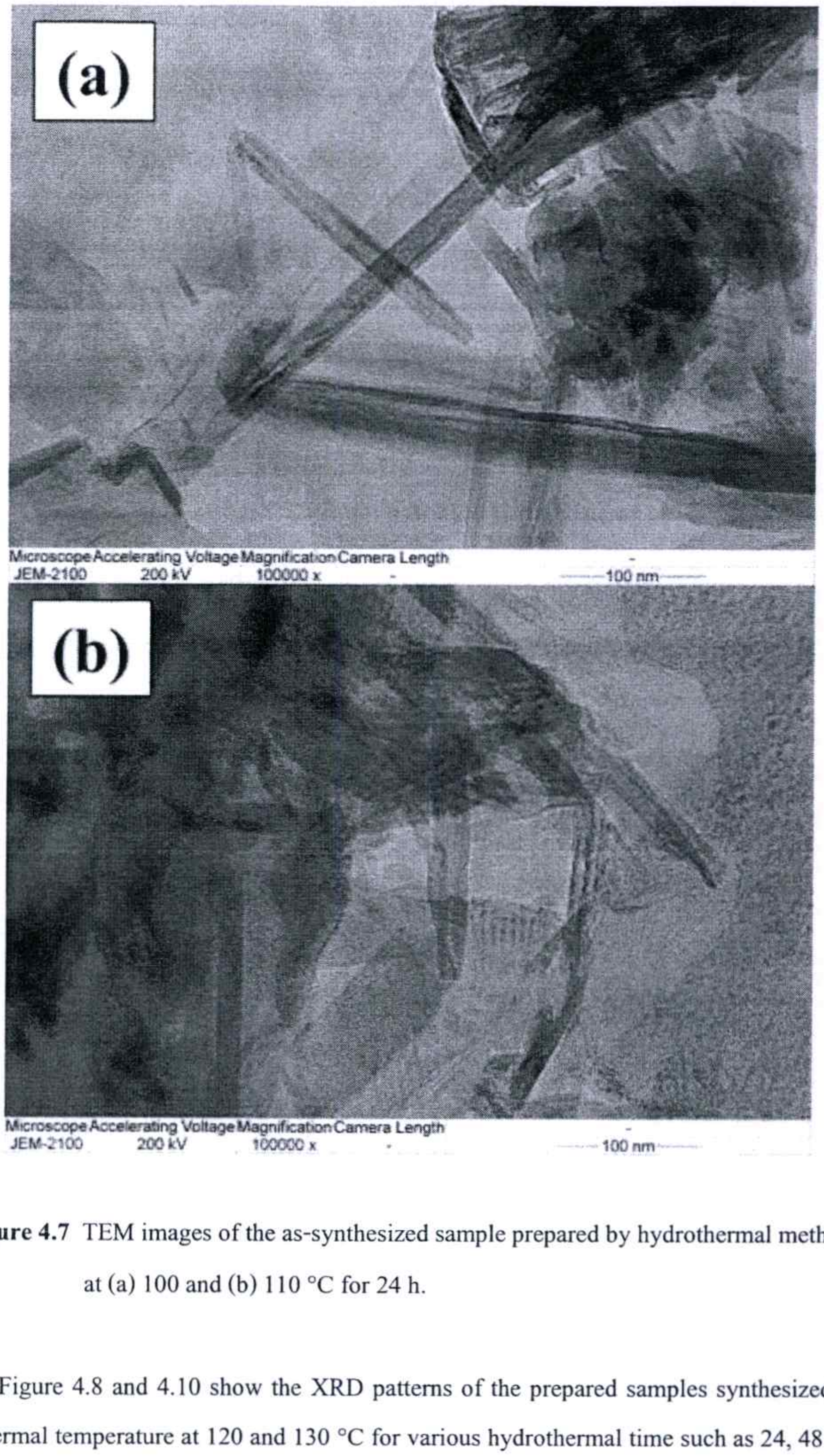

Figure 4.7 TEM images of the as-synthesized sample prepared by hydrothermal method at (a) 100 and (b) 110 °C for 24 h.

Figure 4.8 and 4.10 show the XRD patterns of the prepared samples synthesized under hydrothermal temperature at 120 and 130 °C for various hydrothermal time such as 24, 48 and 72 h. The crystalline structure of the as-synthesized nanofibers prepared under six conditions performed the hydrogen titanate $H_2Ti_xO_{2x+1}$, e.g., trititanate ($H_2Ti_3O_7$) similar to the prepared samples synthesized under hydrothermal temperature at 100 and 110 °C [17, 52]. The rutile phase of the starting ilmenite mineral was not appeared in these samples, indicating to at these conditions the starting ilmenite mineral was almost dissolved and transform to fiber structure. The diffraction peak of the prepared samples became sharper and narrower with rising of hydrothermal time from 24 to 72 h, indicating the formation of more and greater crystallites and an enhancement of crystallization. In addition, the intensity of the diffraction peaks gradually heightened with the increasing of hydrothermal time, which shows that the crystallinity of the products become higher as hydrothermal time increases.

Figure 4.9 (a-c) and 4.11 (a-c) show the SEM images of the as-synthesized sample synthesized under hydrothermal temperature at 120 and 130 °C for various hydrothermal time such as 24, 48, and 72 h. After hydrothermal treatment at different times, the as-synthesized sample synthesized under hydrothermal temperature at 120 and 130 °C for 24-72 h showed the fiber-like morphology. However, nanofiber structured of the as-synthesized sample synthesized under hydrothermal temperature at 120 and 130 °C for 24-48 h was not completely fiber structure and contained a lot of shorter nanofibers with uneven surface. In addition, the nanfibers tended to form aggregated bundles. There was no obvious difference of microstrucutre among the as-synthesized sample synthesized under hydrothermal temperature at 120 and 130 °C for 72 h. These samples were long fiber-like morphology with length in the range of several hundred nm to several μm. This data indicate that the grains become growth with time and temperature. Increasing hydrothermal time, the dissolution of the starting ilmenite mineral in NaOH solution is improved to result in the enhancement of nuclei and promote the growth of nanofibers [17].

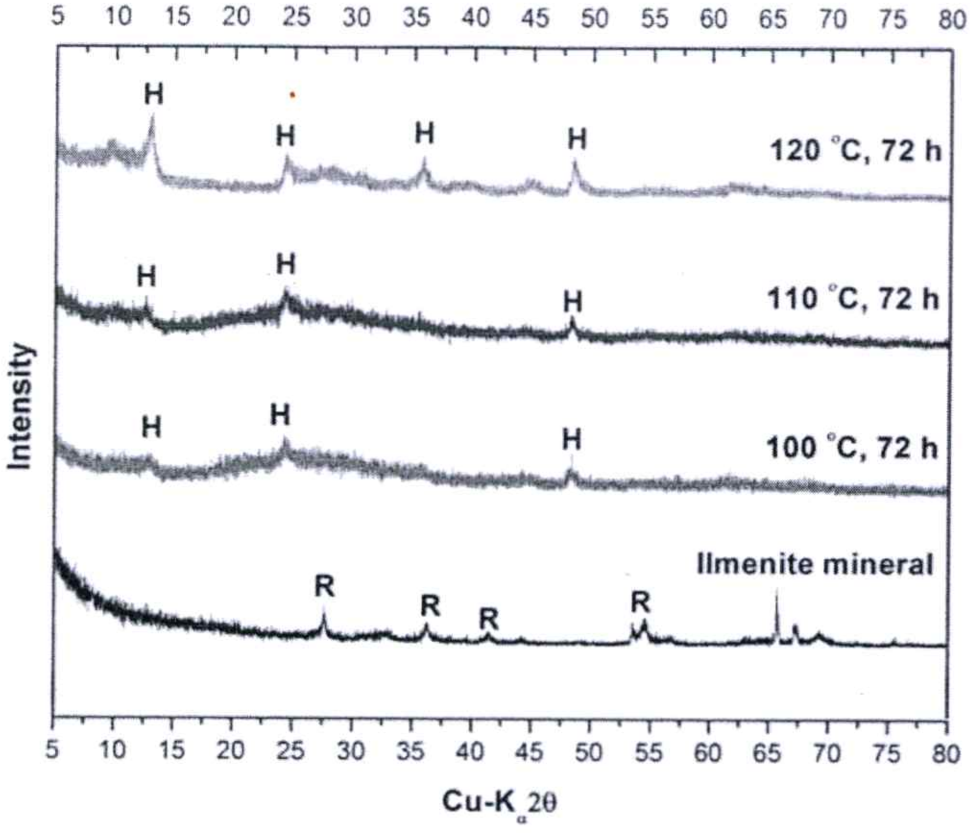

Figure 4.8 XRD patterns of the starting ilmenite mineral and the as-synthesized sample prepared by hydrothermal method at 120 °C for 24, 48 and 72 h, H = hydrogen titanate and R = rutile TiO_2.

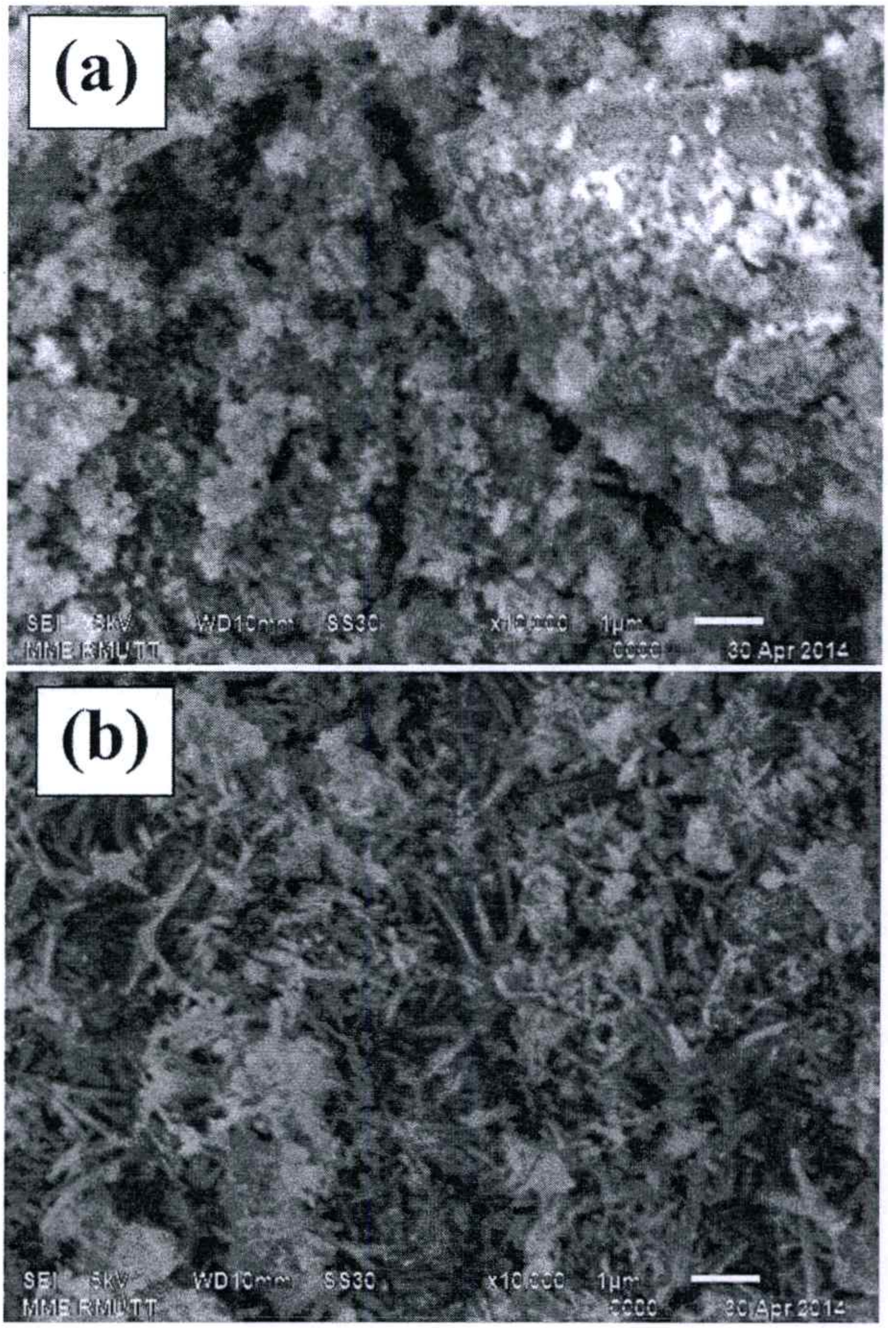

Figure 4.9 SEM images of the as-synthesized sample prepared by hydrothermal method 120 °C for (a) 24, (b) 48 and (c) 72 h.

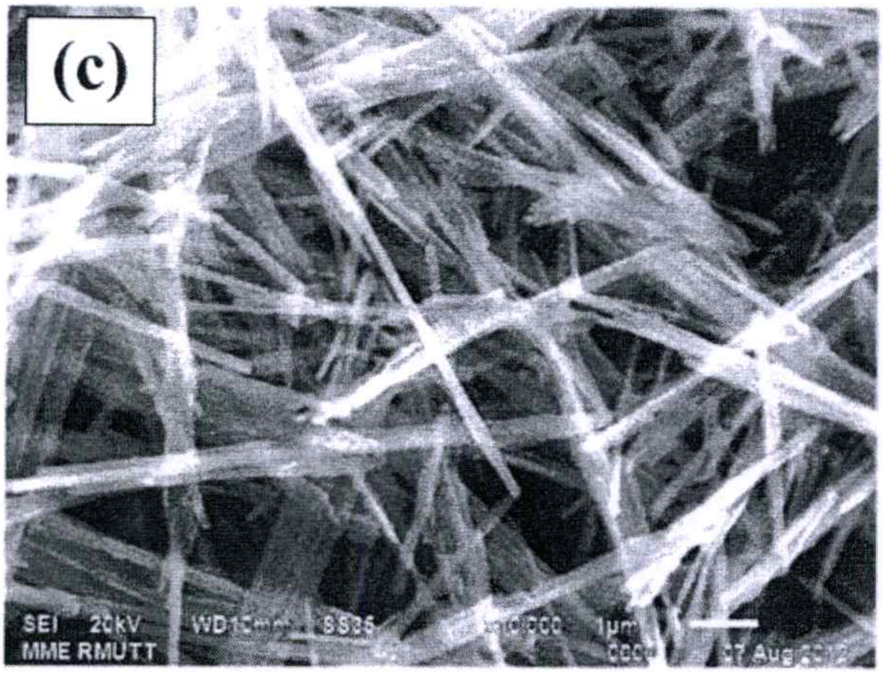

Figure 4.9 (cont.) SEM images of the as-synthesized sample prepared by hydrothermal method 120 °C for (a) 24, (b) 48 and (c) 72 h.

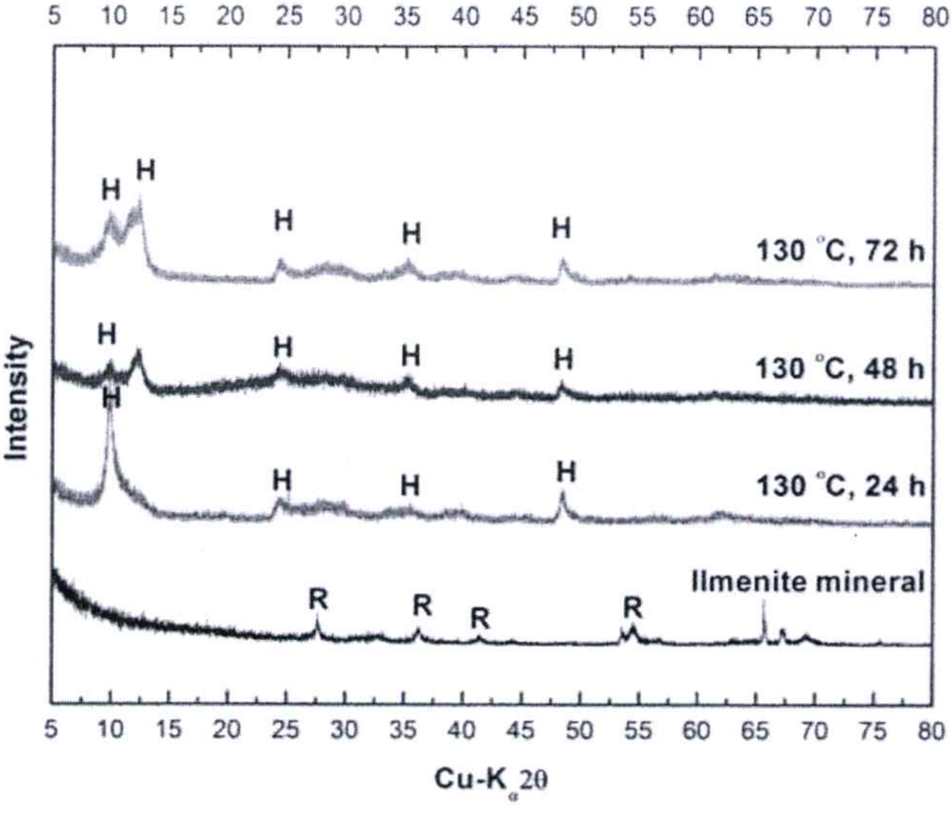

Figure 4.10 XRD patterns of the starting ilmenite mineral and the as-synthesized sample prepared by hydrothermal method at 130 °C for 24, 48 and 72 h, H = hydrogen titanate and R = rutile TiO_2.

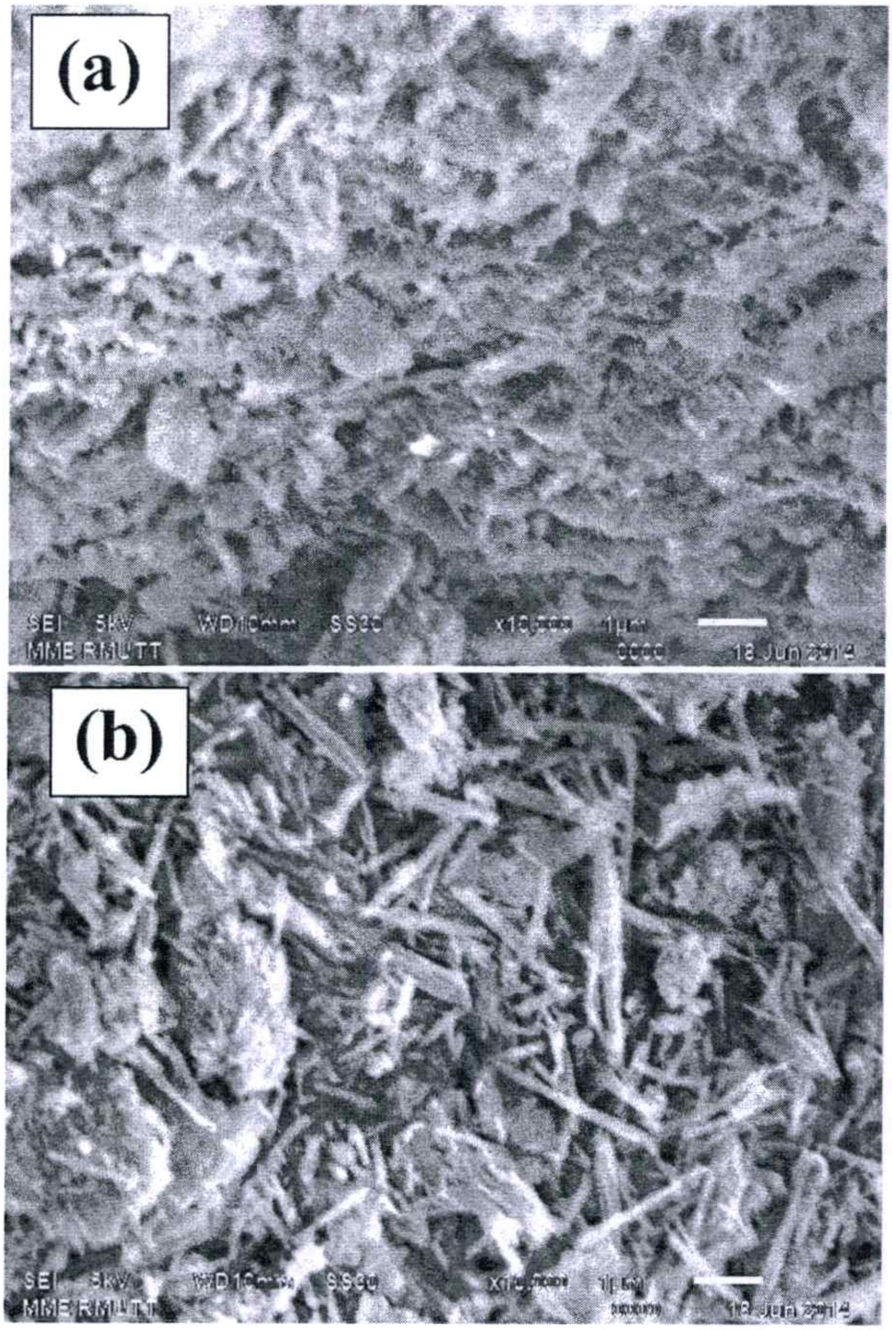

Figure 4.11 SEM images of the as-synthesized sample prepared by hydrothermal method 130 °C for (a) 24, (b) 48 and (c) 72 h.

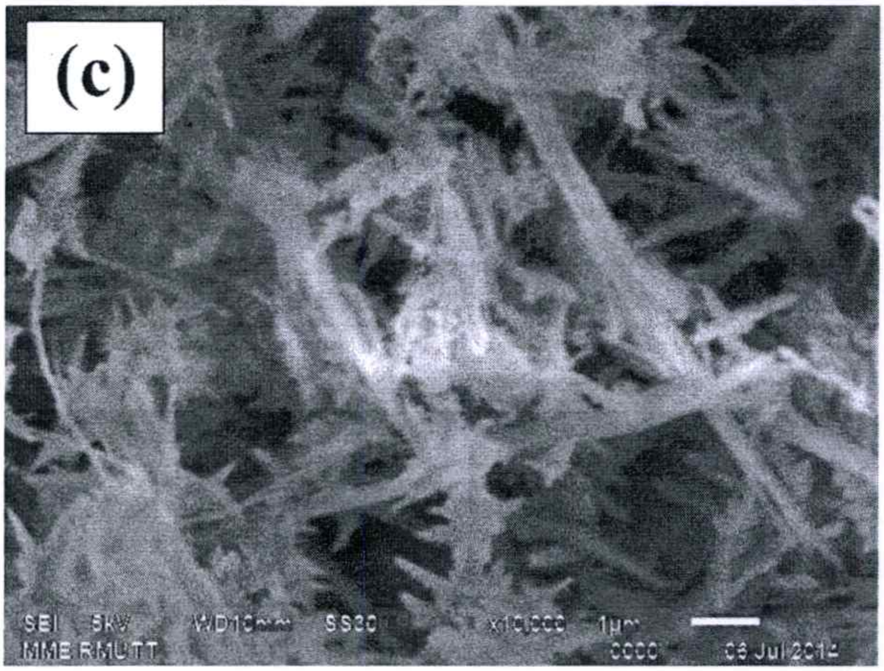

Figure 4.11 (cont.) SEM images of the as-synthesized sample prepared by hydrothermal method 130 °C for (a) 24, (b) 48 and (c) 72 h.

Figure 4.12 (a and b) shows the TEM images of the as-synthesized nanofibers prepared under synthesized under hydrothermal temperature at 120-130 °C for 24 h. From TEM images, it is confirmed that the as-synthesized are solid (not hollow) structure indicating fiber-like morphology.

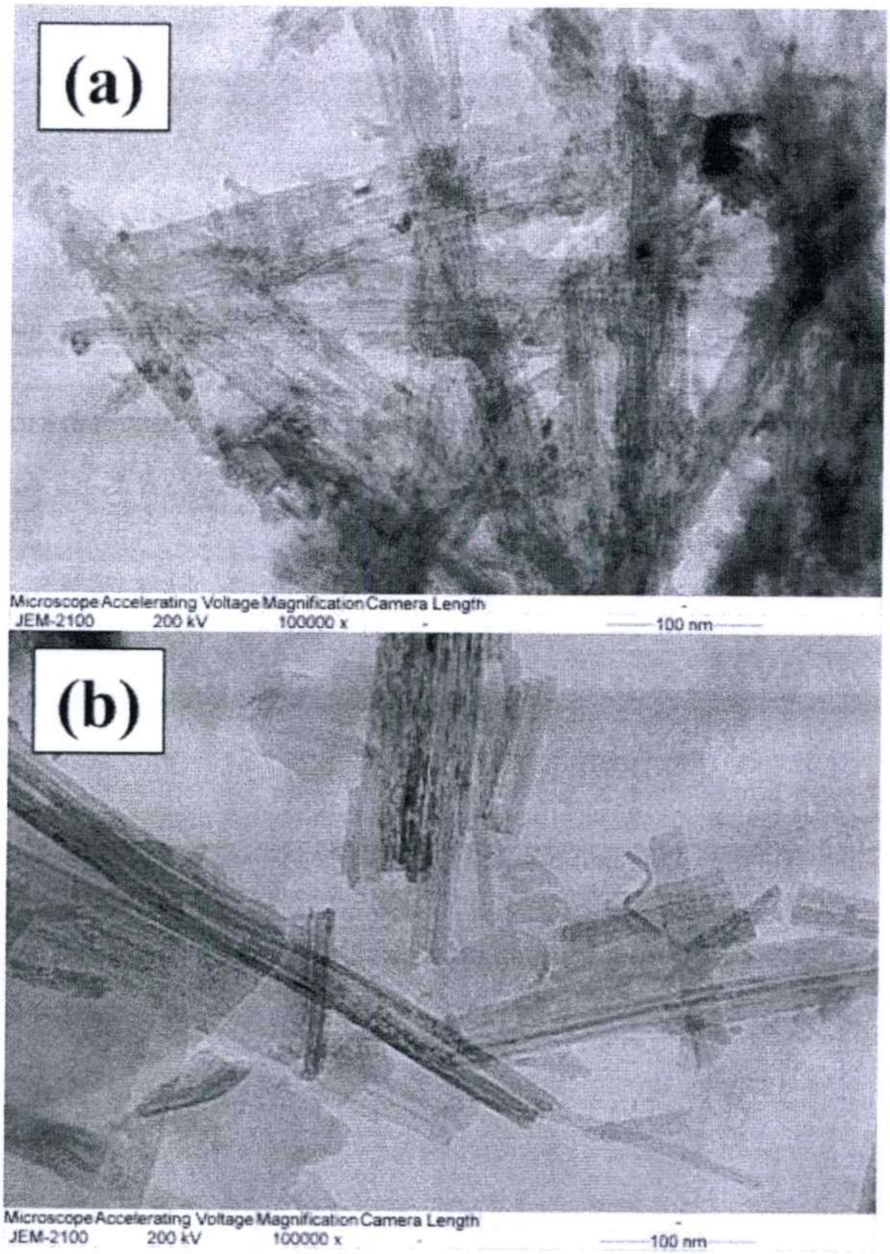

Figure 4.12 TEM images of the as-synthesized sample prepared by hydrothermal method at 120 and 130 °C for 24 h.

These results infer that titanate nanotubes are prepared at low temperature, whereas titanate nanofibers are synthesized at high temperature, which could be attributed the rate of crystallization of the nanosheets [128]. Kim et al. [129] have reported that the nanosheets could be converted to nanotubes by scrolling at a relatively low temperature (100–150 °C), whereas nanofibers or nanoribbons could be produced from the nanosheets at temperatures above 170 °C.

At high temperatures, the rate of crystallization was large enough to make the nanosheet became too thick and rigid to bend before curving could occur.

Figure 4.13 shows the XRD patterns of the prepared samples synthesized under hydrothermal temperature at 100, 110, 120 and 130 °C for 72 h compared with the starting ilmenite mineral. The XRD pattern of the starting ilmenite mineral emerged in rutile phase, while the as-synthesized nanofibers prepared under three conditions exhibited the crystalline structure of hydrogen titanate $H_2Ti_xO_{2x+1}$, e.g., trititanate ($H_2Ti_3O_7$) [17, 52]. The results were similar to those of leucoxene mineral and nanofibers from leucoxene mineral in our previous works [57]. The diffraction peaks of other impurities, such as NaCl and rutile phase of the starting natural ilmenite mineral, were not observed. This was due to the fact that Na content in the nanofibers could be minimized by repeated ion-exchanging treatment with HCl leaching and water washing [17, 52]. The reduced Na in the nanofibers occurred in the post-treatment washing as a result of the replacement of Na^+ in $Na_2Ti_2O_5{\bullet}H_2O$ by H^+ [130]. However, compared with the titanate nanotubes, the nanofibers tended to contain more residual Na ions under the same ion-exchanging conditions due to the geometry of the nanofibers, i.e., more solid and thicker structure, and alkali-metal hexatitanates ($A_2Ti_6O_{13}$, A = Na, K, Rb) tended to be in the form of stable solid fibrous structure and was not easily removed with the aqueous HCl treatment at room temperature [16]. When the hydrothermal temperature is increased from 100 to 130 °C, the diffraction peaks of samples became sharper and narrower, as shown in Figure 4.13, indicating the enhancement of formation and crystallization of crystallites of nanofibers. In addition, the intensity of the diffraction peaks gradually amplified with the increasing of hydrothermal temperature, indicating the crystallinity of the products become higher as hydrothermal temperature elevates [131]. However, the peak position at lower angles $2\theta \sim 10°$ appears again after hydrothermal temperature reaching to 130 °C. The increased interlayer spacing may occur due to adsorbed water molecules [132].

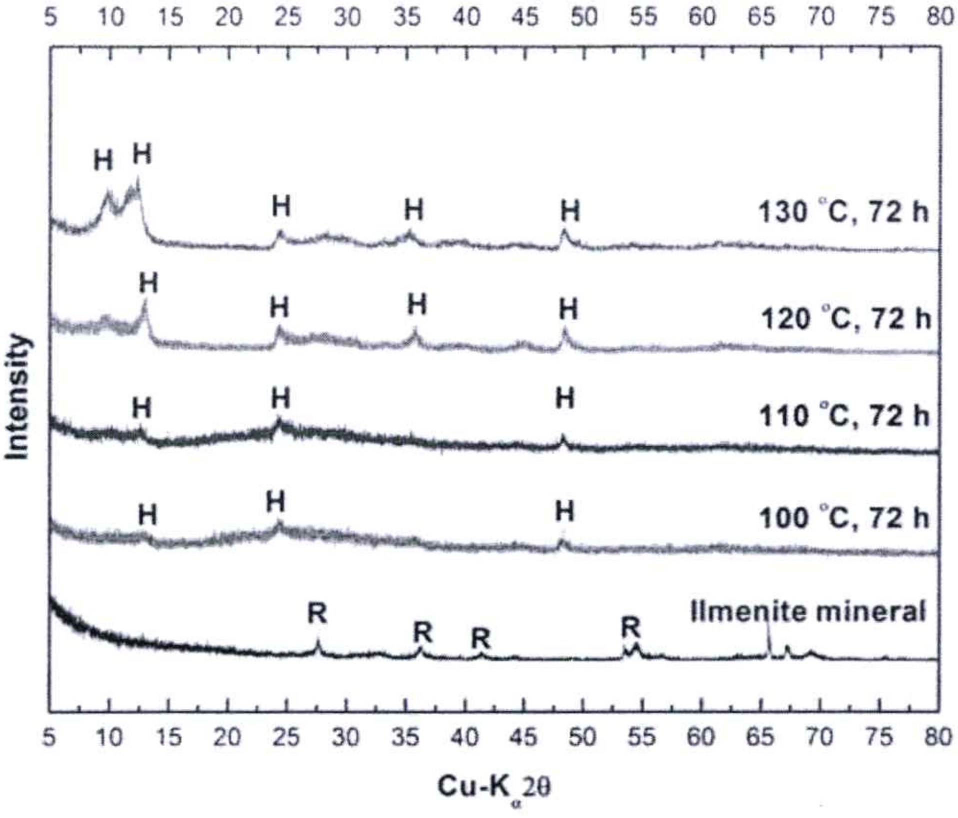

Figure 4.13 XRD patterns of the starting ilmenite mineral and the as-synthesized sample prepared by hydrothermal method at 100, 110, 120 and 130 °C for 72 h, H = hydrogen titanate and R = rutile TiO_2.

Figure 4.14 (a-d) shows the SEM images the as-synthesized sample synthesized under hydrothermal temperature at 100, 110, 120 and 130 °C for 72 h, respectively. After hydrothermal treatment at different temperatures, the as-synthesized sample under various conditions showed the fiber-like morphology. Furthermore, as seen in SEM images of as-synthesized sample obtained at different hydrothermal temperatures in Figure 4.14, it can be deduced that the hydrothermal temperature had significant effect on products' morphology, fibrous size and agglomeration. According to Figure 4.14 (a-b), the nanofibers synthesized at 100-110 °C for 72 h contained a lot of shorter nanofibers with slight agglomeration, around 1-2 μm length with the diameter of approximately 20-70 nm. Meanwhile the nanofibers prepared at 120 and 130 °C for 72 h, as shown in Figure 4.14 (c-d), demonstrated longer nanofibers and even surface, and length of 2-7 μm with approximately 20-90 nm in diameter. However, some nanofibers synthesized at 130 °C for 72 h was agglomerated with other fibers, resulting to aggregated bundles. Armstrong et al. [133] have reported that the hydrothermal treatment using NaOH as the aqueous solution at

170 °C for 72 h yielded solid nanofibers (nanowires in their expression). Our results are basically in good accordance with their results. In addition, most of the nanofibers synthesized at 120 °C for 72 h show in Figure 4.14 (c) tend to stick together in bundles, thus causing some of the nanofibers to appear thicker than others. Results indicated that the nanofibers prepared at high temperature (120 °C) had more dimension aspect ratio than the nanofibers prepared at other temperature (100, 110 and 130 °C). This feature may be due to the sufficiency of thermal energy supplied during the process leading to the formation of bundle of nanofibers. Recent papers, have reported on the dimension of the samples prepared via hydrothermal method could be magnified as the hydrothermal temperature increased [134-137]. The nanofibers prepared at 120 °C for 72 h, as shown in Figure 4.15 (c), demonstrated longer nanofibers with length of several hundred nm to more than 1 μm and diameter range of 20-90 nm as shown in Figure 4.15.

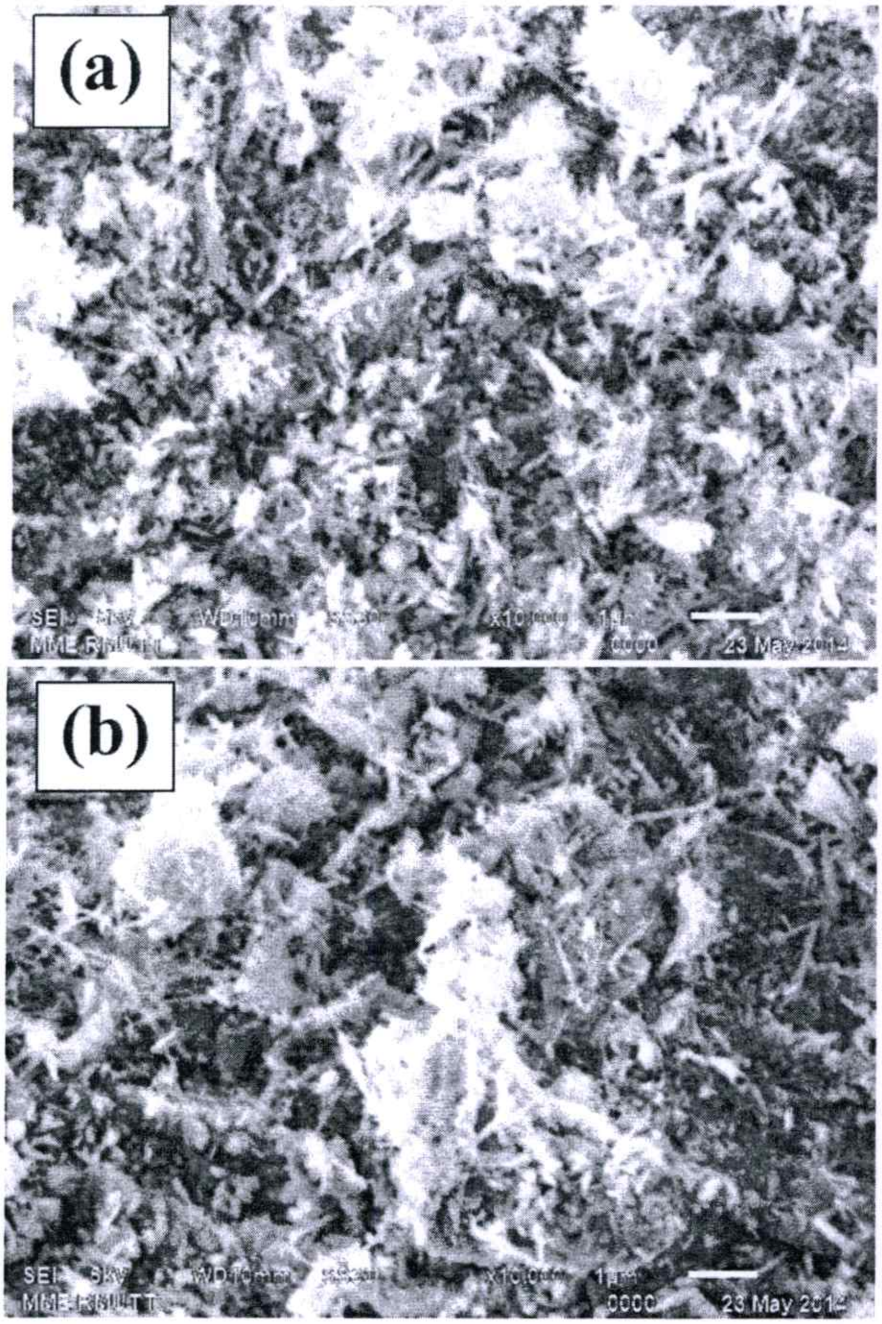

Figure 4.14 SEM images of the as-synthesized nanofibers prepared by hydrothermal method (a) 100, (b) 110, (c) 120 and (d) 130 °C for 72 h.

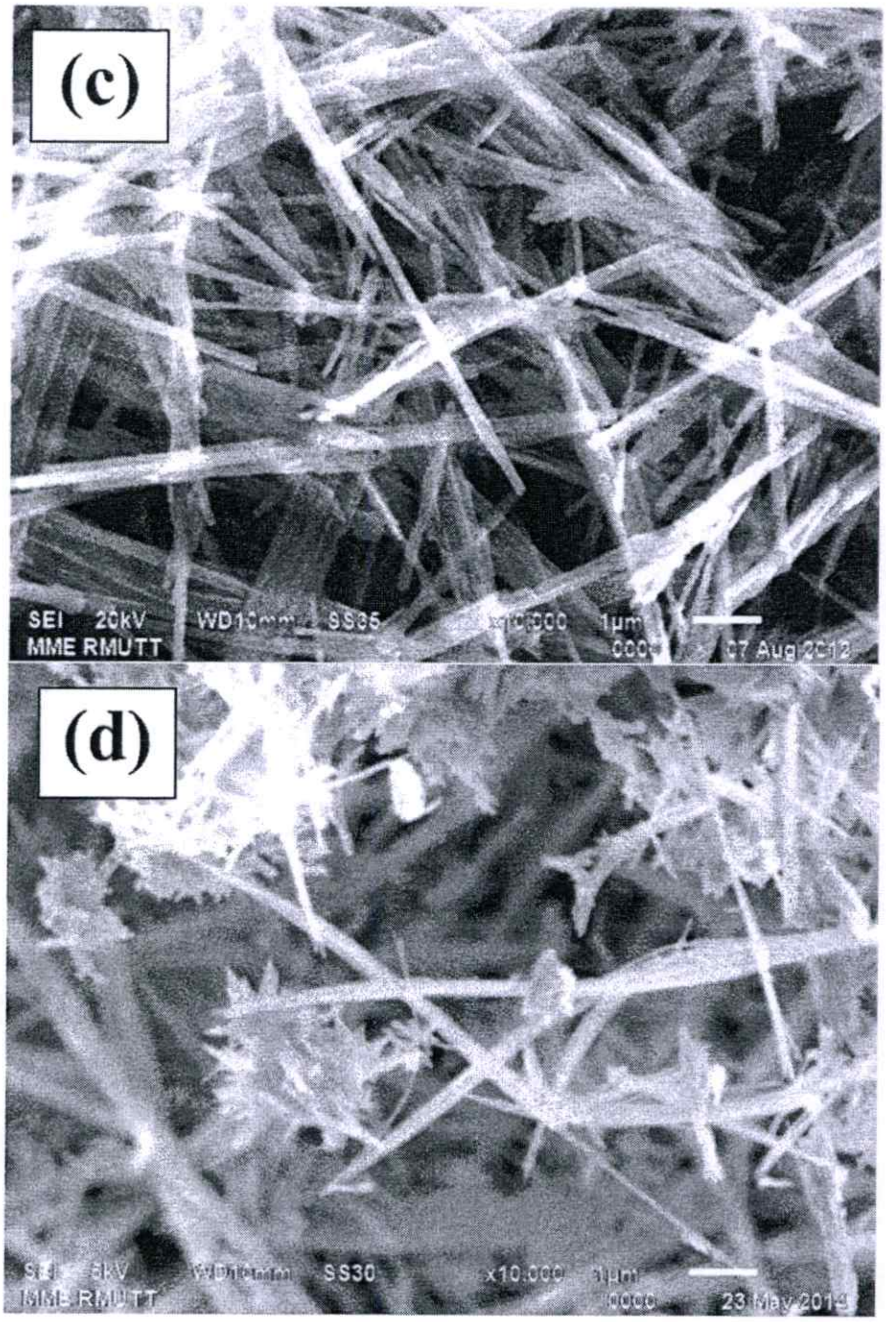

Figure 4.14 (cont.) SEM images of the as-synthesized nanofibers prepared by hydrothermal method (a) 100, (b) 110, (c) 120 and (d) 130 °C for 72 h.

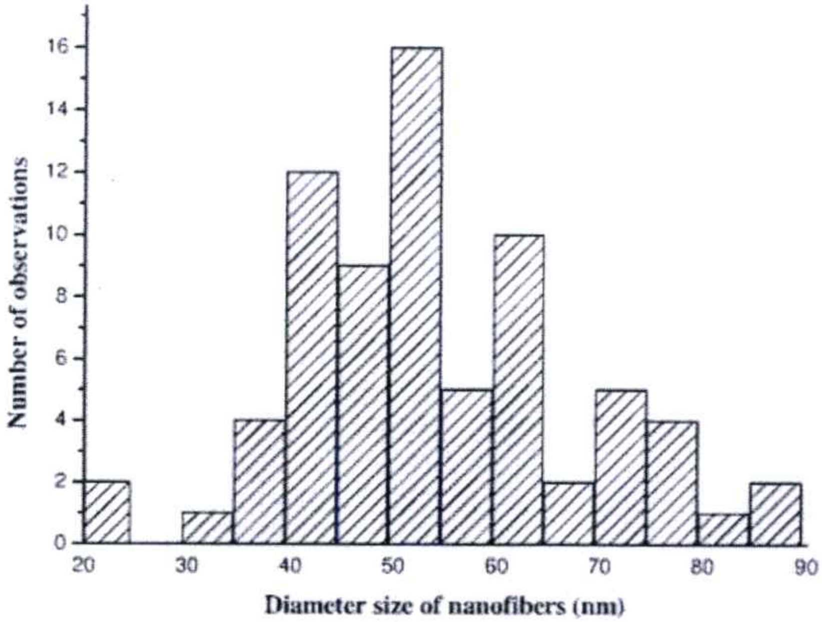

Figure 4.15 Diameter distributions of the prepared nanofibers synthesized at 120 °C for 72 h.

TEM experiment was conducted to prove that nanofibers were solid (not hollow). The TEM image of the as-synthesized nanofibers was illustrated in Figure 4.16, which showed the as-synthesized sample prepared at 120 °C for 72 h to be solid (not hollow), indicating the structure of nanofiber.

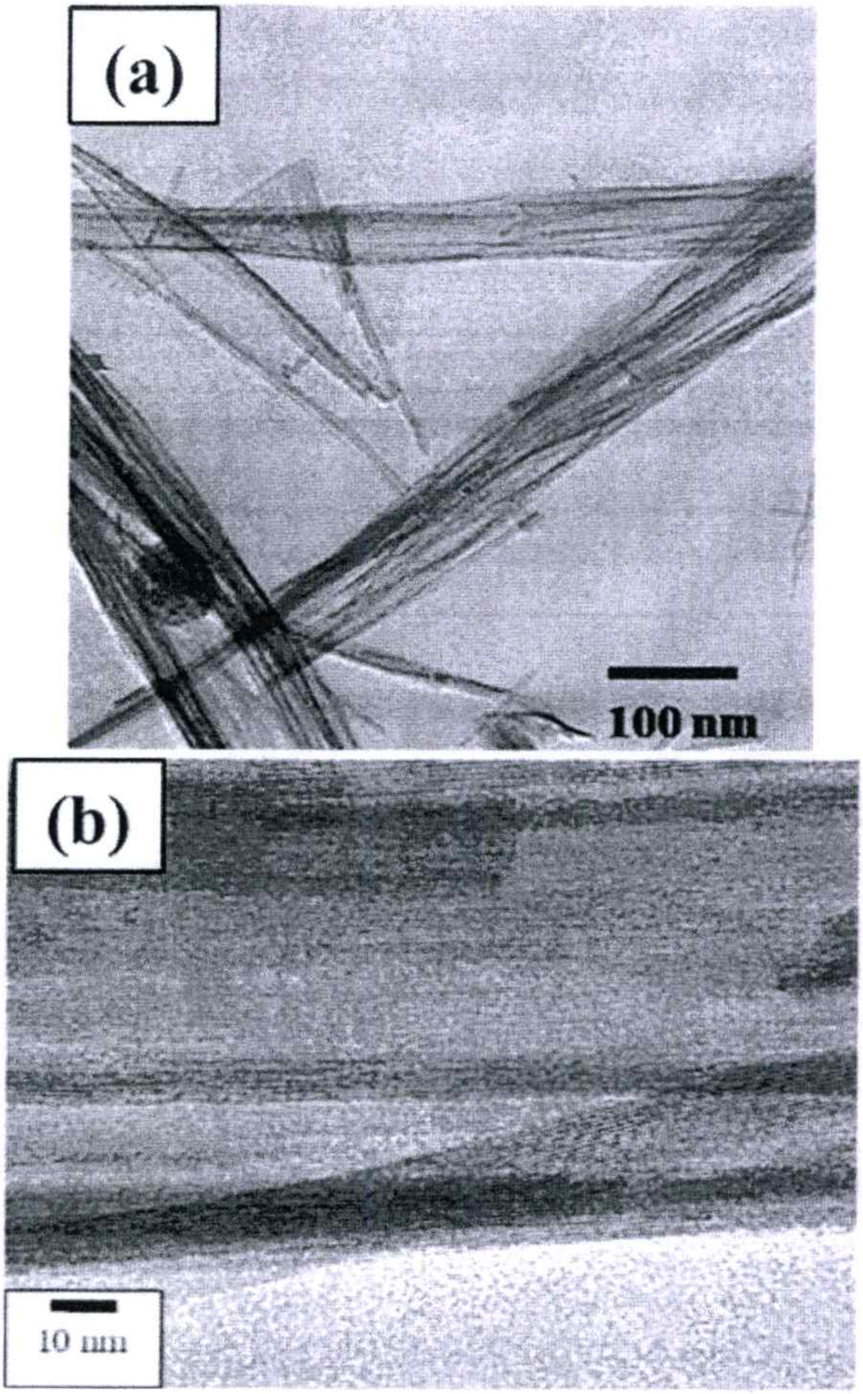

Figure 4.16 TEM images of the as-synthesized nanofibers prepared by hydrothermal method at 120 °C for 72 h at (a) 100,000x and (b) 150,000x magnification.

Many groups have reported the nanotubes/nanofibers during hydrothermal synthesis by nanosheets folding mechanism [138-139]. In this work, the formation of nanotubes/nanofibers can study from the mechanism of nanotubes/nanofibers formation proposed by Nakahira et al.

[138]. In the primary stage of hydrothermal treatment, the nanosheet-like products (layered sodium titanate) were preferentially formed, subsequently, their nanosheets were exfoliated from layered sodium titanate due the excessive intercalation of Na^+ between the spaces of crystal as indicated in Figure 4.17. Then, the nanosheets were curled and scrolled to nanotubes/nanofibers as showed in Figure 4.18. Nakahira et al. [138] proposed the following the three-stage mechanism for nanotube formation (Figure 4.19): (1) Nanosheet-like products, i.e., layer sheets of layered sodium titanate from layered sodium titanate, are formed on the surface of TiO_2 during the primary stage of hydrothermal treatments. (2) Subsequently, nanosheets are exfoliated. (3) Curling and scrolling of exfoiliated nanosheets lead to nanotube/nanofibers formation. Consequently, it is concluded that the scrolling mechanism of an exfoliated TiO_2-derived nanosheet is dominant for nanotube/nanofibers formation.

Kasuga et al. [12-13] suggested that the acid washing process is the important step for removes the electrostatic repulsion and results in the formation of nanotubes from lamellar sheets that are formed during the hydrothermal reaction. Other research reported HCl washing process is not effect to nanotubes formation. The acid treatment is only to remove impurities. The nanotube structure was generated during hydrothermal treatment [69, 140-141]. Thus, hydrothermal treatment imply a key step for the formation of TNTs, while the acid washing process results in the formation of protonated titanates by ion exchange of Na^+ with H^+.

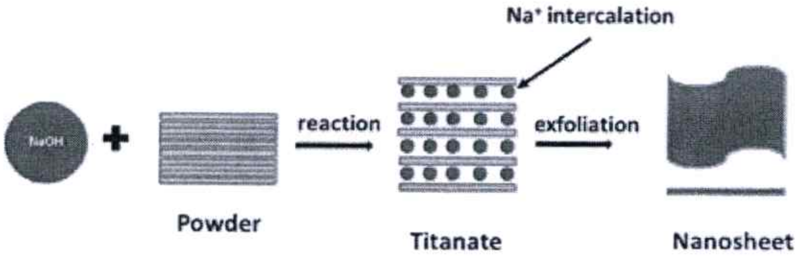

Figure 4.17 The purposed model of the exfoliation mechanism of nanosheets.

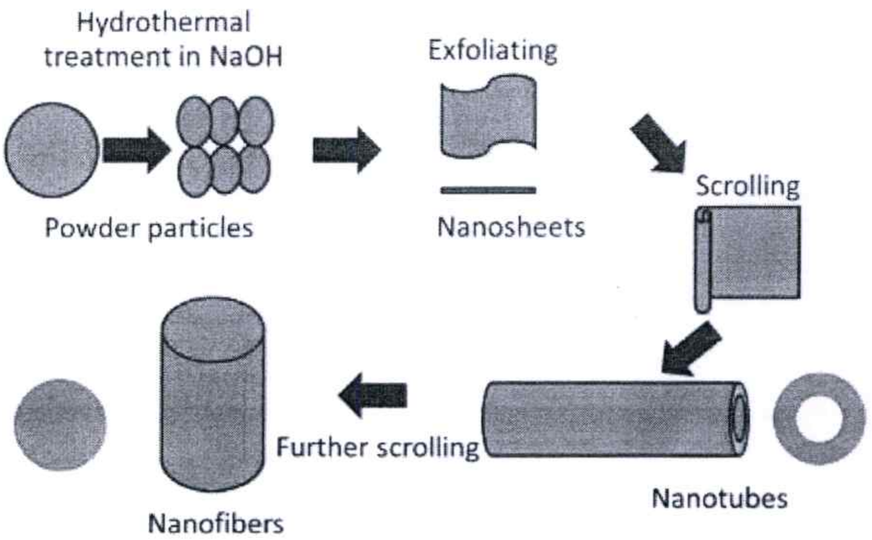

Figure 4.18 The purposed model of the exfoliation and scrolling mechanism of nanosheets.

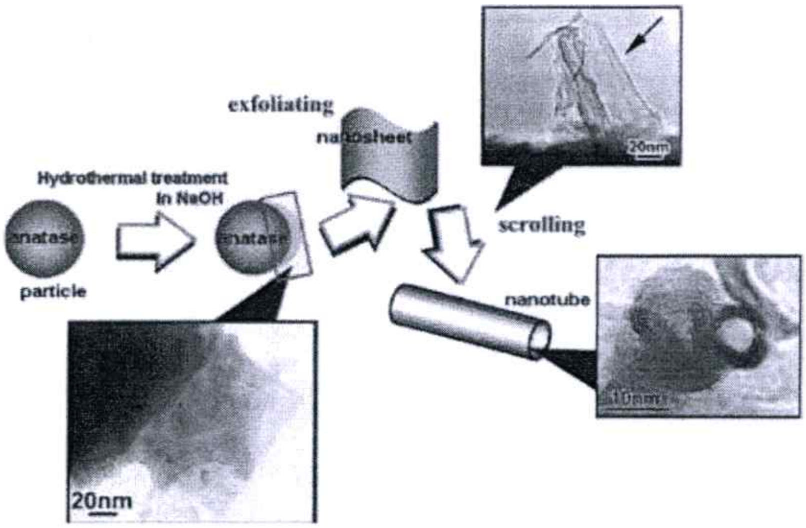

Figure 4.19 Schematic drawing of the exfoliation and scrolling mechanism of nanosheets for nanotubular products proposed by Nakahira et al. [138].

The reactions of transformation of the starting ilmenite mineral to titanate nanofibers can be schematically represented as follows:

$$3FeTiO_3 + 2NaOH \longrightarrow 3FeO + Na_2Ti_3O_7 + H_2O \quad (4.1)$$

$$Na_2Ti_3O_7 + 2HCl \longrightarrow H_2Ti_3O_7 + 2NaCl \quad (4.2)$$

4.1.2 The Brunauer-Emmett-Teller (BET) Specific Area of Nanofibers Measurement

The BET specific surface area of the as-synthesized nanofibers was studied from the as-synthesized nanofibers prepared under hydrothermal temperature at 100, 110, 120 and 130 °C for 72 h as show in Figure 4.20. The BET specific surface area trend to increase with decreasing hydrothermal temperature. This result described to the prepared samples synthesized under higher hydrothermal temperature transformed to completely nanofiber structured. One-dimensional nanostructured such as nanowires, nanofibers and nanorods have high aspect ratio with high specific surface area, especially the prepared samples synthesized at 120 °C for 72 h showed the highest the BET specific surface area approximately 92.24 m^2/g, while the BET surface area of the starting ilmenite mineral was not obtain due to it is non-porous material (Table 4.1). The BET specific surface area of the starting ilmenite mineral was similar to that of leucoxene [57] and rutile minerals [15, 17]. Furthermore, the BET specific surface area of the commercial grade nanoparticles P25 about 48.07 m^2/g. The increase in the BET specific surface area is a result of the starting ilmenite mineral being completely converted into hydrogen titanate nanofibers during the hydrothermal process. Although the nanotube structure is attractive due to its high surface area, titanate nanotubes with free-alkali ions are usually unstable at high temperatures (at ~500 °C) and convert into anatase particles [15, 17, 58, 142]. Increased surface areas are generally accomplished by the synthesis of small particles with high surface to volume ratios or by the manufacture of nanostructured materials from bulk substrates.

Table 4.1 The BET specific surface area of the starting ilmenite mineral, the as-synthesized nanofibers and commercial grade nanoparticles P25.

Samples	Bet surface area (m^2/g)
Starting ilmenite mineral	NA
As-synthesized 100, 72	32.12
As-synthesized 110, 72	58.57
As-synthesized 120, 72	92.24
As-synthesized 130, 72	70.51
P25	48.07

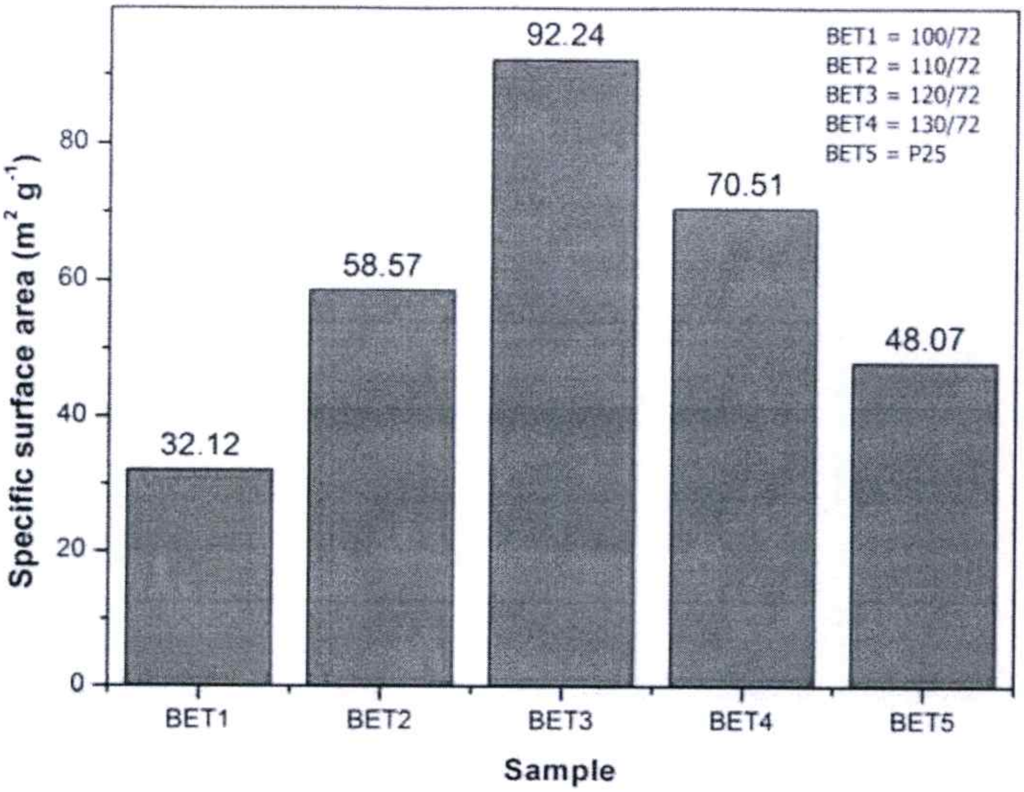

Figure 4.20 The BET specific surface area of the as-synthesized nanofibers and commercial grade nanoparticles P25.

4.1.3 The UV-Vis Absorption of the As-Synthesized Nanofibers

The absorption spectra of the as-synthesized nanofibers and commercially available nanostructured TiO_2 (ST-01) are illustrated in Figure 4.21. The absorption spectra of the as-synthesized nanofibers exhibited a significant enhancement in the wavelength region of 300-500 nm due to the natural Fe-doping characteristic of the ilmenite mineral. Furthermore, the absorption spectra of the as-synthesized nanofibers was greater than ST-01. This phenomenon can described to this reason: (1) the BET specific surface area of the as-synthesized nanofibers prepared at higher temperature exhibited fiber structure in nanosize. The nanofibers have high specific surface area, especially the as-synthesized nanofibers prepared at 120 °C for 72 h, while the as-synthesized nanofibers prepared at lower temperature demonstrated cluster and particle structure with low specific surface area. The high BET specific surface area may be effect to absorption ability of sample [52], (2) nanofiber structure shows the enhancement of light scattering ability of the solar spectrum and promote the light-harvesting efficiency [143], (3) Due to crystalline structure of ST-01 is imperfect, this result is promoted the probability of charge transfer recombination at both surface and bulk traps [52].

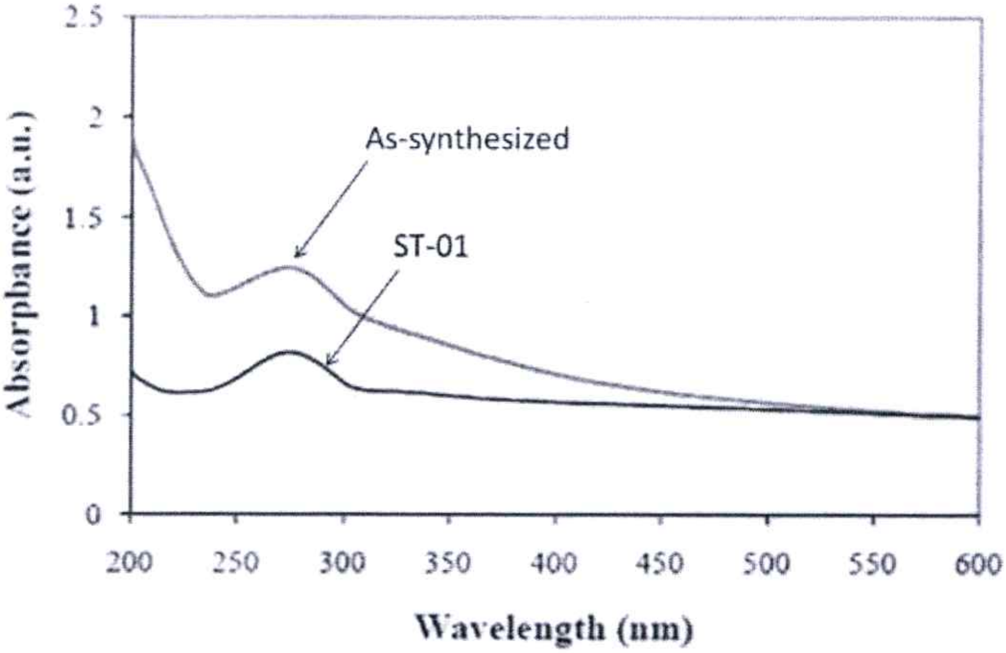

Figure 4.21 UV-Vis absorbance spectra of the as-synthesized nanofibers and commercial grade TiO_2 nanoparticles (ST-01).

From comparison, the data and result from above were considered. The as-synthesized nanofibers prepared by hydrothermal method at 120 °C for 72 h was optimum nanofibers selected to further study and use to application due to it is high crystallinity, great dimension aspect ratio with longer fiber-like morphology, high specific surface area. In addition, it was synthesized at lower temperature than the as-synthesized nanofibers prepared by hydrothermal method at 130 °C for 72 h.

4.1.4 The Chemical Compositions of Nanofibers

For the study on the chemical compositions, the nanofibers synthesized at 120 °C for 72 h were used. The chemical compositions of the ilmenite mineral and that of the as-synthesized samples prepared under hydrothermal temperature at 120 °C for 72 h were evaluated by X-ray fluorescence (XRF) are shown in Table 4.2. During the hydrothermal process, the percentage of impurities, such as Fe_2O_3, Al_2O_3, SiO_2, and MnO, decreased while the TiO_2 content increased from 66.99 to 76.21 %wt. This may be due to higher solubility of the impurities in the NaOH and HCl aqueous solutions during the preparation process [17]. These difference points between nanofibers using ilmenite mineral as the starting materials for this study and nanofibers using leucoxene mineral as the starting materials for previous work [57] were discussed. Interestingly, the chemical composition of nanofibers using leucoxene mineral as the starting materials consist of Fe_2O_3 similar to this study. However, nanofibers using leucoxene mineral as the starting materials showed less the percentage of Fe_2O_3 than nanofibers using ilmenite mineral as the starting materials that is 2.26% and 21.80%, respectively [57]. This difference may be result in the photocatalytic activity [144]. Recent studies indicated doping of Fe^{3+} in the nanofiber matrix leads to significant red shift of optical response towards visible light owing to the reduced band gap energy [145], resulting to brown-colored of the as-synthesized sample in this research. These nanofibers doped with Fe^{3+} could be one of the most alternative with high potential and economic materials for use as the photocatalyst in hydrogen production, dye-sensitized solar cell and decomposition of organic dyes.

Table 4.2 Chemical composition of the ilmenite mineral and as-synthesized sample.

Oxide	Ilmenite mineral (%wt)	As-synthesized sample (%wt)
TiO_2	66.99	76.21
Fe_2O_3	24.01	21.80
Al_2O_3	4.38	0.12
SiO_2	2.11	0.30
MnO	0.82	0.68
ThO_2	0.64	0.01
ZrO_2	0.62	0.12
MgO	0.27	0.09
Cr_2O_3	0.26	<0.01
P_2O_5	0.25	<0.01
SO_3	0.15	0.05
Y_2O_3	0.09	-
ZnO	0.21	<0.01
Nb_2O_5	0.24	0.15
CaO	0.16	0.08

4.1.5 The Surface Elemental Compositions and Electronic State of Nanofibers

X-ray photoelectron spectroscopy (XPS) analysis was performed in order to infer the surface elemental compositions and electronic state of the precursor sample. For the study on the surface elemental compositions, the nanofibers synthesized at 120 °C for 72 h were used. Interesting, impurity in ilmenite sand source might act as a catalyst for the fibrous crystal growth [17]. The chemical composition of titanate nanofibers were analyzed by XPS as shown in Figure 4.22 (a-c). The peaks appearing at 458.7 and 464.3 eV are typically associated to Ti^{4+} $2p^{3/2}$ and Ti^{4+} $2p^{1/2}$ spin-orbital splitting photoelectrons, respectively (Figure 4.21(a)). The Fe oxidation state of the titanate nanofibers can be derived from the Fe 2p spectra as indicated in Figure 4.22 (b). These data assign to Fe_2O_3 with $2p^{3/2}$ and $2p^{1/2}$ positioned at 710.5 and 724.0 eV, respectively, indicating the replacement of Fe^{3+} to Ti^{4+} of TiO_2 lattice forming Fe-O-Ti bonds. These results are in excellent agreement with previous literature values for magnetite [21–25]. In addition, XPS spectrum of O 1s peak located at 529.80 eV is also existed in the sample as shown in Figure 4.22 (c) [21–25].

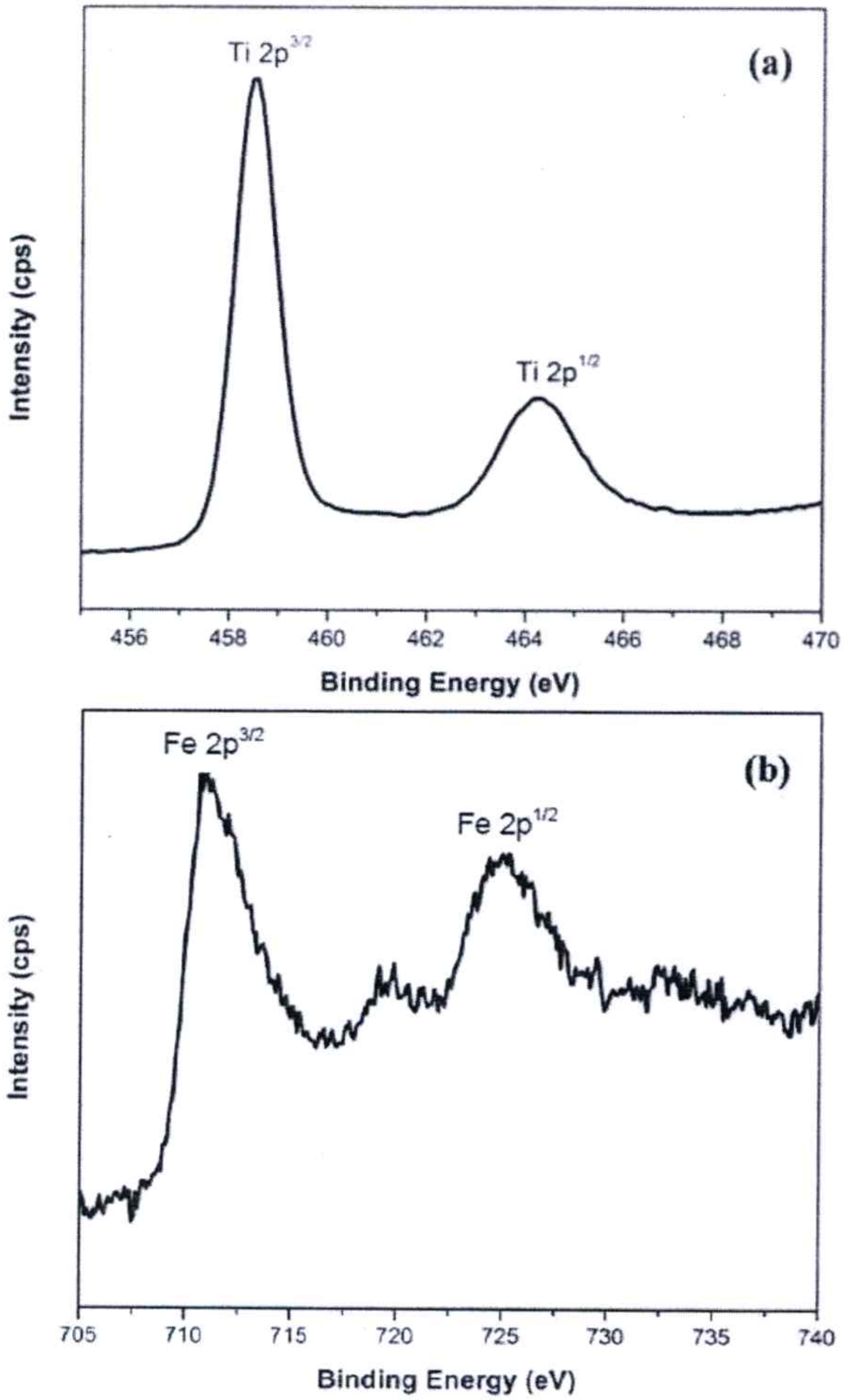

Figure 4.22 XPS spectra of the titanate nanofibers: (a) the Ti 2p regime, (b) the Fe 2p regime and (c) the O 1s regime.

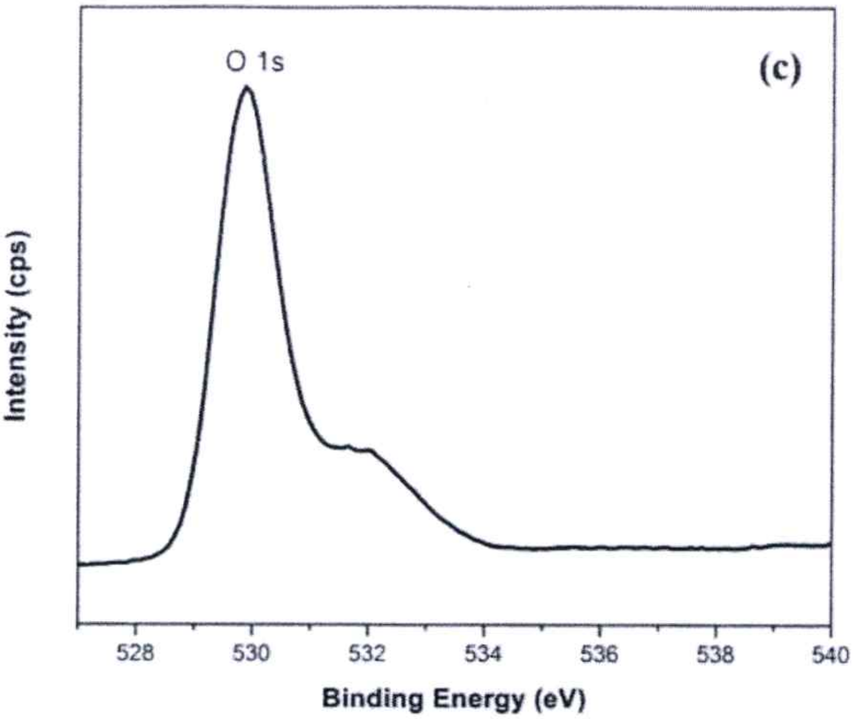

Figure 4.22 (cont.) XPS spectra of the titanate nanofibers: (a) the Ti 2p regime, (b) the Fe 2p regime and (c) the O 1s regime.

4.2 Nanofibers with Heat Treatment

Figure 4.22 (a) also shows the XRD patterns of the prepared samples calcined for 2 h at 300, 400, and 500 °C. After calcination at the temperature range of 300-400 °C, the calcined samples demonstrated TiO_2 (B). The nanofibers were dehydrated and re-crystallized from hydrogen titanate into the metastable form of TiO_2 (B) [16, 17]. Moreover, the peak intensity corresponding to the TiO_2 (B) decreased as the calcination temperature increased. At 500 °C, the calcined nanofibers revealed a bi-crystalline mixture consisting of TiO_2 (B) and anatase TiO_2. Recent research studies found a bi-crystalline mixture consisting of TiO_2 (B) and anatase TiO_2 nanostructured not merely showed similar formation in the temperature ranges of 100-500 °C [63], 300-600 °C [146] or 400-600 °C [147] but promoted great H_2 evolution from neat ethanol as well [57]. Figure 4.26 (a-c) shows the SEM images of the as-synthesized nanofibers calcined for 2 h at 300, 400, and 500 °C. From the SEM images, the nanofibers calcined for 2 h at 300-500 °C maintained their nanofiber morphology [12]. Figure 4.27 shows a typical TEM image of the as-synthesized nanofibers calcined for 2 h at 500 °C. From TEM image, it is seen that the calcined sample maintained nanofibers structure. In many research studies, the nanotube structure was frequently investigated due to its high surface area; however, titanate nanotubes with free-alkali ions were typically unstable at high temperatures (at 500 °C) and converted into anatase particles [16, 58]. To maintain the 1-D nanostructure at higher temperatures (typically at 500-800 °C), solid nanowires or nanofibers are more preferable.

The XRD patterns of the prepared samples calcined at 600, 700, 800, 900, and 1,000 °C for 2 h are shown in Figure 4.23 (b). The prepared samples consisted of a mixture of anatase, rutile phase of TiO_2 [53, 56], and Fe_2O_3. At 600-700 °C, the crystalline of anatase phase of TiO_2 became unstable, TiO_2 (B) disappeared, and the transformation from anatase phase TiO_2 to rutile phase TiO_2 began at this temperature range [2]. Consequently, the calcination temperature rose, increase in rutile phase TiO_2 was observed, especially at the 800-1,000 °C, at which the rutile phase TiO_2 was dominant, and the peaks of rutile become sharper than anatase while the anatase phase TiO_2 was almost non-existent. Furthermore, recent papers reported that doping Fe into TiO_2 enabled the photon absorbing zone of TiO_2 to extend from UV toward visible light as well as reduced TiO_2 band gap energy from 4.2 to 2.67 eV [148-150]. The phase content between anatase and rutile was estimate from Equation 4.3 suggested by Spurr and Myers [151].:

$$FR = 1/\{1 + 0.79[IA(1\ 0\ 1)/IR(1\ 1\ 0)]\} \tag{4.3}$$

The effects of calcination temperatures on phase content and crystalline size of prepared samples are shown in Table 4.3 and Figure 4.24. This observation shows that with increasing calcination temperature from 600 to 1,000 °C, the trend of anatase ratio gradually decreased, meanwhile the rutile ratio became stronger, 73:37, 49:51, 28:72, 32:68 and 22:78 for nanofibers calcined at 600, 700, 800, 900 and 1,000 °C for 2 h. This result indicates that the increase of calcination temperature led to the phase transformation from thermodynamically meta-stable anatase to the most stable form of rutile phase [152–153]. Mostly, anatase phase is not stabilize at high temperature and transform into rutile structure between the range of 500-800 °C. The anatase to rutile transformation is reconstructive involves the breaking and reforming of bonds [154]. This is in difference to a displacive transformation, in which the original bonds are distorted but retained. The reconstructive anatase to rutile transformation involves a contraction of the c-axis and an overall volume contraction of 8%. This phenomenon relates to an enhancement of crystallization of rutile phase. Typically, phase transformation is supplemented with crystal growth [152]. From the XRD spectra, the crystallite sizes can be calculated by the Debye-Scherrer formula as shows in Equation 4.4

$$D = K\lambda/\beta cos\theta \tag{4.4}$$

where D is the crystallite diameter in nm,

K is the shape constant (0.90),

λ is the wavelength of X-ray (1.541874 A°),

β is the peak width (in rad) at half-maximum height

θ is the Bragg angle.

As the calcination temperature is raised, XRD reflections corresponding to both the anatase and rutile phase become narrower, which indicates the increase of crystallite size [152–153]. The crystallite size was shown in Table 4.3 and Figure 4.25. The crystallite size of samples calcined at lower temperature (below 800 °C) increased slightly from about 21 to 33 nm for anatase phase and 12 to 41 nm for rutile phase. At higher temperature (1,000 °C) caused rapid increase of crystallite size up to about 142 nm for both the anatase and rutile. This result is similar to study by Górska et al. [155].

Figure 4.28 (a-e) depicts the SEM images of the prepared samples calcined at 600, 700, 800, 900, and 1,000 °C for 2 h. The nanofibers calcined at 600-700 °C for 2 h maintained their nanofiber morphology (Figure 4.28 (a-b)). Typically, the TiO_2-derived nanotubes after heat-treatment at 400 °C (anatase phase) were destroyed and transformed into nanoparticles [58, 156]. This phenomenon attributed to the shrinkage and partially broken of the nanofibers due to the thermal energy, some particles were inevitably squeezed out from the nanofibers and then distributed along the surface or junction of the nanofibers after agglomeration.

However, in this work, the prepared samples calcined at high temperatures of 600-700 °C for 2 h were stable and maintained nanofiber structure. Therefore, the prepared samples can be utilized in various applications operated at high temperatures. In addition, the prepared samples calcined at 800-1,000 °C for 2 h showed submicron particle structure of rutile TiO_2 (Figure 4.28 (c)-(e)) Figure 4.29 (a-b) shows a typical TEM image of the as-synthesized nanofibers calcined for 2 h at 700 and 1,000 °C, respectively. From TEM image, it is seen that the calcined sample at 700 °C maintained nanofibers structure while the calcined sample at 1,000 °C appeared showed submicron particle structure of rutile TiO_2. The particle size increases dramatically when the phase transformation from anatase to rutile was occurred [24].

Recent papers reported that the submicron particle structure of rutile TiO_2, caused by increasing calcination temperature, decreased the BET specific surface area of the nanofibers [53,58–57]. Other studies reported the influence of phase composition and BET specific surface area of TiO_2 nanostructured on the photocatalyst properties. Indeed, it was found that the photocatalyst properties of anatase phase of TiO_2 were better than those of rutile [53, 57]. However, the band gap of rutile (4.0 eV) was lower than that of anatase (4.2 eV); as such, rutile should be more easily photo-excited. The high recombination possibility of photo-generated electrons and holes was the major limiting factor for the indigent photocatalytic activity of rutile [53, 57]. Generally, phase composition, specific surface area, pore size distribution, particle morphology, particle aggregation, and impurities can play a crucial role in determining the efficiency of specific applications [157]. Thus, the calcination process is required to control the crystalline structure of TiO_2 nanofibers.

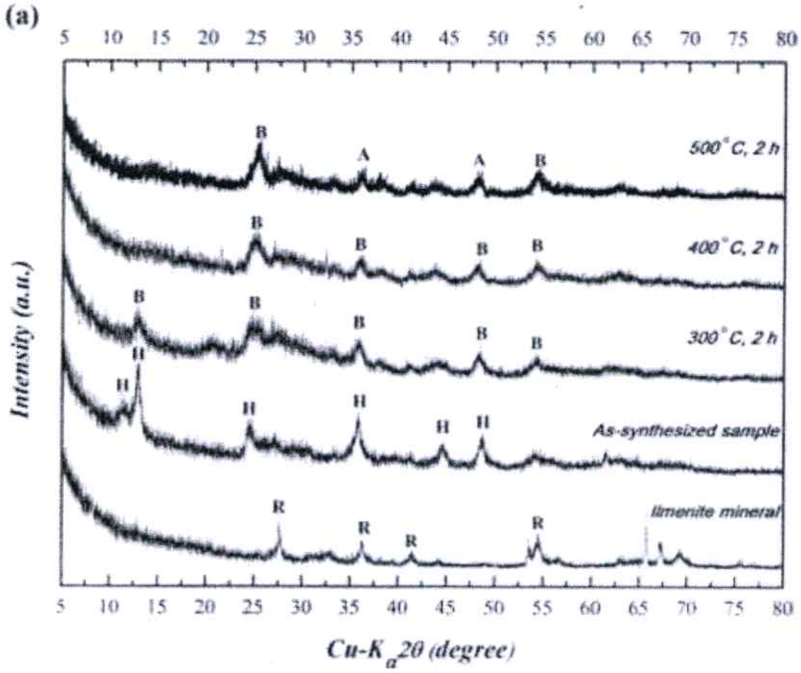

Figure 4.23 XRD patterns of the starting natural ilmenite mineral, the as-synthesized nanofibers, and the calcined nanofibers for 2 h at (a) 100-500 °C and (b) 600-1,000 °C; A = anatase TiO_2, B = TiO_2 (B), H = hydrogen titanate and R = rutile TiO_2.

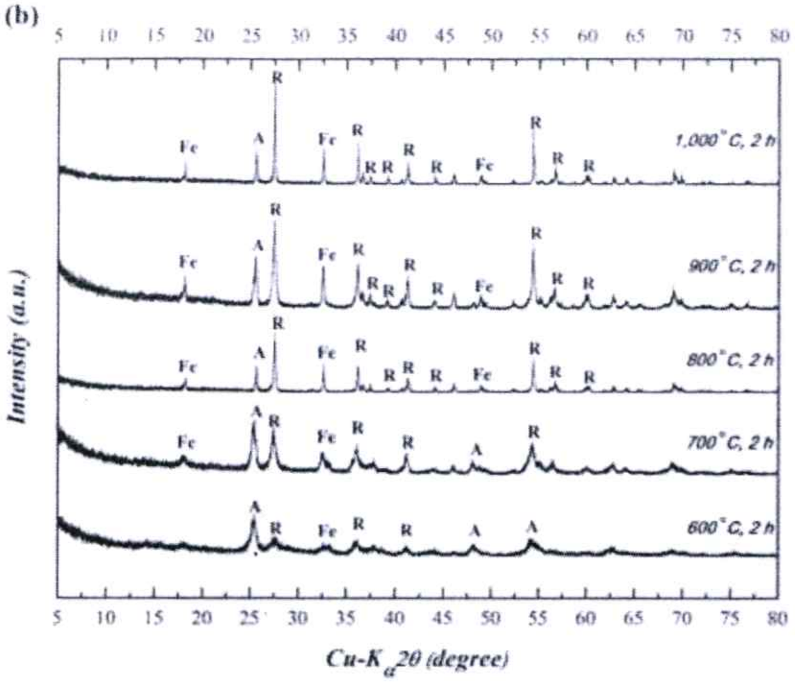

Figure 4.23 (cont.) XRD patterns of the starting natural ilmenite mineral, the as-synthesized nanofibers, and the calcined nanofibers for 2 h at (a) 100-500 °C and (b) 600-1,000 °C; A = anatase TiO_2, B = TiO_2 (B), H = hydrogen titanate and R = rutile TiO_2.

Table 4.3 Effect of temperature on physicochemical properties of prepared samples.

Materials	**Calcination temperature (°C)**	**Anatase (101) over rutile (110) ratio (A:R)**	**Crystalline size (nm)[a]**	
			Anatase (101)	**Rutile (110)**
Nanofibers from ilmenite	As-synthesized	-	-	-
	300	-	-	-
	400	-	-	-
	500	-	-	-
	600	73:37	21	12
	700	49:51	29	19
	800	28:72	33	41
	900	32:68	49	142
	1,000	22:78	142	142

[a] Calculation by using Sherrer Formula.

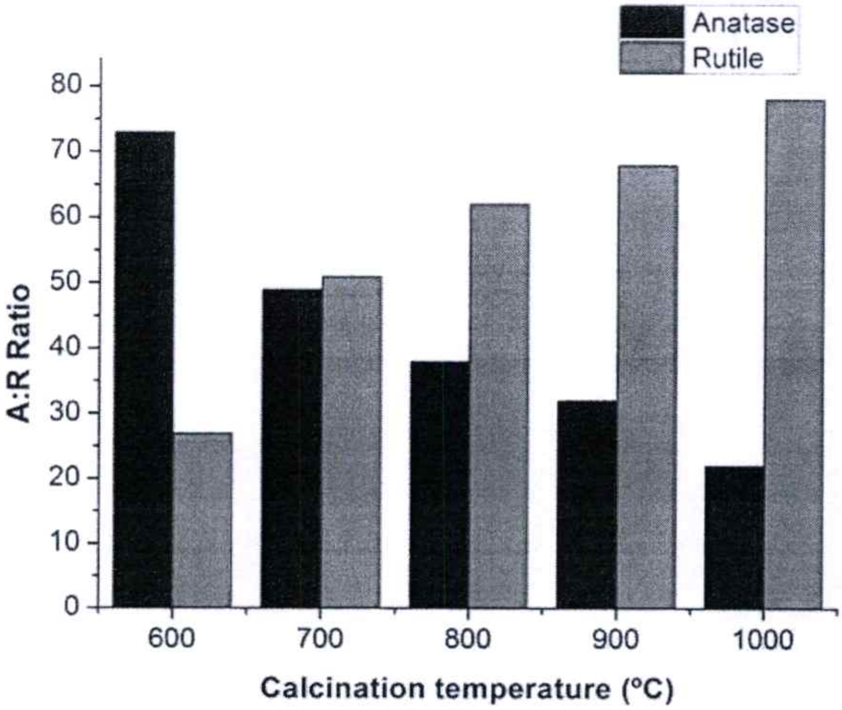

Figure 4.24 The effects of calcination temperatures on phase content of prepared samples.

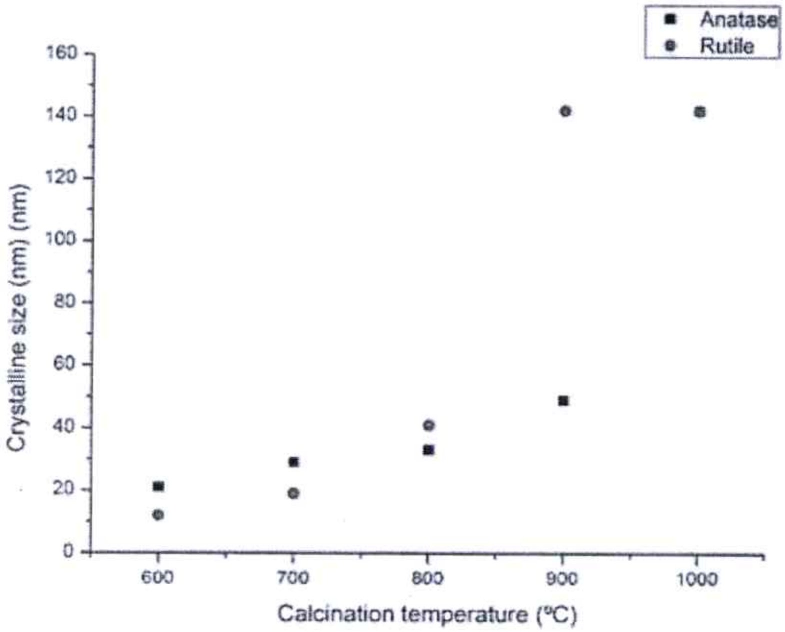

Figure 4.25 The effects of calcination temperatures on crystalline size of prepared samples.

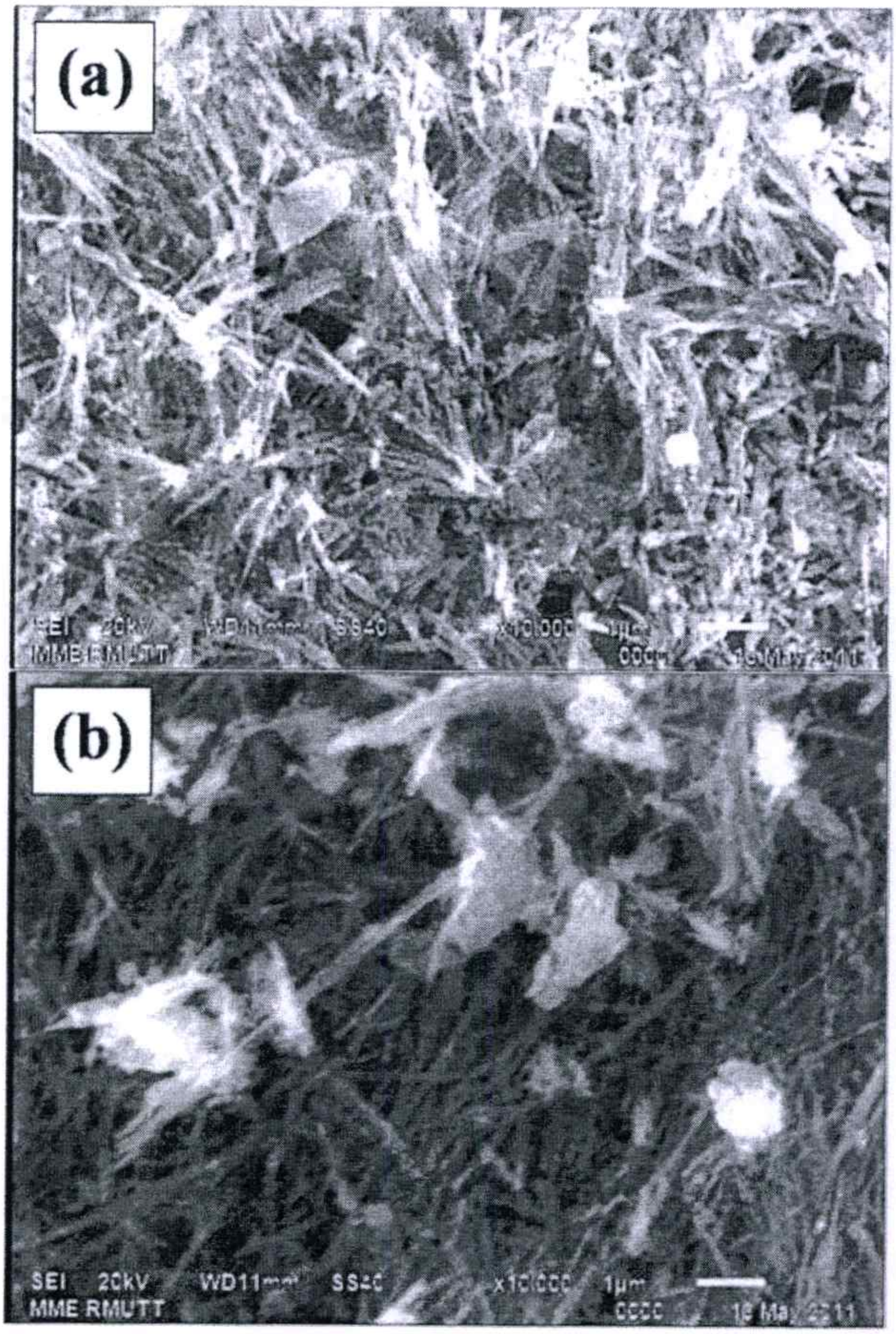

Figure 4.26 SEM images of the calcined nanofibers for 2 h at (a) 300 °C, (b) 400 °C, and (c) 500 °C.

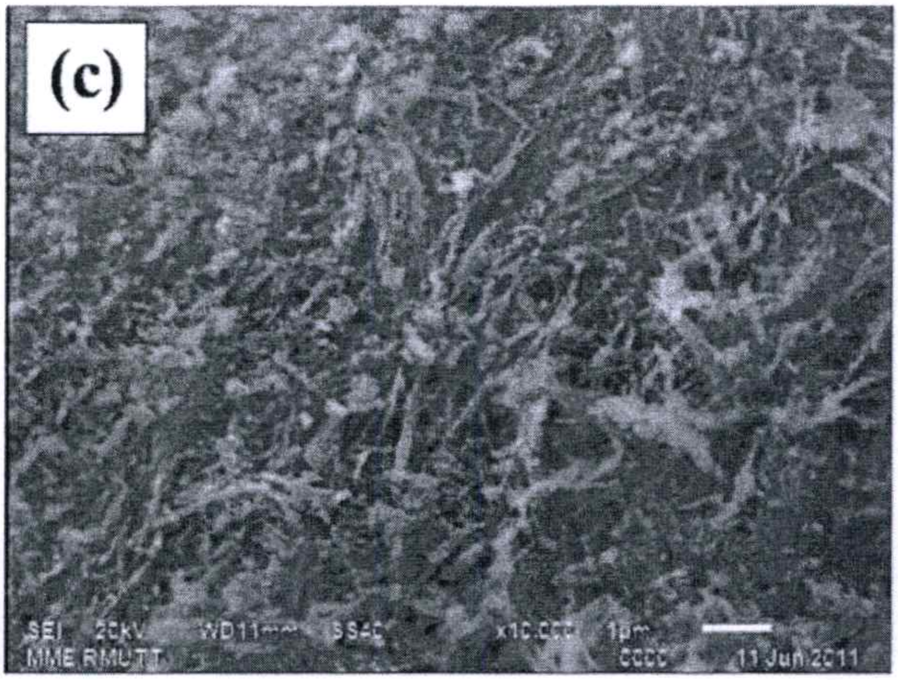

Figure 4.26 (cont.) SEM images of the calcined nanofibers for 2 h at (a) 300 °C, (b) 400 °C, and (c) 500 °C.

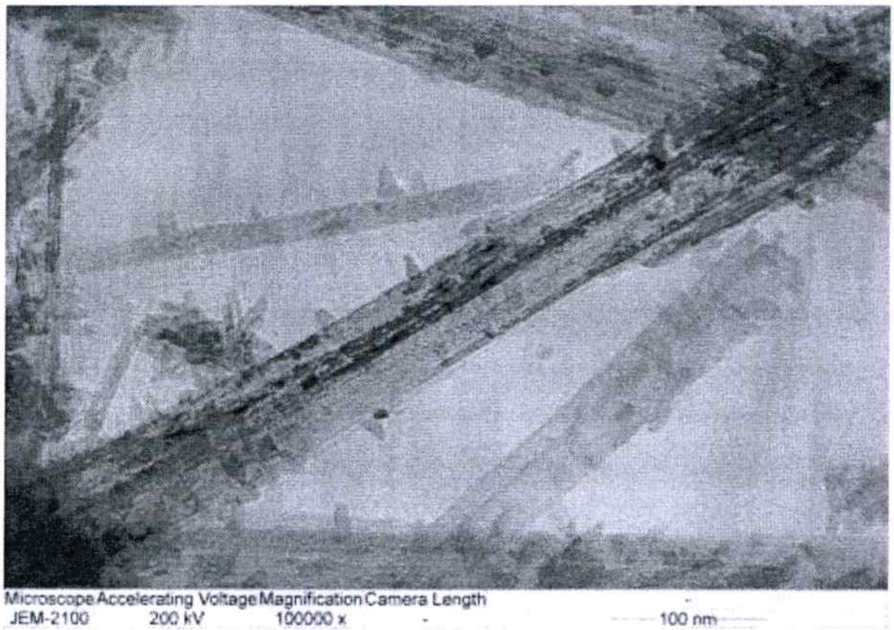

Figure 4.27 TEM images of the calcined nanofibers for 2 h at 500 °C at 100,000x magnification.

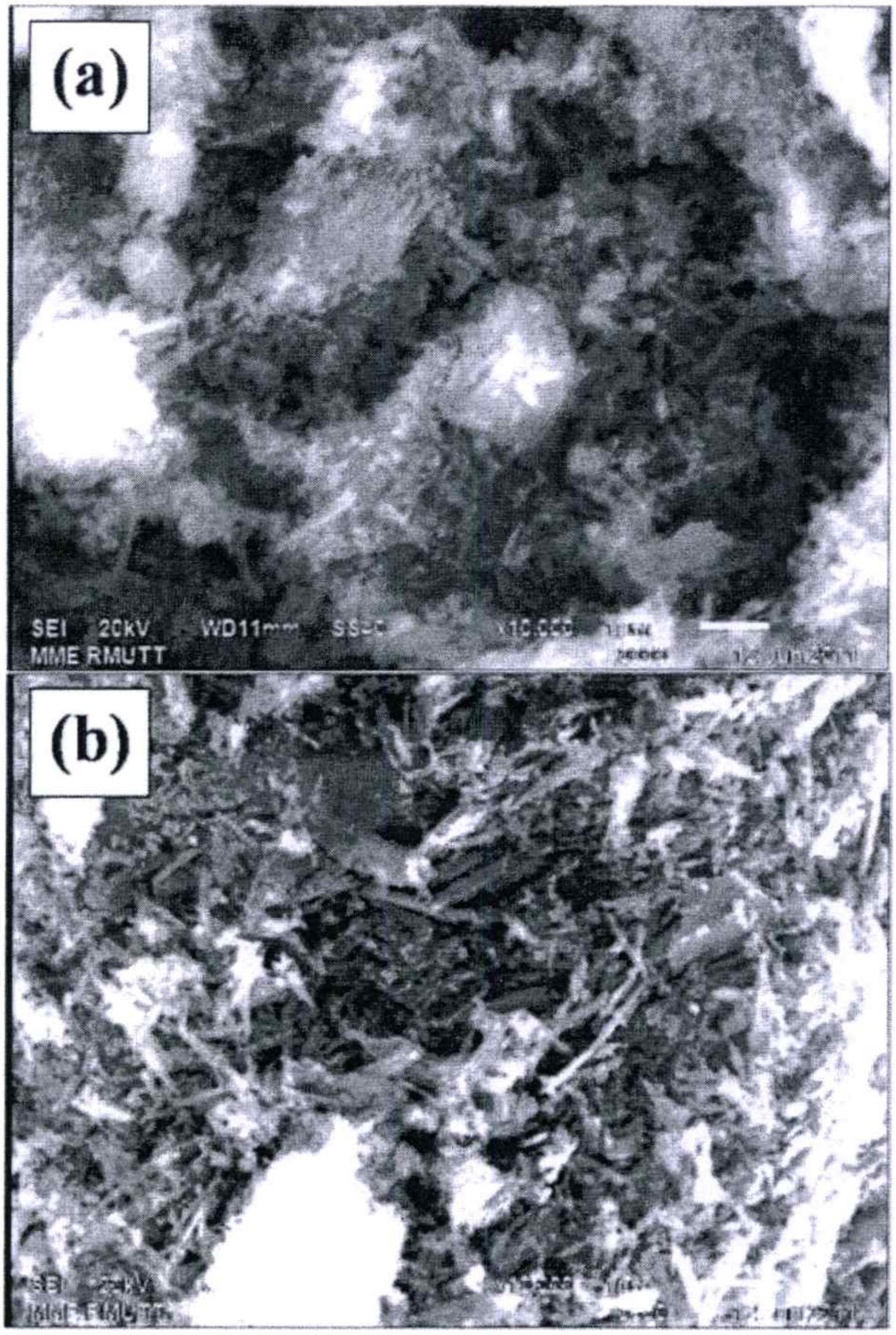

Figure 4.28 SEM images of the calcined nanofibers for 2 h at (a) 600 °C, (b) 700 °C, (c) 800 °C, (d) 900 °C, and (e) 1,000 °C.

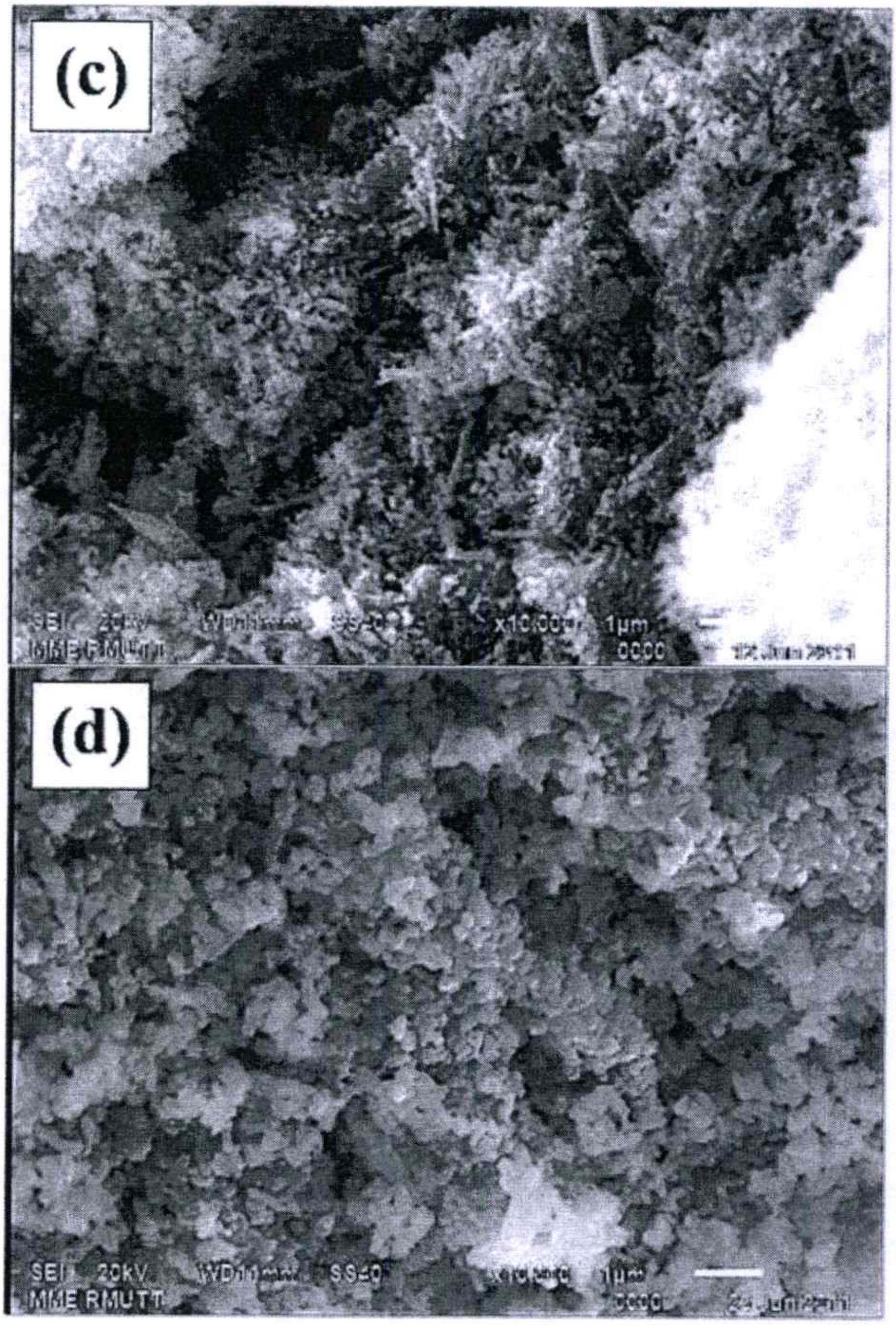

Figure 4.28 (cont.) SEM images of the calcined nanofibers for 2 h at (a) 600 °C, (b) 700 °C, (c) 800 °C, (d) 900 °C, and (e) 1,000 °C.

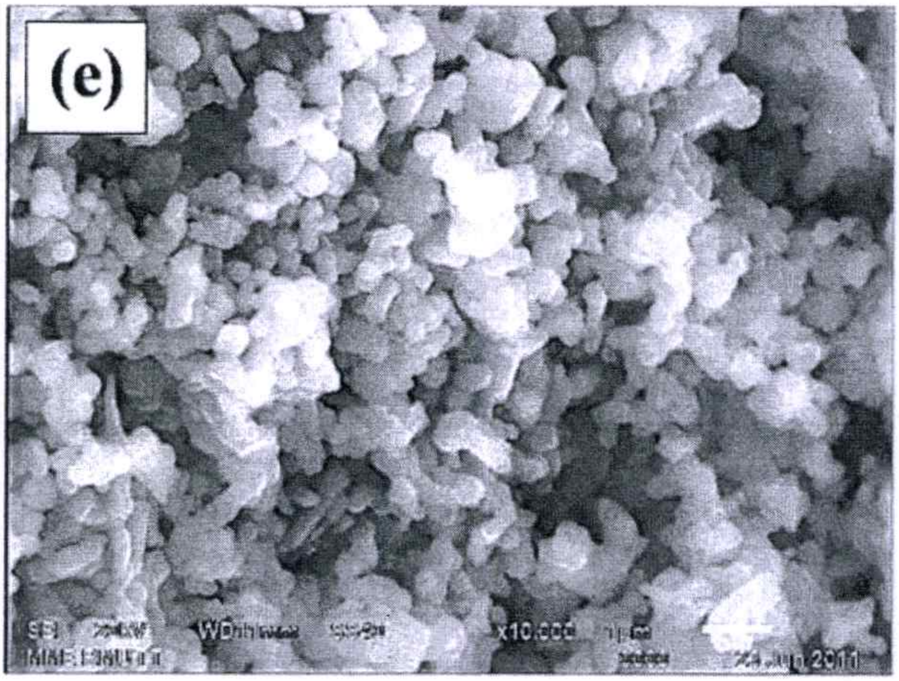

Figure 4.28 (cont.) SEM images of the calcined nanofibers for 2 h at (a) 600 °C, (b) 700 °C, (c) 800 °C, (d) 900 °C, and (e) 1,000 °C.

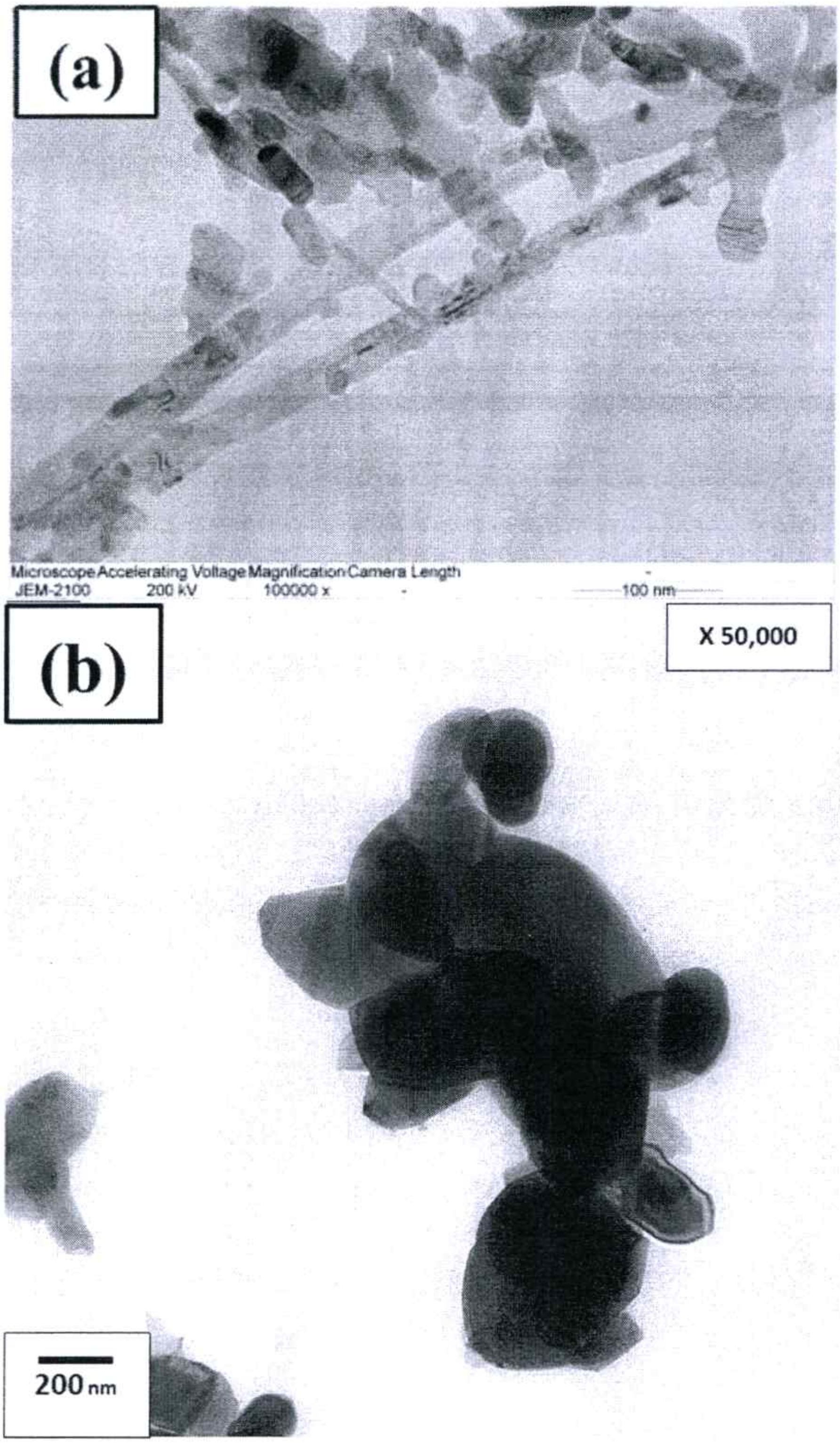

Figure 4.29 TEM images of the calcined nanofibers for 2 h at (a) 700 °C at 100,000x magnification and (b) 1,000 °C at 50,000x magnification.

4.2.1 The Brunauer-Emmett-Teller (BET) Specific Area of Calcined Nanofibers Measurement

The effect of calcination temperature on BET specific surface area was studied from the as-synthesized nanofibers prepared under hydrothermal temperature at 120 °C for 72 h calcined 500, 700, 800 and 1,000 °C as show in Table 4.4 and Figure 4.30. The BET specific surface area seemed to steadily decrease with increasing calcination temperature [158]. This result attributed to the prepared samples calcined at lower temperature maintained fiber structured with high surface area while the prepared samples calcined at higher temperature transformed to rod and particle structured. Therefore, the porosity of the nanofibers decreased with increasing calcination temperature led to reduce surface area. The nanorods and nanoparticles trend to lower specific surface area than nanofibers and nanowires, especially the prepared samples calcined at 1,000 °C for 2 h showed the lowest the BET specific surface area approximately 7.81 m^2/g.

Table 4.4 The BET specific surface area of the as-synthesized nanofibers prepapred under hydrothermal temperature at 120 °C for 72 h and the as-synthesized nanofibers prepared under hydrothermal temperature at 120 °C for 72 h calcined at various temperature.

Samples	**Bet surface area (m^2/g)**
As-synthesized 120 °C,72 h	92.24
Calcined at 500 °C	51.67
Calcined at 700 °C	41.63
Calcined at 800 °C	31.63
Calcined at 1,000 °C	17.85

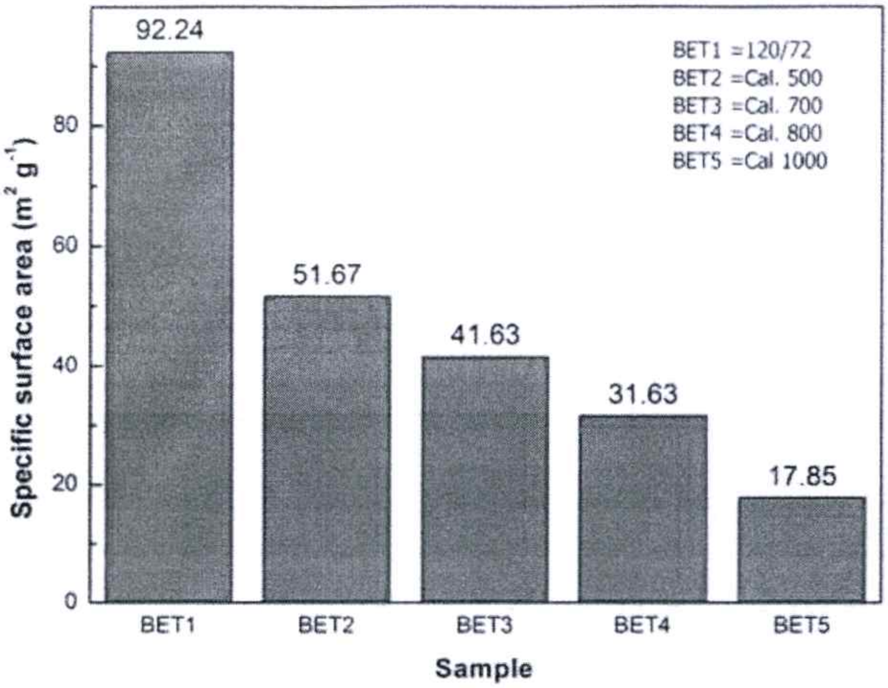

Figure 4.30 The BET specific surface area of the as-synthesized nanofibers synthesized at 120 °C for 72 h and the as-synthesized nanofibers synthesized at 120 °C for 72 h calcined 500, 700, 800 and 1,000 °C for 2 h.

4.2.2 The UV-Vis Absorption of the Calcined Nanofibers

Figure 4.31 shows the UV-Vis spectra of the as-synthesized sample prepared at 120 °C for 72 h and the as-synthesized nanofibers synthesized at 120 °C for 72 h calcined 400, 700, and 1,000 °C for 2 h. The UV-Vis absorption spectra of the samples were recorded using a UV–Vis spectroscopy (UV-2401, Shimadzu). The band gap energy (Eg) was estimated from absorption edge from Equation as shown in Equation 4.5 by Oregan and Gräzel [24].

$$E = hC/\lambda \qquad (4.5)$$

Give: h = Planks constant = $6.623 \times 10^{-34}\ J{\cdot}s$

C = Speed of light = $3.0 \times 10^{8}\ m/s$

λ = Cut off wavelength (m)

The influence of temperature on the light absorption characteristic of prepared samples investigated from the as-synthesized and nanofibers calcined at 400, 700 and 1,000 °C for 2 h. A significant increase at wavelengths shorter than 400 nm could be explained to absorption of light caused by the excitation of electrons from the valence band to the conduction band of TiO_2 [159-160]. A shift to visible light region of the absorption of the prepared samples was observed for the as-synthesized and nanofibers calcined at 400, 700 and 1,000 °C for 2 h. The differences in absorption were described to the change of crystallite size and phase structure [160]. The absorption edges shifted toward longer wavelengths were attributed to the existence of iron (Fe) in the prepared samples, the excitation of 3d electron of Fe^{3+} ion to the TiO_2 conduction band (charge transfer transition) may be extended of absorption of the prepared samples from UV towards visible light [159]. This correlates with the appearance of the brown coloration of the prepared samples.

The band gap energy of the as-synthesized and nanofibers calcined at 400, 700 and 1,000 °C for 2 h estimated from Eq. (4.3) was about 3.80, 2.62, 2.32, 2.12 eV, respectively. Recently paper, reported the Fe_2O_3/TiO_2 composite showed narrower band gap energy was about 2.20-2.63 eV [161]. The difference in band gap energy is due to the result of the change of crystallite size and phase composition in the prepared samples [160]. This data showed that the band gap of prepared samples became narrower with increasing calcination temperature. This result due to following factor, the first reason, an increase in crystallite size leading to the decrease of band gap energy, which was in correspond with recently work reported by Xiao et al. [162] and the second, after calcination at 400, 700 and 1,000 °C for 2 h, lower value of band gap energy for samples was observed, due to phase transformation from anatase to rutile [160]. However, the band gap energy of the as-synthesized showed larger gap may be cause by titanate structure of this sample [163].

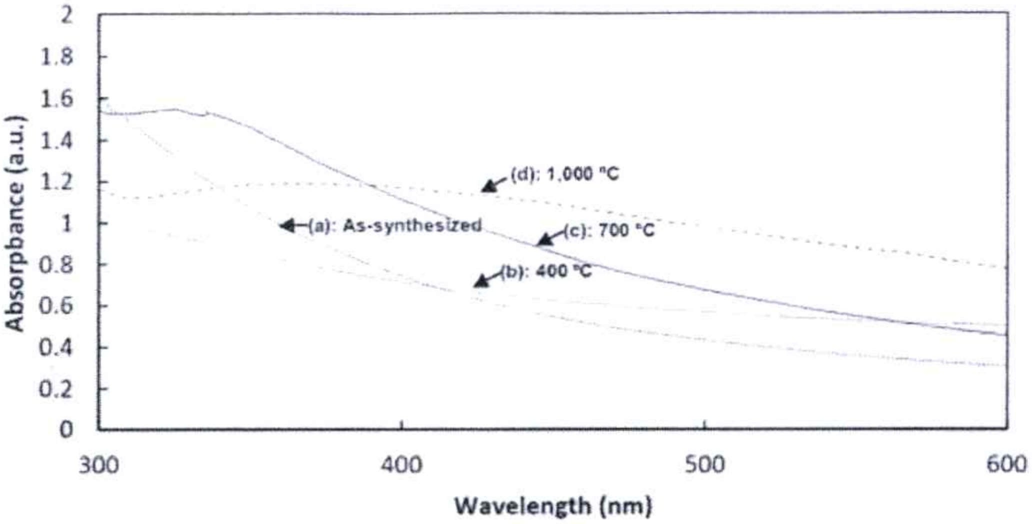

Figure 4.31 UV-Vis spectra of the as-synthesized sample prepared at 120 °C for 72 h and the as-synthesized sample prepared at 120 °C for 72 h calcined at various temperatures.

4.3 The Elemental Composition of the As-Synthesized Nanofibers and Calcined Nanofibers

For the study on the elemental composition, the nanofibers synthesized at 120 °C for 72 h and calcined at 500 and 700 °C for 2 h were used. A sample's elemental composition to be identified by Energy Dispersive X-ray Spectroscopy (EDS) Analysis. An EDS spectrum of the nanofibers is shown on Figure 4.32 (a-c) and Table 4.5-4.7. The EDS spectrum of the nanofibers synthesized at this condition consisting major elemental of Ti, O and Fe ions according to chemical composition of starting ilmenite mineral with little amounts of Calcium, chromium, manganese and gold. Carbon and copper were contaminated in all samples may occur by carbon coating and copper grid in characterization process. Therefore, in calculation of the percentage of elemental compositions, carbon and cupper were negligible. The percentage of three major elementals are similar in all samples. The as-synthesized consists of approximately 37.32% Ti, 44.49% O and 12.70% Fe. The as-synthesized calcined at 500 °C for 2 h is made up of approximately 47.89% Ti, 40.26% O and 11.28% Fe while the as-synthesized calcined at 700 °C for 2 h is compose of 40.19% Ti, 39.96% O and 16.75% Fe.

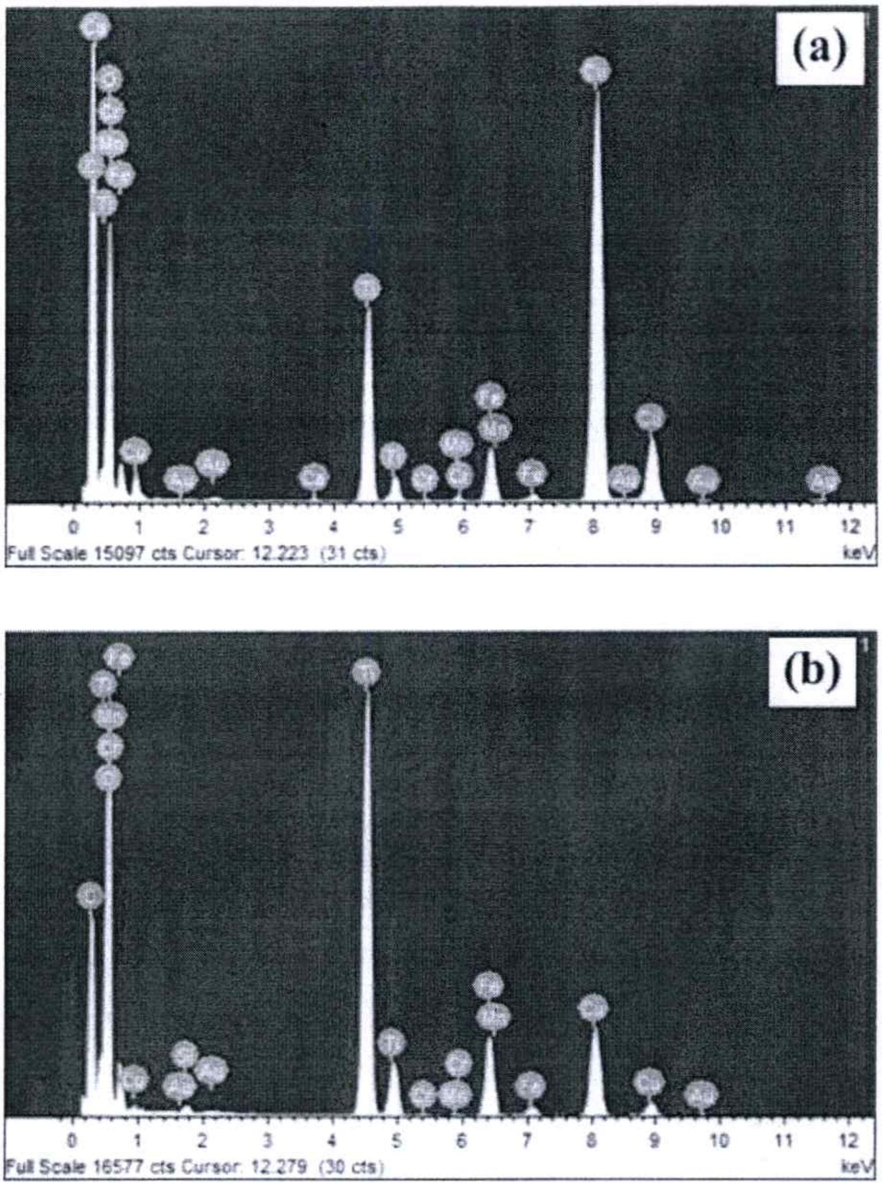

Figure 4.32 EDS spectra of (a) the as-synthesized nanofibers, (b) the as-synthesized nanofibers calcined at 500 °C for 2 h and (c) the as-synthesized nanofibers calcined at 700 °C for 2 h . C and Cu peaks are arisen from the coating and Cu grid for TEM observation and sample stages.

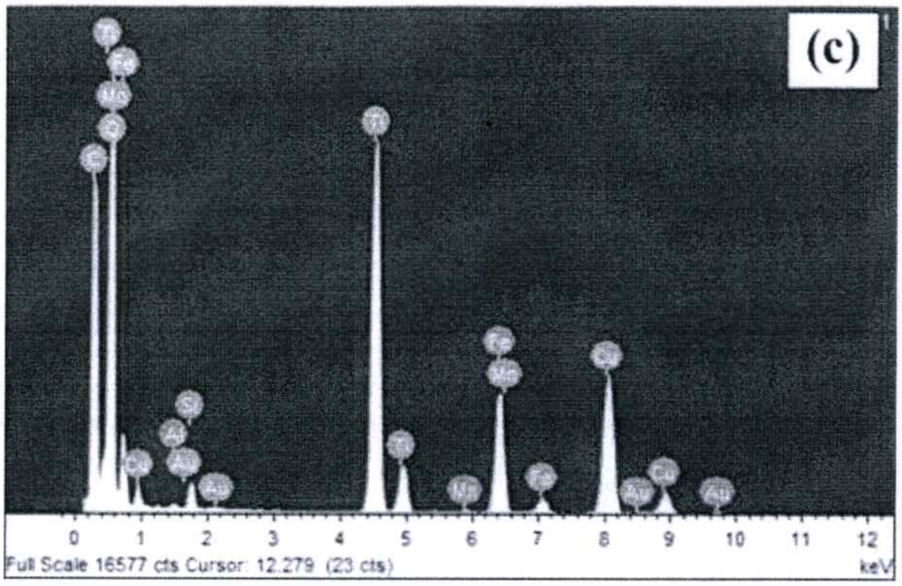

Figure 4.32 (cont.) EDS spectra of (a) the as-synthesized nanofibers, (b) the as-synthesized nanofibers calcined at 500 °C for 2 h and (c) the as-synthesized nanofibers calcined at 700 °C for 2 h . C and Cu peaks are arisen from the coating and Cu grid for TEM observation and sample stages.

Table 4.5 The elemental composition of the nanofibers synthesized at 120 °C for 72 h.

Element	Weight%	Atomic%
Oxygen (O)	44.49	72.32
Calcium (Ca)	0.58	0.39
Titanium (Ti)	37.32	20.28
Chromium (Cr)	0.39	0.18
Manganese (Mn)	1.29	0.60
Iron (Fe)	12.70	5.92
Gold (Au)	3.28	0.42

Table 4.6 The elemental composition of the nanofibers synthesized at 120 °C for 72 h calcined at 500 °C for 2 h.

Element	Weight%	Atomic%
Oxygen (O)	44.49	67.33
Calcium (Ca)	0.49	0.48
Titanium (Ti)	47.89	26.75
Chromium (Cr)	0.19	0.10
Manganese (Mn)	0.22	0.11
Iron (Fe)	11.28	5.39
Gold (Au)	0.72	0.10

Table 4.7 The elemental composition of the nanofibers synthesized at 120 °C for 72 h calcined at 700 °C for 2 h.

Element	Weight%	Atomic%
Oxygen (O)	39.96	67.19
Calcium (Ca)	0.24	0.23
Titanium (Ti)	40.19	22.58
Chromium (Cr)	1.67	1.59
Manganese (Mn)	0.37	0.18
Iron (Fe)	16.75	8.07
Gold (Au)	0.76	0.10

4.4 Characterization of Dye-Sensitized Solar Cells

The photocurrent-voltage curves of the DSSCs are presented in Figure 4.33 and corresponding results are listed in Table 4.8. The device using NF5 composite as working electrode displays superior performance to the others, accompanying the greatest short-circuit photocurrent density (J_{sc}), open-circuit photovoltage (V_{oc}), and energy conversion efficiency (η). This noticeable enhancement of light harvesting efficiency is associated to the increase in electron transport efficiency in one-dimensional nanostructure and increasing number of light scattering of the solar spectrum in nanofiber structure [143]. Furthermore, the incorporation of certain loading content of TiO_2 nanofibers in TiO_2 matrix can significantly increase the amount of absorbed dye molecules in the device, resulting to the improvement of J_{sc} and the reduction of recombination rate of the photo injected electrons in the device [164-165]. However, further increasing loading amount of nanofiber leads to the decrease in device efficiency. This inferiority may be due to light scattering out of cells by high concentration of nanofibers, resulting to lower current density [164-165]. The fill factor in this work shows low value, which is not qualitatively similar to the theoretical curve. This result may be originated from the effect of high internal series resistance (R_s) in solar cells [166]. In addition, the existence of Fe^{3+} in TiO_2 can generate a trapping level in TiO_2, that can retard the electron-hole recombination of electrons in TiO_2 conduction band and dye or electrolytes [166].

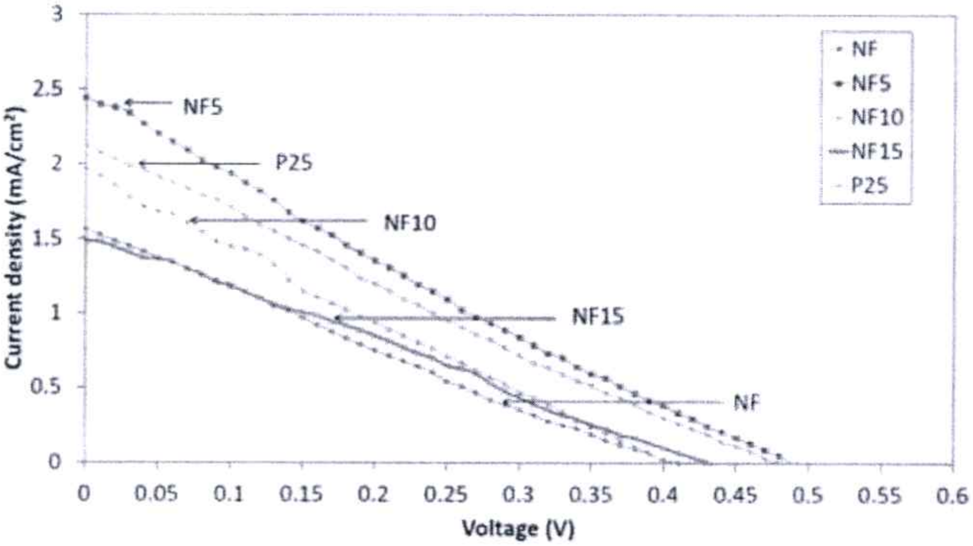

Figure 4.33 Photocurrent-voltage characteristics of the DSSCs based on titanate nanofibers, commercial grade TiO_2 nanoparticles and titanate nanofibers mixed commercial grade TiO_2 nanoparticles with different ratio.

Table 4.8 The photovoltaic properties of the DSSCs based on titanate nanofibers, commercial grade TiO_2 nanoparticles and titanate nanofibers mixed commercial grade TiO_2 nanoparticles with different ratio.

Samples	**Open circuit voltage, V_{oc} (V)**	**Short Circuit current density, J_{sc} (mA/cm^2)**	**Fill Factor, *FF***	**Energy conversion efficiency, η (%)**
NF	0.41	1.56	0.24	0.15
NF5	0.47	2.44	0.23	0.28
NF10	0.40	1.97	0.26	0.20
NF15	0.43	1.48	0.29	0.17
P25	0.45	2.12	0.26	0.25

The photocurrent density–voltage (J-V) curve of the DSSCs was carried out under simulated solar light with intensity of 100 mW/cm^2. Figure 4.34 shows the photocurrent-voltage curve based on various TiO_2 photoanode. The characteristic of the photovoltaic (PV) parameters, including the value of short-circuit photocurrent density (J_{sc}), open-circuit photovoltage (V_{oc}), fill factor (*FF*) and energy conversion efficiency (η) are summarized in Table 4.9. The efficiency of DSSCs based on P25 is about 1.45%. For the device using 5% titanate nanofibers calcined at various temperatures range of 300-1,000 °C for 2 h (NF300-NF1000) mixed with P25 as working electrode, the η of DSSC is improved with increasing calcined temperature (Figure 4.34 and Table 4.9). The DSSC based on NF800 shows the superiority of η approximately 3.90%. It is indicated that the enhanced photovoltaic performance is attributed to the incorporation of nanofibers calcined at 800 °C for 2 h into P25 due to the increasing specific surface area, the porosity and roughness factor of the electrodes [120]. The high surface area of TiO_2 nanofibers or nanorods in TiO_2 matrix can significantly increase the amount of absorbed dye molecules in the device that can assist the electron injection to increase the corresponding current density [120]. Furthermore, the nanoparticles/nanofibers composite electrodes may support the enhancement of light scattering ability of the solar spectrum and promote the light-harvesting efficiency of nanofiber and nanorod structure [120]. The model of light scattering ability of nanorods purposed by V. Thavasi et al. [167] is shown in Figure 4.36. However, with increasing calcination temperature to

900 and 1,000 °C, the η decreases to 1.86 and 1.60%, respectively, which might be due to the agglomeration of the particles and difficulty of electron movement [120].

For one-dimensional nanostructures such as nanofibers and nanorods, the charge recombination could decrease and charge transfer rate could increase because of its straight charge transfer path divided by nanofibers and nanorods, which associate to an increase of electron transport efficiency in the device [120]. The model of straight charge transfer path of nanofibers purposed by S.H. Kang et al. [168] is shown in Figure 4.37. The existence of Fe^{3+} in TiO_2 can generate a trapping level in TiO_2, that can retard the electron-hole recombination of electrons in TiO_2 conduction band and dye or electrolytes and enhance the electron charge transfer of dye to conduction band of TiO_2 [166]. Furthermore, it is reasonable to think that the relatively larger size of the nanofibers and nanorods than nanoparticles could improve the diffusion of liquid electrolyte, which is beneficial for electron transfer in I_3^-/I^- electrolyte [169]. Furthermore, nanorod structure is much shorter than nanofibers and hence can have much lower resistance that in turn can cause higher currents [122].

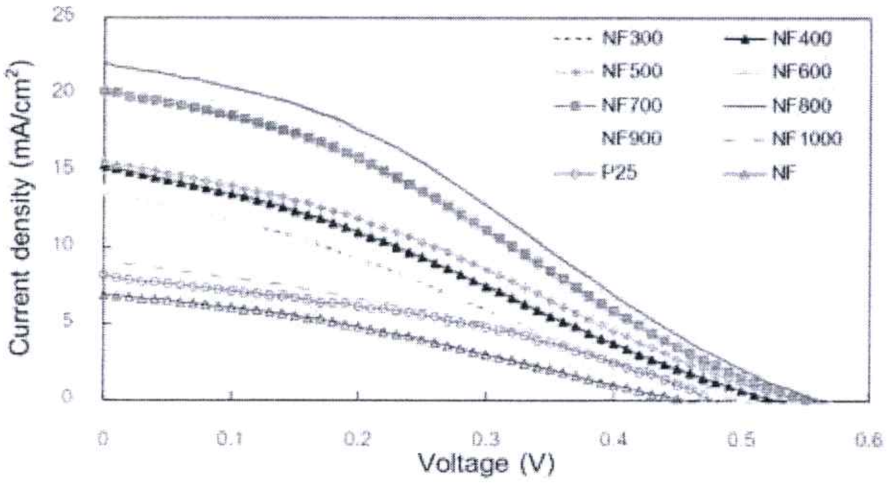

Figure 4.34 Photocurrent–voltage characteristics of the DSSCs based on titanate nanofibers, P25 and 5% titanate nanofibers calcined at various temperatures for 2 h mixed P25.

Table 4.9 The photovoltaic properties of the DSSCs based on titanate nanofibers, P25 and 5% titanate nanofibers calcined at various temperatures for 2 h mixed P25.

Samples	**Open circuit voltage, V_{oc} (V)**	**Short Circuit current density, J_{sc} (mA/cm^2)**	**Fill Factor, FF**	**Energy conversion efficiency, η (%)**
NF	0.45	6.90	0.32	1.01
NF300	0.50	13.55	0.28	1.92
NF400	0.52	15.31	0.29	2.35
NF500	0.54	15.58	0.30	2.63
NF600	0.54	20.23	0.30	3.38
NF700	0.55	20.19	0.30	3.43
NF800	0.56	22.01	0.31	3.90
NF900	0.50	13.75	0.26	1.86
NF1000	0.49	9.07	0.38	1.60
P25	0.47	8.17	0.37	1.45

The effect of various amounts of nanofibers calcined at 800 °C for 2 h mixed P25 on photovoltaic properties is shown in Fig. 4.35 and Table 4.10. The results show that the increase of amount of nanofiber calcined at 800 °C for 2 h leads to enhance in η of DSSCs. The highest η of 3.90% is obtained at about 5 wt.% amount of nanofiber calcined at 800 °C for 2 h. However, when the amount of nanofiber calcined at 800 °C for 2 h is over 5%, the J_{sc} and η tend to decrease. This result may be due to light scattering out of cells by high concentration of nanofibers, resulting to lower current density [120].

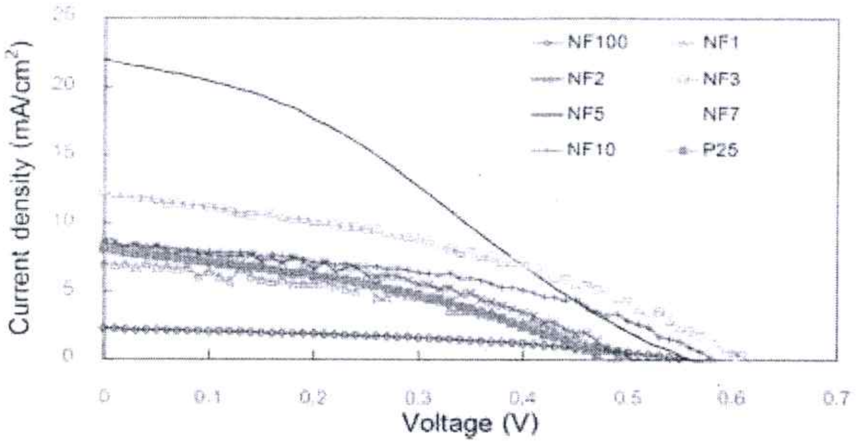

Figure 4.35 Photocurrent–voltage characteristics of the DSSCs based on P25 mixed titanate nanofibers calcined at 800 °C for 2 h with different ratio.

Table 4.10 The photovoltaic properties of the DSSCs based on P25 mixed titanate nanofibers calcined at 800 °C for 2 h with different ratio.

Samples	**Open circuit voltage, V_{oc} (V)**	**Short Circuit current density, J_{sc} (mA/cm^2)**	**Fill Factor, FF**	**Energy conversion efficiency, η (%)**
NF1	0.50	7.11	0.41	1.50
NF2	0.50	8.68	0.42	1.84
NF3	0.58	12.33	0.39	2.85
NF5	0.56	22.01	0.31	3.90
NF7	0.60	12.62	0.38	2.93
NF10	0.58	8.58	0.43	2.16
NF100	0.54	4.57	0.37	0.94
P25	0.47	8.17	0.37	1.45

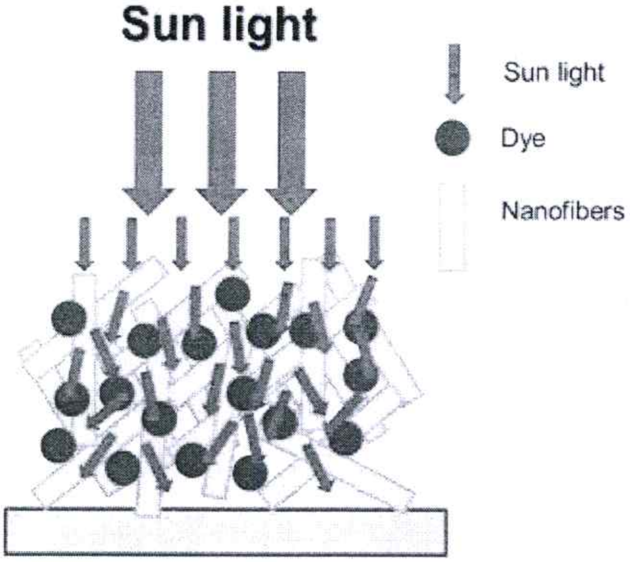

Figure 4.36 The model of light scattering ability of nanofibers.

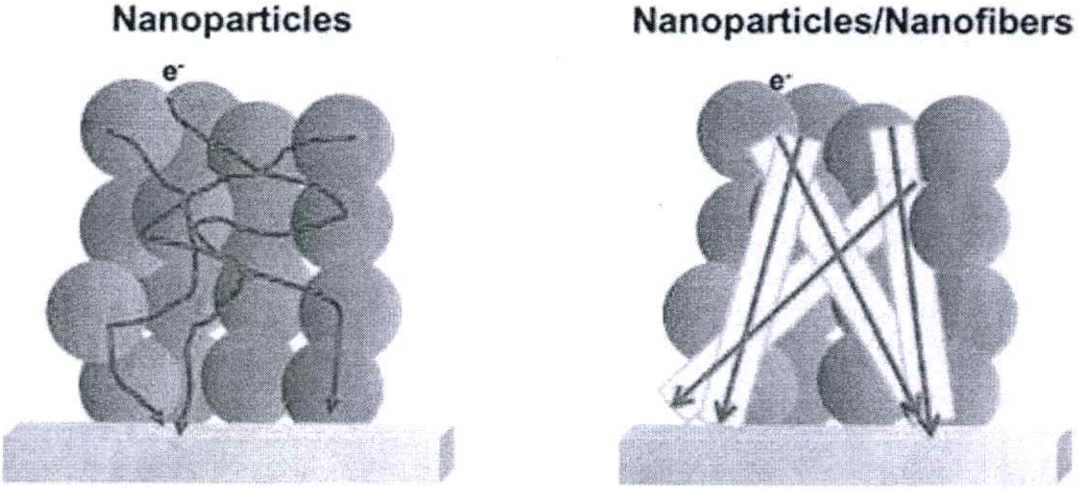

Figure 4.37 The model of straight charge transfer path of nanofibers.

The EIS of the DSSCs based on P25 mixed titanate nanofibers is presented in Nyquist plots in Figure 4.38. EIS spectrum of DSSCs consists of three semicircles In general, the impedance spectrum of a DSSC shows three semicircles in the frequency range of 10mHz to 100 kHz. The first semicircle of 929 Ω is related to the charge transport resistance at counter electrode/electrolyte (R_2), which is measured in the kHz range. The second semicircle of 35.4 kΩ is associated to electron transport in the TiO_2/dye/electrolyte interface (R_3), around 1–100 Hz.

The third semicircle shows the Warburg diffusion process of I^-/I_3^- in the electrolyte [165]. In addition, the R_1 that was related to the sheet resistance of substrate [166]. The equivalent circuit of prepared DSSC is shown in Figure 4.39.

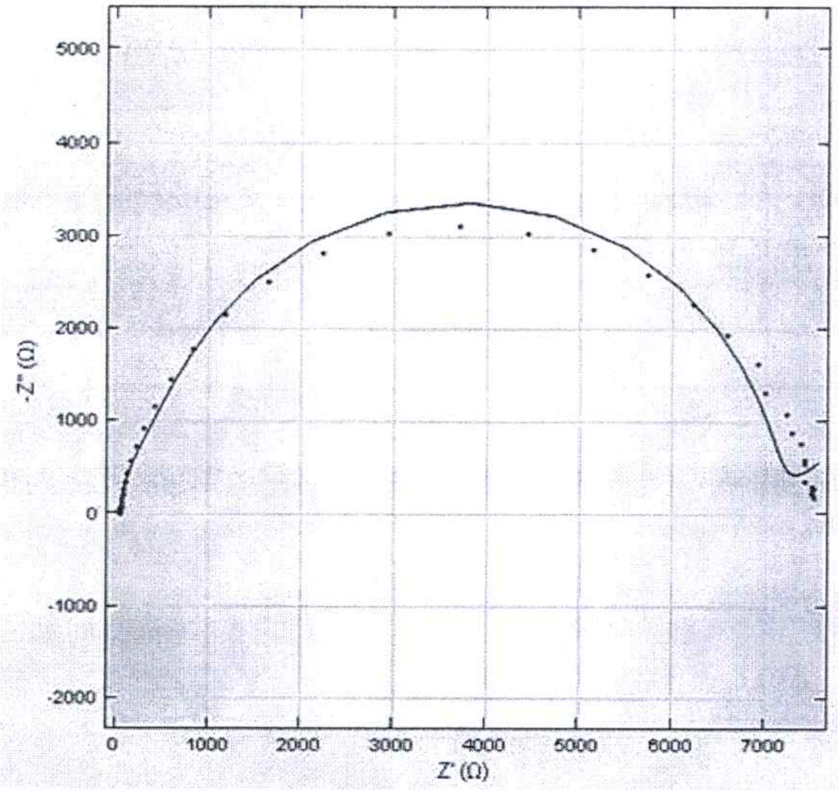

Figure 4.38 Impedance spectrum of the DSSCs based on P25 mixed titanate nanofibers.

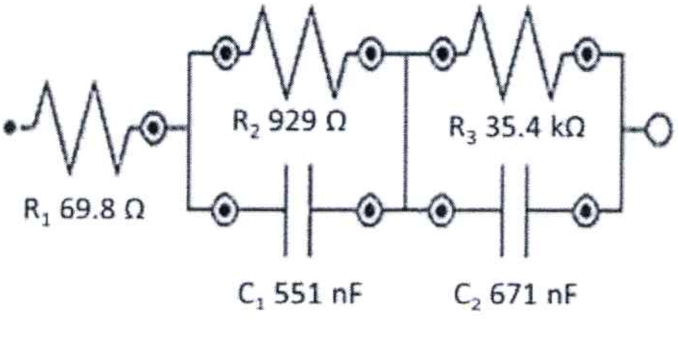

Figure 4.39 The equivalent circuit that was used to represent the interface in the composite solar cells.

CHAPTER 5

CONCLUSION

Titanate nanofibers were synthesized by a hydrothermal method using a low-cost ilmenite mineral as the starting material. The samples were to hydrothermally at different temperatures, 100-130 °C for 24-72 h. The influence of synthesis condition on crystal structure and microstructure was studied. After the synthesis under low hydrothermal temperature and/or short hydrothermal time at 100 °C for 24 and 48 h and 110 °C for 24 h, the as-synthesized sample exhibited the major structure of cluster-like morphology with some structure of tube-like morphology, while the as-synthesized sample synthesized under high hydrothermal temperature and/or and long hydrothermal time at 100 °C for 72 h,110 °C for 48 and 72 h, 120-130 °C for 24, 48 and 72 h showed the some fiber-like morphology. The crystalline structure of all the as-synthesized nanofibers demonstrated a layered titanate $H_2Ti_xO_{2x+1}$ structure, most likely in the form of trititanate ($H_2Ti_3O_7$). However, the prepared samples synthesized under hydrothermal temperature at 100 °C for 24 and 48 h and 110 °C for 24 h consisting rutile phase of the starting ilmenite mineral. The as-synthesized nanofibers prepared under hydrothermal temperature at 120 °C for 72 h showed the highest of BET specific surface area.

The nanofibers calcined at 300–400 °C showed TiO_2 (B) whereas the nanofibers calcined at 500 °C revealed a mixture of TiO_2 (B) and anatase. The nanofibers calcined at high temperatures of 600–1,000 °C showed a mixture of tri-crystalline of anatase, rutile, and Fe_2O_3. The rutile phase rose with increasing calcination temperature. Moreover, the nanofibers calcined at 300–700 °C maintained nanofiber structure while the morphology of nanofibers calcined at 800–1,000 °C transformed into nanoparticles and submicron particles. The transformation of anatase to rutile phase and the increase of crystallite size of prepared samples were observed with increasing calcination temperature. The main chemical composition of the as-synthesized nanofibers and the calcined nanofibers consisted the titanium, oxygen and iron.

The η of DSSC increases with increasing calcination temperature of nanofiber. The greatest η of 3.90% is obtained from DSSC fabricated from 5 wt.% nanofibers calcined at 800 °C for 2 h mixed with P25. This increase in the device efficiency is attributed to high surface area, higher light scattering and light harvesting, low charge recombination and fast electron-transfer rate by nanofibers.

These titanate nanostructured materials, i.e. nanotubes/nanofibers doped by Fe^{3+} could be one of the most alternative and economic materials for working electrode in dye-sensitized solar cell.

REFERENCES

[1] W.H. Jung, N.-S. Kwak, T.S. Hwang and K.B. Yi, "Preparation of Highly Porous TiO_2 Nanofibers for Dye-Sensitized Solar Cells (DSSCs) by Electro-Spinning" **Applied Surface Science**, vol. 261, 2012, pp. 343–352.

[2] T. Sreethawong, Y. Suzuki and S. Yoshikawa, "Synthesis, Characterization, and Photocatalytic Activity for Hydrogen Evolution of Nanocrystalline Mesoporous Titania Prepared by Surfactant-Assisted Templating Sol-Gel Process" **Journal of Solid State Chemistry**, vol. 178, 2005, pp. 329–338.

[3] M. Grätzel, "Photoelectrochemical cells" **Nature**, vol. 414, 2001, pp. 338–344.

[4] A. Testino, I.R. Bellobono, V. Buscaglia, C. Canevali, M. D'Arienzo, S. Polizzi, R. Scotti, F. Morazzoni, Optimizing the Photocatalytic Properties of Hydrothermal TiO_2 by the Control of Phase Composition and Particle Morphology. A Systematic Approach, **Journal of the American Chemical Society**, vol. 129, 2007, pp. 3564–3575.

[5] R. Carbone, I. Marangi, A. Zanardi, L. Giorgetti, E. Chierici, G. Berlanda, A. Podestà, F. Fiorentini, Gero Bongiorno, P. Piseri, P.G. Pelicci and P. Milani, "Biocompatibility of Cluster-Assembled Nanostructured TiO_2 with Primary and Cancer Cells" **Biomaterials**, vol. 27, 2006, 3221–3229.

[6] G.C. Smith, L. Chamberlain, L. Faxius, G.W. Johnston, S. Jin and L.M. Bjursten, "Soft Tissue Response to Titanium Dioxide Nanotube Modified Implants" **Acta Biomater**, vol. 7, 2011, pp. 3209–3215.

[7] W. Nuansing, S. Ninmuang, W. Jarernboon, S. Maensiri and S. Seraphin, "Structural Characterization and Morphology of Electrospun TiO_2 Nanofibers" **Materials Science and Engineering: B**, vol. 131, 2006, pp. 147–155.

[8] B. Li, X. Wang, M. Yan and L. Li, "Preparation and Characterization of Nano-TiO_2 Powder" **Materials Chemistry and Physics**, vol. 78, 2002, pp. 184-188.

[9] O. Harizanov and A. Harizanova, "Development and Investigation of Sol-Gel Solutions for the Formation of TiO_2 Coatings" **Solar Energy Materials and Solar Cells**, vol. 63, 2000, pp. 185-195.

[10] Y. Lei, L.D. Zhang, G.W. Meng, G.H. Li, X.Y. Zhang, C.H. Liang, W. Chen and S.X. Wang, "Preparation and Photoluminescence of Highly Ordered TiO_2 Nanowire Arrays" **Applied Physics Letters** vol. 78, 2001, pp. 1125-1127.

[11] J. Yang, S. Mei, J.M.F. Ferreira, **Journal of the American Ceramic Society**, vol. 83, 2000, pp. 1361–1368.

[12] T. Kasuga, M. Hiramatsu, A. Hoson, T. Sekino and K. Niihara, "Formation of Titanium Oxide Nanotube" **Langmuir**, vol. 14, 1998, pp. 3160–3163.

[13] T. Kasuga, M. Hiramatsu, A. Hoson, T. Sekino, K. Niihara, Titania Nanotubes Prepared by Chemical Processing, **Advanced Materials**, vol. 11, 1999, pp. 1307–1311.

[14] G.H. Du, Q. Chen, R.C. Che, Z.Y. Yuan and L.M. Peng, "Preparation and Structure Analysis of Titanium Oxide Nanotubes" **Applied Physics Letters**, vol. 79, 2001, pp. 3702–3704.

[15] Y. Suzuki and S. Yoshikawa, "Synthesis and Thermal Analyses of TiO_2-Derived Nanotubes Prepared by the Hydrothermal Method" **Journal of Materials Research**, vol. 19, 2004, pp. 982–985.

[16] Y. Suzuki, S. Pavasupree, S. Yoshikawa and R. Kawahata, "Natural Rutile-Derived Titanate Nanofibers Prepared by Direct Hydrothermal Processing" **Journal of Materials Research**, vol. 20, 2005, pp. 1063–1070.

[17] S. Pavasupree, Y. Suzuki, S. Yoshikawa and R. Kawahata, "Synthesis of Titanate, TiO_2 (B), and Anatase TiO_2 Nanofibers from Natural Rutile Sand" **Journal of Solid State Chemistry**, vol. 178, 2005, pp. 3110–3116.

[18] J. Jitputti, P. Charoensirithavorn and S. Yoshikawa, " Hydrothermal Production of $SrTiO_3$ Nanotube Arrays" **Chemistry Letters, vol.** 36, 2007, pp. 1508-1509.

[19] E. K.Stigka, J.A. Paravantis and G.K. Mihalakakou, "Social Acceptance of Renewable Energy Sources: A Review of Contingent Valuation Applications" **Renewable and Sustainable Energy Reviews**, vol. 32, 2014, pp. 100–106.

[20] M. Gabbasa, K. Sopian, Z. Yaakob, M.R.F. Zonooz, A. Fudholi, N. Asim, "Review of the Energy Supply Status for Sustainable Development in the Organization of Islamic Conference" **Renewable and Sustainable Energy Reviews**, vol. 28, 2013, pp. 18–28.

[21] H. Kim, E. Park, S.J. Kwon, J.Y. Ohm and H.J. Chang, "An Integrated Adoption Model of Solar Energy Technologies in South Korea, **Renewable Energy**, vol. 66, 2014, pp. 523-531.

[22] C. Barone, G. Landi, A. De Sio, H.C. Neitzert and S. Pagano, "Thermal Ageing of Bulk Heterojunction Polymer Solar Cells Investigated by Electric Noise Analysis" **Solar Energy Materials and Solar Cells**, vol. 122, 2014, pp. 40-45

[23] M. Zi, M. Zhu, L. Chen, H. Wei, X.Yang and B. Cao, "ZnO Photoanodes with Different Morphologies Grown by Electrochemical Deposition and Their Dye-Sensitized Solar Cell Properties" **Ceramics International**, 2014, http://dx.doi.org/10.1016/j.ceramint.2013.12.146.

[24] B, O'regan and M. Grätzel, "A low-Cost, High-Efficiency Solar Cell based on Dye-Sensitized Colloidal TiO_2 Films" **Nature**, vol. 353, 1991, pp. 737–740.

[25] J.J. Wu, W.P. Liao and M. Yoshimura, Soft Processing of Hierarchical Oxide Nanostructures for Dye-Sensitized Solar Cell Applications" **Nano Energy**, vol. 2, 2013, pp. 1354–1372.

[26] **"TiO_2-Titanium Dioxide."** [Online]. Available : http://alanassad.com/sabbath /Elements/Inorganic/TiO_2-Titanium%20Dioxide.pdf

[27] C. Xiaobo, "Titanium Dioxide Nanomaterials and Their Energy Applications" **Chinese Journal of Catalysis**, vol. 30, 2009. pp. 839–851.

[28] W. Mekprasart. 2012. **"Performance Efficiency Enhancement of TiO_2 Modified in form of Nanocomposites with CuPc and NiO by Ball-milling-assisted Process."** Doctoral thesis of College of Nanotechnology, King Mongkut's Institute of Technology Ladkrabang.

[29] C. Li, B. Liang, H. song, J.-q. Xu and X.-q. Wang, "Preparation of Porous Rutile Titania from Ilmenite by Mechanical Activation and Subsequent Sulfuric Acid Leaching" **Microporous and Mesoporous Materials**, vol. 115, 2008, pp. 293–300.

[30] http://ej.iop.org/images/0953-8984/24/19/195503/Full/cm418730f1_online.jpg

[31] Pollution Control Department. "**Material Safety Data Sheet (MSDS). Titanium dioxide**" [Online]. Available : msds.pcd.go.th/searchName.asp?vID=1421. 2007.

[32] W. Zhang, Z. Zhu and C.Y. Cheng, "A Literature Review of Titanium Metallurgical Processes" **Hydrometallurgy**, vol. 108, 2011, pp. 177–188.

[33] J. Sun, L. Gao and Q.H. Zhang, **Journal of Materials Science Letters**, vol. 22, 2003, pp. 339.

[34] D. Li and Y.N. Xia, "Fabrication of Titania Nanofibers by Electrospinning" **Nano Letters**, vol. 3, 2003, pp. 555–560.

[35] S. Yoo, S.A. Akbar and K.H. Sandhage, "Oriented Single Crystal Titania Nanofibers via Nanocarving with Hydrogen-Bearing Gas" **Advanced Materials**, vol. 16, 2004, pp. 260–264.

[36] **"Ilmenite"** [Online]. Available : http://en.wikipedia.org/wiki/Ilmenite.

[37] **"Ilmenite"** [Online]. Available : http://www.mindat.org/min-2013.html.

[38] http://specialpapers.gsapubs.org/content/421/175/F7.large.jpg.

[39] K. Byrappa and M. Yoshimura, **Handbook of Hydrothermal Technology**, Noyes Publications, New Jersey, USA, 2001.

[40] K. Byrappa and T. Adschiri, "Hydrothermal Technology for Nanotechnology" **Progress in Crystal Growth and Characterization of Materials,** vol. 53, 2007, pp. 117-166.

[41] H. Gleiter, "Nanocrystalline Materials" **Progress in Materials Science**, vol. **33,** 1989, pp. 233-315.

[42] K.F.E. Schafthaul, "Gelehrte Anzeigen Bayer" **Akal,** vol. 20, 1845, pp. 557-593.

[43] Y. Zhu, H. Zheng, Y. Li, L. Gao, Z. Yang and Y.T. Qian, "Synthesis of Ag Dendritic Nanostructures by Using Anisotropic Nickel Nanotubes" **Materials Research Bulletin**, vol. 38, 2003, pp. 1829-1834.

[44] H.L. Niu, Q.W. Chen, Y.S. Lin, Y.S. Jia, H.F. Zhu and M. Ning, "Hydrothermal Formation of Magnetic Ni–Cu alloy Nanocrystallites at Low Temperatures" **Nanotechnology**, vol. 15, 2004, pp. 1054-1058.

[45] X. Jiao, D. Chen and L. Xiao, "Effects of Organic Additives on Hydrothermal Zirconia Nanocrystallites" **Journal of Crystal Growth**, vol. 258, 2003, pp. 158-162.

[46] M. Sorescu, L. Diamandescu, D. Tarabasanu-Mihaila and V.S. Teodorescu, "Nanocrystalline Rhombohedral In_2O_3 Synthesized by Hydrothermal and Postannealing Pathways" **Journal of Materials Science**, vol. 39, 2004, pp. 675-677.

[47] Z. Jing and S. Wu, "Synthesis and Characterization of Monodisperse Hematite Nanoparticles Modified by Surfactants via Hydrothermal Approach" **Materials Letters**, vol. 58, 2004, pp. 3637-3640.

[48] Y. Zheng, Y. Cheng, Y. Wang and F. Bao, "Synthesis and Shape Evolution of α-Fe_2O_3 Nanophase through Two-Step Oriented Aggregation in Solvothermal System" **Journal of Crystal Growth,** vol. 284, 2005, pp. 221-225.

[49] G.S. Li, R.L. Smith Jr., H. Inomata and K. Arai, "Preparation and Magnetization of Hematite Nanocrystals with Amorphous Iron Oxide Layers by Hydrothermal Conditions" **Materials Research Bulletin**, vol. 37, 2002, pp. 949-955.

[50] V. Müller and P. Schmuki, "Efficient Photocatalysis on Hierarchically Structured TiO_2 Nanotubes with Mesoporous TiO_2 Filling" **Electrochemistry Communications**, vol. 42, 2014, pp.21-25.

[51] J. Jitputti, T. Rattanavoravipa, S. Chuangchote, S. Pavasupree, Y. Suzuki and S. Yoshikawa, Low Temperature Hydrothermal Synthesis of Monodispersed Flower-Like Titanate Nanosheets, **Catalysis Communications,** vol. 10, 2009, pp. 378–382.

[52] J. Jitputti, Y. Suzuki and S. Yoshikawa, "Synthesis of TiO_2 Nanowires and Their Photocatalytic Activity for H_2 Evolution" **Catalysis Communications**, vol. 9, 2008, pp. 1265–1271.

[53] L. Dong, K. Cheng, W. Weng, C. Song, P. Du, G. Shen and G. Han, "Hydrothermal Growth of Rutile TiO_2 Nanorod Films on Titanium Substrates" **Thin Solid Films**, vol. 519, 2011, pp. 4634-4640.

[54] S. Pavasupree, S. Ngamsinlapasathian, M. Nakajima, Y. Suzuki and S. Yoshikawa, "Synthesis, Characterization, Photocatalytic Activity and Dye-Sensitized Solar Cell Performance of Nanorods/Nanoparticles TiO_2 with Mesoporous Structure" **Journal of Photochemistry and Photobiology A: Chemistry**, vol. 184, 2006, pp. 163–169.

[55] S. Pavasupree, J. Jitputti, S. Ngamsinlapasathian and S. Yoshikawa, "Hydrothermal Synthesis, Characterization, Photocatalytic Activity and Dye-Sensitized Solar Cell Performance of Mesoporous Anatase TiO_2 Nanopowders" **Materials Research Bulletin**, vol. 43, 2008 pp. 149–157.

[56] J. Jitputti, S. Pavasupree, Y. Suzuki and S. Yoshikawa, "Synthesis and Photocatalytic Activity for Water-Splitting Reaction of Nanocrystalline Mesoporous Titania Prepared by Hydrothermal Method" **Journal of Solid State Chemistry**, vol. 180, 2007, pp. 1743–1749.

[57] S. Pavasupree, N. Laosiripojana, S. Chuangchote and T. Sagawa, "Fabrication and Utilization of Titania Nanofibers from Natural Leucoxene Mineral in Photovoltaic

Applications, **Japanese Journal of Applied Physics**, vol. 50, 2011 pp. 01BJ16-1–01BJ16-4.

[58] R. Yoshida, Y. Suzuki, and S. Yoshikawa, "Effects of Synthetic Conditions and Heat Treatment on the Structure of Partially Ion-Exchanged Titanate Nanotubes, **Materials Chemistry and Physics**, vol. 91, 2005, pp. 409–416.

[59] H. Yu, J. Yu, B. Cheng and M. Zhou, "Effects of Hydrothermal Post-Treatment on Microstructures and Morphology of Titanate Nanoribbons" **Journal of Solid State Chemistry**, vol. 179, 2006, pp. 349–354.

[60] D. Aphairaj, T. Wirunmongkol, S. Pavasupree and P. Limsuwan, "Synthesis of Titanate Nanotubes from Thai Leucoxene Mineral" **Procedia Engineering**, vol. 32, 2012, pp. 1068 –1072.

[61] D. Aphairaj, T. Wirunmongkol, S. Niyomwas, S. Pavasupree and P. Limsuwan, "Synthesis of Anatase TiO_2 Nanotubes Derived from a Natural Leucoxene Mineral by the Hydrothermal Method" **Ceramics International**, http://dx.doi.org/10.1016/j.ceramint.-2014.01.145.

[62] K. Pal, T.P. Majumder, C. Neogy and S.C. Debnath, "Optical, Dielectric and Microscopic Observation of Different Phases TiO_2 Metal Host Nanowires" **Journal of Molecular Structure,** vol. 1016, 2012, pp. 30-38.

[63] R. Yoshida, Y. Suzuki and S. Yoshikawa, "Syntheses of TiO_2(B) Nanowires and TiO_2 Anatase Nanowires by Hydrothermal and Post-Heat Treatments" **Journal of Solid State Chemistry**, vol. 178, 2005, pp. 2179–2185.

[64] K. Asagoe, Y. Suzuki, S. Ngamsinlapasathian and S. Yoshikawa, "TiO_2-Anatase Nanowire Dispersed Composite Electrode for Dye-Sensitized Solar Cells" **Journal of Physics: Conference Series**, vol. 61, 2007, pp. 1112–1116.

[65] Y. Suzuki, S. Ngamsinlapasathian, R. Yoshida and S. Yoshikawa, "Partially Nanowire-Structured TiO_2 Electrode for Dye-Sensitized Solar Cells" **Central European Journal of Chemistry**, vol. 4, 2006, pp. 476–488.

[66] L.T. Mancic, B.A. Marinkovic, P.M. Jardim, O.B. Milosevic and F. Rizzo, "Precursor Particle Size as the Key Parameter for Isothermal Tuning of Morphology from Nanofibers to Nanotubes in the $Na_{2-x}H_xTi_nO_{2n+1}$ System through Hydrothermal Alkali Treatment of Rutile Mineral Sand" **Crystal Growth and Design**, vol. 9, 2009, pp. 2152–2158.

[67] B.X. Wang, D.F. Xue, Y. Shi and F.H. Xue, "**Titania 1D nanostructured materials: Synthesis, properties and applications. In: Prescott, W.V., Schwartz, A.I. (Eds.), Nanorods, Nanotubes and Nanomaterials Research Progress**" New Nova Science Publishers Inc., New York, 2008 pp. 163-201.

[68] H.K. Seo , G.S. Kim, S.G. Ansari, Y.S. Kim, H.S. Shin, K.H. Shim, E.K. Suh,. "A Study on the Structure/Phase Transformation of Titanate Nanotubes Synthesized at Various Hydrothermal Temperatures" **Solar Energy Materials and Solar Cells**, vol. 92, 2008, pp. 1533-1539.

[69] Sreekantan, S., Lai and C.W.,. Study on the Formation and Photocatalytic Activity of Titanate Nanotubes Synthesized via Hydrothermal Method. **Journal of Alloys and Compounds,** vol. 490, 2010, pp. 436-442.

[70] Z.Y. Yuan and B.L. Su, "Titanium Oxide Nanotubes, Nanofibers and Nanowires" **Colloids and Surfaces A**, vol. 241, 2004, pp. 173-183.

[71] H.H. Ou and S.L. Lo, "Review of Titania Nanotubes Synthesized via the Hydrothermal Treatment: Fabrication, Modification and Application" **Separation and Purification Technology**, vol. 58, 2007, pp. 179-191.

[72] R.Z. Ma, K. Fukuda, T. Sasaki, M. Osada and Y. Bando, "Structural Features of Titanate Nanotubes/Nanobelts Revealed by Raman, X-ray Absorption Fine Structure and Electron Diffraction Characterizations" **Journal of Physical Chemistry B**, vol. 109, 2005, pp. 6210-6214.

[73] Y. Lan, X.P. Gao, H.Y. Zhu, Z.F. Zheng, T.F. Yan, F. Wu, S.P. Ringer and D.Y. Song, "Titanate Nanotubes and Nanorods Prepared from Rutile Powder" **Advanced Functional Materials**, vol. 15, 2005, pp. 1310-1318.

[74] C.K. Lee, K.S. Lin, C.F. Wu, M.D. Lyu and C.C. Lo, "Effects of Synthesis Temperature on the Microstructures and Basic Dyes Adsorption of Titanate Nanotubes" **Journal of Hazardous Materials**, vol. 150, 2008, pp. 494-503.

[75] C.K. Lee, M.D. Lyu, S.S. Liu and H.C. Chen. "The Synthetic Parameters for the Preparation of Nanotubular Titanate with Highly Photocatalytic Activity" **Journal of the Taiwan Institute of Chemical Engineers**, vol. 40, 2009, pp. 463-470.

[76] E. Horvath, A. Kukovecz, Z. Konya and I. Kiricsi, “Hydrothermal Conversion of Self-Assembled Titanate Nanotubes into Nanowires in a Revolving Autoclave” **Chemistry of Materials**, vol. 19, 2007, pp. 927-931.

[77] A. Thorne, A. Kruth, D.P. Tunstall, J.T.S. Irvine and W. Zhou “Formation, Structure and Stability of Titanate Nanotubes and Their Photon Conductivity” **Journal of Physical Chemistry B**, vol. 109, 2005, pp. 5439-5444.

[78] J. Gong, J. Liang and K. Sumathy, “Review on Dye-Sensitized Solar Cells (DSSCs): Fundamental Concepts and Novel Materials” **Renewable and Sustainable Energy Reviews**, vol. 16, 2012, pp. 5848–5860.

[79] M. K. Nazeeruddin, A. Kay, I. Rodicio, R. Humphry-Baker, E. Müller, P. Liska, N. Vlachopoulos and M. Grätzel: Conversion of Light to Electricity by cis-X2Bis(2,2'-bipyridyl-4,4'-dicarboxylate)ruthenium(II) Charge-Transfer Sensitizers (X = Cl-, Br-, I-, CN- and SCN-) on Nanocrystalline TiO_2 Electrodes” **Journal of the American Chemical Society**, vol. 115, 1993, pp. 6382-6390.

[80] T. P. Chou, Q. F. Zhang and G. Z. Cao, “Effects of Dye Loading Conditions on the Energy Conversion Efficiency of ZnO and TiO_2 Dye-Sensitized Solar Cells" **Journal of Physical Chemistry C**, vol. 111, 2007, pp. 18804–18811.

[81] M.K. Nazeeruddin, P. Pechy, T. Renouard, S.M. Zakeeruddin, R. Humphry-Baker and P. Comte, et al. Engineering of Efficient Panchromatic Sensitizers for Nanocrystalline TiO_2-Based Solar Cells. **Journal of the American Chemical Society**, vol. 123, 2001, pp. 1613-1624.

[82] K. Kalyanasundaram, “**Dye-sensitized solar cells**” CRC press, Lausanne, Switzerland.

[83] T.W. Hamann, R.A. Jensen, A.B.F. Martinson, H.V. Ryswyk and J.T. Hupp, “Advancing Beyond Current Generation Dye-Sensitized Solar Cells” **Energy and Environmental Science**, vol. 1, 2008, pp. 66–78.

[83] J. Halme, 2002. “Dye-Sensitized Nanostructured and Organic Photovoltaic Cells: Technical Review and Preliminary Tests.” Master thesis of Department of Engineering Physics and Mathematics, Helsinki University of Technology.

[84] M. Grätzel, “Dye-Sensitized Solar Cells” **Journal of Photochemistry and Photobiology C: Photochemistry Reviews.** vol. 4, 2003. Pp. 145-153.

[85] http://i01.i.aliimg.com/img/pb/702/754/426/426754702_444.jpg

[86] M. Muneer, M. Saquib, M. Qamar and D. Bahnemann, "Titanium-Dioxide Mediated Photocatalysis Reaction of Three Selected Pesticide Derivatives" **Research on Chemical Intermediates**, vol. 30, 2004. pp. 663-672.

[87] L. Hugo de, S. Benito and S. Miguel, "**Photocatalytic Reaction Engineering**" [Online]. Available : http://www.springer.com/chemistry/book/978-0-387-23450-2. 2005.

[88] "**X-ray scattering techniques.**" [Online]. Available : http://en.wikipedia.org/wiki/X-ray_scattering_techniques.

[89] Z.L. Wang, "**Characterization of Nanophase Materials**" Wiley-VCH, Weinheim, Germany, 2000.

[90] B. Fultz and J. Howe, "**Transmission Electron Microscopy and Diffractometry of Materials**" Springer-Verlag Berlin Heidelberg, Germany, 2013.

[91] B. Beckhoff, B. Kanngießer, N. Langhoff, R. Wedell and H. Wolff, "**Handbook of Practical X-Ray Fluorescence Analysis**" Springer-Verlag Berlin Heidelberg, Germany, 2006.

[92] "**X-Ray Microscopy and Imaging: X-ray Fluorescence Mapping**" [Online]. Available : http://www.aps.anl.gov.

[93] "**X-Ray Fluorescence (XRF)**" [Online]. Available : http://www.amptek.com/xrf_1.gif.

[94] S. Suga and A. Sekiyama, "**Photoelectron Spectroscopy**" Springer-Verlag Berlin Heidelberg, Germany, 2014.

[95] S. Hofmann, "**Auger- and X-Ray Photoelectron Spectroscopy in Materials Science**" Springer-Verlag Berlin Heidelberg, Germany, 2013.

[96] "**X-ray photoelectron spectroscopy**" [Online]. Available : http://upload.wikimedia.org/wikipedia/commons/thumb/f/f2/System2.gif/350px-System2.gif

[97] S. Hüfner, "**Photoelectron Spectrometry**" Springer-Verlag Berlin Heidelberg, Germany, 2003.

[98] "**X-ray photoelectron spectroscopy**" [Online]. Available : http://www.ifw-dresden.de/typo3temp/pics/2cf1933862.jpg

[99] K. Shimizu and T, Mitani, "**New Horizons of Applied Scanning Electron Microscopy**" Springer-Verlag Berlin Heidelberg, Germany, 2010.

[100] S.J. Pennycook and P.D. Nellist, "**Scanning Transmission Electron Microscopy**" Springer-Verlag New York, United State of America.

[101] S. Amelinckx, D. van Dyck, J. van Landuyt, G. van Tendeloo, "**Electron Microscopy: Principles and Fundamentals**" John Wiley & Sons, 2008.

[102] "**Scanning Electron Microscope.**" [Online]. Available : http://www.microscopy.ethz .ch/ images/sem.jpg

[103] "**Scanning Electron Microscope.**" [Online]. Available : http://www.jeol.co.jp/en/ science/ product_file/file/en_sc7-3.jpg.

[104] D.B. Williams and C.B. Carter, "**Transmission Electron Microscopy**" Springer US, 2009.

[105] Y. Leng, **"Materials Characterization"** Wiley-VCH, Weinheim, 2013.

[106] **"The Transmission Electron Microscope"** [Online]. Available : http://www.nobelprize.org/educational/physics/microscopes/tem/.

[107] S. Lowell, J.E. Shields, M.A. Thomas and M. Thommes, **"Characterization of Porous Solids and Powders: Surface Area, Pore Size and Density of Nanoparticles**" Springer Netherlands, 2004.

[108] M. Naderi, "Brunauer-Emmett-Teller" **Progress in Filtration and Separation**, 2015, pp. 585-608.

[109] **"Brunauer, Emmett and Teller (BET) Theory"** [Online]. Available : http://particle. dk/ methods-analytical-laboratory/surface-area-bet/surface-area-bet-theory/.

[110] J. Workman Jr. **"The Handbook of Organic Compounds: NIR, IR, Raman, and UV-Vis Spectra Featuring Polymers and Surfactants"** Academic Press, 2000.

[111] **"UV-Vis Absorption Spectroscopy"** [Online]. Available : https://www2.chemistry.msu. edu/faculty/reusch/virttxtjml/spectrpy/uv-vis/uvspec.htm.

[112] C. Poole, **"Instrumental Thin-Layer Chromatography**" Elsevier, 2014.

[113] M.M. Ba-Abbad, A.A.H. Kadhum, A.B. Mohamad, M.S. Takriff and K. Sopian, "Synthesis and Catalytic Activity of TiO2 Nanoparticles for Photochemical Oxidation of Concentrated Chlorophenols under Direct Solar Radiation" **International Journal of Electrochemical Science**, vol. 7, 2012, pp. 4871–4888.

[114] S. Pavasupree, S. Ngamsinlapasathian, Y. Suzuki and S. Yoshikawa, "Preparation and Characterization of High Surface Area Nanosheet Titania with Mesoporous Structure" **Materials Letters**, vol. 61, 2007, pp. 2973–2977.

[115] M. Nag, D. Guin, P. Basak and S.V. Manorama, "Influence of Morphology and Surface Characteristics on the Photocatalytic Activity of Rutile Titania Nanocrystals" **Materials Research Bulletin**, vol. 43, 2008, pp. 3270–3285.

[116] S. Ngamsinlapasathian, S. Sakulkhaemaruethai, S. Pavasupree, A. Kitiyanan, T. Sreethawong, Y. Suzuki and S. Yoshikawa, "Highly Efficient Dye-Sensitized Solar Cell using Nanocrystalline Titania Containing Nanotube Structure" **Journal of Photochemistry and Photobiology A: Chemistry**, vol. 164, 2004, pp. 145–151.

[117] S. Ngamsinlapasathian, S. Pavasupree, Y. Suzuki and S. Yoshikawa, "Dye-Sensitized Solar Cell Made of Mesoporous Titania by Surfactant-Assisted Templating Method" **Solar Energy Materials & Solar Cells**, vol 90, 2006, pp. 3187–3192.

[118] J. Jiu, S. Isoda, F. Wang and M. Adachi, "Dye-Sensitized Solar Cells Based on a Single-Crystalline TiO_2 Nanorod Film" **Journal of Physical Chemistry B,** vol. 110, 2006, pp. 2087-2092.

[119] K. Fan, W. Zhang, T. Peng, J. Chen and F. Yang, "Application of TiO_2 Fusiform Nanorods for Dye-Sensitized Solar Cells with Significantly Improved Efficiency" **Journal of Physical Chemistry C**, vol. 115, 2011, pp. 17213–17219.

[120] A.E. Shalan, M.M. Rashad, Y. Yu, M. Lira-Cantu and M.S.A. Abdel-Mottaleb, "Controlling the Microstructure and Properties of Titania Nanopowders for High Efficiency Dye Sensitized Solar Cells" **Electrochimica Acta**, vol. 89, 2013, pp. 469– 478.

[121] J.S. Im, S.K. Lee and Y.-S. Lee, "Cocktail Effect of Fe_2O_3 and TiO_2 Semiconductors for a High Performance Dye-Sensitized Solar Cell" **Applied Surface Science**, vol. 257, 2011, pp. 2164–2169.

[122] L. Francis, A.S. Nair, R. Jose, S. Ramakrishna, V. Thavasi and E. Marsano, "Fabrication and Characterization of Dye-Sensitized Solar Cells from Rutile Nanofibers and Nanorods" **Energy**, vol. 36, 2011, pp. 627–632.

[123] http://www.mtec.or.th

[124] http://www.kratos.com/sites/default/files/styles/product/public/products/AXIS%20 UltraDLD%202012.jpg?itok=KGxEUjRW

[125] O.P. Ferreira, A.S. Filho, J.M. Filho and O.L. Alves, "Unveiling the Structure and Composition of Titanium Oxide Nanotubes through Ion Exchange Chemical Reactions and Thermal Decomposition Processes" **Journal of the Brazilian Chemical Society**, vol.

17, 2006, pp. 393-402.

[126] C.C. Tsai and H. Teng, "Structural Features of Nanotubes Synthesized from NaOH Treatment on TiO_2 with Different Post-Treatments" **Chemistry of Materials**, vol. 18, 2006, pp. 367–373.

[127] C.L. Wong, Y.N. Tan and A.R. Mohamed, "A Review on the Formation of Titania Nanotube Photocatalysts by Hydrothermal Treatment" **Journal of Environmental Management**, vol. 92, 2011, pp. 1669-1680.

[128] C.C. Tsai and H. Teng, "Nanotube Formation from a Sodium Titanate Powder via Low-Temperature Acid Treatment" **Langmuir**, vol. 24, 2008, pp. 3434–3438.

[129] S. Kim, M. Kim, S.H. Hwang and S.K. Lim, "Effects of Hydrothermal Temperature and Acid Concentration on the Transition from Titanate to Titania" **Journal of Industrial and Engineering Chemistry**, vol. 18, 2012, pp. 1141–1148.

[130] H. Yin, Y. Wada, T. Kitamura, S. Kambe, S. Murasawa, H. Mori, T. Sakata and S. Yanagida, "Hydrothermal Synthesis of Nanosized Anatase and Rutile TiO_2 Using Amorphous Phase TiO_2" **Journal of Materials Chemistry**, vol. 11, 2001, pp. 1694–1703.

[131] R. Huang, Y. Shen, L. Zhao and M. Yan, "Effect of Hydrothermal Temperature on Structure and Photochromic Properties of WO_3 Powder" **Advanced Powder Technology**, vol. 23, 2012, pp. 211–214.

[132] E. Ylhäinen, M. Nunes, A. Silvestre and O. Monteiro, "Synthesis of Titanate Nanostructures using Amorphous Precursor Material and Their Adsorption/Photocatalytic Properties" **Journal of Materials Science**, vol. 47, 2012, pp. 4305–4312.

[133] A.R. Armstrong, G. Armstrong, J. Canales, R. Garcia and P.G. Bruce, "Lithium-Ion Intercalation into TiO_2-B Nanowires" **Advanced Materials**, vol. 17, 2005, pp. 862–865.

[134] J. Yu, G. Wang, B. Cheng and M. Zhou, "Effects of Hydrothermal Temperature and Time on the Photocatalytic Activity and Microstructures of Bimodal Mesoporous TiO_2 Powders" **Applied Catalysis B: Environmental,** vol. 69, 2007, pp. 171–180.

[135] C.Y. Huang, Y.C. Hsu, J.G. Chen,V. Suryanarayanan, K.M. Lee and K.C. Ho "The Effects of Hydrothermal Temperature and Thickness of TiO_2 Film on the Performance of a Dye-Sensitized Solar Cell", **Solar Energy Materials and Solar Cells,** vol. 90, 2006, pp. 2391–2397.

[136] M. Guo, P. Diao, X. Wang and S. Cai, "The Effect of Hydrothermal Growth Temperature on Preparation and Photoelectrochemical Performance of ZnO Nanorod Array Films", **Journal of Solid State Chemistry**, Vol. 178, 2005, pp. 3210–3215.

[137] D-S. Seo, J.-K. Lee and H. Kim, "Preparation of Nanotube-Shaped TiO_2 Powder", **Journal of Crystal Growth**, vol. 229, 2001, pp. 428–432.

[138] A. Nakahira, T. Kubo and C. Numako, "Formation Mechanism of TiO_2-Derived Titanate Nanotubes Prepared by the Hydrothermal Process" **Inorganic Chemistry**, vol. 49, 2010, pp. 5845–5852.

[139] N. Liu, X. Chen, J. Zhang and J.W. Schwank, "A Review on TiO_2-Based Nanotubes Synthesized via Hydrothermal Method: Formation Mechanism, Structure Modification, and Photocatalytic Applications" **Catalysis Today**, vol. 225, 2014, pp. 34–51.

[140] Q. Chen, W. Zhou, G.H. Du and L.M. Peng, "Tritanate Nanotubes Made via a Single Alkali Treatment" **Advanced Materials**, vol. 14, 2002, pp. 1208–1211.

[141] M. Zhang, Z. Jin, J. Zhang, X. Guo, J. Yang, W. Li, X. Wang and Z. Zhang, "Effect of Annealing Temperature on Morphology, Structure and Photocatalytic Behavior of Nanotubed $H_2Ti_2O_4(OH)_2$" **Journal of Molecular Catalysis A: Chemical**, vol. 217, 2004, pp. 203–210.

[142] D. Gong, C.A. Grimes, O.K. Varghese, W. Hu, R.S. Singh, Z. Chen and E.C. Dickey, "Titanium Oxide Nanotube Arrays Prepared By Anodic Oxidation" **Journal of Materials Research**, vol. 16, 2001, pp. 3331–3334.

[143] J. B. Baxter, and E. S. Aydil, "Nanowire Based Dye Sensitized Solar Cells" **Applied Physics Letters**, vol 85, 2005, 053114.

[144] T.K. Ghorai, M. Chakraborty and P. Pramanik, "Photocatalytic Performance of Nano-Photocatalyst from TiO_2 and Fe_2O_3 by Mechanochemical Synthesis" **Journal of Alloys and Compounds**, vol. 509, 2011, pp. 8158–8164.

[145] X. Zhang and L. Lei, "Preparation of Photocatalytic Fe_2O_3–TiO_2 Coatings in One Step by Metal Organic Chemical Vapor Deposition" **Applied Surface Science**, vol. 254, 2008, pp. 2406–2412.

[146] A.R. Armstrong, G. Armstrong, J. Canales and P.G. Bruce, "TiO_2-B Nanowires" **Angewandte Chemie International Edition**, vol. 43, 2004, pp. 2286–2288.

[147] Z.-Y. Yuan and B.-Y. Su, "Titanium oxide nanotubes, nanofibers and nanowires" **Colloids Surfaces A**, vol. 241, 2004, pp. 173–183.

[148] Y. Cong, Z. Li, Y. Zhang, Q. Wang and Q. Xu, "Synthesis of α-Fe_2O_3/TiO_2 Nanotube Arrays for Photoelectro-Fenton Degradation of Phenol" **Chemical Engineering Journal**, vol. 191, 2012, pp. 356–363.

[149] C.L. Luu, Q.T. Nguyen and S.T. Ho, "Synthesis and Characterization of Fe-Doped TiO_2 Photocatalyst by the Sol-Gel Method" **Advances in Natural Sciences: Nanoscience and Nanotechnology,** vol. 1, 2010, pp. 015008.

[150] X.X. Slamet, H.W. Nasution, E. Purnama, S. Kosela and J. Gunlazuardi, "Photocatalytic Reduction of CO_2 on Copper-Doped Titania Catalysts Prepared by Improved-Impregnation Method" **Catalysis Communications,** vol. 6, 2005, pp. 313–319.

[151] R.A. Spurr and H. Myers, "Quantitative Analysis of Anatase-Rutile Mixtures with an X-Ray Diffractometer" **Analytical Chemistry**, vol. 29, 2008, pp. 760–763.

[152] G.Wang, L. Xu, J. Zhang, T. Yin and D. Han, Enhanced Photocatalytic Activity of TiO_2 Powders (P25) via Calcination Treatment" **International Journal of Photoenergy**, vol. 2012, 2012, 265760.

[153] S. Mozia, A. Heciak and A.W. Morawski, "The Influence of Physico-Chemical Properties of TiO_2 on Photocatalytic Generation of C1-C3 Hydrocarbons and Hydrogen from Acetic Acid" **Applied Catalysis B: Environmental**, vol. 104, 2011, pp. 21–29.

[154] M. Batzill, E.H. Morales and U. Diebold, "Influence of Nitrogen Doping on the. Defect Formation and Surface Properties of TiO2 Rutile and Anatase" **Physical Review Letters**, vol. 96, 2006, pp. 26103–26122.

[155] P. Górska, A. Zaleska, E. Kowalska, T. Klimczuk, J.W. Sobczak, E. Skwarek, W. Jjanusz and J. Hupka, "TiO_2 Photoactivity in Vis and UV Light: the Influence of Calcination Temperature and Surface Properties" **Applied Catalysis B: Environmental**, vol. 84, 2008, pp. 440–447.

[156] C.C. Tsai and H. Teng, "Regulation of the Physical Characteristics of Titania Nanotube Aggregates Synthesized from Hydrothermal Treatment" **Chemistry of Materials**, vol. 16, 2004, pp. 4352–4358.

[157] X. Deng, Y. Yue and Z. Gao, "Gas-Phase Photo-Oxidation of Organic Compounds Over Nanosized TiO_2 Photocatalysts by Various Preparations" **Applied Catalysis B:**

Environmental, vol. 39, 2002, pp. 135–147.

[158] L. Curkovic and M. Fuduric, "Dissolution of Alumina Ceramics in HCl Aqueous Solution", **Ceramics International**, vol. 35, 2009, pp. 2041–2045.

[159] Y. Liu, J.H. Wei, R. Xiong, C.X. Pan and J. Shi, "Enhanced Visible Light Photocatalytic Properties of Fe-Doped TiO_2 Nanorod Clusters and Monodispersed Nanoparticles", **Applied Surface Science**, vol. 257, 2011, pp. 8121–8126.

[160] G. Wang, L. Xu, J. Zhang, T. Yin, D. Han, "Enhanced Photocatalytic Activity of Powders (P25) via Calcination Treatment", **International Journal of Photoenergy**, vol. 2012, 2012, 265760.

[161] T.K. Ghorai, M. Chakraborty, P. Pramanik, "Photocatalytic Performance of Nano-Photocatalyst from TiO_2 and Fe_2O_3 by Mechanochemical Synthesis", **Journal of Alloys and Compounds**, vol. 509, 2011, pp. 8158–8164.

[162] Q. Xiao and L.L. Ouyang, "Photocatalytic Activity and Hydroxyl Radical Formation of Carbon-Doped TiO_2 Nanocrystalline: Effect of Calcination Temperature", **Chemical Engineering Journal**, vol. 148, 2009, pp. 248–253

[163] L.L. Costa, A.G.S. Prado, TiO_2 Nanotubes as Recyclable Catalyst for Efficient Photocatalytic Degradation of Indigo Carmine Dye", **Journal of Photochemistry and Photobiology A: Chemistry**, vol. 201, 2009, pp. 45–49.

[154] J. B. Baxter, and E. S. Aydil, "Nanowire Based Dye Sensitized Solar Cells" **Applied Physics Letters**, vol 85, 2005, 053114.

[165] M. Law, L. E. Greene, J. C. Johnson, R. Saykally, and P. Yang, "Nanowire Dye-Sensitized Solar Cells", **Nature Materials**, vol. 4, 2005, pp. 455–459.

[166] M. Wolf, and H. Rauschenbacht, Series Resistance Effects on Solar Cell Measurements. **Advanced Energy Conversion**, vol. 3, 1963, pp. 455-479.

[167] V. Thavasi, V. Renugopalakrishnan, R. Jose and S. Ramakrishna, "Controlled electron injection and transport at materials interfaces in dye sensitized solar cells", **Materials Science and Engineering: R: Report**, vol. 63, 2009, pp. 81–99.

[168] S.H. Kang, S.H. Choi, M.S. Kang, J.Y. Kim, H.S. Kim, T. Hyeon and Y.E. Sung, "Nanorod=Based Dye-Sensitized Solar Cells with Improved Charge Collection Efficiency", **Advanced Materials**, vol. 20, 2008, pp. 54–58.

[169] J.G. Yu, J.J. Fan and K. Lv, "Anatase TiO_2 Nanosheets with Exposed (001) Facets: Improved Photoelectric Conversion Efficiency in Dye-Sensitized Solar Cells", **Nanoscale,** vol. 2, 2010, pp. 2144-2149.

[170] K. Pan, Y. Dong, C. Tian, W. Zhou, G. Tian, B. Zhao and H. Fu, TiO_2-B Narrow Nanobelt/TiO_2 Nanoparticle Composite Photoelectrode for Dye-Sensitized Solar Cells, **Electrochimica Acta**, vol. 54, 2009, pp. 7350–7356.

[171] J. Sheng, L. Hu, W. Li, L. Mo, H. Tian and S. Dai, Formation of Single-Crystalline Rutile TiO_2 Splitting Microspheres for Dye-Sensitized Solar Cells, **Solar Energy**, vol. 85, 2011, pp. 2697–2703.

Appendix A

Degradation of Rhodamine-B

Photocatalytic Reaction is one of advanced oxidation processes (AOPs) defined as the acceleration of photoreaction in the presence of catalyst. The photocatalytic reaction system is composed of photocatalyst, light source, water and oxygen or oxidant. In photogenerated catalysis, the photocatalytic activity (PCA) depends on the ability of the catalyst to create electron–hole pairs, which generate free radicals (e.g. hydroxyl radicals: •OH) able to undergo secondary reactions. Its practical application was made possible by the discovery of water electrolysis by means of TiO_2. Semiconductors, such as TiO_2, are chosen as the photocatalyst because of good working functionality in near- UV and visible light source, high chemical resistance and reusable material. When TiO_2 photocatalyst absorbs UV irradiation from sunlight or illuminated light source (fluorescent lamps), excited electrons of the valence band (VB) are promoted to the conduction band (CB) therefore the production of the negative electron (e_{CB}^-) and positive-hole (h_{VB}^+) pairs is obtained in equation 1;

$$TiO_2 + h\nu \rightarrow e_{CB}^- + h_{VB}^+ \tag{1}$$

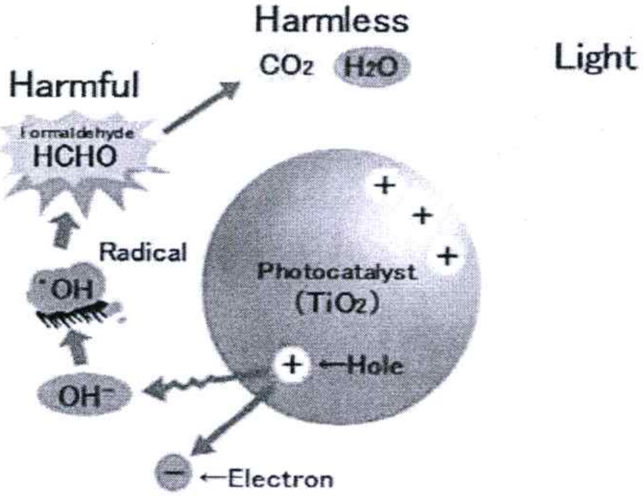

Appendix Figure A1 Mechanism of TiO_2 photocatalyst [86].

These electron-hole pairs can react in a redox reaction with other species on the surface. The production of hydroxyl radical ($OH^{\bullet}$) was easily occurred by the reaction of h_{VB}^{+} with water molecule (H_2O) followed as equation 2. Whereas, the reaction of e_{CB}^{-} with oxygen (O_2) leads to super oxide radical anions ($O_2^{\bullet -}$) shown in equation 3 [87].

$$H_2O + h_{VB}^{+} \rightarrow OH^{\bullet} + H^{+} \qquad (2)$$

$$O_2 + e_{CB}^{-} \rightarrow O_2^{\bullet -} \qquad (3)$$

It has been suggested that the hydroxyl radicals and superoxide radical anions are the primary oxidizing species in the photocatalytic processes as shown in Appendix Figure A1. The reaction of super oxide radical with H_2O may increase hydroxyl radical in the system due to decomposition of H_2O_2 product as followed equation 4 and 5;

$$O_2^{\bullet -} + H_2O \rightarrow H_2O_2 \qquad (4)$$

$$H_2O_2 \rightarrow 2OH^{\bullet} \qquad (5)$$

The hydroxyl is extremely powerful oxidation agent because of its potential. This radical is very reactive and attack pollutant molecules to degrade into other species including carbon dioxide and water [88]. This mechanism is related to decolorization of dye or complete mineralization as followed equation 6 and 7;

$$OH^{\bullet} + dye \rightarrow dye_{OX}^{*} \qquad (6)$$

$$dye_{OX}^{*} + O_2^{\bullet -} \; or \; OH^{\bullet} \rightarrow \text{degraded product} \qquad (7)$$

Experiment

The as-synthesized nanofibers were carried out by dye photodegradation of Rhodamine B (RhB) under visible light via fluorescent lamp (15 W). 50 mg of the as-synthesized and ST-01 were dispersed in 1 mM of RhB and stirred for 20 min in the dark condition. The solution was irradiated in visible light at room temperature and measured every 15 min until the experiment time about 60 min. RhB degradation was investigated by the decrease of its absorbance at maximum wavelength (λmax) via Helios UV-Vis spectrometer.

Result and Discussion

The as-synthesized nanofibers were measured of degradation of RhB. The decreasing in absorption is associated to the destruction of dye chromogen. Appendix Figure A2 shows absorption spectra of the photo-degradation of RhB in aqueous solution under visible light for 1 hour of the as-synthesized nanofibers compared commercial grade TiO_2 nanoparticles (ST-01). The absorption spectrum of RhB degraded by the as-synthesized nanofibers demonstrated that the decreased absorbance was higher than ST-01 may due to improvement photocatalytic activity of naturally Fe-doped feature of ilmenite mineral. Furthurmore, the fiber-like morphology of as-synthesized sample may be high specific surface area than particle-like morphology of ST-01. Recent research, detailed the submicron particle morphology directing to smaller specific surface area leading to reduce of photocatalytic activity [16, 23].

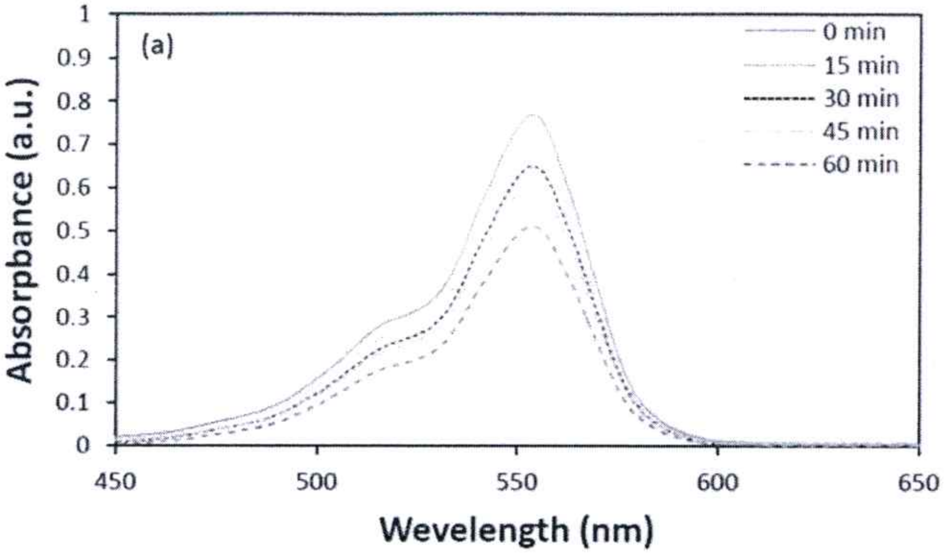

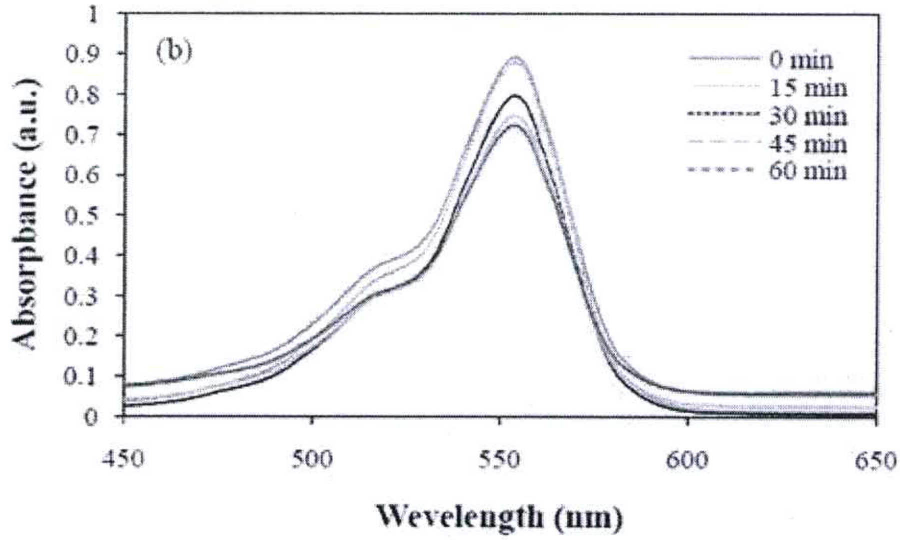

Appendix Figure A2 Absorption of RhB under visible light by using (a) as-synthesized nanofibers, (b) ST-01 and (c) At 60 min of irradiated time.

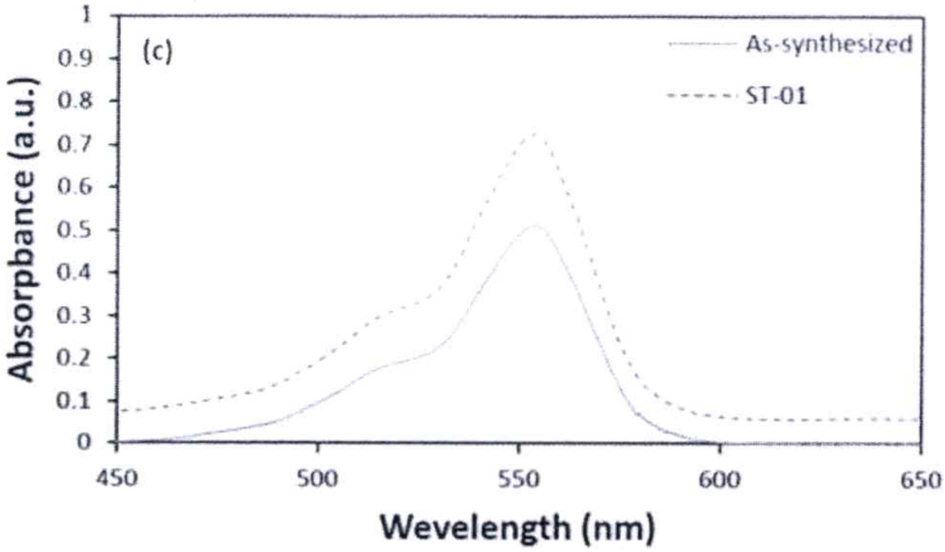

Appendix Figure A2 (cont.) Absorption of RhB under visible light by using (a) as-synthesized nanofibers, (b) ST-01 and (c) At 60 min of irradiated time.

BIOGRAPHY

Mr. Athapon Simpraditpan

DATE OF BIRTH	30 September 1984, Nakhon Si Thammarat
ADDRESS	99, Klong Hok, Klong Luang, Pathum Thani, Thailand 12120
EDUCATION	Bachelor of Engineering in Plastics Engineering, Faculty of Engineering from Rajamangala University of technology Thanyaburi (RMUTT), Pathum Thani, Thailand. Master of Engineering in Energy Technology, School of Energy, Environment and Materials from King Mongkut's University of Technology Thonburi (KMUTT), Bangkok, Thailand.

PUBLICATION;

1. A. Simpraditpan, T. Wirunmongkol, S. Pavasupree, W. Pecharapa, "**Simple Hydrothermal Preparation of Nanofibers from Natural Ilmenite Mineral**", Ceramics International 39 (2013) 2497–2502 (IF = 2.110).
2. A. Simpraditpan, T. Wirunmongkol, S. Pavasupree, W. Pecharapa, "**Effect of Calcination Temperature on Structural and Photocatalyst Properties of Nanofibers Prepared from Low-Cost Natural Ilmenite Mineral by Simple Hydrothermal Method**", Materials Research Bulletin 48 (2013) 3211–3217 (IF = 2.108).
3. A. Simpraditpan, T. Wirunmongkol, S. Pavasupree, W. Pecharapa, "**Hydrothermal Synthesis of Nanofibers from Natural Ilmenite Mineral and Their Utilization for Dye-Sensitized Solar Cell**", Integrated Ferroelectrics, 149 (2013) 135–142 (IF= 0.371).
4. A. Simpraditpan, T. Wirunmongkol, S. Pavasupree, W. Pecharapa, "**Efficiency Enhancement in Dye-Sensitized Solar Cell using TiO_2 /Ilmenite-derived Nanofiber Composite as Working Electrode**", Advanced Materials Research 925 (2014) 600–604.

CONFERENCE PRESENTATION;

1. A. Simpraditpan, T. Wirunmongkol, S. Pavasupree, W. Pecharapa, "**Preparation of Nanofibers from Natural Ilmenite Mineral by Simple Hydrothermal Method**", Industrial Engineering Network Conference 2011, October 20-21, 2011 Chonburi, Thailand.
2. A. Simpraditpan, T. Wirunmongkol, S. Pavasupree, W. Pecharapa, "**Effect of Hydrothermal Temperature on Structure of Titanate Nanofibers Prepared from Low-Cost Natural Ilmenite Mineral**", 1st International Symposium on Technology for Sustainability, ISTS 2011, 26-29 January 2012, KMITL, Bangkok, Thailand.
3. A. Simpraditpan, T. Wirunmongkol, S. Pavasupree, W. Pecharapa, "**Synthesis and Optical Properties of Ilmenite Nanofibers Prepared via Hydrothermal Method**", Siam Physics Congress SPC2012 Past, Present and Future of Physic, 9-12 May 2012, Krungsri River Hotel, Phra Nakhon Si Ayutthaya, Thailand.
4. อรรถพล สิมประดิษฐ์พันธุ์, ธนกรณ์ วิรุฬห์มงคล, สรพงษ์ ภวสุปรีย์ และวิษณุ เพชรภา, "**การเตรียมสารกึ่งตัวนำชนิดเอ็นประเภทเส้นใยนาโนจากแร่อิลเมไนท์ของไทย**", การประชุมวิชาการการประชุมวิชาการเครือข่ายวิศวกรรมไฟฟ้ามหาวิทยาลัยเทคโนโลยีราชมงคล ครั้งที่ 4 (EENET 2012), 3-5 เมษายน 2555 ณ โรงแรมแกรนด์ พาราไดซ์ จังหวัดหนองคาย
5. A. Simpraditpan, T. Wirunmongkol, S. Pavasupree and W. Pecharapa, "**Preparation and Characterization of Titanate Nanofibers from Low-Cost Natural Ilmenite Sand**", 10th Eco-Energy and Materials Science and Engineering Symposium, 5-8 December 2012, Sunee Grand Hotel, Ubon Ratchathani, Thailand.
6. A. Simpraditpan, T. Wirunmongkol, S. Pavasupree and W. Pecharapa, "**Hydrothermal Synthesis of Nanofibers from Natural Ilmenite Mineral and Their Utilization for Dye-Sensitized Solar Cell**", The INAMM-Special International Workshop and Symposium on Emerging Frontiers in Multiferroics and Electronic Metamaterials (organized in conjunction with The 8th Asian Meeting on Ferroelectrics (AMF-8)), 9-10 December 2012, Amari Orchid Hotel, Chonburi, Thailand.

7. A. Simpraditpan, T. Wirunmongkol, S. Pavasupree and W. Pecharapa, "**Efficiency Enhancement in Dye-Sensitized Solar Cell using TiO_2 /Ilmenite-derived Nanofiber Composite as Working Electrode**", International Conference on Nanoscience, Engineering, and Management (BOND21), 19-21 August 2013, Bayview Beach Resort, Batu Ferringhi, Penang, Malaysia.
8. อรรถพล สิมประดิษฐ์พันธุ์, ธนกรณ์ วิรุฬห์มงคล, สรพงษ์ ภวสุปรีย์ และวิษณุ เพชรภา, "**การเตรียมสารกึ่งตัวนำประเภทเส้นใยนาโนจากแร่อิลเมไนท์ของไทยสำหรับใช้เป็นขั้วไฟฟ้าในเซลล์พลังงานแสงอาทิตย์ชนิดสีย้อมไวแสง**", การประชุมวิชาการทางวิศวกรรมไฟฟ้า ครั้งที่ 36 (EECON 36), 11-13 ธันวาคม 2556 ณ เฟลิกซ์ ริเวอร์แควรีสอร์ท จังหวัดกาญจนบุรี

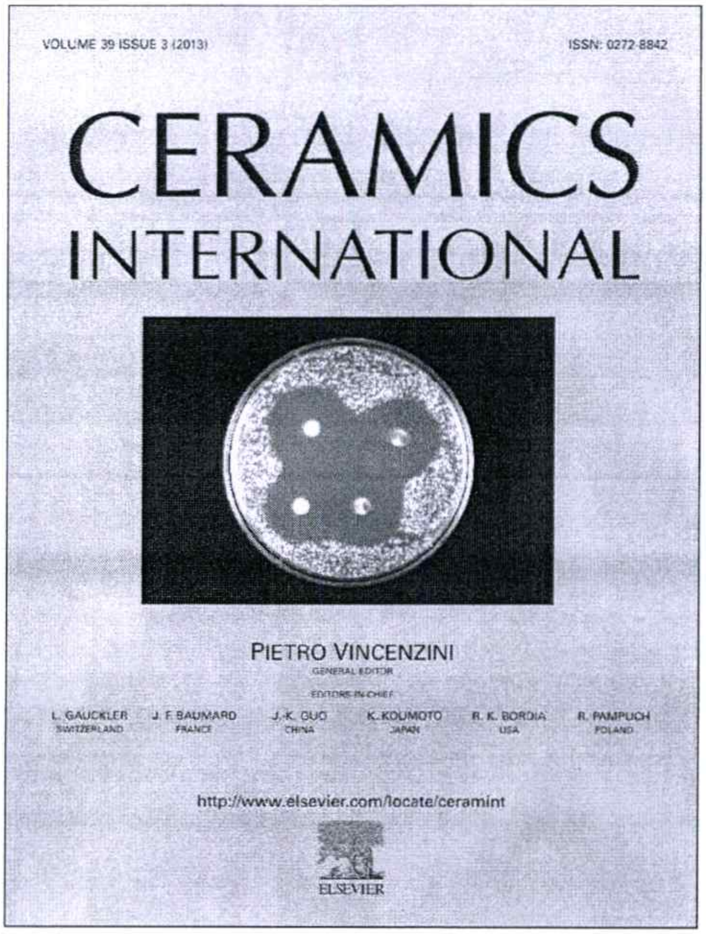
VOLUME 39 ISSUE 3 (2013)
ISSN: 0272-8842
CERAMICS
INTERNATIONAL
PIETRO VINCENZINI
GENERAL EDITOR
EDITORS-IN-CHIEF
L. GAUCKLER SWITZERLAND
J. F. BAUMARD FRANCE
J.-K. GUO CHINA
K. KOUMOTO JAPAN
R. K. BORDIA USA
R. PAMPUCH POLAND
http://www.elsevier.com/locate/ceramint
ELSEVIER

Available online at www.sciencedirect.com

SciVerse ScienceDirect

Ceramics International 39 (2013) 2497–2502

CERAMICS INTERNATIONAL

www.elsevier.com/locate/ceramint

Simple hydrothermal preparation of nanofibers from a natural ilmenite mineral

Athapon Simpraditpan[a], Thanakorn Wirunmongkol[c], Sorapong Pavasupree[c,*], Wisanu Pecharapa[a,b]

[a]College of Nanotechnology, King Mongkut's Institute of Technology Ladkrabang, Ladkrabang, Bangkok 10520, Thailand
[b]Thailand and Center of Excellence in Physics (ThEP Center), Commission on Higher Education, 328 Si Ayutthaya Road, Bangkok 10400, Thailand
[c]Department of Materials and Metallurgical Engineering, Faculty of Engineering, Rajamangala University of Technology Thanyaburi, Klong 6, Pathumthani 12110, Thailand

Received 5 August 2012; received in revised form 1 September 2012; accepted 3 September 2012
Available online 11 September 2012

Abstract

Titanate nanofibers were synthesized by a simple hydrothermal method using a natural ilmenite mineral as the starting material. The chemical composition, crystalline structure, shape, size, and specific surface area of the prepared samples were characterized by X-ray fluorescence (XRF), X-ray diffraction (XRD), scanning electron microscopy (SEM), transmission electron microscopy (TEM) and the Brunauer–Emmett–Teller analysis (BET). The crystalline structure of the as-synthesized nanofibers demonstrated a layered titanate form, $H_2Ti_xO_{2x+1}$. The length of the prepared nanofibers ranged from 2 to 7 μm with diameters ranging from 20 to 90 nm. The as-synthesized nanofibers were solids with BET surface areas of approximately 50 m^2/g. This synthetic method provides a simple route for the fabrication of one-dimensional (1-D) nanostructured materials from a low-cost natural mineral.

Keywords: B. Nanofibers; C. Hydrothermal; D. Ilmenite; D. Titanium dioxide

1. Introduction

One-dimensional TiO_2 nanostructures including nanowires, nanorods, nanowhiskers, nanotubes and nanofibers have been intensively studied and researched due to their exceptional properties including chemical stability [1], biocompatibility [2,3], high photocatalytic reactivity [1,4], and cost-effectiveness. TiO_2 is one of the most attractive metal oxides for a versatile range of potential and novel applications [4–9], such as humidity sensors [10], optoelectronic devices [11], lithium ion batteries [12–14], hydrogen storage [15,16], dye sensitized solar cells (DSSC) [17–19], water treatment materials, catalysts, and gas sensors [20–25]. Low-dimensional TiO_2-related nanomaterials can be synthesized by various methods including electrospinning [26], hydrogen treatment [27], anodic porous alumina templating [28,29], carbon nanotube inner templating [30], supramolecular assembly templating [31], anodic oxidation of a titanium sheet [32], and hydrothermal NaOH (aq.) treatment [33,34]. Among these methods, the hydrothermal method for the synthesis of TiO_2 nanotubes, first proposed by Kasuga et al. [33,34], has been widely exploited for low-dimensional nanostructures [35–37]. The hydrothermal method is a straightforward synthesis that is cost effective and environmentally innocuous [38–41]. Furthermore, this technique can also be applied to the preparation of a wide range of low-dimensional TiO_2 nanostructures, such as nanoparticles [42], nanowires [43], nanofibers [38,39,41] and nanoribbons [43]. Ilmenite ($FeTiO_3$) is a natural source of low titanium content TiO_2 (usually approximately 50–60%) [44,45]. In our previous work, nanofibers were prepared by a simple hydrothermal method from a leucoxene mineral [41].

In this work, the direct synthesis of nanofibers from an ilmenite mineral is first reported. The nanofibers are prepared by the simple hydrothermal method using a low-cost ilmenite mineral as the starting material. Characterization of the prepared nanofibers is also reported.

---

*Corresponding author. Tel.: +66 2549 3480; fax: +66 2549 3483.
E-mail address: sorapongp@yahoo.com (S. Pavasupree).

0272-8842/$ - see front matter © 2012 Elsevier Ltd and Techna Group S.r.l. All rights reserved.
http://dx.doi.org/10.1016/j.ceramint.2012.09.008

2. Experimental

2.1. Synthesis

Titanate nanofibers are synthesized by the hydrothermal method using a natural ilmenite mineral (Sakorn Minerals Co., Ltd., Thailand) as the starting material. These materials are made from 5 g of the black granules of ilmenite mineral (used without purification) are placed in a Teflon-lined stainless steel autoclave. To the autoclave was then added 200 mL of 10 M NaOH (aq.), followed by heating at 120 °C for 72 h with stirring. This process resulted in the formation of solid nanowires and long nanofibers [41]. After the autoclave was allowed to cool to room temperature, the resulting product was washed several times with an HCl (aq.) solution and then several times with distilled water, followed by drying with hot air. The experimental procedure is schematically shown in Fig. 1.

2.2. Characterization

The chemical compositions of the as-synthesized samples are analyzed by X-ray fluorescence (XRF, Philips, PW-2404, 4 kW). The phase and crystallinity of the samples were characterized by X-ray diffraction (XRD, X'Pert PRO MPD model pw 3040/60, PANalytical) with Cu $K\alpha$ ($\lambda=0.154$ nm) irradiation at a scan rate of 0.02° $2\theta\ s^{-1}$ and a 2θ range of 10–90°. The microstructure of the as-synthesized product was analyzed by scanning electron microscopy (SEM, JEM-6510, JEOL), with accelerating voltages of 5–20 kV and transmission electron microscopy (TEM, JEOL JEM-2010 Electron Microscope). The distribution of the sizes of the nanofiber diameters was analyzed by SEM. Nitrogen adsorption measurements (Quantachrome Instruments, Autosorb-1) are used to determine the Brunauer–Emmett–Teller (BET) specific surface area.

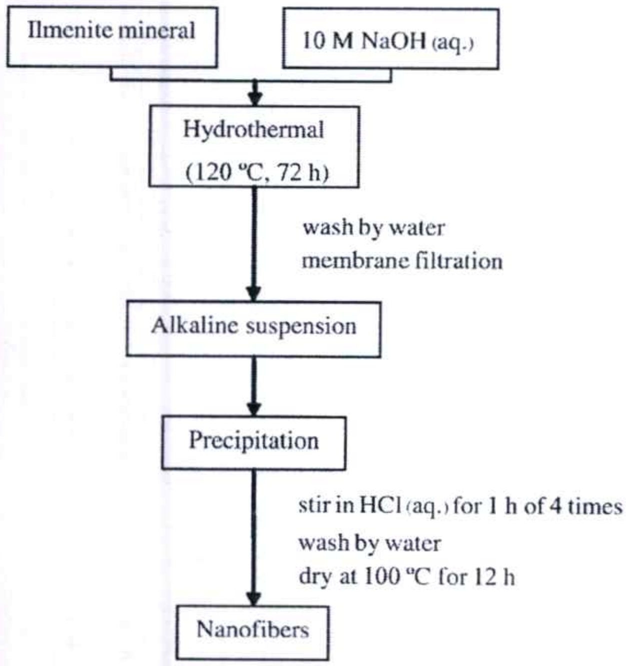

Fig. 1. Schematic representation of the experimental procedure.

3. Results and discussion

The as-synthesized sample was brown, whereas the starting ilmenite mineral was black (Fig. 2). This result

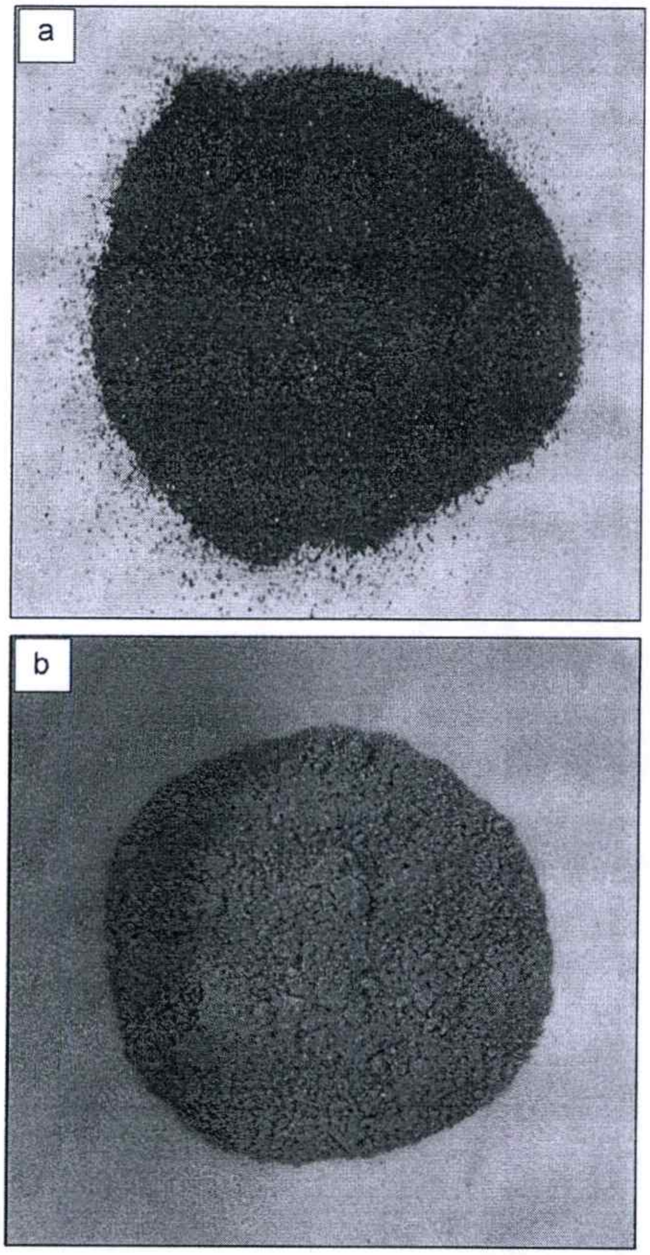

Fig. 2. Powders of (a) the starting ilmenite mineral and (b) the as-synthesized sample. (For interpretation of the references to color in this figure, the reader is referred to the web version of this article.)

Table 1
Chemical composition of the ilmenite mineral and an as-synthesized sample.

Oxide	Ilmenite mineral (wt%)	As-synthesized sample (wt%)
TiO_2	66.99	76.21
Fe_2O_3	24.01	21.80
Al_2O_3	3.38	0.12
SiO_2	2.11	0.30
MnO	0.82	0.68
ThO_2	0.64	0.01
ZrO_2	0.62	0.12
MgO	0.27	0.09
Cr_2O_3	0.26	< 0.01
P_2O_5	0.25	< 0.01
SO_3	0.15	0.05
Y_2O_3	0.09	–
ZnO	0.21	< 0.01
Nb_2O_5	0.24	0.15
CaO	0.16	0.08

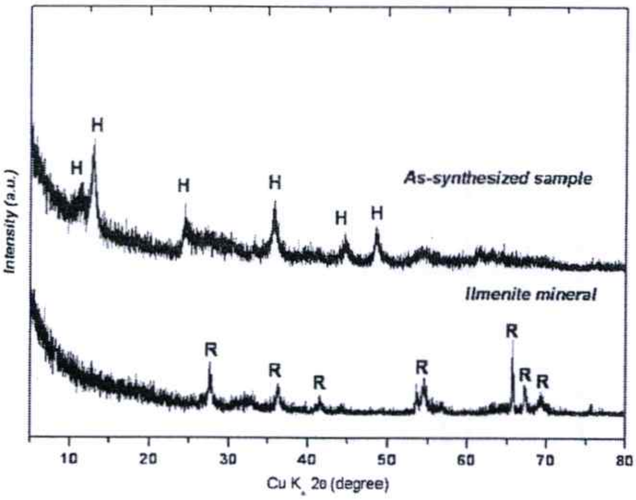

Fig. 3. XRD patterns of the starting ilmenite mineral and the as-synthesized sample, H = hydrogen titanate and R = rutile TiO_2.

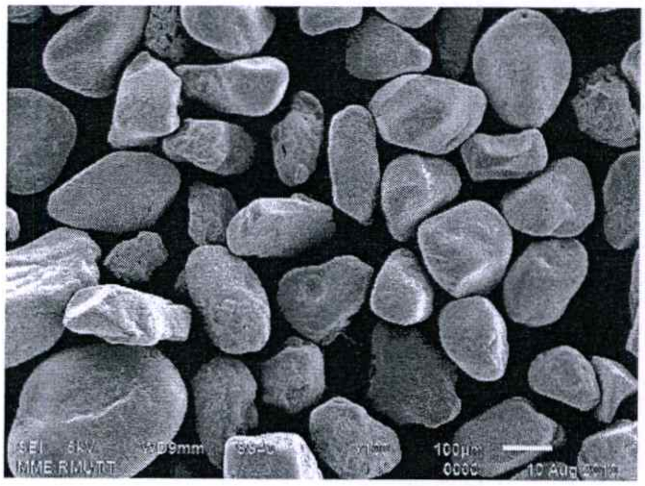

Fig. 4. SEM image of the starting ilmenite mineral.

indicates that a large portion of Fe impurities were removed by the NaOH (aq.) hydrothermal treatment and the neutralization/washing processes [38]. The chemical compositions of the ilmenite mineral and of the as-synthesized samples found using X-ray fluorescence are shown in Table 1. During the hydrothermal process, the quantities of impurities, such as Fe_2O_3, Al_2O_3, SiO_2, and MnO, decreased while the TiO_2 content increased from 66.99 to 76.21 wt% This may be due to higher solubility of the impurities in the NaOH and HCl aqueous solutions during the preparation process [46,47]. The doping of Fe^{3+} in the nanofiber matrix leads to a significant red shift in the optical response toward the visible spectrum caused by a reduction in the band gap energy [48], resulting in the brown-color of the as-synthesized samples. The nanofibers doped with Fe^{3+} could be an alternative, economically efficient material used as a photocatalyst in hydrogen production, dye-sensitized solar cells and the decomposition of organic dyes.

The XRD patterns of the starting ilmenite mineral and the as-synthesized sample are shown in Fig. 3. The crystalline structure of the starting ilmenite mineral appears to be of the rutile phase, while the crystalline structure of the as synthesized nanofibers demonstrated a layered titanate $H_2Ti_xO_{2x+1}$ structure, most likely trititanate ($H_2Ti_3O_7$), indicating the existence of hydrogen in the prepared nanofibers [38–41]. No diffraction peaks of other impurities (such as starting rutile and NaCl) are observed. This result is due to the reduction of the Na content in the nanofibers from repeated HCl leaching and water washes [36,49]. However, when compared with titanate nanotubes, the nanofibers contain more residual Na ions under the same ion exchanging conditions because of the geometry of the nanofibers, i.e., their solid and thicker structure. In addition, alkali-metal hexatitanates ($A_2Ti_6O_{13}$, A = Na, K, and Rb) tend to form stable solid fibrous structures that do not leach out easily during aqueous HCl treatments at room temperature [38]. An SEM image of the starting ilmenite mineral is shown in Fig. 4; this illustrates the granular structure of the material, with grain sizes of 150–200 µm. After the hydrothermal treatment, the as-synthesized sample exhibited a uniform fiber-like morphology (Fig. 5). To confirm the formation of nanofibers, TEM analysis was used, and a representative image can be seen in Fig. 6. From the TEM images, it can be observed that the as-synthesized nanofibers are solid rather than hollow.

The nanofibers tend to form bundles; thus some of the nanofibers look thicker than others. The prepared nanofibers had lengths from 2 to 7 µm with diameters of 20–90 nm (Fig. 6). The nanofiber formation can be explained by the coarseness of the ilmenite granules, which retarded their dissolution in the NaOH solution, suppressing nucleation and assisting preferential crystal growth along the 010 direction of the trititanate [38]. The diameters (Fig. 7) of the as-prepared nanofibers were found to

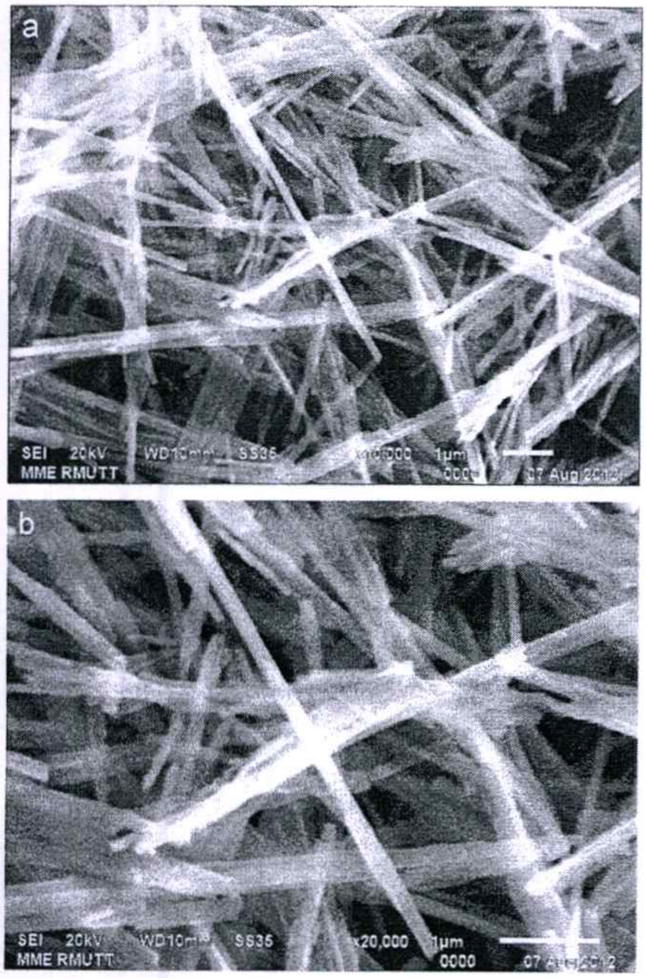

Fig. 5. SEM images of the as-synthesized nanofibers at (a) 10,000 × and (b) 20,000 × magnification.

be smaller than the diameters of nanofibers prepared by electrospinning [4,50–52], anodic oxidation [32] or template assisted methods [28].

The BET specific surface area of the as-synthesized nanofibers was approximately 49 m^2/g, while the BET surface area of the starting ilmenite mineral was very low at approximately 0 m^2/g (Table 2). The BET specific surface area of the starting ilmenite mineral was similar to that of leucoxene [41] and rutile minerals [38,39]. The increase in the BET specific surface area is a result of the starting ilmenite mineral being completely converted into hydrogen titanate nanofibers during the hydrothermal process. Although the nanotube structure is attractive due to its high surface area, titanate nanotubes with free-alkali ions are usually unstable at high temperatures (at ~500 °C) and convert into anatase particles [36,39,53,54]. To maintain 1-D nanostructures at higher temperature (typically at 500–800 °C), solid nanowires or nanofibers forms should be more favorable [36,39,53,54]. The absorption spectra of the as-synthesized nanofibers and commercially available nanostructured TiO_2 (ST-01) are illustrated in Fig. 8. The absorption spectra of the as-synthesized nanofibers exhibit a significant enhancement in the wavelength region of 300–500 nm due to the natural Fe-doping characteristic of the ilmenite mineral. Further studies on the synthesis and characterization of this material are currently being performed.

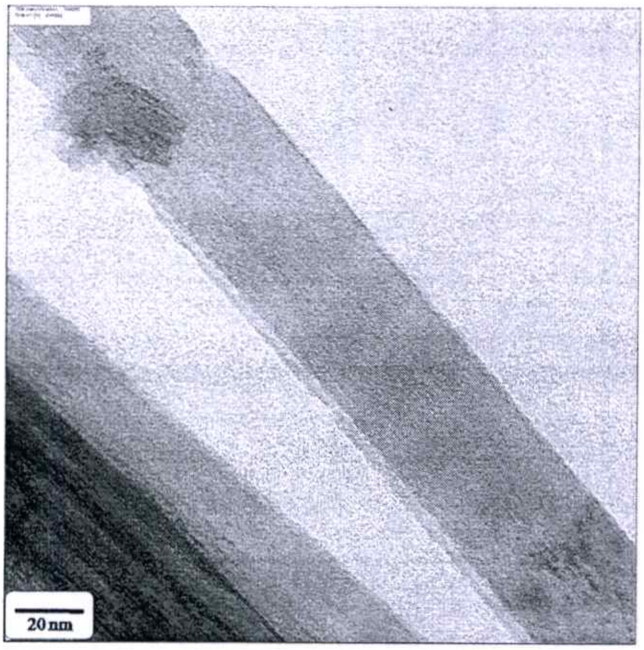

Fig. 6. TEM image of the as-synthesized nanofibers at 100,000 × magnification.

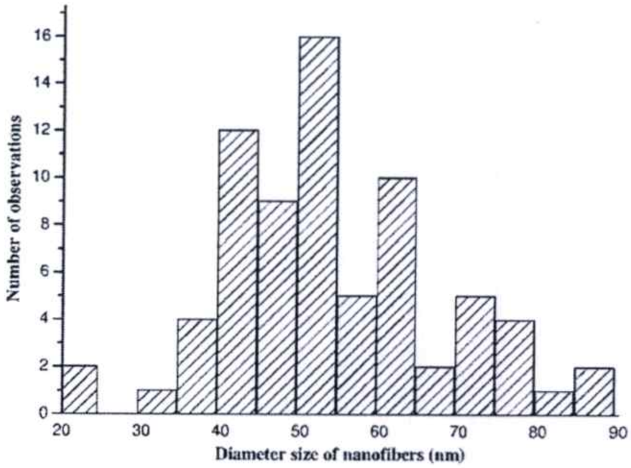

Fig. 7. Diameter distributions of the prepared nanofibers.

4. Conclusion

In summary, titanate nanofibers are synthesized by a hydrothermal method using a low-cost ilmenite mineral as the starting material. After the hydrothermal synthesis, solid nanofibers showed an increased TiO_2 content were obtained. Analysis of the crystalline structure of the

Table 2
The BET specific surface area of the starting ilmenite mineral and the as-synthesized nanofibers.

Samples	Bet surface area (m^2/g)
Starting ilmenite mineral	0
As-synthesized	~49

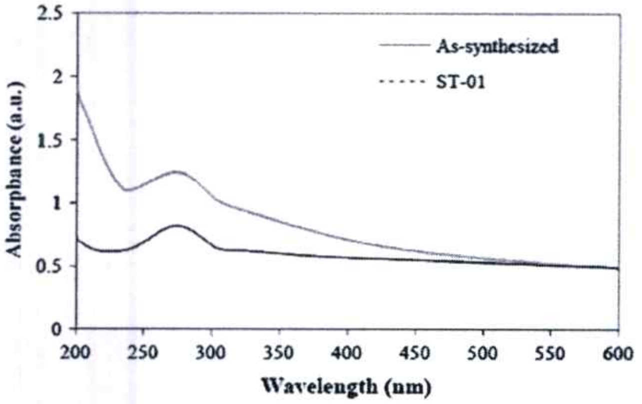

Fig. 8. UV–vis absorbance spectra of the as-synthesized nanofibers and commercial grade TiO_2 nanoparticles (ST-01).

as-synthesized nanofibers demonstrated a layered titanate $H_2Ti_xO_{2x+1}$ structure, most likely in the form of trititanate ($H_2Ti_3O_7$). The prepared nanofibers showed lengths of 2–7 μm with diameters of approximately 20–90 nm and a corresponding BET specific surface area of approximately 49 m^2/g. These Fe^{3+} doped nanofibers may show utility as a novel photocatalyst material for hydrogen production, dye-sensitized solar cells and the decomposition of organic dyes.

Acknowledgments

This work has been supported by the National Nanotechnology Center (NANOTEC) (P-10-1079), NSTDA, Ministry of Science and Technology, Thailand and through the NANOTEC Program of the Centers of Excellence Network. The authors would like to thank Sakorn Minerals Co., Ltd., Thailand, the College of Nanotechnology, King Mongkut's Institute of Technology Ladkrabang (KMITL), and the Nanotechnology for Textile and Polymer Research Group (NanoTeP) of the Faculty of Engineering, Rajamangala University of Technology Thanyaburi (RMUTT), Thailand.

References

[1] A. Testino, I.R. Bellobono, V. Buscaglia, C. Canevali, M. D'Arienzo, S. Polizzi, R. Scotti, F. Morazzoni, Optimizing the photocatalytic properties of hydrothermal TiO_2 by the control of phase composition and particle morphology. A systematic approach, Journal of the American Chemical Society 129 (2007) 3564–3575.

[2] R. Carbone, I. Marangi, A. Zanardi, L. Giorgetti, E. Chierici, G. Berlanda, A. Podestà, F. Fiorentini, Gero Bongiorno, P. Piseri, P.G. Pelicci, P. Milani, Biocompatibility of cluster-assembled nanostructured TiO_2 with primary and cancer cells, Biomaterials 27 (2006) 3221–3229.

[3] G.C. Smith, L. Chamberlain, L. Faxius, G.W. Johnston, S. Jin, L.M. Bjursten, Soft tissue response to titanium dioxide nanotube modified implants, Acta Biomaterialia 7 (2011) 3209–3215.

[4] W. Nuansing, S. Ninmuang, W. Jarernboon, S. Maensiri, S. Seraphin, Structural characterization and morphology of electrospun TiO_2 nanofibers, Materials Science and Engineering B 131 (2006) 147–155.

[5] C.N.R. Rao, M. Nath, Inorganic nanotubes, Dalton Transactions 1 (2003) 1–24.

[6] K. Funakoshi, T. Nonami, Influences of saturation ratios on crystallization of anatase titanium dioxide by a titanium alkoxide hydrolysis, Ceramics International 34 (2008) 1637–1642.

[7] R. Nirmala, H.Y. Kim, R. Navamathavan, C Yi, J.J. Won, K. Jeon, A. Yousef, R. Afeesh, M. El-Newehy, Photocatalytic activities of electrospun tin oxide doped titanium dioxide nanofibers, Ceramics International 38 (2012) 4533–4540.

[8] J. Kaewsaenee, P. Visal-athaphand, P. Supaphol, V. Pavarajarn, Fabrication and characterization of neat and aluminium-doped titanium (IV) oxide fibers prepared by combined sol–gel and electrospinning techniques, Ceramics International 36 (2010) 2055–2061.

[9] J. Garcia-Martinez, Nanotechnology for the Energy Challenge, Wiley-VCH Verlag GmbH & Co. KGaA, Weinheim, 2009.

[10] R.J. Wu, Y.L. Sun, C.C. Lin, H.W. Chen, M. Chavali, Composite of TiO_2 nanowires and nafion as humidity sensor material, Sensors and Actuators B 115 (2006) 198–204.

[11] J.M. Wu, H.C. Shih, W.T. Wu, Formation and photoluminescence of single-crystalline rutile TiO_2 nanowires synthesized by thermal evaporation, Nanotechnology 17 (2006) 105–109.

[12] A.R. Armstrong, G. Armstrong, J. Canales, P.G. Bruce, TiO_2-B nanowires, Angewandte Chemie—International Edition 43 (2004) 2286–2288.

[13] A.R. Armstrong, G. Armstrong, J. Canales, R. Garcia, P.G. Bruce, Lithium-ion intercalation into TiO_2-B nanowires, Advanced Materials 17 (2005) 862–865.

[14] P.G. Bruce, Energy materials, Solid State Sciences 7 (2005) 1456–1463.

[15] S.H Lim, J.Z. Luo, Z.Y. Zhong, W. Ji, J.Y. Lin, Room-temperature hydrogen uptake by TiO_2 nanotubes, Inorganic Chemistry 44 (2005) 4124–4126.

[16] D.V. Bavykin, A.A. Lapkin, P.K. Plucinski, J.M. Friedrich, F.C. Walsh, Reversible storage of molecular hydrogen by sorption into multilayered TiO_2 nanotubes, Journal of Physical Chemistry B 109 (2005) 19422–19427.

[17] S. Uchida, R. Chiba, M. Tomiha, N. Masaki, M. Shirai, Application of titania nanotubes to a dye-sensitized solar cells, Electrochemistry 70 (2002) 418–420.

[18] M.Y. Song, D.K. Kim, K.J. Ihn, S.M. Jo, D.Y. Kim, Electrospun TiO_2 electrodes for dye-sensitized solar cells, Nanotechnology 15 (2004) 1861–1865.

[19] Y. Suzuki, S. Ngamsinlapasathian, R. Yoshida, S. Yoshikawa, Partially nanowire-structured TiO_2 electrode for dye-sensitized solar cells, Central European Journal of Chemistry 4 (2006) 476–488.

[20] M. Grätzel, Photoelectrochemical cells, Nature 414 (2001) 338–344.

[21] A. Fujishima, T.N. Rao, D.A. Tryk, Titanium dioxide photocatalysis, Journal of Photochemistry and Photobiology C: Photochemistry Reviews 1 (2000) 1–21.

[22] S. Ngamsinlapasathian, T. Sreethawong, Y. Suzuki, S. Yoshikawa, Single- and double-layered mesoporous TiO_2/P25 TiO_2 electrode for dye-sensitized solar cell, Solar Energy Materials and Solar Cells 86 (2005) 269–282.

[23] S. Pavasupree, Y. Suzuki, S. Pivsa-Art, S. Yoshikawa, Preparation and characterization of mesoporous MO_2 (M = Ti, Ce, Zr, and Hf) nanopowders by a modified sol–gel method, Ceramics International 31 (2005) 959–963.

[24] S. Pavasupree, Y. Suzuki, S. Pivsa-Art, S. Yoshikawa, Preparation and characterization of mesoporous TiO_2–CeO_2 nanopowders

respond to visible wavelength, Journal of Solid State Chemistry 178 (2005) 128–134.
[25] T. Sreethawong, Y. Suzuki, S. Yoshikawa, Synthesis, characterization, and photocatalytic activity for hydrogen evolution of nanocrystalline mesoporous titania prepared by surfactant-assisted templating sol–gel process, Journal of Solid State Chemistry 178 (2005) 329–338.
[26] D. Li, Y.N. Xia, Fabrication of titania nanofibers by electrospinning, Nano Letters 3 (2003) 555–560.
[27] S. Yoo, S.A. Akbar, K.H. Sandhage, Oriented single crystal titania nanofibers via nanocarving with hydrogen-bearing gas, Advanced Materials 16 (2004) 260–264.
[28] P. Hoyer, Formation of titanium dioxide nanotube array, Langmuir 12 (1996) 1411–1413.
[29] H. Imai, Y. Takei, K. Shimizu, M. Matsuda, H. Hirashima, Direct preparation of anatase TiO_2 nanotubes in porous alumina membranes, Journal of Materials Chemistry 9 (1999) 2971–2972.
[30] J. Sun, L. Gao, Q.H. Zhang, TiO_2 tubes synthesized by using ammonium sulfate and carbon nanotubes as templates, Journal of Materials Science Letters 22 (2003) 339–341.
[31] S. Kobayashi, K. Hanabusa, N. Hamasaki, M. Kimura, H. Shirai, S. Shinkai, Preparation of TiO_2 hollow-fibers using supramolecular assemblies, Chemistry of Materials 12 (2000) 1523–1525.
[32] D. Gong, C.A. Grimes, O.K. Varghese, W.C. Hu, R.S. Singh, Z. Chen, E.C. Dickey, Titanium oxide nanotube arrays prepared by anodic oxidation, Journal of Materials Research 16 (2001) 3331–3334.
[33] T. Kasuga, M. Hiramatsu, A. Hoson, T. Sekino, K. Niihara, Formation of titanium oxide nanotube, Langmuir 14 (1998) 3160–3163.
[34] T. Kasuga, M. Hiramatsu, A. Hoson, T. Sekino, K. Niihara, Titania nanotubes prepared by chemical processing, Advanced Materials 11 (1999) 1307–1311.
[35] G.H. Du, Q. Chen, R.C. Che, Z.Y. Yuan, L.M. Peng, Preparation and structure analysis of titanium oxide nanotubes, Applied Physics Letters 79 (2001) 3702–3704.
[36] Y. Suzuki, S. Yoshikawa, Synthesis and thermal analyses of TiO_2-derived nanotubes prepared by the hydrothermal method, Journal of Materials Research 19 (2004) 982–985.
[37] Y. Suzuki, S. Sakulkhaemaruethai, R. Yoshida, S. Yoshikawa, Heat treatment effect on the structure of TiO_2-derived nanotubes prepared by hydrothermal method, Ceramic Transactions 159 (2005) 185–192.
[38] Y. Suzuki, S. Pavasupree, S. Yoshikawa, R. Kawahata, Natural rutile-derived titanate nanofibers prepared by direct hydrothermal processing, Journal of Materials Research 20 (2005) 1063–1070.
[39] S. Pavasupree, Y. Suzuki, S. Yoshikawa, R. Kawahata, Synthesis of titanate, TiO_2 (B), and anatase TiO_2 nanofibers from natural rutile sand, Journal of Solid State Chemistry 178 (2005) 3110–3116.
[40] J. Jitputti, Y. Suzuki, S. Yoshikawa, Synthesis of TiO_2 nanowires and their photocatalytic activity for hydrogen evolution, Catalysis Communications 9 (2008) 1265–1271.
[41] S. Pavasupree, N. Laosiripojana, S. Chuangchote, T. Sagawa, Fabrication and utilization of titania nanofibers from natural leucoxene mineral in photovoltaic applications, Japanese Journal of Applied Physics 50 (2011) 01BJ16.
[42] S. Pavasupree, J. Jitputti, S. Ngamsinlapasathian, S. Yoshikawa, Hydrothermal synthesis, characterization, photocatalytic activity and dye-sensitized solar cell performance of mesoporous anatase TiO_2 nanopowders, Materials Research Bulletin 43 (2008) 149–157.
[43] Z.Y. Yuan, B.L. Su, Titanium oxide nanotubes, nanofiber and nanowires, Colloids and Surfaces A 241 (2004) 173–183.
[44] S. Samal, B.K. Mohapatra, P.S. Mukherjee, S.K. Chatterjee, Integrated XRD, EPMA and XRF study of ilmenite and titania slag used in pigment production, Journal of Alloys and Compounds 474 (2009) 484–489.
[45] J.N. Nian, H. Teng, Hydrothermal synthesis of single-crystalline anatase TiO_2 nanorods with nanotubes as the precursor, Journal of Physical Chemistry B 110 (2006) 4139–4198.
[46] K. Ishikawa, T. Yoshioka, T. Sato, A. Okuwaki, Solubility of hematite in LiOH, NaOH and KOH solutions, Hydrometallurgy 45 (1997) 129–135.
[47] I.I. Diakonov, J. Schott, F. Martin, J.C. Harrichourry, J. Escalier, Geochim, iron(III) solubility and speciation in aqueous solutions. Experimental study and modelling: Part 1. Hematite solubility from 60 to 300 °C in NaOH–NaCl solutions and thermodynamic properties of $Fe(OH)_4^-$(aq), Geochimica et Cosmochimica Acta 63 (1999) 2247–2261.
[48] M.A. Khan, S.I. Woo, O.-B. Yang, Hydrothermally stabilized Fe(III) doped titania active under visible light for water splitting reaction, International Journal of Hydrogen Energy 33 (2008) 5345–5351.
[49] A. Nakahira, T. Kubo, C. Numako, Formation mechanism of TiO_2-derived titanate nanotubes prepared by the hydrothermal process, Inorganic Chemistry 49 (2010) 5845–5852.
[50] S.J. Lee, N.I. Cho, D.Y. Lee, Effect of collector grounding on directionality of electrospun titania fibers, Journal of the European Ceramic Society 27 (2007) 3651–3654.
[51] Z. Zhang, C. Shao, L. Zhang, X. Li, Y. Liu, Electrospun nanofibers of V-doped TiO_2 with high photocatalytic activity, Journal of Colloid and Interface Science 351 (2010) 57–62.
[52] H. Kim, Y. Choi, N. Kanuka, H. Kinoshita, T. Nishiyama, T. Usami, Preparation of Pt-loaded TiO_2 nanofibers by electrospinning and their application for WGS reactions, Applied Catalysis 352 (2009) 265–270.
[53] R. Yoshida, Y. Suzuki, S. Yoshikawa, Effects of synthetic conditions and heat-treatment on the structure of partially ion-exchanged titanate nanotubes, Materials Chemistry and Physics 91 (2004) 409–416.
[54] R. Yoshida, Y. Suzuki, S. Yoshikawa, Synthesis of TiO_2(B) nanowires and TiO_2 anatase nanowires by hydrothermal and post-heat treatments, Journal of Solid State Chemistry 178 (2005) 2179–2185.

Materials Research Bulletin 48 (2013) 3211–3217

Contents lists available at SciVerse ScienceDirect

Materials Research Bulletin

journal homepage: www.elsevier.com/locate/matresbu

Effect of calcination temperature on structural and photocatalyst properties of nanofibers prepared from low-cost natural ilmenite mineral by simple hydrothermal method

Athapon Simpraditpan [a], Thanakorn Wirunmongkol [b], Sorapong Pavasupree [b,*], Wisanu Pecharapa [a,c]

[a] *College of Nanotechnology, King Mongkut's Institute of Technology Ladkrabang, Ladkrabang, Bangkok 10520, Thailand*

[b] *Department of Materials and Metallurgical Engineering, Faculty of Engineering, Rajamangala University of Technology Thanyaburi, Klong 6, Pathumthani 12110, Thailand*

[c] *Thailand and Center of Excellence in Physics (ThEP Center), Commission on Higher Education, 328 Si Ayutthaya Rd., Bangkok 10400, Thailand*

ARTICLE INFO

Article history:
Received 16 July 2012
Received in revised form 24 March 2013
Accepted 29 April 2013
Available online 27 May 2013

Keywords:
A. Composites
A. Nanostructures
B. Chemical synthesis
D. Catalytic properties

ABSTRACT

Titanate nanofibers were synthesized via the hydrothermal method (120 °C for 72 h) using natural ilmenite mineral ($FeTiO_3$) as the starting material. The samples were characterized by X-ray diffraction (XRD), X-ray fluorescent (XRF), scanning electron microscopy (SEM), transmission electron microscopy (TEM), and Brunauer–Emmett–Teller (BET) for specific surface area. The nanofibers were 20–90 nm in diameter and 2–7 μm in length. The as-synthesized nanofibers calcined at 300–400 °C showed TiO_2 (B) whereas the nanofibers calcined at 500 °C revealed a mixture of two phases of TiO_2 (B) and anatase. The nanofibers calcined at high temperature of 600–1000 °C showed a mixture of tri-crystalline of anatase, rutile, and Fe_2O_3. The rutile phase increased with increasing calcination temperature. The nanofibers calcined at 300–700 °C maintained their structure while the morphology of the nanofibers calcined at 800–1000 °C transformed into submicron rod-like structure. This increase of calcination temperature led to the phase transformation from thermodynamically metastable anatase to the most stable form of rutile phase. The crystallite size of prepared samples increased with increasing calcination temperature. Interestingly, with increasing calcination temperature, the absorption edge of the prepared samples shows an obvious shift to visible light region due to the change of crystallite phase and increased crystallite size. Therefore, the band gap energy of the prepared samples became narrower with increasing calcination temperature. Furthermore, the photocatalytic activity of the nanofibers calcined at 400 °C for 2 h was found to be not merely higher than those of the commercially available TiO_2 nanoparticles powders (P-25, JRC-01, and JRC-03) but also the highest of all the samples in this study.

1. Introduction

Over the past three decades, nanostructured materials derived from TiO_2 have been regarded as the most suitable semiconductor in such applications as photocatalyst of water splitting [1–5] and degradation of organic contaminants in water treatment [6–13]. The rate of the photocatalytic reaction is controllable at various steps in the process: light absorption, transport of photogenerated charges (electron (e^-) and hole (h^+)) onto the photocatalyst surface, and recombination of e^- and h^+ on the photocatalyst surface [14]. Therefore, the crystalline structure and surface morphology of a photocatalyst, such as the particle shape and size, are significant parameters in photocatalytic reactions [15–17]. In addition, TiO_2 derived materials possess a number of good points, such as high photovoltaic effect, medium dielectric permittivity, high chemical stability, and low toxicity [18]. Thus, TiO_2 derived materials were introduced into a number of applications, e.g., catalysts [19], gas sensors [20], and dye-sensitized solar cells [21,22].

TiO_2 exists in various crystalline structures, i.e., anatase (band gap energy 3.2 eV), rutile (band gap energy 3.0 eV), brookite, and monoclinic of TiO_2 (B) [18,23]. Several methods were employed in the preparation of the TiO_2-derived nanomaterials, examples of which were inert gas condensation [24] sol–gel method [25,26] electrospinning [27,28], and hydrothermal [29–38]. In our previous works, the hydrothermal method was selected to synthesize nanofibers from leucoxene mineral because it was simple, low-cost, and environmentally friendly [38,39].

The nanofibers in this study were prepared by the simple hydrothermal method using inexpensive natural ilmenite mineral (~0.5–0.7 dollar/kg) as the starting material. The calcined nanofibers were treated with the calcination process. The chemical composition, crystalline structures, morphology, and BET specific

---

[*] Corresponding author. Tel.: +66 2 549 3480; fax: +66 2 549 3483.
E-mail addresses: sorapongp@yahoo.com, sorapong.p@en.rmutt.ac.th (S. Pavasupree).

0025-5408/$ – see front matter © 2013 Elsevier Ltd. All rights reserved.
http://dx.doi.org/10.1016/j.materresbull.2013.04.083

surface areas of the prepared samples and calcined nanofibers were investigated and reported. Besides, the effects of calcination temperature on structural and photocatalyst properties of the nanofibers prepared from natural ilmenite mineral by the hydrothermal method were discussed.

2. Experimental procedure

2.1. Preparation of nanofibers

The nanofibers were prepared by the hydrothermal method in which natural ilmenite mineral (Sakorn Minerals Co., Ltd., Thailand) was used as the starting material. 5 g of ilmenite mineral and 10 M NaOH aqueous solution (200 ml) were placed inside a Teflon-lined stainless autoclave. The autoclave was heated and stirred at 120 °C for 72 h. Afterward, the mixture was cooled down to room temperature and was washed with 0.1 M HCl aqueous solution and DI water a number of times. Then, the precipitated sample was dried at 100 °C for 12 h.

2.2. Characterization

The chemical composition of the ilmenite mineral and that of the as-synthesized sample were evaluated by X-ray fluorescence (XRF, Philips, PW-2404, 4 kW). The microstructures of the ilmenite mineral, the as-synthesized nanofibers and the calcined nanofibers were investigated by scanning electron microscopy (SEM; JEOL, JEM-6510) and transmission electron microscopy (TEM; JEOL, JEM-2010). The X-ray diffraction (XRD) patterns of the as-synthesized samples were obtained with PANalytical diffractometer (X'Pert PRO MPD model pw 3040/60) using Cu Kα ($\lambda = 0.154$ nm) irradiation at a scan rate (2θ) of $0.02° \text{ s}^{-1}$ and a 2θ range of 5–80° operated at 40 kV and 30 mA. The BET specific surface areas of the samples were measured using nitrogen adsorption (Quantachrome Instruments, Autosorb-1).

2.3. Photocatalytic activity measurement

The photocatalytic activity was measured through the formation rate of I_3^- due to the oxidation photoreaction of I^- to I_2 in excess I^- conditions [15]. A reaction system was set up by adding 50 mg of a sample powder into 10 ml of 0.2 M of potassium iodide (KI) aqueous solution; the mixture was then stirred and irradiated at room temperature with UV light with maximum emission of approximately 365 nm. Following the irradiation for 15, 30, 45, and 60 min, the suspension was withdrawn and centrifuged. After the clear supernatant was diluted 10 times, the concentration of liberated I_3^- ions was determined by the absorbance at 288 nm using an UV-Vis spectrophotometer (Shimadzu UV 2450). The molar extinction coefficient was found to be 4.0×10^4 (cm mol/l)$^{-1}$; no I_3^- formation was observed when the experiments were performed in the dark or in the absence of the TiO_2 samples. Three different commercially available TiO_2 nanoparticle powders, i.e., P-25 (Nippon Aerosil Co., Ltd., Japan), JRC-01, and JRC-03 (The Catalysis Society of Japan) were tested for use as reference.

3. Results and discussion

3.1. As-synthesized nanofibers

After the reaction in the hydrothermal process, the as-synthesized nanopowders become brown (Fig. 2(b)) while the starting ilmenite mineral is black (Fig. 2(a)). The findings indicated that a large fraction of Fe impurities could be eliminated by the NaOH (aq.) hydrothermal treatment and neutralization/washing processes [34]. The chemical composition of ilmenite mineral and that of the as-synthesized sample were evaluated by XRF. Following the hydrothermal process, the percentage of impurities (Fe_2O_3, Al_2O_3, SiO_2, MnO) decreased while that of TiO_2 increased from 66.99 to 76.21 wt%. The results were consistent with those of leucoxene mineral and nanofibers from leucoxene mineral in our previous works [38,39], but the as-synthesized nanofibers showed a higher percentage of Fe_2O_3 than the nanofibers prepared from leucoxene mineral. The aforementioned could be due to solubility of the impurities in NaOH and HCl aqueous solutions during preparation process [14,15]. Recent studies indicated Fe doping significantly enhanced the optical response of visible light owing to the reduced band gap energy [16], probably contributing to the brown color of the as-synthesized sample in this research. The nanofibers doped with Fe could be an alternative material with high potential for use as photocatalyst in hydrogen generation, dye-sensitized solar cell (DSSC), and decomposition of organic dyes.

Fig. 1(a) shows the XRD patterns of the prepared samples compared with the starting ilmenite mineral. The XRD pattern of the starting ilmenite mineral emerged in rutile phase, while the structure of the as-synthesized nanofibers revealed the hydrogen

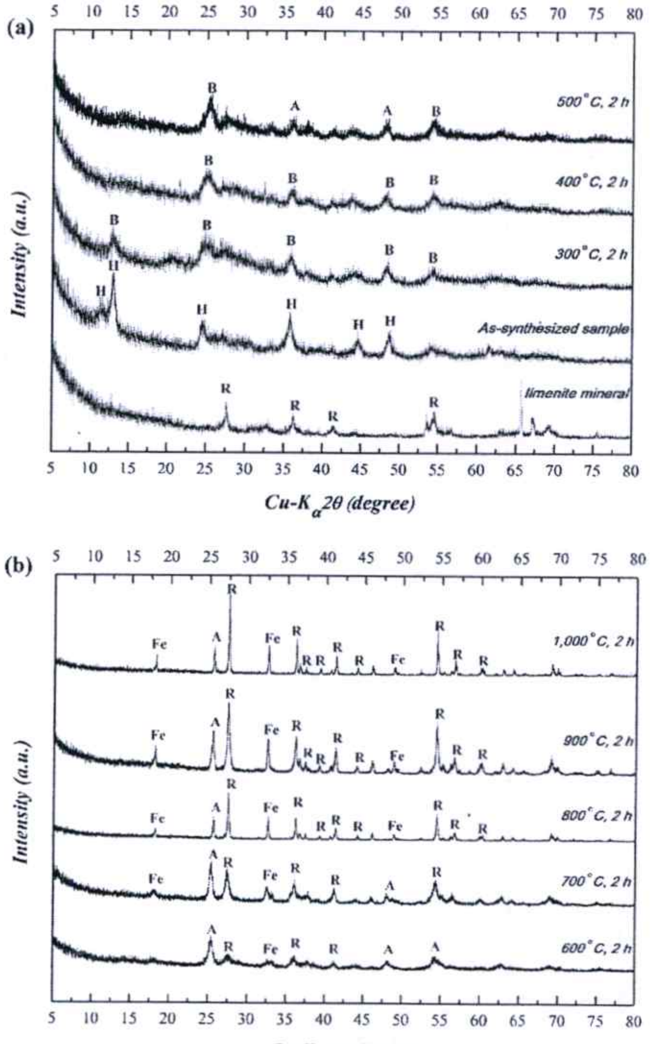

Fig. 1. XRD patterns of the starting natural ilmenite mineral, the as-synthesized nanofibers, and the calcined nanofibers for 2 h at (a) 100–500 °C and (b) 600–1000 °C; A: anatase TiO_2, B: TiO_2 (B), H: hydrogen titanate, and R: rutile TiO_2.

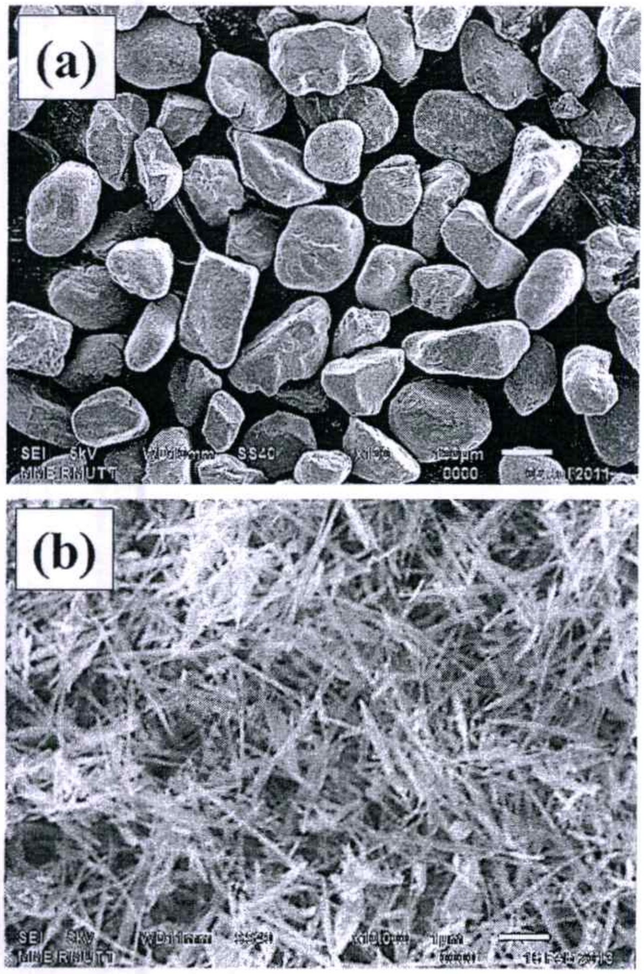

Fig. 2. SEM images of (a) the starting ilmenite mineral and (b) the as-synthesized nanofibers.

titanate $H_2Ti_xO_{2x+1}$, e.g., trititanate ($H_2Ti_3O_7$) [18,31]. The results were similar to those of leucoxene mineral and nanofibers from leucoxene mineral in our previous works [38,39]. The difference points between nanofibers using ilmenite mineral as the starting materials for this study and nanofibers using leucoxene mineral as the starting materials for previous work [38] were discussed. Interestingly, the chemical composition of nanofibers using leucoxene mineral as the starting materials consist of Fe_2O_3 similar to this study. However, nanofibers using leucoxene mineral as the starting materials showed less the percentage of Fe_2O_3 than nanofibers using ilmenite mineral as the starting materials that is 2.26% and 21.80%, respectively [38,40]. This difference may be result in the photocatalytic activity [41,42].

The diffraction peaks of other impurities, such as NaCl and rutile phase of the starting natural ilmenite mineral, were not observed. This was due to the fact that Na content in the nanofibers could be minimized by repeated ion-exchanging treatment with HCl leaching and water washing [34,36,43]. Nevertheless, compared with the titanate nanotubes, the nanofibers tended to contain more residual Na ions under the same ion-exchanging conditions due to the geometry of the nanofibers, i.e., more solid and thicker structure, and alkali-metal hexatitanates ($A_2Ti_6O_{13}$, A = Na, K, Rb) tended to be in the form of stable solid fibrous structure and was not easily removed with the aqueous HCl treatment at room temperature [34].

Fig. 2 shows the SEM images of the starting ilmenite mineral and as-synthesized sample. The starting ilmenite mineral is in granule form of 150–200 μm in diameter (Fig. 2(a)). The as-synthesized nanofibers possess the fiber-like morphology with the lengths and diameters of 2–7 μm and 20–90 nm, respectively (Fig. 2(b)). Furthermore, most of the nanofibers tend to stick together in bundles, thus causing some of the nanofibers to appear thicker than others. TEM experiment was conducted to prove that nanofibers were solid (not hollow). The TEM image of the as-synthesized nanofibers was illustrated in Fig. 3, which showed the as-synthesized sample to be solid (not hollow), indicating the structure of nanofiber.

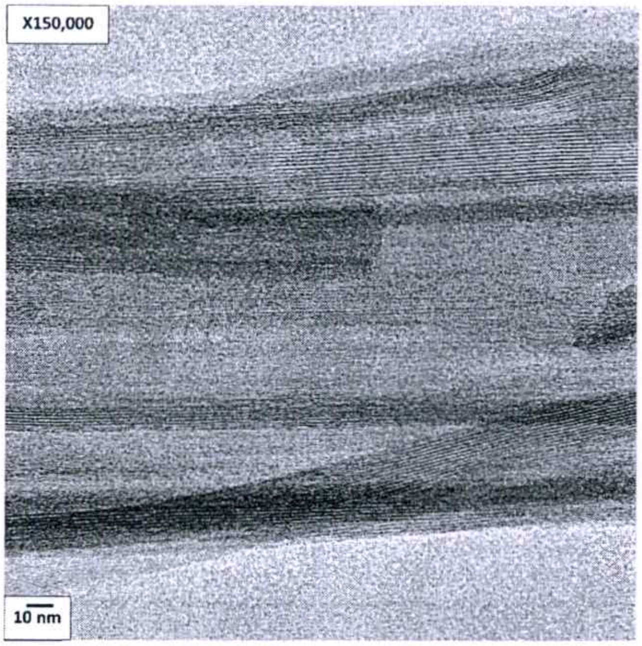

Fig. 3. TEM image of the as-synthesized nanofibers at 150,000× magnification.

Interestingly, the BET specific surface area of the as-synthesized nanofibers was about 50 m^2/g, while the BET specific surface area of the starting natural rutile sand was about 0 m^2/g. Increased surface areas are generally accomplished by the synthesis of small particles with high surface to volume ratios or by the manufacture of nanostructured materials from bulk substrates.

3.2. Nanofibers with calcination treatment (300–500 °C)

Fig. 1(a) also shows the XRD patterns of the prepared samples calcined for 2 h at 300, 400, and 500 °C. After calcination at the temperature range of 300–400 °C, the calcined samples demonstrated TiO_2 (B). The nanofibers were dehydrated and re-crystallized into the metastable form of TiO_2 (B) [5,33–38]. Moreover, the peak intensity corresponding to the TiO_2 (B) decreased as the calcination temperature increased. At 500 °C, the calcined nanofibers revealed a bi-crystalline mixture consisting of TiO_2 (B) and anatase TiO_2. Recent research studies found a bi-crystalline mixture consisting of TiO_2 (B) and anatase TiO_2 nanostructured not merely showed similar formation in the temperature ranges of 100–500 °C [37], 300–600 °C [44] or 400–600 °C [45] but promoted great H_2 evolution from neat ethanol as well [5,38,46].

Fig. 4 shows the SEM images of the as-obtained nanofibers calcined for 2 h at 300, 400, and 500 °C. From the SEM images, the nanofibers calcined for 2 h at 300–500 °C maintained their nanofiber morphology [31]. In many research studies, the nanotube structure was frequently investigated due to its high surface area; however, titanate nanotubes with free-alkali ions

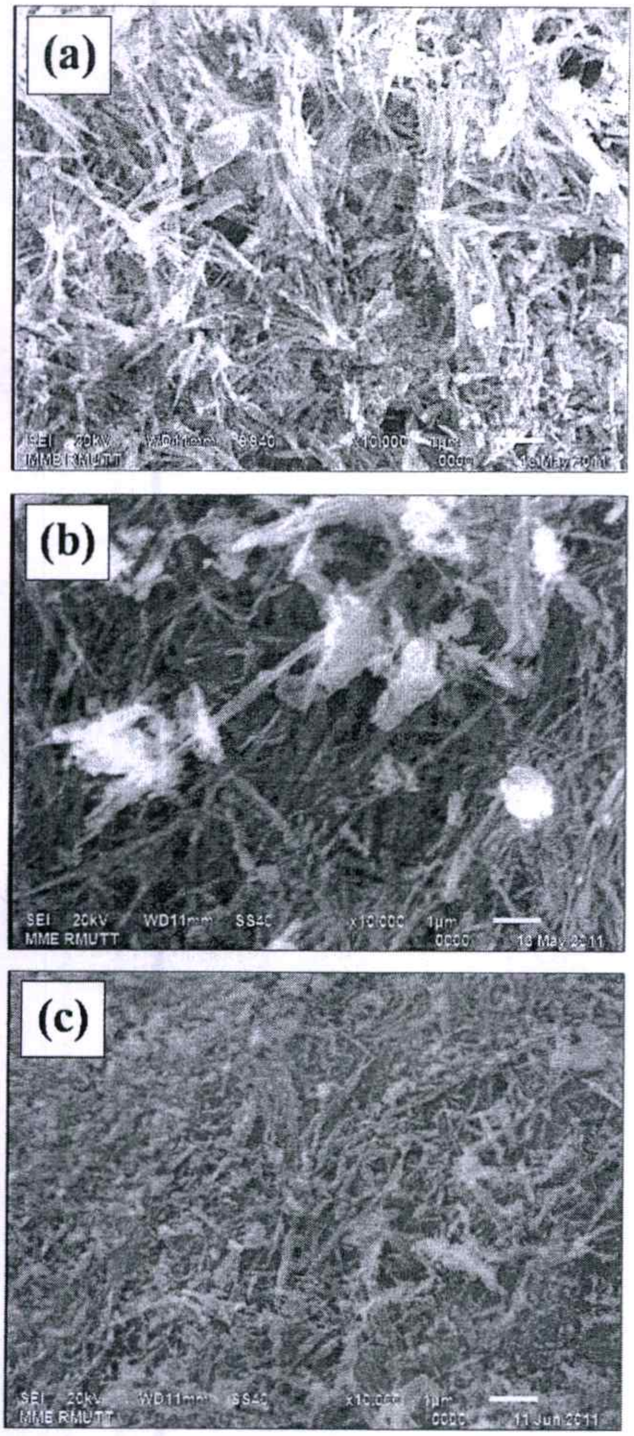

Fig. 4. SEM images of the calcined nanofibers for 2 h at (a) 300 °C, (b) 400 °C, and (c) 500 °C.

were typically unstable at high temperatures (at ~500 °C) and converted into anatase particles [33–35,37]. To maintain the 1-D nanostructure at higher temperatures (typically at 500–800 °C), solid nanowires or nanofibers are more preferable.

3.3. Nanofibers with calcination treatment (600–1000 °C)

The XRD patterns of the prepared samples calcined at 600, 700, 800, 900, and 1000 °C for 2 h are shown in Fig. 1(b). The prepared samples consisted of a mixture of anatase, rutile phase of TiO_2 [4,5], and Fe_2O_3. At 600–700 °C, the crystalline of anatase phase of TiO_2 became unstable, TiO_2 (B) disappeared, and the transformation from anatase phase TiO_2 to rutile phase TiO_2 began at this temperature range [30,47]. Consequently, the calcination temperature rose, increase in rutile phase TiO_2 was observed, especially at the 800–1000 °C, at which the rutile phase TiO_2 was dominant while the anatase phase TiO_2 was almost non-existent. Furthermore, recent papers reported that doping Fe into TiO_2 enabled the photon absorbing zone of TiO_2 to extend from UV toward visible light as well as reduced TiO_2 band gap energy from 3.2 to 2.67 eV [48,49].

Table 1
Effect of temperature on physicochemical properties of the prepared samples.

Materials	Calcination temperature (°C)	Anatase (1 0 1) over rutile (1 1 0) ratio (A:R)	Crystalline size (nm)[a]	
			Anatase (1 0 1)	Rutile (1 1 0)
Nanofibers from ilmenite	As-synthesized	–	–	–
	300	–	–	–
	400	–	–	–
	500	–	–	–
	600	73:37	21	12
	700	49:51	29	19
	800	28:72	33	41
	900	32:68	49	142
	1000	22:78	142	142

[a] Calculated by using Sherrer formula.

The phase content between anatase and rutile was estimate from the equation: $FR = 1/\{1 + 0.79[IA(1\,0\,1)/IR(1\,1\,0)]\}$ suggested by Spurr and Myers [50]. The effects of calcination temperatures on phase content and crystalline size of prepared samples are shown in Table 1. This observation shows that with increasing calcination temperature from 600 to 1000 °C, the trend of anatase ratio gradually decreased, meanwhile the rutile ratio became stronger. This result indicates that the increase of calcination temperature led to the phase transformation from thermodynamically metastable anatase to the most stable form of rutile phase [51–53]. This phenomenon relates to an enhancement of crystallization of rutile phase. Typically, phase transformation is supplemented with crystal growth [51].

From the XRD spectra, the crystallite sizes can be calculated by the Debye–Scherrer formula $D = K\lambda/\beta\cos\theta$, where D is the crystallite diameter in nm, K is the shape constant (0.90), λ is the wavelength of X-ray (1.541874 Å), β is the peak width (in rad) at half-maximum height and h is the Bragg angle. As the calcination temperature is raised, XRD reflections corresponding to both the anatase and rutile phase become narrower, which indicates the increase of crystallite size [51,53]. The crystallite size was shown in Table 1. The crystallite size of samples calcined at lower temperature (below 800 °C) increased slightly from about 21 to 33 nm for anatase phase and 12 to 41 nm for rutile phase. At higher temperature (1000 °C) caused rapid increase of crystallite size up to about 142 nm for both the anatase and rutile. This result is similar to study by Górska et al. [54].

Fig. 5 depicts the SEM images of the prepared samples calcined at 600, 700, 800, 900, and 1000 °C for 2 h. The nanofibers calcined at 600–700 °C for 2 h maintained their nanofiber morphology (Fig. 5(a) and (b)). Typically, the TiO_2-derived nanotubes after heat-treatment at 400 °C (anatase phase) were destroyed and transformed into nanoparticles [33,55]. However, in this work, the prepared samples calcined at high temperatures of 600–700 °C for 2 h were stable. Therefore, the prepared samples can be utilized in various applications operated at high

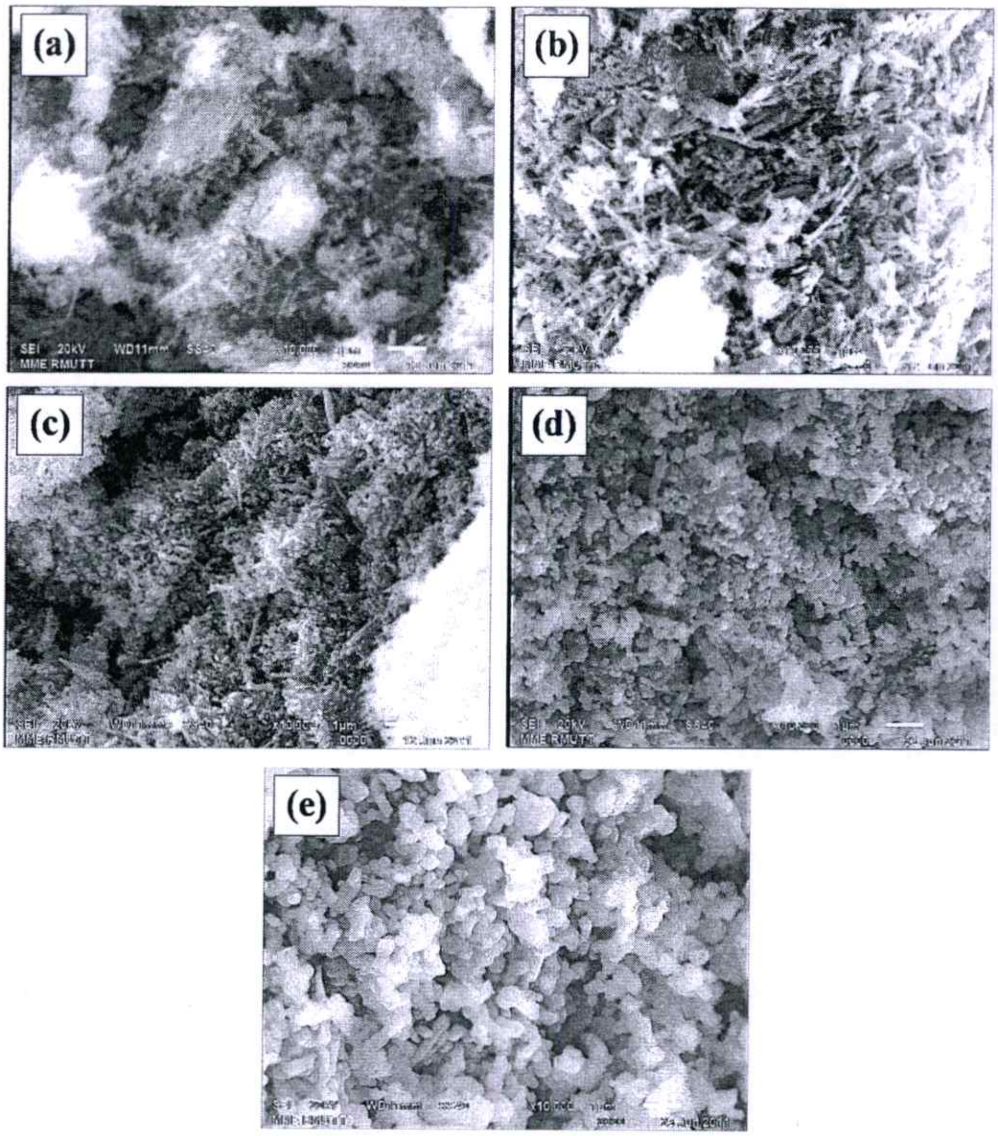

Fig. 5. SEM images of the calcined nanofibers for 2 h at (a) 600 °C, (b) 700 °C, (c) 800 °C, (d) 900 °C, and (e) 1000 °C.

temperatures. In addition, the prepared samples calcined at 800–1000 °C for 2 h showed submicron particle structure of rutile TiO_2 (Fig. 5(c)–(e)) Recent papers reported that the submicron particle structure of rutile TiO_2, caused by increasing calcination temperature, decreased the BET specific surface area of the nanofibers [5,33,35,38].

Other studies reported the influence of phase composition and BET specific surface area of TiO_2 nanostructured on the photocatalyst properties. Indeed, it was found that the photocatalyst properties of anatase phase of TiO_2 were better than those of rutile [4,5,38]. However, the band gap of rutile (3.0 eV) was lower than that of anatase (3.2 eV); as such, rutile should be more easily photo-excited. The high recombination possibility of photogenerated electrons and holes was the major limiting factor for the indigent photocatalytic activity of rutile [5,38]. Generally, phase composition, specific surface area, pore size distribution, particle morphology, particle aggregation, and impurities can play a crucial role in determining the efficiency of specific applications [56]. Thus, the calcination process is required to control the crystalline structure of TiO_2 nanofibers.

3.4. UV–Vis diffuse reflectance spectrum

The UV–Vis absorption spectra of the samples were recorded using a UV–Vis spectroscopy (UV-2401, Shimadzu). The band gap energy (E_g) was estimated from absorption edge from equation as shown in Eq. (1) by Oregan and Grätzel [57].

$$E_g = \frac{hC}{\lambda} \quad (1)$$

where h is the Planks constant = 6.623×10^{-34} J s, C the speed of light = 3.0×10^8 m/s and λ is the cut off wavelength (m).

The influence of temperature on the light absorption characteristic of prepared samples investigated from the as-synthesized and nanofibers calcined at 400, 700, and 1000 °C for 2 h and shown in Fig. 6. A significant increase at wavelengths shorter than 400 nm could be explained to absorption of light caused by the excitation of electrons from the valence band to the conduction band of TiO_2 [51,58]. A shift to visible light region of the absorption of the prepared samples was observed for the as-synthesized and nanofibers calcined at 400, 700, and 1000 °C for 2 h. The differences

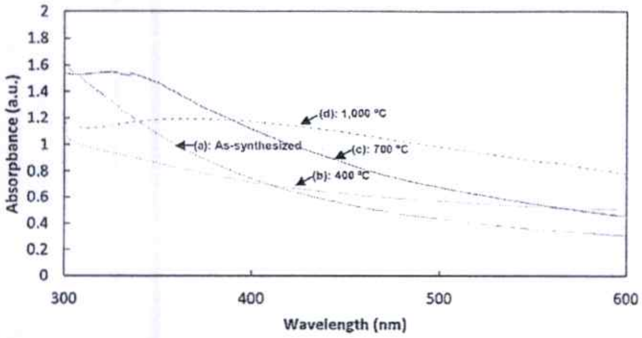

Fig. 6. UV–Vis spectra of the as-synthesized nanofibers and the calcined nanofibers for 2 h at various temperatures.

in absorption were described to the change of crystallite size and phase structure [51,53]. The absorption edges shifted toward longer wavelengths were attributed to the existence of iron (Fe) in the prepared samples, the excitation of 3d electron of Fe^{3+} ion to the TiO_2 conduction band (charge transfer transition) may be extended of absorption of the prepared samples from UV toward visible light [41,58,59]. This correlates with the appearance of the brown coloration of the prepared samples.

The band gap energy of the as-synthesized and nanofibers calcined at 400, 700, and 1000 °C for 2 h estimated from Eq. (1) was about 3.80, 2.62, 2.32, and 2.12 eV, respectively. Recently paper, reported the Fe_2O_3/TiO_2 composite showed narrower band gap energy was about 2.20–2.63 eV [42]. The difference in band gap energy is due to the result of the change of crystallite size and phase composition in the prepared samples [51,54]. This data showed that the band gap of prepared samples became narrower with increasing calcination temperature. This result due to following factor, the first reason, an increase in crystallite size leading to the decrease of band gap energy, which was in correspond with recently work reported by Xiao et al. [60] and the second, after calcination at 400, 700, and 1000 °C for 2 h, lower value of band gap energy for samples was observed, due to phase transformation from anatase to rutile [51,53,54]. However, the band gap energy of the as-synthesized showed larger gap may be cause by titanate structure of this sample [61].

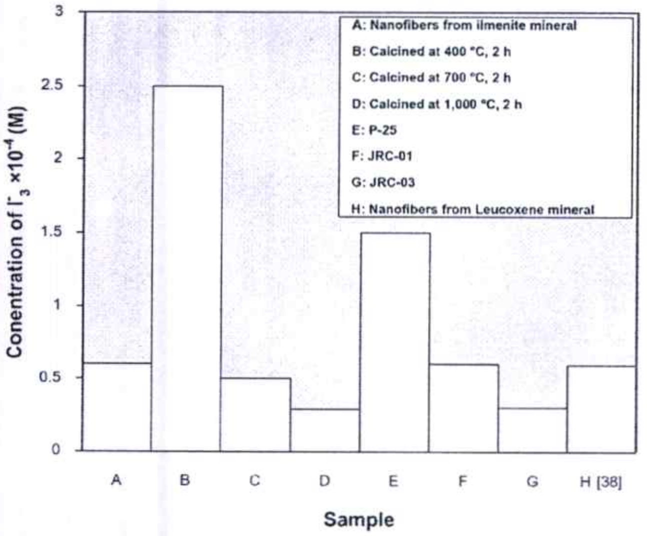

Fig. 7. Photocatalytic activity (I_3^- concentration) of the as-synthesized nanofibers, the calcined nanofibers for 2 h at various temperatures, commercial TiO_2 nanoparticles (P-25, JRC-01, and JRC-03), and nanofibers from leucoxene mineral.

3.5. Photocatalytic activity

Fig. 7 shows the photocatalytic activity of the as-synthesized nanofibers, nanofibers calcined at various temperatures for 2 h, and commercial grade TiO_2 nanoparticles, i.e., P-25, JRC-01, and JRC-03. The photocatalytic activities of all the samples calculated as the concentration of I_3^- in 10 ml of 0.2 M KI solution per unit mass. After UV irradiation for 60 min, the nanofibers calcined at 400 °C for 2 h showed the highest photocatalytic activity in which I_3^- concentration was approximately 2.50×10^{-4} M, whereas the nanofibers calcined at 1000 °C for 2 h showed the lowest photocatalytic activity with I_3^- concentration of roughly 0.29×10^{-4} M. The nanofibers calcined at 400 °C for 2 h exhibited higher photocatalytic activity (2.50×10^{-4} M) than the as-synthesized nanofibers, the nanofibers calcined at 700 °C, the as-synthesized nanofibers from leucoxene mineral, and commercial grade TiO_2 nanoparticles, i.e., P-25, JRC-01, and JRC-03, each of which respectively yielded I_3^- concentration of 0.60×10^{-4}, 0.50×10^{-4}, 0.59×10^{-4}, 1.50×10^{-4}, 0.60×10^{-4}, and 0.30×10^{-4} M. The results indicated that the calcination process significantly influenced the photocatalytic activity of the TiO_2 nanofibers, which could be attributed to: (1) the nanofibers calcined at 400 °C for 2 h showed TiO_2 (B), which promoted the photocatalytic activity [38]. The BET specific surface areas of the nanofibers calcined at low temperatures tended to be larger than those of the nanofibers calcined at high temperatures, and the larger BET specific surface area improved the photocatalytic activity [36,38,62–70]; (2) the hydrogen titanate structure of the as-synthesized nanofibers from ilmenite and leucoxene (previous work) [38] mineral had a larger band gap of approximately 3.80 eV corresponding to recently work, resulting in decreases in both photoreaction and photocatalytic activity of the as-synthesized sample [61,71–73]; (3) the nanofibers calcined at 700 and 1000 °C for 2 h showed not just a mixture of tri-crystalline phase of anatase, rutile, and Fe_2O_3 but also submicron particle structure. Generally, the rutile phase has high recombination rates of photogenerated e^- and h^+, leading to a decrease of photocatalytic activity [4,36,38,65]. Recent research studies reported that the submicron particle morphology decreased the specific surface areas and thereby the photocatalytic activity [36,38,62–68]. Thus, the photocatalytic activity decreased as the calcination temperature increased. In addition, although, nanofibers calcined at 700 and 1000 °C for 2 h showed the absorption higher than the nanofibers calcined at 400 °C for 2 h, but the narrower band gap energy is a result of the recombination of electron and hole that may be result in the decrease of the photocatatytic activity [74]. Furthermore, nanofibers calcined at 400 °C for 2 h showed greater photocatalytic activity than nanofibers calcined at 700 and 1000 °C for 2 h due to the overall increase in light absorbance [41].

4. Conclusion

The as-synthesized nanofibers (typically 2–7 μm in length and 20–90 nm in diameter) were prepared by simple hydrothermal processing using natural ilmenite mineral (rutile phase) as the starting material. The as-synthesized nanofibers were light brown-colored powder. The nanofibers calcined at 300–400 °C showed TiO_2 (B) whereas the nanofibers calcined at 500 °C revealed a mixture of TiO_2 (B) and anatase. The nanofibers calcined at high temperatures of 600–1000 °C showed a mixture of tri-crystalline of anatase, rutile, and Fe_2O_3. The rutile phase rose with increasing calcination temperature. Moreover, the nanofibers calcined at 300–700 °C maintained nanofiber structure while the morphology of nanofibers calcined at 800–1000 °C transformed into nanoparticles and submicron particles.

The transformation of anatase to rutile phase and the increase of crystallite size of prepared samples were observed with increasing calcination temperature. The absorption spectra of the as-synthesized and nanofibers calcined at 400, 700, and 1000 °C for 2 h shift to visible light region. The band gap energy of the as-synthesized and nanofibers calcined at 400, 700, and 1000 °C for 2 h was about 3.80, 2.62, 2.32, and 2.12 eV, respectively, indicating that the reduce of band gap energy of prepared samples was achieved with increasing calcination temperature. The photocatalytic activity of the nanofibers calcined at 400 °C for 2 h was not just higher than those of the commercial TiO_2 nanoparticles (P-25, JRC-01, and JRC-03) and nanofibers from leucoxene (previous work) but also the highest of all the samples. Therefore, the Fe-doped nanofibers have been increasingly applied to various applications, examples of which are in exciting low-energy visible wavelengths, photocatalyst of hydrogen generation, dye-sensitized solar cells, and decomposition of water pollution.

Acknowledgements

This work has been supported by the National Nanotechnology Center (NANOTEC) (P-10-1079), NSTDA, Ministry of Science and Technology, Thailand and through the NANOTEC program of the Centers of Excellence Network. Deep appreciation goes to Sakorn Minerals Co., Ltd., Thailand; to College of Nanotechnology, King Mongkut's Institute of Technology Ladkrabang (KMITL); and to Nanotechnology for Textile and Polymer Research Group (NanoTeP) of Faculty of Engineering of Rajamangala University of Technology Thanyaburi (RMUTT) for a myriad of support and assistance.

References

[1] B. O'Regan, M. Grätzel, Nature 353 (1991) 737–740.
[2] N.G. Park, J. Lagemaat, A.J. Frank, J. Phys. Chem. B 104 (2000) 8989–8994.
[3] S.U.M. Khan, M. Al-Shahry, W.B. Ingler, Science 297 (2002) 2243–2245.
[4] J. Jitputti, S. Pavasupree, Y. Suzuki, S. Yoshikawa, J. Solid State Chem. 180 (2007) 1743–1749.
[5] J. Jitputti, Y. Suzuki, S. Yoshikawa, Catal. Commun. 9 (2008) 1265–1271.
[6] A. Fujishima, K. Honda, Nature 238 (1972) 37–38.
[7] H.J. Yun, H. Lee, J.B. Joo, W. Kim, J. Yi, J. Phys. Chem. C 113 (2009) 3050–3055.
[8] M.A. Fox, M.T. Dulay, Chem. Rev. 93 (1993) 341–357.
[9] X. Tao, W.H. Ma, T.Y. Zhang, J.Y. Zhao, Angew. Chem. Int. Ed. 40 (2001) 3014–3016.
[10] D.J. Yang, Z.F. Zheng, H.W. Liu, H.Y. Zhu, X.B. Ke, Y. Xu, D. Wu, Y. Sun, J. Phys. Chem. C 112 (2008) 16275–16280.
[11] J.Y. Li, C.C. Chen, J.C. Zhao, H.Y. Zhu, J. Orthman, Appl. Catal. B: Environ. 37 (2002) 331–338.
[12] K. Chen, J.Y. Li, J. Li, Y.M. Zhang, W.X. Wang, Colloids Surf. A: Physicochem. Eng. Aspects 360 (2010) 47–56.
[13] S.N. Frank, A.J. Bard, J. Am. Chem. Soc. 99 (1977) 303–305.
[14] K. Chen, J. Li, W. Wang, Y. Zhang, X. Wang, H. Su, Mater. Sci. Semicond. 15 (2012) 20–26.
[15] S. Sakulkhaemaruethai, S. Pavasupree, Y. Suzuki, S. Yoshikawa, Mater. Lett. 59 (2005) 2965–2968.
[16] F. Pan, J. Zhang, H. Liu, T. Wang, W. Hao, Key Eng. Mater. 280–283 (2005) 293–296.
[17] K. Koci, L. Obalova, L. Matejova, D. Placha, Z. Lacny, J. Jirkovsky, O. Solcova, Appl. Catal. B: Environ. 89 (2009) 494–502.
[18] A. Testino, I.R. Bellobono, V. Buscaglia, C. Canevali, M. D'Arienzo, S. Polizzi, R. Scotti, F. Morazzoni, J. Am. Chem. Soc. 129 (2007) 3564–3575.
[19] Ch. Bougheloum, A. Messalhi, Phys. Procedia 2 (2009) 1055–1058.
[20] J.-Y. Jung, C.-S. Lee, J. Ind. Eng. Chem. 17 (2011) 237–242.
[21] M. Grätzel, Nature 414 (2001) 338–344.
[22] I.C. Flores, J.N. de Freitas, C. Longo, M.-A. De Paoli, H. Winnischofer, A.F. Nogueira, J. Photochem. Photobiol. A: Chem. 189 (2007) 153–160.
[23] B.X. Wang, D.F. Xue, Y. Shi, F.H. Xue, in: W.V. Prescott, A.I. Schwartz (Eds.), Nanorods, Nanotubes and Nanomaterials Research Progress, New Nova Science Publishers Inc., New York, 2008.
[24] H. Hahn, R.S. Averback, Nanostruct. Mater. 1 (1992) 95–100.
[25] H. Yin, Y. Wada, T. Kitamura, S. Kambe, S. Murasawa, H. Mori, T. Sakata, S. Yanagida, J. Mater. Chem. 11 (2001) 1694–1703.
[26] M.K. Akhtar, S. Vermury, S.E. Pratsinis, Nanostruct. Mater. 4 (1994) 537–544.
[27] Z. Cai, J. Li, Y. Wang, J. Alloys Compd. 489 (2010) 167–169.
[28] Z. Zhang, C. Shao, L. Zhang, X. Li, Y. Liu, J. Colloid Interface Sci. 351 (2010) 57–62.
[29] S. Ngamsinlapasathian, T. Sreethawong, Y. Suzuki, S. Yoshikawa, Sol. Energy Mater. Sol. Cells 86 (2005) 269–282.
[30] T. Sreethawong, Y. Suzuki, S. Yoshikawa, J. Solid State Chem. 178 (2005) 329–338.
[31] T. Kasuga, M. Hiramatsu, A. Hoson, T. Sekino, K. Niihara, Langmuir 14 (1998) 3160–3163.
[32] T. Kasuga, M. Hiramatsu, A. Hoson, T. Sekino, K. Niihara, Adv. Mater. 11 (1999) 1307–1311.
[33] R. Yoshida, Y. Suzuki, S. Yoshikawa, Mater. Chem. Phys. 91 (2005) 409–416.
[34] Y. Suzuki, S. Pavasupree, S. Yoshikawa, R. Kawahata, J. Mater. Res. 20 (2005) 1063–1070.
[35] S. Pavasupree, Y. Suzuki, S. Yoshikawa, R. Kawahata, J. Solid State Chem. 178 (2005) 3110–3116.
[36] Y. Suzuki, S. Yoshikawa, J. Mater. Res. 19 (2004) 982–985.
[37] R. Yoshida, Y. Suzuki, S. Yoshikawa, J. Solid State Chem. 178 (2005) 2179–2185.
[38] S. Pavasupree, N. Laosiripojana, S. Chuangchote, T. Sagawa, Jpn. J. Appl. Phys. 50 (2011), 01BJ16-1–01BJ16-4.
[39] D. Aphairaj, T. Wirunmongkol, S. Pavasupree, P. Limsuwan, Energy Procedia 9 (2011) 539–544.
[40] A. Simpraditpan, T. Wironmongkol, S. Pavasupree, W. Pecharapa, Ceram. Int. 39 (2013) 2497–2502.
[41] Y.R. Smith, K.J.A. Raj, V. Subramanian, B. Viswanathan, Colloids Surf. A: Physicochem. Eng. Aspects 367 (2010) 140–147.
[42] T.K. Ghorai, M. Chakraborty, P. Pramanik, J. Alloys Compd. 509 (2011) 8158–8164.
[43] A. Nakahira, T. Kubo, C. Numako, Inorg. Chem. 49 (2010) 5845–5852.
[44] A.R. Armstrong, G. Armstrong, J. Canales, P.G. Bruce, Angew. Chem. Int. Ed. 43 (2004) 2286–2288.
[45] Z.-Y. Yuan, B.-Y. Su, Colloids Surf. A 241 (2004) 173–183.
[46] H.-L. Kuo, C.-Y. Kuo, C.-H. Liu, J.-H. Chao, C.-H. Lin, Catal. Lett. 113 (2007) 7–12.
[47] K.C. Song, S.E. Pratsinis, J. Colloid Interface Sci. 231 (2000) 289–298.
[48] C.L. Luu, Q.T. Nguyen, S.T. Ho, Adv. Nat. Sci.: Nanosci. Nanotechnol. 1 (2010) 015008.
[49] X.X. Slamet, H.W. Nasution, E. Purnama, S. Kosela, J. Gunlazuardi, Catal. Commun. 6 (2005) 313–319.
[50] Z.R.A. Spurr, H. Myers, Anal. Chem. 29 (2008) 760–763.
[51] G. Wang, L. Xu, J. Zhang, T. Yin, D. Han, Int. J. Photoenergy 2012 (2012) 265760.
[52] J.G. Yu, Y.R. Su, B. Cheng, Adv. Funct. Mater. 17 (2007) 1984–1990.
[53] S. Mozia, A. Heciak, A.W. Morawski, Appl. Catal. B: Environ. 104 (2011) 21–29.
[54] P. Górska, A. Zaleska, E. Kowalska, et al. Appl. Catal. B: Environ. 84 (2008) 440–447.
[55] C.C. Tsai, H. Teng, Chem. Mater. 16 (2004) 4352–4358.
[56] X. Deng, Y. Yue, Z. Gao, Appl. Catal. B 39 (2002) 135–147.
[57] B. Oregan, M. Grätzel, Nature 353 (1991) 737–739.
[58] Y. Liu, J.H. Wei, R. Xiong, C.X. Pan, J. Shi, Appl. Surf. Sci. 257 (2011) 8121–8126.
[59] M.A. Klan, S.I. Woo, O.B. Yang, Int. J. Hydrogen Energy 33 (2008) 5345–5351.
[60] Q. Xiao, L.L. Ouyang, Chem. Eng. J. 148 (2009) 248–253.
[61] L.L. Costa, A.G.S. Prado, J. Photochem. Photobiol. A: Chem. 201 (2009) 45–49.
[62] G.S. Guo, C.N. He, Z.N. Wang, F.B. Gu, D.M. Han, Talanta 72 (2007) 1687–1692.
[63] R.R. Bacsa, J. Kiwi, Appl. Catal. B 16 (1998) 19–29.
[64] T. Peng, D. Zhao, K. Dai, W. Shi, K. Hirao, J. Phys. Chem. B 109 (2005) 4947–4952.
[65] C.L. Wong, Y.N. Tan, A.R. Mohamed, J. Environ. Manage. 92 (2011) 1669–1680.
[66] J. Zhang, X. Xiao, J. Nan, J. Hazard. Mater. 176 (2010) 617–622.
[67] S. Kaewgun, D. Mckinney, J. White, A. Smith, M. Tinker, J. Ziska, B.I. Lee, J. Photochem. Photobiol. A: Chem. 202 (2009) 154–158.
[68] D. Gumy, C. Morais, P. Bowen, C. Pulgarin, S. Giraldo, R. Hajdu, J. Kiwi, Appl. Catal. B 63 (2006) 76–84.
[69] S. Pavasupree, J. Jitputti, S. Ngamsinlapasathian, S. Yoshikawa, Mater. Res. Bull. 43 (2008) 149–157.
[70] Z. Zhu, X. Li, Q. Zhao, Z. Qu, Y. Hou, L. Zhao, S. Liu, G. Chen, Mater. Res. Bull. 45 (2010) 1889–1893.
[71] R. Mu, Z. Xu, L. Li, Y. Shao, H. Wan, S. Zheng, J. Hazard. Mater. 176 (2010) 495–502.
[72] H.H. Ou, C.H. Liao, Y.H. Liou, J.H. Hong, S.L. Lo, Environ. Sci. Technol. 42 (2008) 4507–4512.
[73] S. Song, J.J. Tu, Z.Q. He, F.Y. Hong, W.P. Liu, J.M. Chen, Appl. Catal. A 378 (2010) 169–174.
[74] A. Yamakata, T. Ishibashi, H. Onishi, J. Mol. Catal. A: Chem. 199 (2003) 85–94.

This article was downloaded by: [Wisanu Pecharapa]
On: 10 December 2013, At: 07:09
Publisher: Taylor & Francis
Informa Ltd Registered in England and Wales Registered Number: 1072954 Registered office: Mortimer House, 37-41 Mortimer Street, London W1T 3JH, UK

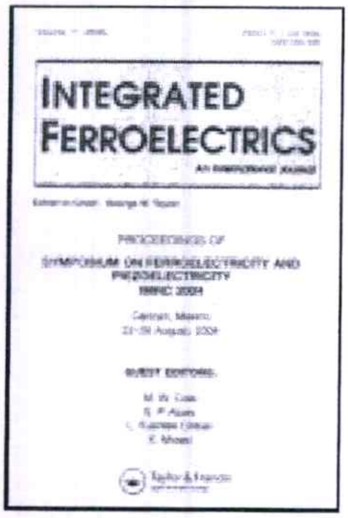

Integrated Ferroelectrics: An International Journal
Publication details, including instructions for authors and subscription information:
http://www.tandfonline.com/loi/ginf20

Hydrothermal Synthesis of Nanofibers from Natural Ilmenite Mineral and Their Utilization for Dye-Sensitized Solar Cell

Athapon Simpraditpan [a] , Thanakorn Wirunmongkol [c] , Sorapong Pavasupree [c] & Wisanu Pecharapa [a b]

[a] College of Nanotechnology , King Mongkut's Institute of Technology Ladkrabang , Ladkrabang , Bangkok , 10520 , Thailand

[b] Thailand Center of Excellence in Physics , Commission on Higher Education , 328 Si Ayutthaya Rd., Bangkok , 10400 , Thailand

[c] Department of Materials and Metallurgical Engineering, Faculty of Engineering , Rajamangala University of Technology Thanyaburi , Klong 6, Pathumthani , 12110 , Thailand

Published online: 07 Dec 2013.

To cite this article: Athapon Simpraditpan , Thanakorn Wirunmongkol , Sorapong Pavasupree & Wisanu Pecharapa (2013) Hydrothermal Synthesis of Nanofibers from Natural Ilmenite Mineral and Their Utilization for Dye-Sensitized Solar Cell, Integrated Ferroelectrics: An International Journal, 149:1, 135-142, DOI: 10.1080/10584587.2013.853592

To link to this article: http://dx.doi.org/10.1080/10584587.2013.853592

PLEASE SCROLL DOWN FOR ARTICLE

Taylor & Francis makes every effort to ensure the accuracy of all the information (the "Content") contained in the publications on our platform. However, Taylor & Francis, our agents, and our licensors make no representations or warranties whatsoever as to the accuracy, completeness, or suitability for any purpose of the Content. Any opinions and views expressed in this publication are the opinions and views of the authors, and are not the views of or endorsed by Taylor & Francis. The accuracy of the Content should not be relied upon and should be independently verified with primary sources of information. Taylor and Francis shall not be liable for any losses, actions, claims, proceedings, demands, costs, expenses, damages, and other liabilities whatsoever or howsoever caused arising directly or indirectly in connection with, in relation to or arising out of the use of the Content.

This article may be used for research, teaching, and private study purposes. Any substantial or systematic reproduction, redistribution, reselling, loan, sub-licensing,

Integrated Ferroelectrics, 149:135–142, 2013
Copyright © Taylor & Francis Group, LLC
ISSN: 1058-4587 print / 1607-8489 online
DOI: 10.1080/10584587.2013.853592

Taylor & Francis
Taylor & Francis Group

Hydrothermal Synthesis of Nanofibers from Natural Ilmenite Mineral and Their Utilization for Dye-Sensitized Solar Cell

ATHAPON SIMPRADITPAN,[1,*]
THANAKORN WIRUNMONGKOL,[3]
SORAPONG PAVASUPREE,[3] AND WISANU PECHARAPA[1,2]

[1]College of Nanotechnology, King Mongkut's Institute of Technology Ladkrabang, Ladkrabang, Bangkok 10520, Thailand
[2]Thailand Center of Excellence in Physics, Commission on Higher Education, 328 Si Ayutthaya Rd., Bangkok 10400, Thailand
[3]Department of Materials and Metallurgical Engineering, Faculty of Engineering, Rajamangala University of Technology Thanyaburi, Klong 6, Pathumthani 12110, Thailand

Titanate nanofibers were synthesized by a hydrothermal method using a low-cost ilmenite mineral as the starting material. The crystalline structure of the as-synthesized nanofibers demonstrated titanate structure ($H_2Ti_xO_{2x+1}$). The bi-crystalline mixture consisting of TiO2 (B) and anatase TiO_2 nanofibers was obtained by heat treatment at 500°C for 2 h. Dye-sensitized solar cells (DSSCs) with photoanode consisting of the nanocomposite of nanoparticles and nanofibers (5%) rendered a light-to-electricity conversion efficiency (η) of 0.28%. In contrast, the cells with photoanodes consisting of only nanoparticles and nanofibers exhibited η of 0.25% and 0.15%, respectively.

Keywords Titanate nanofibers; nanocomposite; hydrothermal; dye-sensitized solar cells

1. Introduction

TiO_2 materials have potential applications as an efficient photocatalyst for the water splitting to produce hydrogen, degradation of organic pollution, and dye-sensitized solar cells [1]. In addition, one-dimensional TiO_2 nanostructures such as nanowires, nanorods, nanowhiskers, nanotubes and nanofibers have been widely studied and researched due to their extraordinary properties including high active surface area, excellent photocatalytic reactivity and cost-effectiveness [1]. The hydrothermal method for the synthesis of TiO_2 nanotubes, first proposed by Kasuga et al. [2], has been extensively exploited for low-dimensional nanostructures [1]. The hydrothermal method of nanomaterials has lots of advantages such as wide range of chemical compositions, single-step process, simple equipped process, lower energy requirement, fast reaction time, environmentally and a host of other

---

Received December 9, 2012; in final form August 25, 2013.
[*]Corresponding author. E-mail: kukki555@hotmail.com

applications [1]. Dye-sensitized solar cells (DSSCs) proposed by O'Regan and Grätzel [3] in 1991 have existed substantial attention due to their high conversion efficiency, simple fabrication technique, and low cost [1,2,4]. TiO_2 nanofiber, nanowire and nanotube can play key role as a photoanode material in DSSCs, that exhibit significant improvement in electron transport efficiency and enhancement of light harvesting efficiency by light scattering of the solar spectrum of nanotube structure and thus cause higher current density [5]. Meanwhile, nanoparticles can provide large surface areas for the dye adsorption. It is conceived that the incorporation of nanofibers, nanowires or nanotubes into nanoparticle matrix could efficiently enhance the light harvesting, electron transport rate, and also the mechanical properties of the device. In this report, a bi-crystalline nanofiber mixture of TiO_2 (B) and anatase TiO_2 was prepared via hydrothermal method and heat treatment. Furthermore, the composites of commercial grade TiO_2 nanoparticles (Degussa P-25) and as-prepared mixture were utilized as modified working electrode material of DSSC.

2. Experimental

TiO_2 nanofibers were prepared via the hydrothermal method using a natural ilmenite mineral (Sakorn Minerals Co., Ltd., Thailand) as starting material. First, 5 g of black granules of ilmenite mineral without any purification were put into a Teflon-lined stainless steel autoclave containing 200 mL of 10 M NaOH (aq.). The hydrothermal process was conducted at 120°C for 72 h with magnetic stirring and then. After the autoclave was allowed to naturally cool to room temperature, the obtained precipitate was quickly washed with small amount of deionized water to remove the excess of NaOH solution, and then washed three times with an HCl (aq.) solution followed by distilled water. After washing, the obtained precipitate was dried overnight with hot air oven at 100°C. Finally, the sample was calcined at various temperatures at 300, 500 and 700°C for 2 h. Phases and crystal structure of the samples were investigated by mean of X-ray diffraction (XRD) pattern using X-ray diffractometer (X'Pert PRO MPD model pw 3040/60, PANalytical) with Cu $K\alpha$ ($\lambda = 0.154$ nm) irradiation at a scan rate of $0.02° \, 2\theta \, s^{-1}$ over 2θ range of 5–80°. The morphologies of the prepared samples and DSSCs films were analyzed by scanning electron microscopy (SEM, JEM-6510, JEOL), with accelerating voltages of 5–20 kV. The distribution of the size and diameter of the nanofiber was additionally examined by SEM. The chemical composition and valence states of the films were studied in detail by X-ray photoelectron spectroscopy (XPS) (AXIS Ultra with dual anode Mg and Al K_α X-ray source).

Five pastes containing mixed TiO_2 nanoparticles (Degussa P-25) and nanofibers (labeled as NF0, NF5, NF10, NF15 and NF100) were prepared with nanofibers concentration of 0, 5, 10, 15 and 100 wt%, respectively. A paste of the composite was placed in a mortar with acetic acid, absolute ethanol solution and distilled water as dispersive materials. The mixed solution was ground for 40 min then transferred into 100 mL absolute ethanol solution, followed by stirring and sonication for several times. The mixed solution was then added with ethyl cellulose and terpineol followed by heating to obtain a viscous paste. The TiO_2 composite films were prepared by the doctor blade technique. Paste was flattened on F-doped SnO_2-coated glass (FTO glass) with a glass rod. The films were annealed at 500°C for 60 min then cooled down to 80°C. Dye sensitization was performed by immersing a TiO_2 film in dye solution (N719, Solaronix SA, Switzerland) for at least 24 h in a sealed beaker. The sensitization was completed after the colors at the top and the bottom were the same. The sensitized films were washed once in absolute ethanol solution, and then dried in hot air condition. A solar cell was assembled in a typical sandwich-type cell by placing a

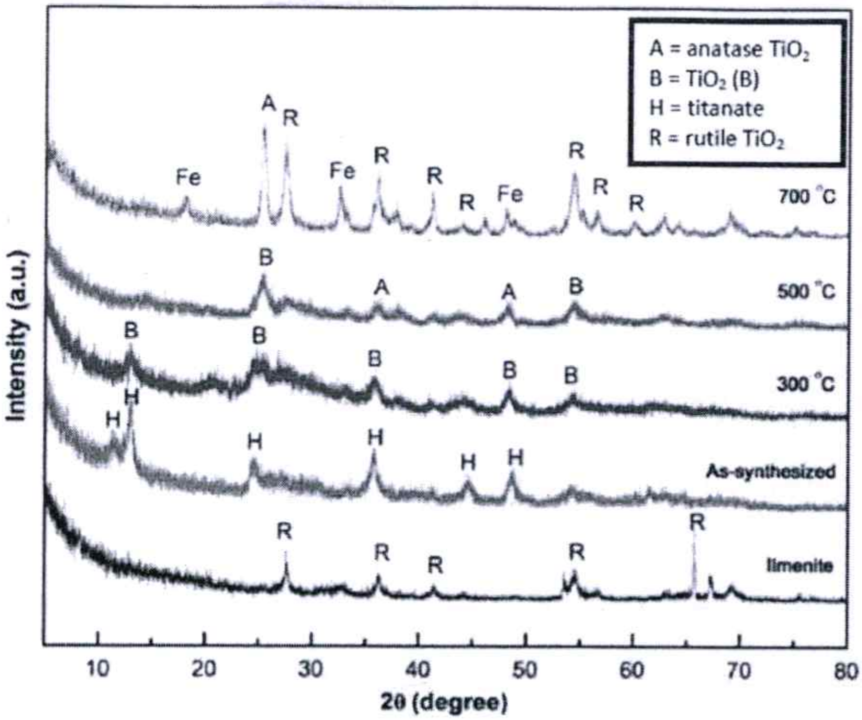

Figure 1. XRD patterns of the starting natural ilmenite mineral, the as-synthesized nanofibers and the calcined nanofibers for 2 h at 300, 500 and 700°C. (Color figure available online.)

platinum-coated conducting glass on the dye-sensitized electrode separated by surlyn film. They were clipped to immobilize by binder clip. Then, an electrolyte was injected into the electrodes. Finally, the photovoltaic properties of the prepared samples were immediately investigated by a solar simulator under AM1.5G condition.

3. Results and Discussion

The crystallinity of the starting ilmenite mineral, the as-synthesized samples and the calcined samples was verified by XRD. As seen in Fig. 1, the crystalline structure of the starting ilmenite mineral is assigned to the rutile phase, while the crystalline structure of the as-synthesized nanofibers is attributed to a layered titanate $H_2Ti_xO_{2x+1}$ phase, most likely trititanate ($H_2Ti_3O_7$), indicating the hydrogen atom was remained in the prepared nanofibers [1]. No diffraction peaks of other impurities (such as starting rutile, NaCl) were detected. The phase combination between anatase and rutile of as-synthesized product is considered to be the cause of rather low photocatalytic activity due to greater recombination rate of photogenerated electrons and holes of rutile phase than that of anatase phase [1]. After calcination at the temperature range of 300°C, the calcined samples demonstrated TiO_2 (B) due to dehydration and re-crystallization to metastable form of TiO_2 (B) [1]. After further calcination at 500°C, the result reveals a bi-crystalline mixture consisting of TiO_2 (B) and anatase TiO_2. The prepared nanofibers are consisted of a mixture of anatase, rutile phase of TiO_2 and Fe_2O_3 as calcination temperature elevates to 700°C. Generally, the rutile phase has high recombination rates of photogenerated e^- and h^+, leading to a decrease of photocatalytic activity [1]. Furthermore, recent papers reported that an appropriate doing of Fe into TiO_2 could extend the photon absorbing zone of TiO_2 from UV toward visible light and reduce TiO_2 band gap energy from 3.2 to 2.67 eV [6]. Based on this fact, the

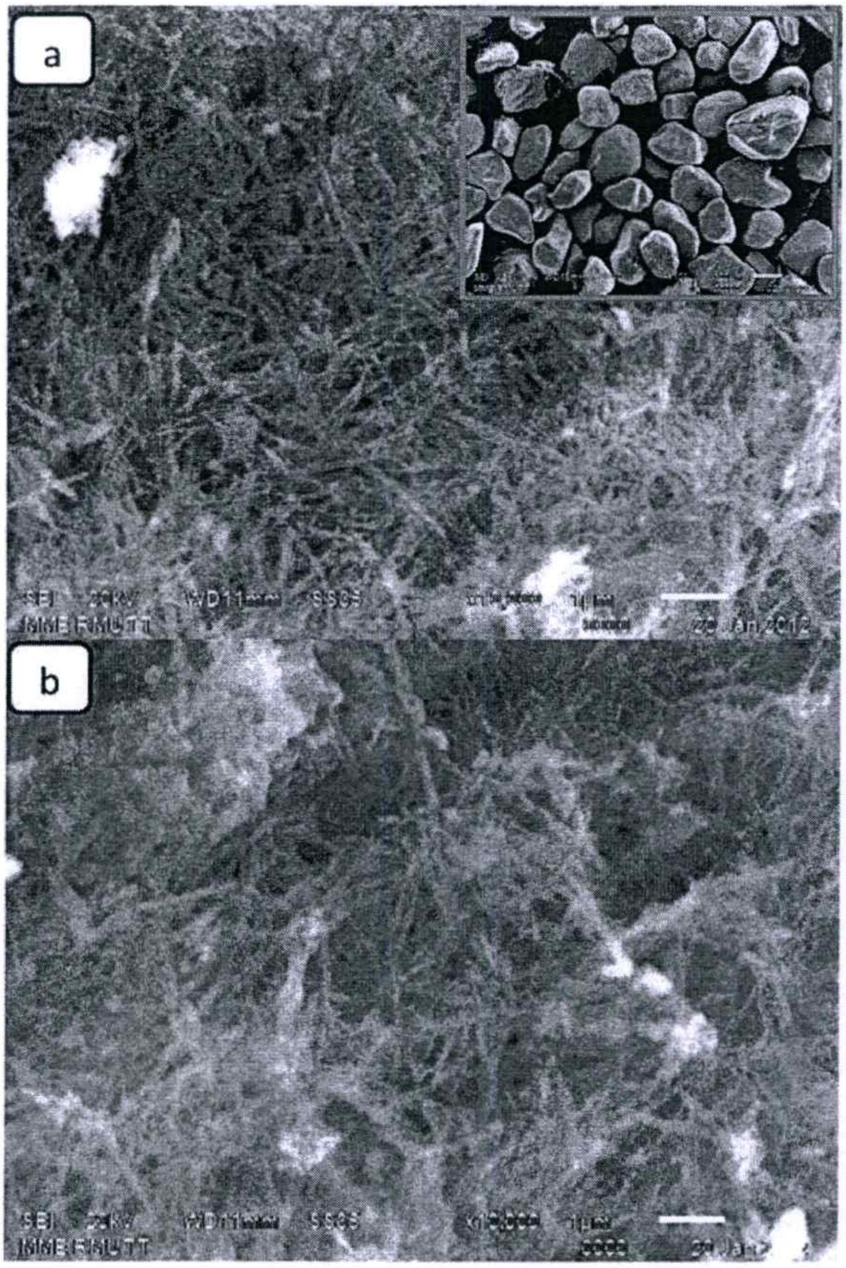

Figure 2. SEM images of (a) the as-synthesized nanofibers and the starting ilmenite mineral (inset) and (b) the calcined nanofibers for 2 h at 500°C (×10,000 magnified). (Color figure available online.)

suitable calcination temperature for the nanofibers is designated to be at 500°C. The inset of Fig. 2(a) represents the SEM image of the starting ilmenite mineral. It can be seen that the starting ilmenite mineral has the granular structure with sizes of 150–200 μm. After hydrothermal process, the as-synthesized sample exhibits a uniform fiber-like morphology (Fig. 2(a)). The nanofibers tend to form bundles so that some of the nanofibers appear in thicker feature than others. The length of prepared nanofibers was about 2–7 μm with diameters of 20–90 nm. The nanofiber formation can be explained by the coarseness of the ilmenite granules that retard their dissolution in the NaOH solution and suppress nucleation but effectively assist preferential crystal growth along the 010 direction of the trititanate [1]. Fig. 2(b) shows the SEM images of the nanofibers calcined at 500°C for 2 h, indicating

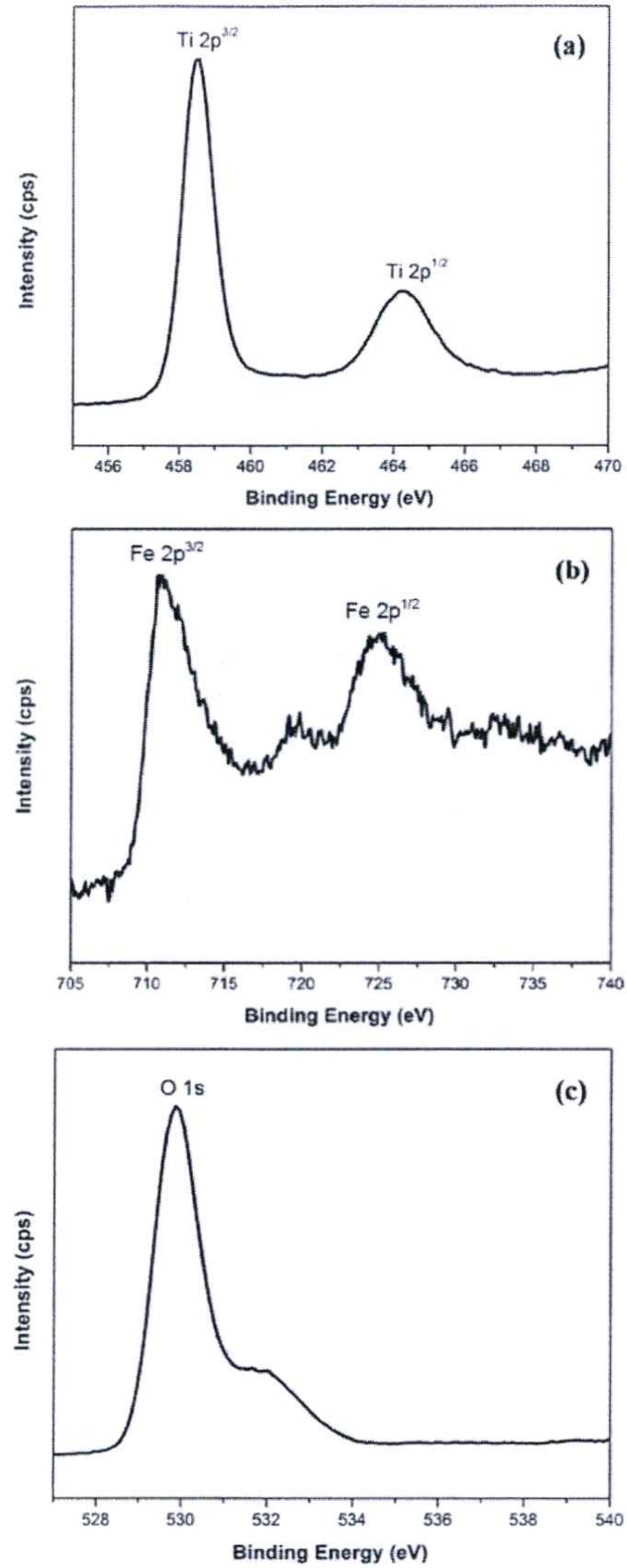

Figure 3. XPS spectra of the titanate nanofibers: (a) the Ti 2p regime, (b) the Fe 2p regime and (c) the O 1s regime.

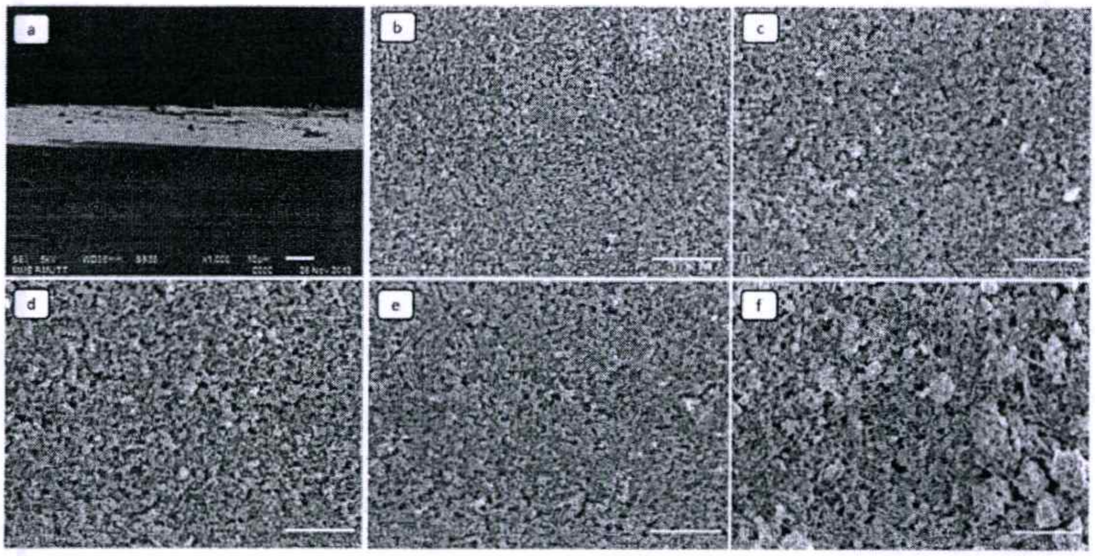

Figure 4. SEM images of (a) the cross-section of NF film, (b) P-25, (c) P-25/NF (5%), (d) P-25/NF (10%), (e) P-25/NF (15%) and (f) NF.

nanofiber feature. The chemical composition of titanate nanofibers were analyzed by XPS as shown in Fig. 3(a-c). The peaks appearing at 458.7 and 464.3 eV are typically associated to Ti^{4+} $2p^{3/2}$ and Ti^{4+} $2p^{1/2}$, respectively (Fig. 3(a)). The Fe oxidation state of the titanate nanofibers can be derived from the Fe 2p spectra as indicated in Fig. 3(b). These data assign to Fe_2O_3 with $2p^{3/2}$ and $2p^{1/2}$ positioned at 710.5 and 724.0 eV, respectively, indicating the replacement of Fe^{3+} to Ti^{4+} of TiO_2 lattice forming Fe-O-Ti bonds. These results are in excellent agreement with previous literature values for magnetite [7]. In addition, XPS spectrum of O 1s peak located at 529.8 eV is also existed in the sample as shown in Fig. 3(c) [7]. The cross-section and surface images of the composite film electrodes are shown in Fig. 4. It can be seen from Fig. 4(a) that the thickness of porous composite films was approximately 15 μm. The compact packing of nanoparticles and nanofibers was obtained by the composite films as shown in Fig. 4(b–e). Contrary, the surface of pure nanofiber film appears in bundles of nanofibers and less compact packing than others (Fig. 4(f)).

Table 1

The photovoltaic properties of the DSSCs based on titanate nanofibers, commercial grade TiO_2 nanoparticles and titanate nanofibers mixed commercial grade TiO_2 nanoparticles with different ratio

Samples	Open circuit voltage, V_{oc} (V)	Short Circuit current density, J_{sc} (mA/cm^2)	Fill Factor, FF	Energy conversion efficiency, η (%)
NF	0.41	1.56	0.24	0.15
NF5	0.47	2.44	0.23	0.28
NF10	0.40	1.97	0.26	0.20
NF15	0.43	1.48	0.29	0.17
P25	0.45	2.12	0.26	0.25

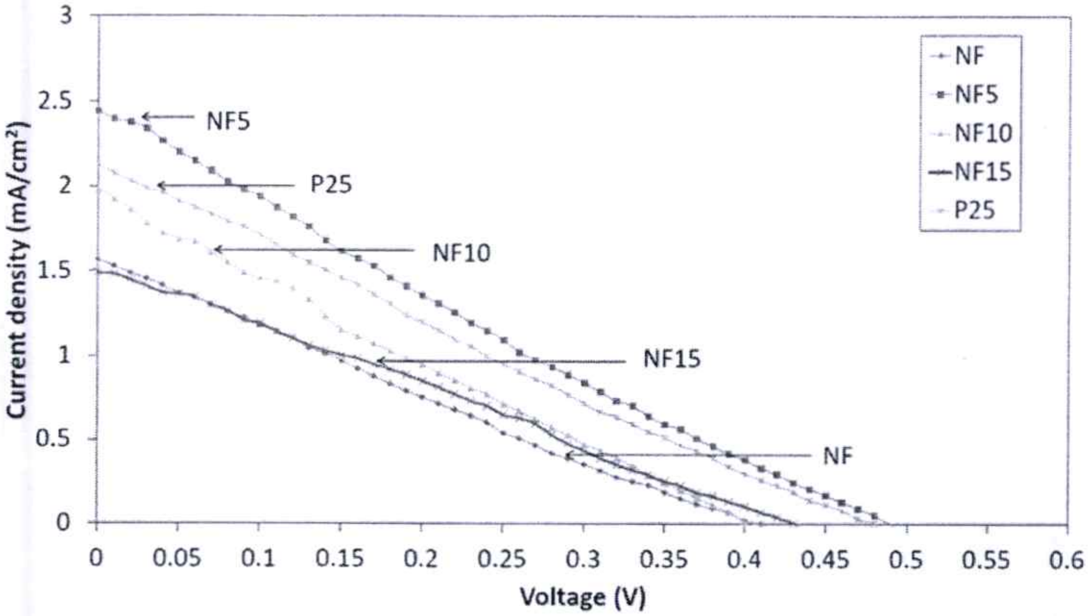

Figure 5. Photocurrent-voltage characteristics of the DSSCs based on titanate nanofibers, commercial grade TiO_2 nanoparticles and titanate nanofibers mixed commercial grade TiO_2 nanoparticles with different ratio. (Color figure available online.)

The photocurrent–voltage curves of the DSSCs are presented in Fig. 5 and corresponding results are listed in Table 1. The device using NF5 composite as working electrode displays superior performance to the others, accompanying the greatest short-circuit photocurrent density (J_{sc}), open-circuit photovoltage (V_{oc}), and energy conversion efficiency (η). This noticeable enhancement of light harvesting efficiency is associated to the increase in electron transport efficiency in one-dimensional nanostructure and increasing number of light scattering of the solar spectrum in nanofiber structure [5]. Furthermore, the incorporation of certain loading content of TiO_2 nanofibers in TiO_2 matrix can significantly increase the amount of absorbed dye molecules in the device, resulting to the improvement of J_{sc} and the reduction of recombination rate of the photo injected electrons in the device [5, 8]. However, further increasing loading amount of nanofiber leads to the decrease in device efficiency. This inferiority may be due to light scattering out of cells by high concentration of nanofibers, resulting to lower current density [5, 8]. The fill factor in this work shows low value, which is not qualitatively similar to the theoretical curve. This result may be originated from the effect of high internal series resistance (R_s) in solar cells [9]. In addition, the existence of Fe^{3+} in TiO_2 can generate a trapping level in TiO_2, that can retard the electron-hole recombination of electrons in TiO_2 conduction band and dye or electrolytes [9].

4. Conclusion

Titanate nanofibers were successfully synthesized by a hydrothermal method using a low-cost ilmenite mineral as the starting material. The crystalline structure of as-synthesized nanofibers demonstrate titanate structure ($H_2Ti_xO_{2x+1}$). The bi-crystalline mixture consisting of TiO_2 (B) and anatase TiO_2 nanofibers was obtained after heat treatment at 500°C for 2 h. As-prepared nanofiber was employed as an assisting agent in commercial P25-TiO_2

in form of composite for working electrode in DSSC. Based on the results, it is acknowledged that the amelioration in device performance can be achieved by the incorporation of specific loading of the nanofibers that can efficiently assist the charge transport and retard the recombination of photo-generated charges in the device. Further research on this aspect including structures of the films, the dispersion and concentration of nanofibers in the composite and other crucial relevant parameters is still underway in order to obtain higher cell performance and better understanding.

Acknowledgments

This work has been supported by the National Nanotechnology Center (NANOTEC), NSTDA, Ministry of Science and Technology, Thailand and through the NANOTEC program of the Centers of Excellence Network. The authors would like to thank Energy Policy and Planning Office, Ministry of Energy, Thailand, Sakorn Minerals Co., Ltd., Thailand, the College of Nanotechnology, King Mongkut's Institute of Technology Ladkrabang (KMITL), and the Nanotechnology for Textile and Polymer Research Group (NanoTeP) of the Faculty of Engineering, Rajamangala University of Technology Thanyaburi (RMUTT), Thailand.

References

1. S. Pavasupree, Y. Suzuki, S. Yoshikawa, and R. Kawahata, Synthesis of titanate, TiO_2 (B), and anatase TiO_2 nanofibers from natural rutile sand. *J. Solid State Chem.*, **178**(10), 3110–3116 (2005).
2. T. Kasuga, M. Hiramatsu, A. Hoson, T. Sekino, and K. Niihara, Formation of titanium oxide nanotube. *Langmuir*, **14**(12), 3160–3163 (1998).
3. B. O' Regan, and M. Grätzel, A low-cost high-efficiency solar cell based on dye sensitized colloidal TiO_2 films. *Nature*, **353**(6346), 737–739 (1991).
4. A. Simpraditpan, T. Wirunmongkol, S. Pavasupree, and W. Pecharapa, Simple hydrothermal preparation of nanofibers from a natural ilmenite mineral. *Ceram. Inter.*, **39**(3), 2497–2502 (2013).
5. J. B. Baxter, and E. S. Aydil, Nanowire based dye sensitized solar cells. *Appl. Phys. Lett.*, **86**(5), 053114 (2005).
6. C. L. Luu, Q. T. Nguyen, and S. T. Ho, Synthesis and characterization of Fe-doped TiO_2 photocatalyst by the sol–gel method. *Adv. Nat. Sci., Nanosci. Nanotechnol.*, **1**, 015008 (2010).
7. Y. Liu, J. H. Wei, R. Xiong, C. X. Pan, and J. Shi, Enhanced visible light photocatalytic properties of Fe-doped TiO_2 nanorod clusters and monodispersed nanoparticles. *Appl. Surf. Sci.*, **257**(18), 8121–8126 (2011).
8. M. Law, L. E. Greene, J. C. Johnson, R. Saykally, and P. Yang, Nanowire dye-sensitized solar cells. *Nat. Mater.*, **4**(6), 455–459 (2005).
9. M. Wolf, and H. Rauschenbacht, Series resistance effects on solar cell measurements. *Adv. Energy Conv.*, **3**(2), 455–479 (1963).

Advanced Materials Research Vol. 925 (2014) pp 600-604
Online available since 2014/Apr/17 at www.scientific.net
© (2014) Trans Tech Publications, Switzerland
doi:10.4028/www.scientific.net/AMR.925.600

Efficiency Enhancement in Dye-Sensitized Solar Cell using TiO_2 /Ilmenite-derived Nanofiber Composite as Working Electrode

Athapon Simpraditpan[1, a], Thanakorn Wirunmongkol[2], Sorapong Pavasupree[2] and Wisanu Pecharapa[1,3]

[1]College of Nanotechnology, King Mongkut's Institute of Technology Ladkrabang,
Ladkrabang, Bangkok 10520, Thailand
[2]Department of Materials and Metallurgical Engineering, Faculty of Engineering,
Rajamangala University of Technology Thanyaburi, Klong 6, Pathumthani 12110, Thailand
[3]Thailand and Center of Excellence in Physics (ThEP Center), Commission on Higher Education,
328 Si Ayutthaya RD, Bangkok 10400, Thailand
[a]kukki555@hotmail.com

Keywords: Dye-sensitized solar cell, Nanocomposite, Nanofiber

Abstract. TiO_2 nanocomposite films of calcined TiO_2 nanofibers and commercial-grade TiO_2 nanoparticles Degussa (P25) utilized as working electrode of dye-sensitized solar cells (DSSCs) are prepared by a doctor blade method. TiO_2 nanofibers were synthesized from ilmenite mineral by hydrothermal process in combination with calcinations process. The prepared samples are characterized by XRD, XPS and TEM. The photoelectric conversion performance of the DSSC based on nanocomposite film electrode was compared to the device fabricated by pure P25 at the same film thickness. The result shows that as calcination temperature increases, the transformation of nanofibers to nanorods and nanoparticles were observed. The energy conversion efficiency (η) of the device tends to with increasing calcined temperature. The greatest η is 3.90% obtained from DSSC fabricated from nanocomposite film electrode of 5 wt.% nanofibers calcined at 800 °C for 2 h mixed with P25, indicating the significant enhancement in its performance by the incorporation of the nanofibers. This enhancement of DSSCs may correlate to high surface area, higher light scattering and light harvesting, low charge recombination and fast electron-transfer rate by nanofibers.

Introduction

Dye-sensitized solar cells (DSSCs) based on TiO_2 electrodes have been firstly studied by Grätzel and co-workers in the early 1990s [1], In the current, DSSCs have attracted worldwide attention to academic and industrial section for the conversion of sunlight into electricity because of their low manufacturing cost, easy fabrication, accessible renewable energy production and environmentally friendly photovoltaics with good efficiencies comparable to those of silicon-based solar cells [1]. DSSC typically consists of a working electrode formed by TiO_2 film that function as the electron acceptor and electron transport pathway coated with a thin layer of sensitizer-dye molecules for light absorption and electron injection into the TiO_2 conduction band. A liquid electrolyte generally consists of an organic solvent such as acetonitrile and a redox couple I^-/I_3^- that serve as a redox agent to reduce the photoexcited dye molecules [2]. TiO_2 nanorods, nanowires, nanofibers and nanotubes possess extraordinary properties such as high surface area, thermal and chemical stability at high temperature, wide semiconductoring band gap and high photo-conversion efficiency and photo-stability [3]. The reaction in a DSSC firstly starts from the absorption of solar light by dye molecules excites electrons from the highest occupied molecule orbital (HOMO) to the lowest unoccupied molecule orbital (LUMO) in the dye molecules. The excited electrons are diffused into the conduction band (CB) of TiO_2. These electrons travel through the working electrode to a counter electrode. The oxidized dye is restored by electron donation via a redox reaction in the electrolyte (usually $3I^- \rightarrow I_3^- + 2e^-$). In this process, some electrons in the CB of TiO_2 travel back to either the electrolyte or the HOMO in the dye molecules, which results in a loss of efficiency in the DSSC. Therefore, the decrease the recombination of electrons in the dye or electrolyte leading to generate high efficiency DSSCs by enhance electron movement towards the counter electrode and through the working electrode [2]. In this work, we fabricate DSSC based on the composite of TiO_2 nanoparticles/nanofibers. The composite of TiO_2 nanoparticles/nanofibers have great advantages in the high surface area of nanoparticles, long electron diffusion length and good light scattering effect of nanofibers [4].

Experimental

Preparation of nanofibers

The nanofibers were prepared by the hydrothermal method using the low-cost ilmenite mineral (Sakorn Minerals Co., Ltd., Thailand) as the starting material. The mixture of ilmenite mineral and 10 M NaOH aqueous solution (200 ml) were located in a Teflon-lined stainless autoclave. The autoclave was heated and stirred at 120 °C for 72 h. After that, the mixture was naturally cooled to room temperature and was washed with 0.1 M HCl aqueous solution and DI water for several times. The precipitated sample was dried at 100 °C for 12 h. The nanofibers were calcined at various temperature range of 300-1,000 °C for 2 h by natural air condition.

Characterization

Powder X-ray diffraction (XRD) patterns of the as-synthesized samples were acquired using a PANalytical diffractometer; X'Pert PRO MPD model pw 3040/60 (Cu K_α; $\lambda = 0.154$ nm). The microstructures of the calcined nanofibers were investigated by transmission electron microscopy (TEM; JEOL, JEM-2010). The chemical composition of the sample was characterized by X-ray photoelectron spectroscopy (XPS) (AXIS Ultra with dual anode Mg and Al K_α X-ray source).

Preparation and measurement of the DSSCs

In this work, the pastes of containing mixed between TiO_2 nanoparticles (Degussa P25) and 5 wt.% nanofibers calcined at 300-1,000 °C for 2 h (labeled as NF, NF300, NF400, NF500, NF600, NF700, NF800, NF900 and NF1000, respectively) were prepared and the effect of calcination temperature of the nanofibers on the photovoltaic properties was investigated. The optimized nanofibers obtianed in first step was selected to study effect of the mixture concentration by DSSCs device. Seven pastes containing mixed P25 and the optimized nanofibers (labeled as NF1, NF2, NF3, NF5, NF7, NF10 and NF100) were prepared with nanofibers concentration of 1, 2, 3, 5, 7, 10 and 100 wt.%, respectively. The TiO_2 composite films were prepared by the doctor blade technique. Dye sensitization was performed by immersing the compositefilms in dye solution (N719, Solaronix SA, Switzerland) for at least 24 h in a sealed beaker. An electrolyte was injected into the electrodes. Finally, the photovoltaic properties of the prepared samples were immediately investigated by a solar simulator under AM1.5G condition.

Results and discussion

Fig. 1(a) shows XRD patterns of the starting ilmenite mineral, as-synthesized nanofibers and calcined nanofibers at 300-1,000 °C for 2 h. The crystalline structure of the starting ilmenite mineral appears in rutile phase, while the as-synthesized nanofibers are in the hydrogen titanate $H_2Ti_xO_{2x+1}$, e.g., trititanate ($H_2Ti_3O_7$) [3,5]. After calcination at temperature range of 300-400 °C, the calcined samples demonstrate TiO_2(B). The nanofibers were dehydrated and re-crystallized into the metastable form of TiO_2 (B) [5]. At 500 °C, the calcined nanofibers reveal a bi-crystalline mixture consisting of TiO_2 (B) and anatase TiO_2 (Fig. 1(a)). The XRD patterns of the samples calcined at 600, 700, 800, 900 and 1,000 °C for 2 h are consisted of a mixture of anatase, rutile phase of TiO_2

[5] and Fe_2O_3 (Fig. 1(b)). At 600-700 °C, the crystalline of TiO_2 (B) phase disappears and the transformation from anatase phase TiO_2 to rutile phase TiO_2 initiates at this temperature range. Besides, as the calcination temperature increases to 800-1,000 °C, the anatase phase TiO_2 is almost non-observed, while the rutile phase TiO_2 is dominant.

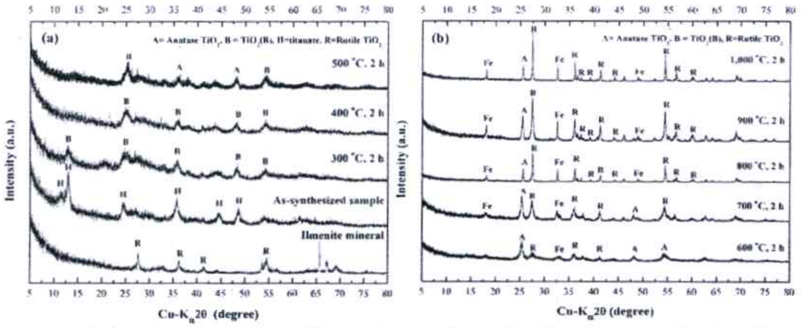

Fig. 1 XRD patterns of (a) the starting ilmenite mineral, the as-synthesized nanofibers and the calcined nanofibers for 2 h at 100-500 °C and (b) the calcined nanofibers for 2 h at 600-1,000 °C.

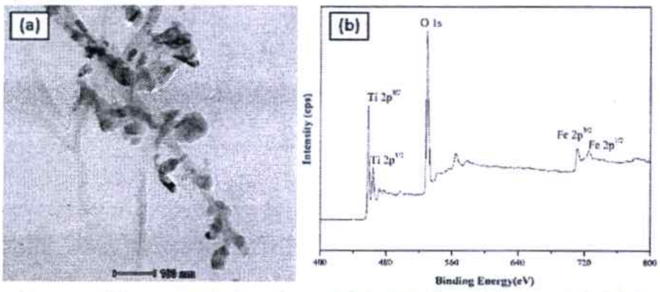

Fig. 2 (a) TEM image of nanofibers calcined at 800 °C for 2 h at 43,000 magnified and (b) XPS spectra of nanofibers.

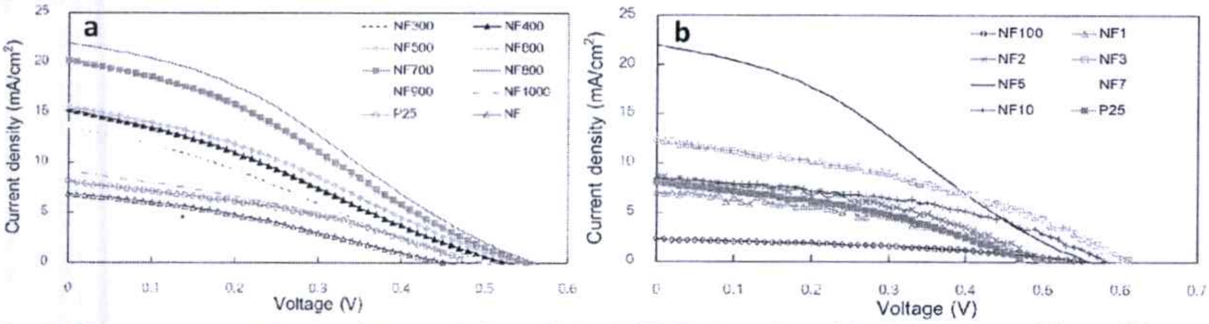

Fig. 3 Photocurrent–voltage characteristics of the DSSCs based on (a) titanate nanofibers, P25 and 5% titanate nanofibers calcined at various temperatures for 2 h mixed P25 and (b) P25 mixed titanate nanofibers calcined at 800 °C for 2 h with different ratio.

Table 1. The photovoltaic properties of the DSSCs based on titanate nanofibers, P25 and 5% titanate nanofibers calcined at various temperatures for 2 h mixed P25.

Samples	Open circuit voltage, V_{oc} (V)	Short Circuit current density, J_{sc} (mA/cm^2)	Fill Factor, FF	Energy conversion efficiency, η (%)
NF	0.45	6.90	0.32	1.01
NF300	0.50	13.55	0.28	1.92
NF400	0.52	15.31	0.29	2.35
NF500	0.54	15.58	0.30	2.63
NF600	0.54	20.23	0.30	3.38
NF700	0.55	20.19	0.30	3.43
NF800	0.56	22.01	0.31	3.90
NF900	0.50	13.75	0.26	1.86
NF1000	0.49	9.07	0.38	1.60
P25	0.47	8.17	0.37	1.45

Fig. 2(a) shows TEM image of the calcined nanofibers at 800 °C for 2 h. Before calcination treatment, the microstructure of as-synthesized nanofibers demonstrate the fiber-like structure with the lengths and diameters of 2-7 μm and 20-90 nm, respectively. The as-synthesized nanofibers calcined for 2 h at 300-700 °C for 2 h preserve their nanofiber morphology (not shown in this paper). Therefore, the synthesized samples can maintain 1-D nanostructure and utilized in various applications operated at high temperatures. Interestingly, the nanofibers transform to nanorods as calcined temperature elevates to 800 °C (Fig. 2(a)). Recent papers reported that the transformation of nanorod and submicron particle structure majorly caused by increasing calcination temperature [5]. Additionally, the chemical composition of titanate nanofibers was analyzed by XPS as shown in Fig. 2(b). The titanate nanofibers exhibit Ti2p photoelectron peaks accompanying the position of the Ti^{4+} $2p^{3/2}$ and Ti^{4+} $2p^{1/2}$ peak positioned at 458.7 and 464.3 eV, respectively. The peak located at 710.5 and 724.0 eV, indicatethe existence of Fe_2O_3 with $2p^{3/2}$ and $2p^{1/2}$, respectively. This result suggeststhe replacement of Fe^{3+} to Ti^{4+} of TiO_2 lattice forming Fe-O-Ti bonds [6]. In addition, XPS spectrum of O 1s peak located at 529.80 eV also exists in the sample [6].

The photocurrent density–voltage (J-V) curve of the DSSCs was carried out under simulated solar light with intensity of 100 mW/cm^2. Fig. 3(a-b) show the photocurrent-voltage curve based on various TiO_2 photoanode. The characteristic of the photovoltaic (PV) parameters, including the value of short-circuit photocurrent density (J_{sc}), open-circuit photovoltage (V_{oc}), fill factor (*FF*) and energy conversion efficiency (η) are summarized in Table 1 and 2. The efficiency of DSSCs based on P25 is about 1.45%. For the device using 5% titanate nanofibers calcined at various temperatures range of 300-1,000 °C for 2 h (NF300-NF1000) mixed with P25 as working electrode, the η of DSSC is improved with increasing calcined temperature (Fig. 3(a)) and Table 1). The DSSC based on NF800 shows the superiority of η approximately 3.90%. It is indicated that the enhanced photovoltaic performance is attributed to the incorporation of nanofibers calcined at 800 °C for 2 h into P25 due to the increasing specific surface area, the porosity and roughness factor of the electrodes [7]. The high surface area of TiO_2 nanofibers or nanorods in TiO_2 matrix can significantly increase the amount of absorbed dye molecules in the device that can assist the electron injection to increase the corresponding current density [7]. Furthermore, the nanoparticles/nanofibers composite electrodes may support the enhancement of light scattering ability of the solar spectrum and promote the light-harvesting efficiency of nanofiber and nanorod structure [7]. However, with increasing calcination temperature to 900 and 1,000 °C, the η decreases to 1.86 and 1.60%, respectively, which might be due to the agglomeration of the particles and difficulty of electron movement [7].

For one-dimensional nanostructures such as nanofibers and nanorods, the charge recombination could decrease and charge transfer rate could increase because of its straight charge transfer path divided by nanofibers and nanorods, which associate to an increase of electron transport efficiency in the device [7]. The existence of Fe^{3+} in TiO_2 can generate a trapping level in TiO_2, that can retard the electron-hole recombination of electrons in TiO_2 conduction band and dye or electrolytes and enhance the electron charge transfer of dye to conduction band of TiO_2 [8]. Furthermore, it is reasonable to think that the relatively larger size of the nanofibers and nanorods than nanoparticles could improve the diffusion of liquid electrolyte, which is beneficial for electron transfer in I_3^-/I^- electrolyte [4]. Furthermore, nanorod structure is much shorter than nanofibers and hence can have much lower resistance that in turn can cause higher currents [9]. The effect of various amounts of nanofibers calcined at 800 °C for 2 h mixed P25 on photovoltaic properties is shown in Fig. 3(b) and Table 2. The results show that the increase of amount of nanofiber calcined at 800 °C for 2 h leads to enhance in η of DSSCs. The highest η of 3.90% is obtained at about 5 wt.% amount of nanofiber calcined at 800 °C for 2 h. However, when the amount of nanofiber calcined at 800 °C for 2 h is over 5%, the J_{sc} and η tend to decrease. This result may be due to light scattering out of cells by high concentration of nanofibers, resulting to lower current density [7].

Table 2. The photovoltaic properties of the DSSCs based on P25 mixed titanate nanofibers calcined at 800 °C for 2 h with different ratio.

Samples	**Open circuit voltage, V_{oc} (V)**	**Short Circuit current density, J_{sc} (mA/cm^2)**	**Fill Factor, FF**	**Energy conversion efficiency, η (%)**
NF1	0.50	7.11	0.41	1.50
NF2	0.50	8.68	0.42	1.84
NF3	0.58	12.33	0.39	2.85
NF5	0.56	22.01	0.31	3.90
NF7	0.60	12.62	0.38	2.93
NF10	0.58	8.58	0.43	2.16
NF100	0.54	4.57	0.37	0.94
P25	0.47	8.17	0.37	1.45

Conclusion

Nanofibers were synthesized via hydrothermal method using the low-cost ilmenite mineral as the starting material. The prepared sample shows titanate phase ($H_2Ti_xO_{2x+1}$). As calcination temperature increases to 300-700 °C, the prepared samples maintain fiber-like morphology. The transformation of nanofiber to nanorod/nanoparticle is occurred at calcination temperature raises to 800 °C. The η of DSSC increases with increasing calcination temperature of nanofiber. The greatest η of 3.90% is obtained from DSSC fabricated from 5 wt.% nanofibers calcined at 800 °C for 2 h mixed with P25. This increase in the device efficiency is attributed to high surface area, higher light scattering and light harvesting, low charge recombination and fast electron-transfer rate by nanofibers.

References

[1] B. O'Regan, M. Grätzel, A low-cost, high-efficiency solar cell based on dye-sensitized colloidal TiO_2 films, Nature 353 (1991) 737-740.

[2] J. Jiu, S. Isoda, F. Wang, M. Adachi, Dye-sensitized solar cells based on a single-crystalline TiO_2 nanorod film, J. Phys. Chem. B 110 (2006) 2087-2092.

[3] A. Simpraditpan, T. Wirunmongkol, S. Pavasupree, W. Pecharapa, Simple hydrothermal preparation of nanofibers from a natural ilmenite mineral, Ceram. Inter. 39 (2013), 2497-2502.

[4] J.G. Yu, J.J. Fan, K. Lv, Anatase TiO_2 nanosheets with exposed (001) facets: improved photoelectric conversion efficiency in dye-sensitized solar cells, Nanoscale 2 (2010) 2144-2149.

[5] A. Simpraditpan, T. Wirunmongkol, S. Pavasupree, W. Pecharapa, Effect of calcination temperature on structural and photocatalyst properties of nanofibers prepared from low-cost natural ilmenite mineral by simple hydrothermal method, Mater. Res. Bull. (2013), http://dx.doi.org/10.1016/j.materresbull.2013.04.083

[6] B. Tian, C. Li, J. Zhang, One-step preparation, characterization and visible-light photocatalytic activity of Cr-doped TiO_2 with anatase and rutile bicrystalline phases, Chem. Eng. J. 191 (2012) 402-409.

[7] A.E. Shalan, M.M. Rashad, Y. Yu, M. Lira-Cantu, M.S.A. Abdel-Mottaleb, Controlling the microstructure and properties of titania nanopowders for high efficiency dye sensitized solar cells, Electrochim. Acta 89 (2013) 469-478.

[8] M. Wolf, H. Rauschenbacht, Series resistance effects on solar cell measurements, Adv. Energy Conv. 3 (1963) 455-479.

[9] L. Francis, A.S. Nair, R. Jose, S. Ramakrishna, V. Thavasi, E. Marsano, High efficiency dye sensitized solar cells from rutile nanorods, Energy 36 (2011) 627-632.

Micro/Nano Science and Engineering

10.4028/www.scientific.net/AMR.925

Efficiency Enhancement in Dye-Sensitized Solar Cell Using TiO_2 /Ilmenite-Derived Nanofiber Composite as Working Electrode

10.4028/www.scientific.net/AMR.925.600